NUMERICAL MODELLING OF MAGNETIC MATERIALS FOR COMPUTER AIDED DESIGN OF ELECTROMAGNETIC DEVICES

by

Jian Guo Zhu, M. Eng. Sc., B.E. (Elec.)

Submitted for the Degree of Doctor of Philosophy

at

University of Technology, Sydney

July, 1994

SUMMARY

In design and simulation of electromagnetic devices, it is essential to model the properties of magnetic materials, such as the relation between magnetic flux density B and magnetic field H or B-H curve and electromagnetic power losses or core losses with various kinds of magnetic field excitations, in order to assess the performance correctly.

The major part of the work is concerned with the modelling of hysteresis loops with alternating magnetic field, and core losses with alternating and/or rotating magnetic fields. Various novel models are developed.

A critical comparison between various available models of magnetic hysteresis shows that the Preisach theory appears to be suitable for practical engineering applications. A new normal Preisach model is obtained with the help of a graphical representation of the theory. The new model features simple formulation and easy parameter identification. The input data is the limiting hysteresis loop. It can provide correct results for a medium or large magnetic field, but fails when the hysteresis loop to be predicted is close to the origin of the B-H plane owing to some intrinsic defects of the model. These defects are eliminated in a new generalised model, which contains a reversible magnetisation component and a magnetisation feed back. The input data required by the generalised model are the limiting hysteresis loop and the normal magnetisation curve. These can be obtained from either manufacturers' data sheets or from simple measurements. Better accuracy is achieved by the generalised model.

New dynamic discrete circuit models with hysteresis, eddy current, and anomalous losses included are developed to simulate the performance of magnetic cores in devices with non-sinusoidal alternating flux. At low frequencies, a simple equivalent circuit model consisting of a constant equivalent resistor for eddy current loss, a nonlinear equivalent resistor for anomalous loss, and a non-ideal inductor for modelling the hysteresis loop and hysteresis loss is used. This model is generalised into a ladder network model for simulation at high frequency by subdividing the cross section of the core into a few assumed eddy current paths. All parameters of these models can be identified from data sheets provided by manufacturers.

For rotational core loss measurement, a single sheet square specimen tester is developed. The precision of two dimensional field strength measurement at the surface of the specimen is improved by a novel sandwich H sensing coil arrangement. The relationship between the core loss due to the rotational component of magnetic field and the total core loss is clarified using a new equation and the arguments are supported by the experimental results.

Rotational core losses in grain oriented and non-oriented silicon steel sheets were measured using the testers at the University of Technology, Sydney and the Physikalisch-Technische Bundesanstalt, Braunschweig, Germany. These measurements provided much useful information for both understanding of the loss mechanisms and modelling of the losses.

Similar to the case of alternating core losses, rotational core loss can also be separated into rotational hysteresis, eddy current, and anomalous losses. The rotational hysteresis loss is fitted by a novel model based on a strong analogy between the retarding torque due to the rotational hysteresis loss and the electromagnetic torque in a single phase induction machine. With a circular flux density, the rotational eddy current loss is twice as much as the alternating eddy current loss. The rotational anomalous loss can be modelled using the same formula as for alternating anomalous loss, but the coefficient of rotational anomalous loss is generally a function of flux density, and eventually reduces to zero when the material is saturated and all domain walls disappear.

Total core losses with an elliptical flux density are predicted from the pure rotational and alternating core losses by a new formulation derived from the total core loss formula used in rotational core loss measurement. The new model is applicable to hysteresis as well as total core losses. Comparisons with experimental data show that this new model is more accurate than a linear interpolation between alternating and pure rotational core losses.

Core losses in an AC permanent magnet motor are modelled. The magnetic flux density distribution is calculated by a finite element code. Fourier series analysis is used for an arbitrary two dimensional rotating flux density. The total core loss is finally calculated by summing up all the contributions from different elliptically rotating harmonics of flux density in each finite element. The discrepancy between calculated and measured results is about 13%.

ACKNOWLEDGMENTS

The author wishes to express his deep appreciation to his supervisor, Prof. V.S. Ramsden, for his patience, encouragement, and expert technical guidance given throughout the development of this work.

He would like to thank his co-supervisor, Dr. S.Y.R. Hui, Department of Electrical Engineering, University of Sydney, for his advice and co-operation in dynamic modelling of magnetic cores, especially, application of the TLM method.

Acknowledgment and gratitude are accorded to Dr. J.D. Sievert, Magnetic measurement Techniques Laboratory, Physikalisch-Technische Bundesanstalt (PTB), Braunschweig, Germany, for fruitful discussions and co-operation in improvement of rotational core loss measuring techniques.

Thanks to Dr. P.A. Watterson, School of Electrical Engineering, University of Technology, Sydney, for friendly and helpful discussions and co-operation in finite element analysis of rotating electrical machines.

Useful discussions were provided by Dr. J.B. Dunlop, Commonwealth Scientific and Industrial Research Organisation (CSIRO), Division of Applied Physics, Lindfield, NSW, Australia, (National Measurement Laboratory), Dr. G. Bertotti and Dr. F. Fiorillo, Istituto Elettrotecnico Nazionale Galileo Ferraris, Torino, Italy, and Mr. H. Ahlers, Magnetic Measurement Techniques Laboratory, PTB, Braunschweig, Germany.

Experimental assistance from Dr. R. Day and Mr. B. Kalan, CSIRO, and other colleagues from this university, especially, Mr. A. Curgenven, Mr. W. Holliday, and Mr. G. Hunter are gratefully acknowledged.

Special thanks are due to:

(1) Department of Employment, Education and Training, Australia, for an Overseas Postgraduate Research Scholarship (OPRS), which allowed the author to carry out the work for this dissertation;

(2) CSIRO and UTS for a joint grant on rotational core loss measurement;

(3) Department of Industry, Technology and Regional Development (DITRD), Australia, and PTB, Germany, for the financial support to a bilateral collaborative research project on improvement of measuring techniques and models of rotational core losses.

Finally, but perhaps most important, the author wishes to thank his wife (Yuan), his son (Jiang), and his parents for their encouragement and understanding. Their enthusiasm for his work is something for which he will always be grateful.

CONTENTS

LIST OF SYMBOLS*

A	Cross sectional area of a magnetic core (m^2)
B	Magnetic flux density (T)
B_a	Alternating component of an elliptically rotating flux density (T)
B_{maj}	Major axis of an elliptically rotating flux density (T)
B_{min}	Minor axis of an elliptically rotating flux density (T)
B_p	Peak value of flux density (T)
B_r	Rotational component of an elliptically rotating flux density (T)
B_x	X component of flux density (T)
B_y	Y component of flux density (T)
B_Δ	Incremental magnetic flux density (T)
b	Thickness of a silicon steel sheet (m)
C_a	Alternating anomalous loss coefficient (SI units)
C_{ar}	Rotational anomalous loss coefficient (SI units)
C_e	Eddy current loss coefficient (SI units)
E	Electric field intensity (V/m)
f	Frequency (Hz)
H	Magnetic field strength (A/m)
H_a	Alternating component of an elliptically rotating field strength (A/m)
H_b	Biasing magnetic field strength (A/m)
H_{maj}	Major axis of an elliptically rotating field strength (A/m)
H_{min}	Minor axis of an elliptically rotating field strength (A/m)
H_r	Rotational component of an elliptically rotating field strength (A/m)
H_s	Magnetic field strength at the surface of a specimen (A/m)
H_{sat}	Saturation magnetic field strength (A/m)
H_x	X component of magnetic field strength (A/m)
H_y	Y component of magnetic field strength (A/m)
H_Δ	Incremental magnetic field strength (A/m)
I	Current (A)
i_a	Current in an equivalent resistor for anomalous loss (A)
i_e	Current in an equivalent resistor for eddy current loss (A)
i_L	Current in an inductor (A)
i_s	Excitation current (A)
J	Current density (A/m^2)
J_x	X component of current density (A/m^2)

* symbols which are not listed here are defined where they appear.

K_H	Coil coefficient of an H sensing coil (SI units)
L	Inductance (H)
l_m	Mean length of a flux path in an annular ring sample (m)
M	Magnetisation (A/m)
M_{anh}	Anhysteretic magnetisation (A/m)
$M_d(H)$	Magnetisation on the downward trajectory of the limiting hysteresis loop for a given H (A/m)
$M_i(H)$	Magnetisation on the initial magnetisation curve for a given H (A/m)
M_{irr}	Irreversible component of magnetisation (A/m)
M_{rev}	Reversible component of magnetisation (A/m)
M_s	Saturation magnetisation (A/m)
$M_u(H)$	Magnetisation on the upward trajectory of the limiting hysteresis loop for a given H (A/m)
m	Magnetic moment (J/T)
N	Number of turns of a coil
P_a	Alternating anomalous loss (W)
P_c	Alternating core loss (W)
P_e	Alternating eddy current loss (W)
P_{ea}	Sum of alternating eddy current and anomalous losses (W)
P_h	Alternating hysteresis loss (W)
p_a	Average specific alternating anomalous loss over a cycle (W/kg)
p_e	Average specific alternating eddy current loss over a cycle (W/kg)
p_h	Average specific alternating hysteresis loss over a cycle (W/kg)
P_r	Specific core loss due to rotational component of an elliptically rotating magnetic field (W/kg)
P_{ar}	Specific rotational anomalous loss (W/kg)
P_{er}	Specific rotational eddy current loss (W/kg)
P_{hr}	Specific rotational hysteresis loss (W/kg)
P_t	Total specific core loss (W/kg)
P_{ta}	Total specific anomalous loss (W/kg)
P_{te}	Total specific eddy current loss (W/kg)
P_{th}	Total specific hysteresis loss (W/kg)
R_a	Equivalent resistance for alternating anomalous loss (Ω)
R_B	Axis ratio of an elliptically rotating flux density
R_{DC}	DC resistance of an assumed eddy current path in a solid magnetic core (Ω)
R_e	Equivalent resistance for alternating eddy current loss (Ω)
R_H	Axis ratio of an elliptical rotating field strength

R_w	Winding resistance (Ω)
r_c	Correction factor to R_{DC} when anomalous loss is included
r_J	Correction factor to R_{DC} when variation of eddy current density is considered
T	Time period, and T=1/f (s)
T_p	Propagation time in the TLM method (s)
T_r	Retarding torque per unit volume due to P_r (Nm/m^3)
t	Time instant (s)
V_L	Voltage across an inductor or induced emf across the secondary coil of an annular ring sample (V)
V_s	Excitation voltage (V)
W	Energy (J)
δ	Skin depth, and $\delta = \sqrt{\frac{2}{\sigma\omega\mu_r\mu_o}}$ (m)
Φ	Magnetic flux (Wb)
$\gamma_{\alpha\beta}(H)$	Switching function of the elementary dipoles in the normal Preisach model of magnetic hysteresis
λ	Magnetic flux linkage (Wb)
$\mu(\alpha,\beta)$	Distribution function of the elementary magnetic dipoles in the normal Preisach model of magnetic hysteresis
μ_o	Permeability of a vacuum (Tm/A)
μ_r	Relative permeability
μ_Δ	Incremental permeability, and $\mu_\Delta = \frac{B_\Delta}{\mu_o H_\Delta}$
ρ_m	Mass density of material (kg/m^3)
σ	Conductivity ($\Omega^{-1}m^{-1}$)
ω	Angular frequency, and $\omega=2\pi f$ (rad/s)
χ_i	Susceptibility of the initial magnetisation curve, and $\chi_i = \frac{dM_i}{dH}$
χ_{io}	Initial susceptibility, and $\chi_{io} = \left.\frac{dM_i}{dH}\right\|_{H=0}$
χ_{ano}	Gradient or susceptibility of anhysteretic magnetisation curve at the origin, and $\chi_{ano} = \left.\frac{dM_{anh}}{dH}\right\|_{H=0}$

CHAPTER 1. INTRODUCTION

The wide variety of magnetic materials used in construction of electromagnetic devices can be rather sharply divided into two groups, the magnetically soft (easy to magnetise and demagnetise) and the magnetically hard (hard to magnetise and demagnetise) [1-5]. Soft magnetic materials, such as mild steel, silicon iron sheets (electrical steel), amorphous materials, nickel-alloys, soft ferrites (ceramic magnetic materials), and garnets, feature in high permeability, and are commonly used as cores in power transformers, stator and rotor materials for motors and generators, small special-purpose transformers and inductors in electronic systems, and microwave system components. On the other hand, hard magnetic materials, which have the distinguishing characteristic of high coercivity, are used for applications requiring permanent magnets, such as the permanent magnets in loudspeakers, pickups, actuators, synchronous machines, brushed and brushless DC motors.

In the design and simulation of electromagnetic devices, it is essential to model the properties of magnetic materials with various kinds of magnetic field excitations, such as the relation between magnetic flux density B and magnetic field strength H or B-H curve and electromagnetic power losses or core losses, in order to assess the performance correctly. For some materials, the dependence of B-H curves and core losses on temperature and in some cases even magnetostriction need to be considered.

Depending upon the circumstances it may be sufficient to use an empirically derived, lossless, but possibly nonlinear, relationship between flux and magnetising current. If the full power of the computer is to be applied to an accurate design and/or simulation of nonlinear devices, then the model must be extremely faithful to the actual response of the material. The development of numerical methods used in the computer aided design and analysis of electromagnetic devices in the last a few decades has enabled a more accurate and complete representation of the magnetic characteristics to be used to predict effects due to the intrinsic nonlinearity of magnetic materials [5-80].

For example, in power transformer analysis, models of the core based on the B-H characteristic have been used to predict phenomena occurring in power systems such as ferroresonance and transient voltages and currents, where saturation and hysteresis have a significant effect.

There has also been a need to represent the characteristics of hard magnetic materials; e.g. for the calculation of recoil effects in permanent magnet motors, skin effect in Alcomax, prediction of the performance of hysteresis motors, or in the analysis of magnetic-tape or disk recording.

Core losses of magnetic materials also have strong effects on the performance of electromagnetic devices. For a specified capacity, less material is required if high quality magnetic material of low core loss is used, and hence the size and weight can be reduced. This is especially true for high efficiency electrical machines. Besides efficiency, temperature rise in permanent magnet machines should be kept at a very low level in order to maintain the superior characteristic of modern permanent magnets, such as Neodymium Iron Boron (NdFeB). Therefore, core losses need to be precisely calculated in design, but unfortunately, the models currently in use are far from being satisfactory, owing to the very complicated mechanisms of core losses. Sometimes, the discrepancies are very large.

In devices like single phase transformers and inductors, core losses are caused by the alternating magnetic flux, of which only the magnitude varies with time, and they are generally attributed to hysteresis and eddy currents. With sinusoidal alternating magnetic flux, the hysteresis loss can be empirically determined by the Steinmetz law, and the eddy current loss by the classical calculation proportional to the square of the product of frequency and flux density magnitude [2-5]. Further studies, however, show that a considerable amount of core loss is caused by the motion of magnetic domain walls inside the magnetic material, and is known as anomalous loss or excess loss [2,3,5,81-103]. Although the exact mechanisms of this extra loss component has not yet been thoroughly understood, the dependence of this loss on excitation frequency and magnetic flux density magnitude has been theoretically established and corroborated experimentally to be an exponent of 1.5 [94,95,97,99,100]. The alternating core loss becomes much more difficult to predict when these devices are used in power electronic switching circuits, where the voltages and currents, hence the flux density and field strength, are non-sinusoidal [99,100,102,104-108].

In the simulation of electrical or electronic systems containing nonlinear inductors, transformers, and similar devices with alternating magnetic flux, equivalent circuits are commonly used [109-118]. In the conventional circuit model of magnetic cores, the magnetisation nonlinearity is modelled by an ideal inductor, and the core losses, including the hysteresis and eddy current losses, are modelled by a constant equivalent resistor [109-112]. The effects of magnetic hysteresis and anomalous loss, however, are not properly incorporated in this model. For dynamic modelling, the nonlinear B-H relationship and the hysteresis loss dissipated in the core are simulated by mathematical models of magnetic hysteresis, such as the Jiles-Atherton model [114] and the Preisach model [115-118], while

the eddy current and anomalous losses are accounted for by a constant equivalent resistor and a nonlinear equivalent resistor, respectively [115]. At high frequency, however, a ladder network can be used for the consideration of skin effect [116-118].

Moreover, in some parts of multiphase devices, such as the T joints of three phase transformers and the yokes of rotating electrical machines, both the magnitude and direction of the magnetic flux vary with time, that is the flux has a rotational component. The power loss caused by a rotating magnetic flux in magnetic material is referred as rotational core loss. Although rotational core loss has been under investigation for quite a long time, the underlying mechanisms of rotational core loss are still not completely understood [119-185].

Rotational core losses in electrical steel sheets with different types of rotating magnetic fluxes have been measured by various measuring techniques and instruments since 1889 [119-181], when the rotational hysteresis loss was first quantitatively determined by Baily [120]. In 1990, the Central Office of the International Electrotechnical Commission (IEC) started preparatory work for the standardisation of methods of measurement of rotational power loss [182]. For the standardisation, the Magnetic Measurement Techniques Laboratory, Physikalisch-Technische Bundesanstalt (PTB), Braunschweig, Germany, is currently organising an European intercomparison of rotational core loss measurements [186,187].

Considerable progress has also been achieved in the understanding of loss mechanisms and modelling. As for alternating core loss, rotational core loss can also be separated into three components due to hysteresis, eddy currents, and domain wall movement [168,179,184]. Based on experimental measurements and observations, the ratio of the rotational hysteresis loss to the alternating hysteresis loss in different electrical steel sheets has been studied, and the mechanisms of rotational hysteresis loss have been discussed in terms of domain wall motion and domain rotation [125-127,130,132,147,162,184]. The modelling of rotational hysteresis loss, however, is still far from being useful for practical engineering applications. With a purely rotational flux, the rotational eddy current loss is twice as much as the alternating eddy current loss. The rotational anomalous loss can be modelled using the same formula as for alternating anomalous loss, but the coefficient of rotational anomalous loss is generally a function of flux density, and eventually reduces to zero when the material is saturated and all domain walls disappear.

The rotating magnetic flux in rotating electrical machines is much more complicated. Owing to the lack of a proper model and data for rotational core losses, alternating core loss models were generally employed [188-191]. Recently, a few researchers included rotational core

losses in their calculations of core losses in rotating electrical machines. The discrepancies between the calculations and the experiments were from 10% to 20% [192-196].

The main topic of this dissertation is the development of practical models of magnetic materials for computer aided design and analysis of electromagnetic devices. In the development of these models, a few rules, which are considered as essential aspects for practical engineering applications, have been followed:

(1) The model should be able to describe the magnetic behaviour of the materials to sufficient accuracy for engineering design via numerical optimisation;

(2) All model parameters should be obtainable either from the manufacturer's data sheets or from some simple measurements;

(3) The resultant equations should be as convenient as possible for numerical implementation;

(4) As far as possible, the model should bear some physical background to explain the macroscopic phenomena and the underlying mechanisms of magnetic materials.

Chapter 2 discusses the modelling of magnetic hysteresis for practical engineering applications. After a critical comparison between various available models of magnetic hysteresis, the Preisach model is chosen for further study.

The theory of the normal Preisach model is represented graphically by the Preisach diagrams for different magnetisation states. The resultant formulation is very simple. For the convenience of application, a new simplified parameter identification method is developed, and the only data required for this model is the limiting hysteresis loop. The software implementation is illustrated in detail. The model is compared with the experimental data of different magnetic materials on major and minor hysteresis loops, hysteresis losses, and normal and incremental permeabilities. The calculation and measurement are in substantial agreement for an intermediate or large magnetic field, but the discrepancies in the hysteresis loss and the normal and incremental permeabilities become very large for a small magnetic field. This is attributed to two intrinsic defects of the normal Preisach model.

For more accurate simulation of magnetic hysteresis, a new generalised Preisach model is developed by combining the Stoner-Wohlfarth theory, Jiles-Atherton theory, and Vajda-Torre theory with the Preisach theory. A reversible magnetisation component and a magnetisation

feedback are added to the normal Preisach model. New methods for parameter identification are developed. The extra data required is the normal magnetisation curve. The new theory is verified with experiments on major and minor hysteresis loops, and the normal and incremental permeabilities.

In chapter 3, core losses with non-sinusoidal alternating magnetic flux are studied. New dynamic circuit models of magnetic cores for both low and high frequency applications with hysteresis, eddy current, and anomalous losses included are developed. For low frequencies, a simple equivalent circuit model consisting of a constant equivalent resistor for eddy current loss, a nonlinear equivalent resistor for anomalous loss, and a non-ideal inductor for modelling the hysteresis loop and hysteresis loss is used. This model is generalised into a ladder network model for simulation at high frequencies by subdividing the cross section of the core into a few assumed eddy current paths. Methods for parameter identification are given. All the parameters of these models can be identified from data sheets provided by manufacturers. The theory is verified by experiments on different magnetic materials under non-sinusoidal voltage excitations at both low and high frequencies.

In chapter 4, a review of rotational core loss measurement and modelling is represented. Measuring techniques of magnetic field strength and flux density, methods for evaluation of rotational core losses, and development of measuring apparatus are investigated. Current knowledge on the measurement, understanding, and modelling in both electrical steel sheets and rotating electrical machines are summarised and discussed.

In chapter 5, a new two dimensional single sheet square specimen tester for rotational core loss measurement is described. This tester is capable of measuring core losses with any magnetic flux patterns and any flux waveforms. It is fully computerised for control signal generation and data acquisition. A novel sandwich two dimensional magnetic field intensity sensing coil arrangement is described. This sandwich sensing coil arrangement is superior to the conventional surface magnetic field intensity sensing coils.

Rotational core losses of non-oriented silicon steel sheet Lycore-130 with both circular and elliptical flux densities at different excitation frequencies were measured with the new apparatus. The relationship between the core loss due to the rotational component of magnetic field and the total core loss is discussed using a new equation and the arguments are supported by the experimental results.

From December 8, 1993 to February 24, 1994, the author was invited to visit PTB as a guest scientist for a bilateral collaborative research project on the improvement of rotational core

loss measuring techniques. The visit was funded by PTB and Department of Industry, Technology and Regional Development (DIARD), Australia. As part of the project, it was agreed to carry out an inter-comparison between the testers at PTB and University of Technology, Sydney (UTS). This comparison will follow all the regulations used in the European Inter-Comparison of Rotational Core Loss Measurements, which is currently organised by PTB. The rotational core losses in four specimens of grain oriented (ORSI-100) and non-oriented (V270-35A) electrical steel sheets (part of the specimen set used for the European inter-comparison) will be used and compared. Core losses of these specimens have been measured with various magnetic flux patterns using the tester at PTB, and will be reported in chapter 5. Because of insufficient time, however, it has not been possible to complete the measurements using the tester at UTS and report the results of the inter-comparison in this thesis.

In chapter 6, various models of rotational core losses are developed. Firstly, the measured rotational core loss of electrical steel Lycore-130 is separated into rotational hysteresis, eddy current and anomalous losses by a loss separation procedure similar to the one used for alternating core loss separation in chapter 3.

The rotational hysteresis loss is then fitted by a novel model based on a strong analogy between the retarding torque due to the rotational hysteresis loss and the electromagnetic torque in a single phase induction machine. Possible underlying physics is discussed with the help of magnetic domain theory. Rotational hysteresis losses measured by various researchers show good agreement with the new model.

Total core losses with an elliptical flux density are predicted from the pure rotational and alternating core losses by a new formulation derived from the total core loss formula used in rotational core loss measurement. Comparisons with experimental data show that this new model is more accurate than a linear interpolation between alternating and pure rotational core losses.

Core losses in an AC permanent magnet motor are modelled. The magnetic flux density distribution is calculated by a finite element code. Loci of rotating flux density vectors at different positions in the stator core are illustrated. Fourier series analysis is used for an arbitrary two dimensional rotating flux density. The total core loss is finally calculated by summing up all the contributions from different elliptically rotating harmonics of flux density in each finite element. The discrepancy between calculated and measured results is about 13%.

In chapter 7, the developed models of magnetic hysteresis, alternating and rotational core losses, and possible future work are discussed.

Appendix A lists the publications based on the thesis work.

CHAPTER 2. MODELLING OF MAGNETIC HYSTERESIS

2.1 INTRODUCTION

A basic property of any magnetic material is the relation between magnetic flux density B and magnetic field strength H, or the B-H loop. During a magnetisation process, the medium exchanges energy with the source of the magnetic field. If the medium magnetisation is a single-valued function of the applied field, then the process is reversible and it conserves energy. In this case, the medium stores the energy supplied to it during magnetisation. When the applied field is reduced to zero, the medium returns this energy to the source. When the magnetisation is a multiple-valued function of the applied field, some energy is dissipated. For a very slow variation of magnetic field, this loss is caused by hysteresis, which is defined as the lagging of the changes in magnetisation behind the changes in magnetic field.

Although hysteresis of magnetic materials has long been of interest to scientists and engineers, significant progress in the understanding and modelling of hysteresis has been achieved in the last two decades, when the problem of accurately describing the B versus H or hysteresis characteristics of the materials assumed a greater importance, as computer calculations of magnetic fields and eddy-currents in nonlinear ferromagnetic materials became more sophisticated.

Early investigators in the field of magnetism explained the phenomenon of ferrohysteresis by the strong mutual interactions between magnetic moments, and postulated the existence of a frictional resistance to a rotation of the "magnetic molecules" [1], an idea which explains the most obvious effects of magnetic hysteresis. It was realised later that the frictional force is due to pinning of domain walls by defect sites inside the solid, which causes an opposing force to resist any changes in magnetisation [3,5,19].

When a magnetic field is applied to a solid, the magnetic domains less inclined to the applied field will expand while the others shrink. The motion of a domain wall occurs in two steps. Firstly, for a small increment of the applied field, the domain wall motion occurs in the form of reversible domain wall bowing, because of the pinning of the domain wall by a defect site inside the solid. Secondly, when the applied field is sufficient to get the domain wall away from the pinning site, the domain wall will take an irreversible jump to a new pinning site. This is known as a Barkhausen jump [3].

Another mechanism which gives rise to hysteresis is caused by magnetocrystalline anisotropy [5]. Ferromagnetic materials with higher anisotropy have greater hysteresis. In an anisotropic solid certain crystallographic axes are favoured by the magnetic moments which will prefer to lie along these directions as this leads to a lower energy. The magnetic moments can be dislodged from the direction they are occupying by application of a magnetic field but when this occurs they jump to crystallographically equivalent axes which are closer to the field direction, and hence lower energy. This results in discontinuous and irreversible rotation of the magnetic moments which leads to a kind of switching action.

Early attempts to model hysteresis started from fitting equations to actual magnetisation data, but no single satisfactory equation has been developed to describe the processes involved in this [3]. Power series [6-8], rational polynomials [9-12] and some other analytical expressions [13-15] have been used as the usual approaches to the empirical curve fitting method. A recent application of the rational function method was made by Rivas, Zamarro, Martin and Pereira [16] in 1981, in which families of major hysteresis loops were generated and the results showed good agreement with experimental data. Such approaches can be accurate in the representation of some part of B-H curves, but would not be able to describe all processes of magnetisation, since they usually do not bear any theoretical basis.

With better understanding of magnetic hysteresis various models of hysteresis have been developed based on a theoretical approach to the problem. In 1948, Stoner-Wohlfarth [17] postulated a theory based on the rotation of the magnetic moments of single-domain particles with respect to their easy axes. This model does not account for the interaction between domains, however, and as a result, it does not describe nonsymmetrical minor loops. In 1990, Atherton and Beattie [18] suggested a modification to incorporate particle interaction into the Stoner-Wohlfarth model by the addition of a mean field term, but numerical implementation and experimental verification of the theory was not reported.

Another competing mathematical description is the Preisach model [22-41]. This was developed in 1935 but has received general attention only within the last two decades. It assumes that each of the domains possesses an individual rectangular hysteresis loop, of which the positive and negative transition points for each domain are different, and the interaction between domains can be introduced by assuming local fields acting on the domains. Even though the Preisach model is based on such simple assumptions, it gives valuable results that are in agreement with experiments on different magnetic materials [42-46], and all the various types of hysteresis curves, including minor hysteresis loops, can readily be generated by considering a distribution of these domains.

In recent years, the Preisach model has been greatly improved and generalised to represent dynamic hysteresis [41,47], which accounts for the influence of the rate of variation of magnetic field strength on branching, and magnetisation-dependent hysteresis [41,48-50,53-59], which assumes that the magnetisation for a given field strength depends on both the previous magnetic history and the current value of magnetisation. It has also been generalised to represent vector hysteresis of two and three dimensions [41,60-67], which takes into account rotational hysteresis, i.e. the hysteresis when the direction of the applied magnetic field varies in space. According to Mayergoyz [41] the generalised Preisach model can deal with hysteresis phenomena of any physical nature.

In 1970, based on the fact that a trajectory of flux linkage vs. current is uniquely determined by the last point at which the time derivative of flux linkage changes sign, Chua and Stromsmoe worked out a lumped circuit model for nonlinear inductors exhibiting hysteresis loops [73], which included a restoring function and a dissipating function, and further generalised the model to include static hysteresis. This model exhibits many important hysteretic properties commonly observed in practice. According to the study of Saito, Hayano, Yamamura, and Tsuya [74], both the Preisach and Chua type models can be derived from a common picture illustrating the magnetic field reversals in a magnetisation process.

In 1986, an interesting differential equation model of hysteresis in ferromagnetically soft magnetic materials was derived by Coleman and Hodgdon [68,69], and was further generalised to describe rate dependent magnetisation process by Hodgdon [70,71]. Agreement with experimental data was achieved in simulations of an RLC circuit containing a ferromagnetic core [72]. This model is simple to understand and to implement, but it requires a numerical integration, which lowers the speed of computation, and the identification of model parameters is particularly empirical, since they are very sensitive to experimental errors [44].

Also in 1986, Jiles and Atherton developed a theory based on the inhibition of domain wall motion by pinning sites (i.e. inclusions, voids, crystal boundaries, and lattice defects) [5,19]. This theory is most helpful for describing the behaviour of materials in which domain motion is the primary hysteresis mechanism, while the practical application to magnetic field analysis is handicapped by the difficulty of parameter identification, despite the fact that the methods to calculate the parameters of this model from a set of experimental magnetisation measurements were developed later by Jiles and Thoelke [5,20,21].

In 1991, Hayano, Namiki, and Saito derived a Chua type model based on a simple bar-like domain-wall model, and showed that the Hodgdon model [70] mentioned above was one of the Chua type models [75].

Recently, hysteresis models based on micromagnetic approaches [76-79] have been proposed, but they generally require too much computing power to be useful for calculating hysteresis curves for bulk ferromagnetic materials.

Based on the strong macroscopic analogy between the elastohysteresis and the magnetic hysteresis, Favier, Guelin, and Cammarano proposed a model of the magnetisation of magnetic materials using a phenomenological elastohysteresis theory [80]. This model involves judicious choice of the thermodynamic potential function and empirical estimation of parameters. So far, the modelling of magnetisation of any practical magnetic material has not been reported in the literature, using this method.

In summary, the analytical expressions used in curve fitting approaches are simple and accurate as long as only the major loops are concerned, but they are not able to describe the minor loops correctly for the lack of physical background [44]. The Jiles-Atherton model and the Stoner-Wohlfarth model are strongly related with the underlying physical principles, but they both have the demerits of difficult parameter identification and low accuracy in minor loop simulations. The Hodgdon model and the Chua type models are easy to understand and implement, while the parameter identification is more or less empirical, and the accuracy in minor loop modelling is lower than the Preisach model, from comparison with experimental data [44]. The Preisach model appears to be one of the most promising candidates for practical engineering applications. It is strongly related with the mechanisms of magnetic hysteresis, and can describe various macroscopic hysteretic phenomena. It may be argued that the Preisach model is not simple to understand, nor to implement: the experimental data needed are very numerous and delicate to interpolate and the control of the memorised turning or reversal points must also be done properly, but the final formula is rather simple to compute. It requires only "plus" and "minus" operators, and the results fit the experimental behaviour of different magnetic materials [44-46].

In order to determine the magnetic domain distribution function in the Preisach model a set of first and second order transition curves are required [41]. At present, this is difficult, since for practical engineering applications of the model, it is generally desired that all parameters are obtainable either from standard experimental data provided by manufacturers of magnetic materials, or from simple experimental measurements readily performed by users, such as the limiting hysteresis loop and the normal magnetisation curve.

In this chapter, new methods are developed to enable Preisach models of magnetic hysteresis to be obtained and used for engineering applications.

In section 2.2, the Preisach theory of magnetic hysteresis is explained graphically with the Preisach diagrams for various magnetisation states. With the help of these Preisach diagrams, the magnetisation for a given field strength is expressed in terms of the magnetisation of the last reversal point and the area integration of the elementary magnetic dipole distribution function over a right triangle bounded by the magnetic field strength of the last reversal point and the given magnetic field strength on the Preisach diagram. This area integration is related to the limiting hysteresis loop, and hence the determination of the distribution function itself is avoided.

Aspects of the numerical implementation of the new normal Preisach model are illustrated in detail, and theoretical predictions are compared with measured hysteresis loops, hysteresis losses, and permeabilities (normal and incremental) of different magnetic materials. It is suggested that errors at low values of field strength are due to intrinsic properties of the normal Preisach model, such as zero initial susceptibility and congruent minor loops.

Section 2.3 presents a new generalised Preisach model. A new combination of the Stoner-Wohlfarth theory, Jiles-Atherton theory, and Vajda-Torre theory of magnetic hysteresis with the normal Preisach model leads to a new model which includes reversible and irreversible magnetisation components and a new nonlinear magnetisation feedback. Parameter identification requires only the normal magnetisation curve and the limiting hysteresis loop. Experimental verification shows enhanced accuracy.

2.2 NORMAL PREISACH MODEL OF HYSTERESIS

2.2.1 General Theory

The Preisach theory describes the hysteresis of a magnetic material via an infinite set of magnetic dipoles, which have rectangular elementary hysteresis loops of different switching values of magnetic field strength (α,β), as shown in Fig.2-1(a), where α and β are the magnetic field strength in the increasingly positive and negative directions respectively. The magnetisation M and flux density B induced by the applied magnetic field H are expressed as

$$\begin{aligned} M &= \int_S \mu(\alpha,\beta)\gamma_{\alpha\beta}(H)\,d\alpha d\beta \\ &= \int_{S^+} \mu(\alpha,\beta)\,d\alpha d\beta - \int_{S^-} \mu(\alpha,\beta)\,d\alpha d\beta \end{aligned} \tag{2.1}$$

and

$$B = \mu_o(H+M) \tag{2.2}$$

where S is the triangular region $H_{sat} \geq \alpha \geq \beta \geq -H_{sat}$ on the (α,β) plane shown in Fig.2-1(b) (known as the Preisach diagram), H_{sat} the saturation magnetic field strength, $\mu(\alpha,\beta)$ the distribution function of the dipoles, $\mu(\alpha,\beta)=0$ if $(\alpha,\beta)\notin S$, $\gamma_{\alpha\beta}(H)=1$ on S^+, $\gamma_{\alpha\beta}(H)=-1$ on S^-, and μ_o the permeability of a vacuum.

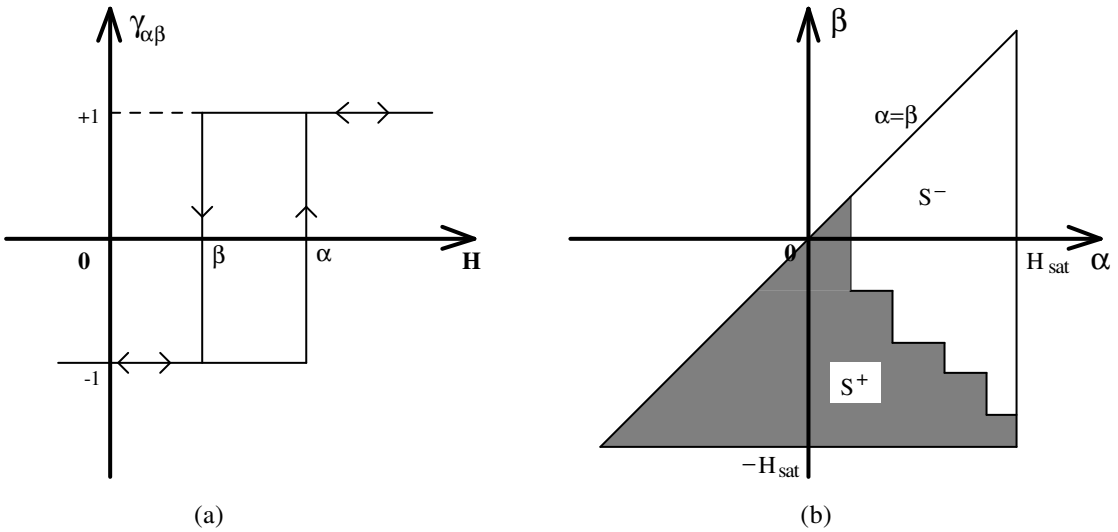

Fig.2-1 (a) Rectangular hysteresis loop of dipoles, and (b) Preisach diagram

Because of the symmetry of major hysteresis loops, we have

$$\mu(\alpha,\beta) = \mu(-\beta,-\alpha) \tag{2.3}$$

The interface between S^+ and S^- is determined by the history and the present state of magnetisation, as will be illustrated further in section 2.2.2.

2.2.2 Magnetisation Process and Preisach Diagrams

(1) The initial unmagnetised state

In the unmagnetised state, the origin O in Fig.2-2(a), the number of positively switched dipoles equals the number of negatively switched dipoles. Therefore,

$$\begin{aligned} M &= \int_{S^+} \mu(\alpha,\beta)\,d\alpha d\beta - \int_{S^-} \mu(\alpha,\beta)\,d\alpha d\beta \\ &= 0 \end{aligned} \tag{2.4}$$

The corresponding Preisach diagram is shown in Fig.2-2(b).

(2) On the initial magnetisation curve

When a magnetic material is magnetised from the initial unmagnetised state, it follows the initial magnetisation curve, as depicted by curve O-P_1 in Fig.2-2(a). According to the Preisach diagram shown in Fig.2-2(c), the induced magnetisation can be calculated by

$$\begin{aligned} M_i(H) &= \int_{S^+} \mu(\alpha,\beta)\,d\alpha d\beta - \int_{S^-} \mu(\alpha,\beta)\,d\alpha d\beta \\ &= \int_{\Delta ABC} \mu(\alpha,\beta)\,d\alpha d\beta \\ &= T(H,-H) \end{aligned} \tag{2.5}$$

where

$$T(\alpha,\beta) = \int_{\beta}^{\alpha}\int_{y}^{\alpha} \mu(x,y)\,dxdy$$

$$= \int_{\beta}^{\alpha}\int_{\beta}^{x} \mu(x, y)dydx \tag{2.6}$$

is the area integration over the right triangle of vertex (α,β), $T(\alpha,\alpha)=0$, and the subscript i denotes the initial M-H curve. Substituting (2.3) into (2.6) yields

$$T(\alpha,\beta)=T(-\beta,-\alpha) \tag{2.7}$$

(3) On the downward trajectory of the limiting loop

After reaching the positive saturation, the magnetic field strength H decreases, and the magnetisation M will vary following the downward trajectory, as illustrated by curve P_2-P_3 in Fig.2-2(a). The Preisach diagram is shown accordingly in Fig.2-2(d). The magnetisation can then be calculated by

$$\begin{aligned} M_d(H) &= \int_{S^+} \mu(\alpha,\beta)d\alpha d\beta - \int_{S^-} \mu(\alpha,\beta)d\alpha d\beta \\ &= M_i(H_{sat}) - 2T(H_{sat},H) \end{aligned} \tag{2.8}$$

where the subscript d denotes the downward trajectory of the limiting loop.

(4) On the upward trajectory of the limiting loop

Similarly after reaching negative saturation, the magnetic field strength H increases, and the magnetisation M varies along the upward trajectory, as illustrated by curve P_4-P_5 in Fig.2-2(a). The corresponding Preisach diagram is depicted in Fig.2-2(e), and the magnetisation is calculated as

$$\begin{aligned} M_u(H) &= \int_{S^+} \mu(\alpha,\beta)d\alpha d\beta - \int_{S^-} \mu(\alpha,\beta)d\alpha d\beta \\ &= -M_i(H_{sat}) + 2T(H,-H_{sat}) \end{aligned} \tag{2.9}$$

where the subscript u denotes the upward trajectory of the limiting loop.

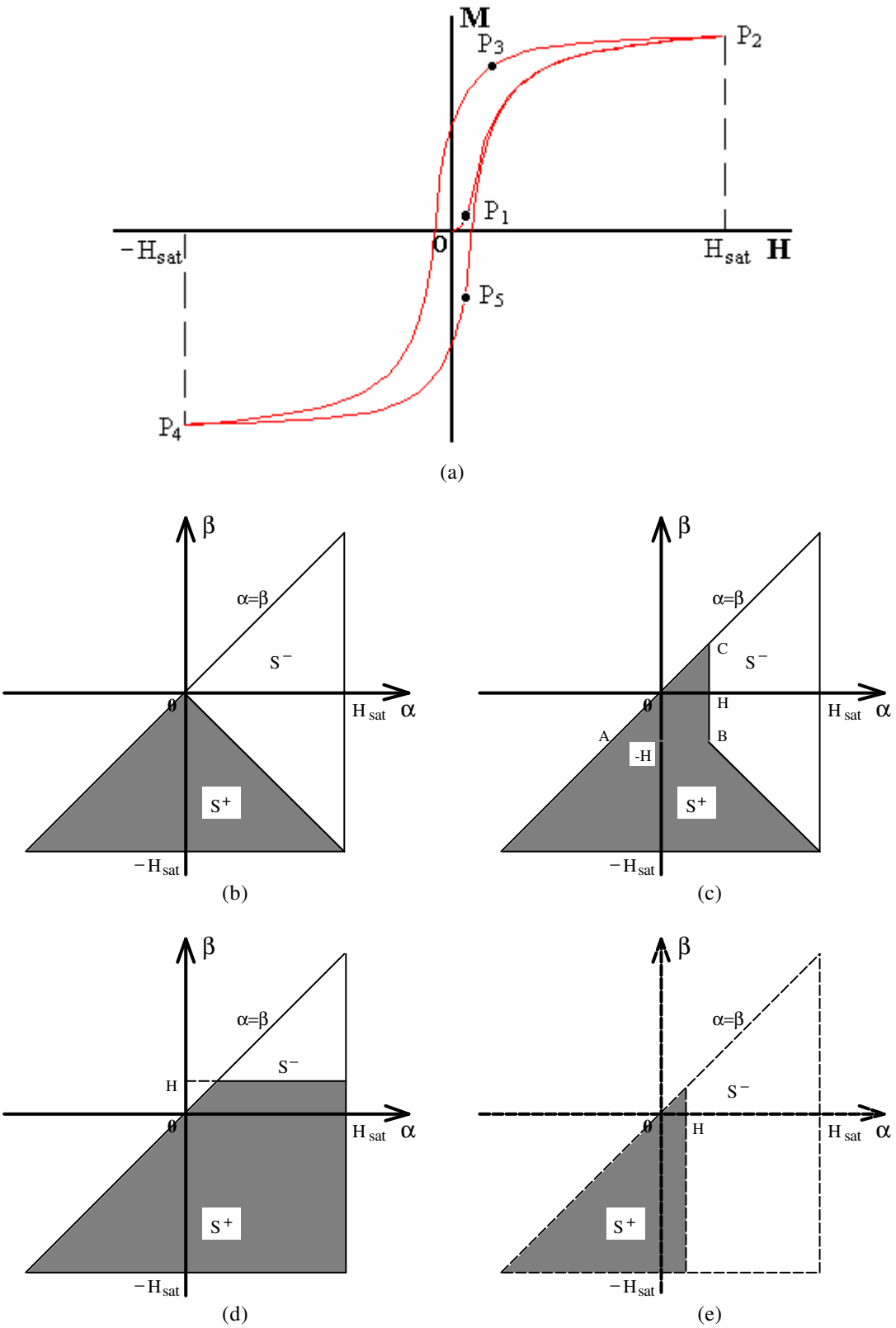

Fig.2-2 Magnetisation states and corresponding Preisach diagrams
(a) Initial magnetisation curve and limiting loop;
(b) Preisach diagram of unmagnetised state;
(c) Preisach diagram when magnetised along the initial magnetisation curve;
(d) Preisach diagram on the downward trajectory of the limiting loop;
(e) Preisach diagram on the upward trajectory of the limiting loop.

(5) General situation

For the general situation of the Preisach diagram as shown in Fig.2-3(a), where the operating point of magnetisation process is on a downward trajectory after n reversal points, the magnetisation can be similarly derived as

$$M(H) = M(H_n) - 2T(H_n,H) \tag{2.10}$$

while for the case of Preisach diagram shown in Fig.2-3(b), where the operating point of magnetisation process is on an upward trajectory after n reversal points, the magnetisation can then be calculated by

$$M(H) = M(H_n) + 2T(H,H_n) \tag{2.11}$$

where H_n is the magnetic field strength of the *n*-th (last) reversal point, and $M(H_n)$ is the corresponding magnetisation.

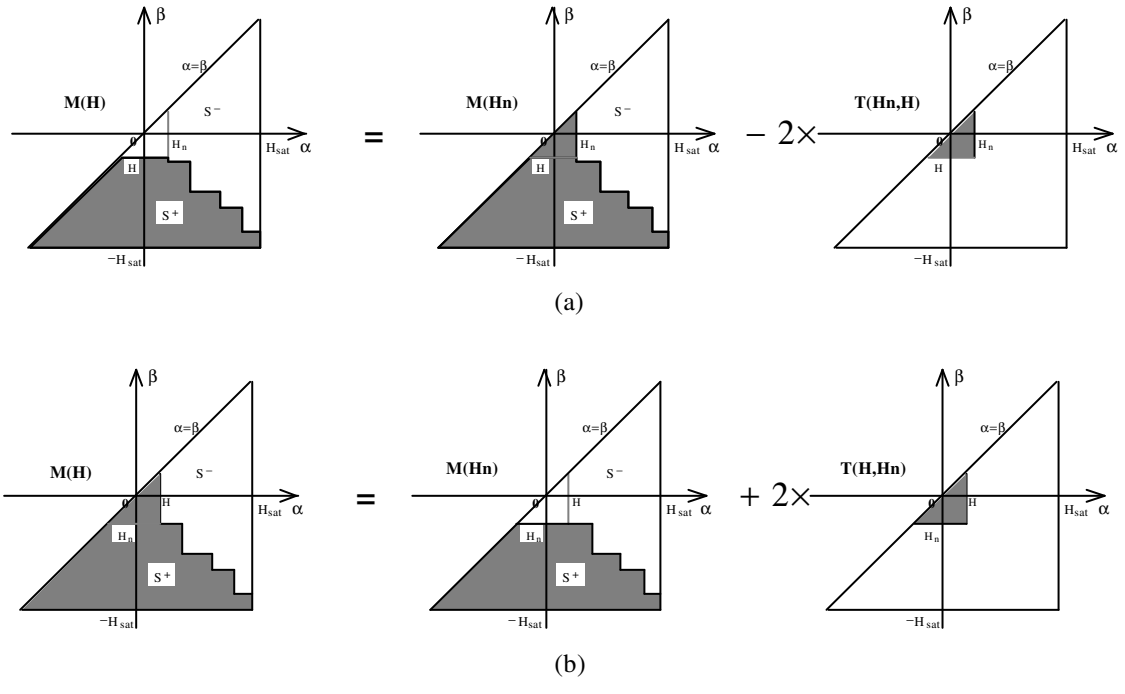

Fig.2-3 Preisach diagram for general situations after n reversals
(a) on a downward trajectory, and
(b) on an upward trajectory

2.2.3 Parameter Identification

From the description of magnetisation process by Preisach diagrams in section 2.2.2, it can be seen that the magnetisation for a given magnetic field strength can be related to the previous magnetisation history (previous reversal points, or local extrema of magnetisation) and the area integration of the distribution function of the elementary magnetic dipoles over a right triangle bounded by the current value and the last reversal point of magnetic field strength. Therefore, the only parameter to be identified is $T(\alpha,\beta)$, where $H_{sat} \geq \alpha \geq \beta \geq -H_{sat}$.

The function $T(\alpha,\beta)$ can be related to the limiting hysteresis loop, using the principle of superposition, as shown in Fig.2-4. Analytically, it can be written as

$$T(\alpha,\beta) = \frac{M_u(\alpha) - M_d(\beta)}{2} + \int_{-H_{sat}}^{\beta} \int_{\alpha}^{H_{sat}} \mu(x, y)\,dxdy \qquad (2.12)$$

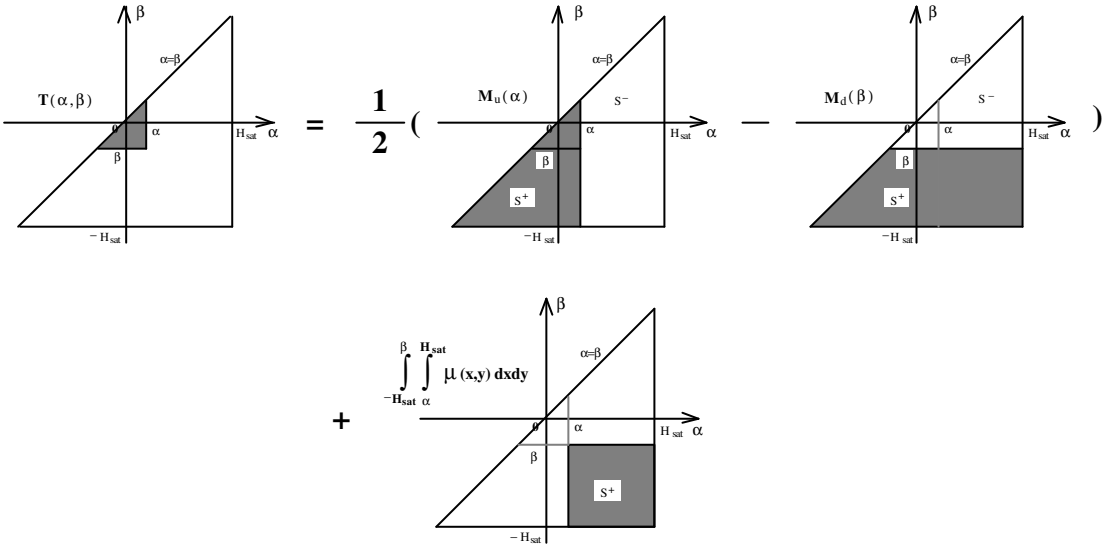

Fig.2-4 Relationship between $T(\alpha,\beta)$ and limiting loop data

In order to circumvent the difficulty of determining the distribution function $\mu(\alpha,\beta)$, a simple function transform is used to separate the dependence of the distribution function on the variables α and β as follows:

Let

$$\mu(\alpha,\beta) = m_A(\alpha)\, m_B(\beta) \qquad (2.13)$$

Because

$$\begin{aligned}\mu(\alpha,\beta) &= \mu(-\beta,-\alpha) \\ &= m_A(-\beta)\, m_B(-\alpha)\end{aligned} \tag{2.14}$$

therefore, the functions employed in the transform can be related as

$$m_A(\alpha) = m_B(-\alpha) \tag{2.15}$$

and

$$m_B(\beta) = m_A(-\beta) \tag{2.16}$$

Then, (2.12) can be further written as

$$\begin{aligned}T(\alpha,\beta) &= \frac{M_u(\alpha) - M_d(\beta)}{2} + \int_{-H_{sat}}^{\beta} m_B(y)dy \int_{\alpha}^{H_{sat}} m_A(x)dx \\ &= \frac{M_u(\alpha) - M_d(\beta)}{2} + F(\alpha)F(-\beta)\end{aligned} \tag{2.17}$$

where

$$F(\alpha) = \int_{\alpha}^{H_{sat}} m_A(x)dx \tag{2.18}$$

Again, by superposition of the Preisach diagrams in Figs.2-2(c)-(e), when $H \geq 0$, $M_d(H)$, $M_u(H)$, and $M_i(H)$ can also be expressed in terms of $F(H)$ and $F(-H)$ as following

$$\begin{aligned}M_u(H) &= M_i(H) - \int_{H}^{H_{sat}} m_A(\alpha)d\alpha \int_{-H_{sat}}^{H} m_B(\beta)d\beta \\ &= M_i(H) - [F(H)]^2\end{aligned} \tag{2.19}$$

$$M_d(H) = M_u(H) + 2F(H)F(-H) \tag{2.20}$$

and

$$M_i(H) = \int_{-H}^{H}\int_{-H}^{H} \mu(\alpha,\beta)d\alpha d\beta$$

$$= \int_{-H}^{H} m_A(\alpha)d\alpha \int_{-H}^{H} m_B(\beta)d\beta$$
$$= [F(-H) - F(H)]^2 \qquad (2.21)$$

Notice that $\mu(\alpha,\beta)=0$ when $(\alpha,\beta)\notin S$.

Therefore,

$$F(\alpha) = \frac{M_d(\alpha) - M_u(\alpha)}{2\sqrt{M_d(\alpha)}} \qquad (\alpha \geq 0) \qquad (2.22)$$

or,

$$F(\alpha) = \sqrt{M_d(-\alpha)} \qquad (\alpha < 0) \qquad (2.23)$$

2.2.4 Software Implementation

From the analysis in sections 2.2.2 and 2.2.3, it can be seen that the magnetisation M for a given magnetic field strength H in a magnetic material can be determined by (2.5) if the operating point is on the initial curve, or by (2.10) if the operating point is on a downward trajectory, or by (2.11) if the operating point is on an upward trajectory. The corresponding flux density B can then be obtained by (2.2). The data required by (2.5), (2.10), and (2.11) are $M(H_n)$, the magnetisation of the last reversal point, and $T(\alpha,\beta)$, the area integration of the distribution function of the elementary magnetic dipoles over a right triangle with vertex (α,β) in the half plane $H_{sat} \geq \alpha \geq \beta \geq -H_{sat}$, where $\alpha=H$ and $\beta=-H$ in (2.5), $\alpha=H_n$ and $\beta=H$ in (2.10), and $\alpha=H$ and $\beta=H_n$ in (2.11). $M(H_n)$ can be obtained by recording the magnetisation history of the material, and $T(\alpha,\beta)$ can be calculated by (2.17), (2.22), and (2.23) from the limiting hysteresis loop of the material. Therefore, the distribution function of the assumed magnetic dipoles $\mu(\alpha,\beta)$ and its area integration are not required in the software implementation of the normal Preisach model of hysteresis. This makes the normal Preisach model more useful for engineering applications. Fig.2-5 illustrates the flow chart of the program.

The input data are the data table of the limiting hysteresis loop, and the specified magnetic field strength H for simulation. Because limiting loops are symmetric, it is only required to input data of $M_d(H)$ and $M_u(H)$ for $H\geq 0$. For $M_d(H)$ and $M_u(H)$ when $H<0$, the symmetric conditions $M_d(H)=M_u(-H)$ and $M_u(H)=M_d(-H)$ are imposed.

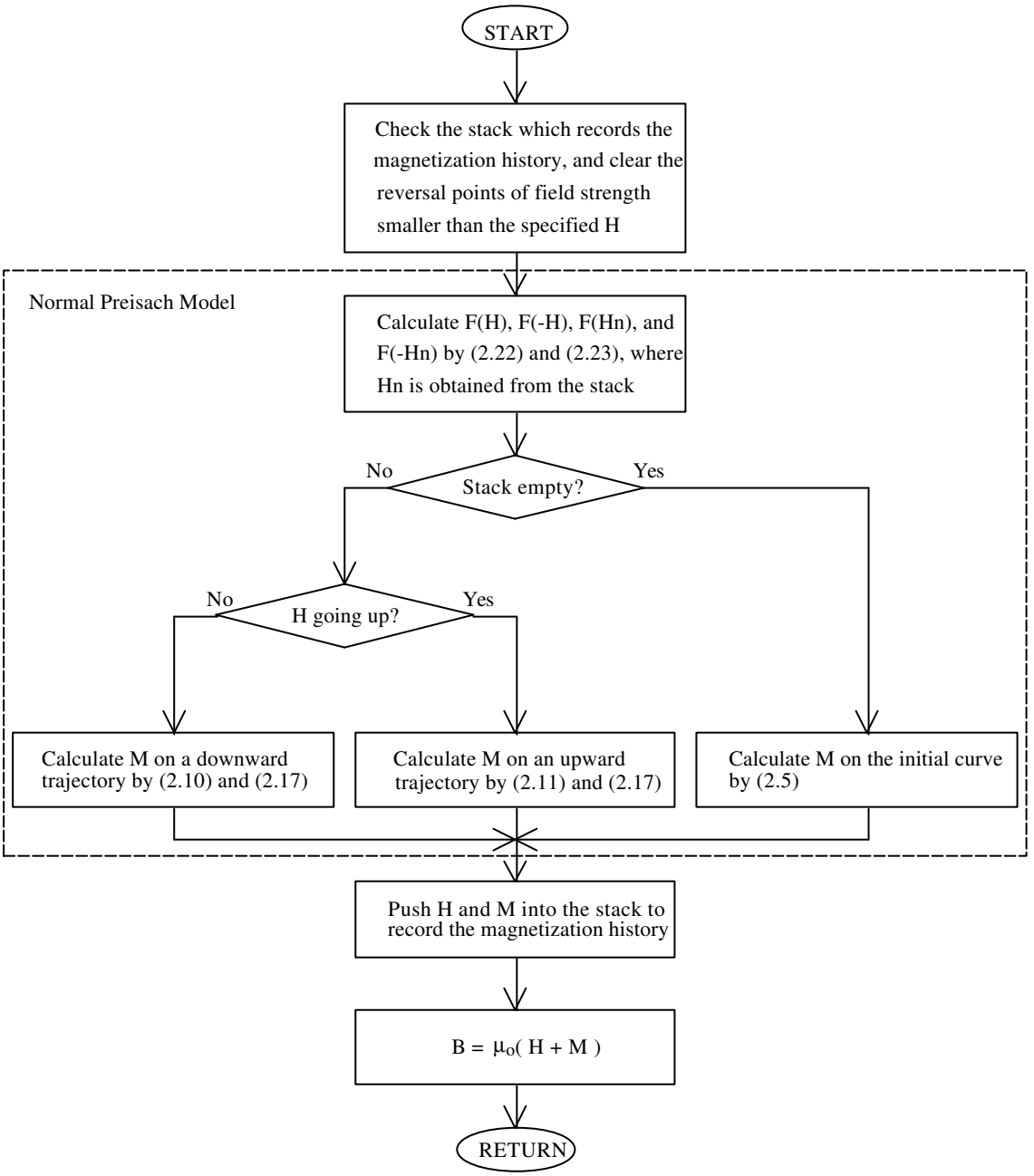

Fig.2-5 Flow chart of the normal Preisach model subroutine

A stack is used to keep the information of the magnetisation history, including the values of the magnetisation and magnetic field strength of each reversal point (local extremum), and can be either initialised empty for starting from the initial curve or preset with a given history of magnetisation before the routine is invoked for the first time. In checking the stack, the specified H is compared with the stack elements. A pair of reversal points is popped out of the stack whenever the specified H exceeds the value of the previous reversal point on the same

trajectory kept in the stack. This is to wipe out a completed minor loop since it will no longer have any effect on the future state of magnetisation.

The trajectory on which the operating point resides can be determined by comparing the specified H with the top element of the stack, which is pushed in at the end of the last calculation of the operating point. If the stack is empty, the operating point is on the initial magnetisation curve, since there is no reversal point kept in the stack above the current operating point.

To further illustrate how the record of the magnetisation history is kept in the stack and updated according to the current operating point, let us consider a practical magnetisation process with a pair of minor loops on a major loop, as shown in Fig.2-6(a). These minor loops are caused by two pairs of extra small reversals (local extrema) in the waveform of magnetic field strength, as shown in Fig.2-6(b), where the flux density waveform consists of a primary fundamental component plus a small third harmonic component.

Figs.2-7(a)-(f) illustrate the Preisach diagrams and the elements of the stack for recording the magnetisation history corresponding to the time instants (or operating points) a,b,c,d,e, and f in Fig.2-6, respectively.

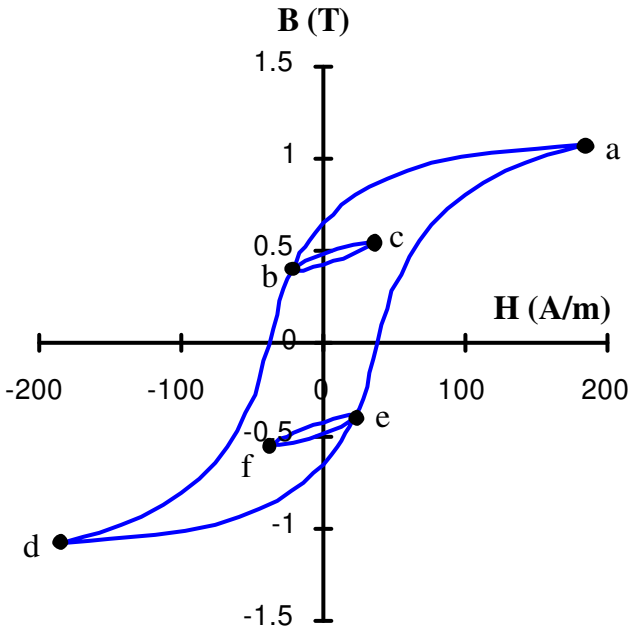

(a)

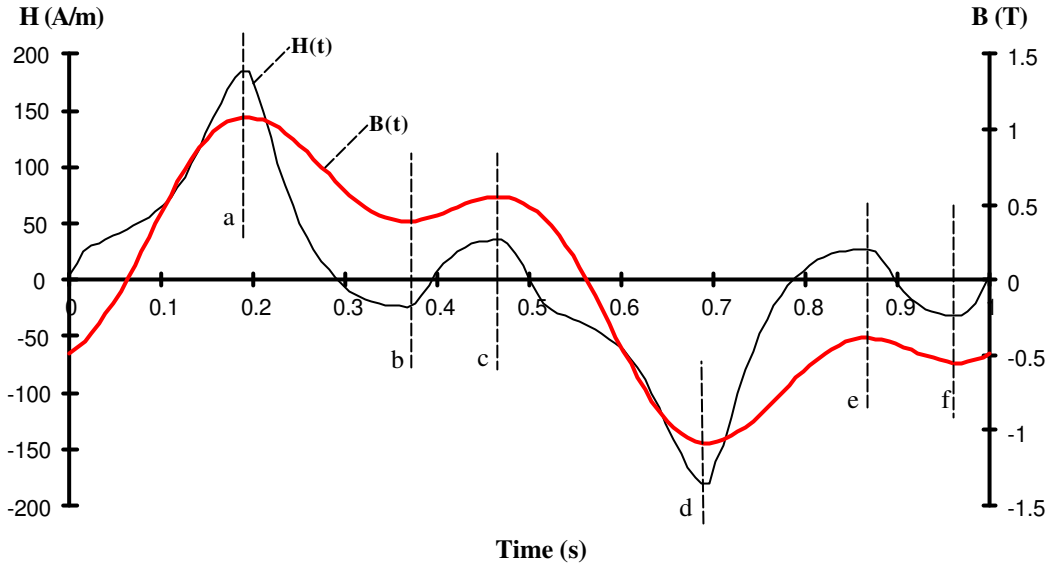

(b)

Fig.2-6 A practical magnetisation process with a pair of minor loops on a major loop (a) measured hysteresis loop, and (b) B and H waveforms.

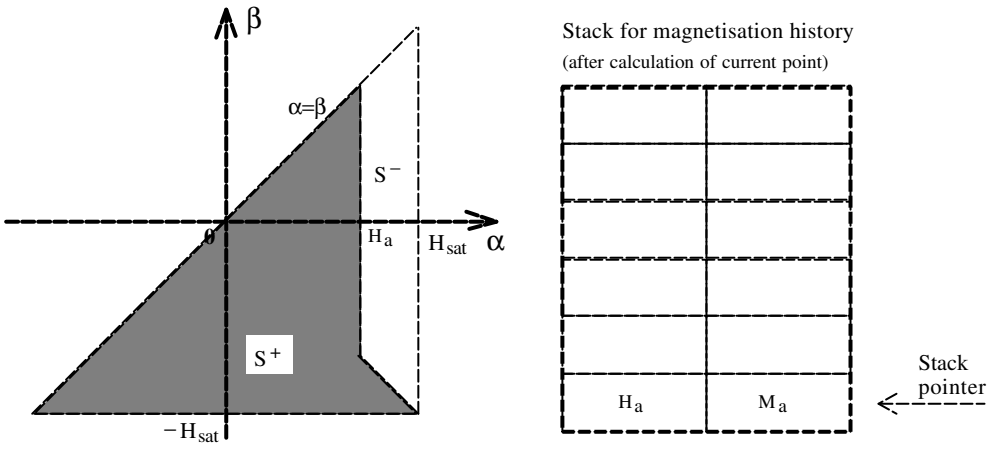

(a)

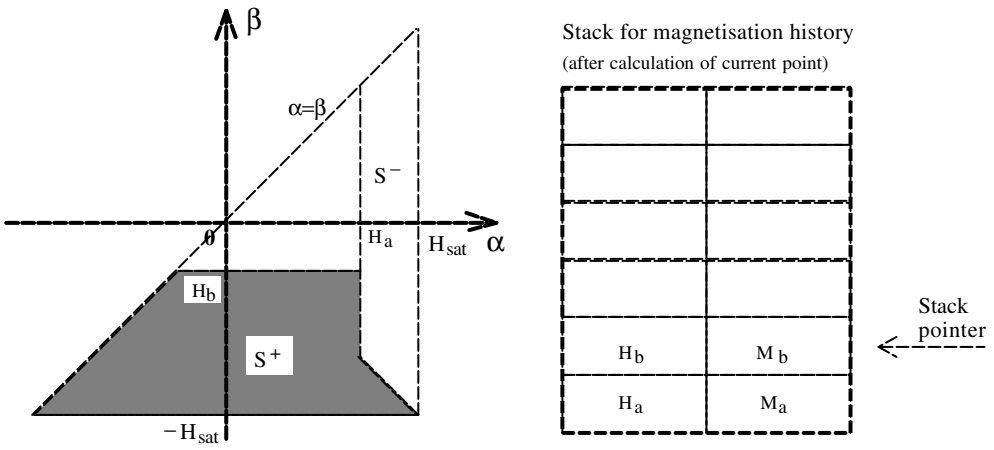

(b)

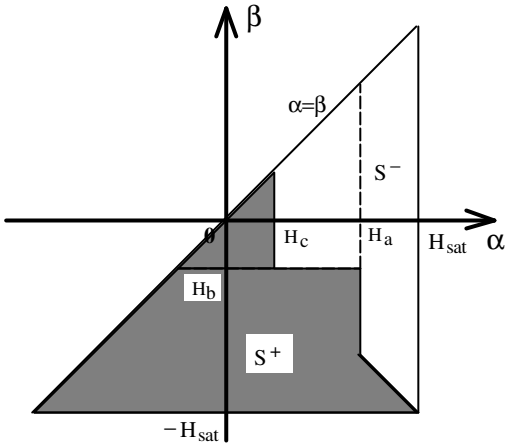

Stack for magnetisation history
(after calculation of current point)

H_c	M_c
H_b	M_b
H_a	M_a

Stack pointer

(c)

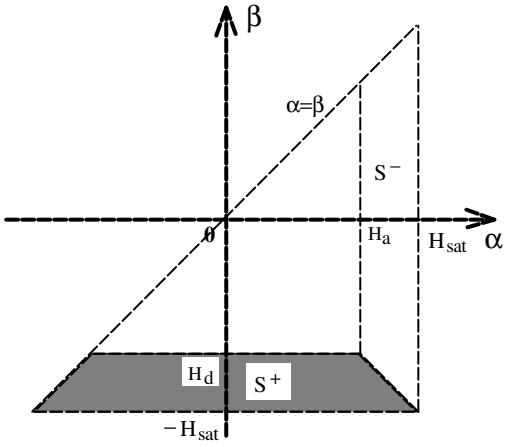

Stack for magnetisation history
(after calculation of current point)

H_d	M_d
H_a	M_a

Stack pointer

(d)

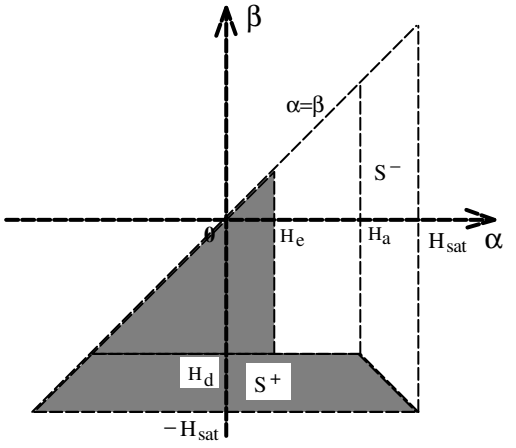

Stack for magnetisation history
(after calculation of current point)

H_e	M_e
H_d	M_d
H_a	M_a

Stack pointer

(e)

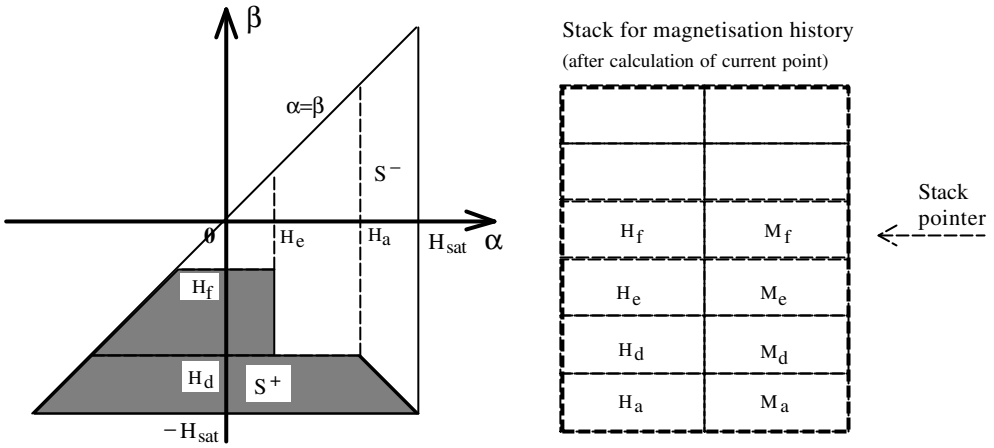

(f)

Fig.2-7 Preisach diagrams and the stack elements corresponding to time instants a,b,c,d,e, and f as illustrated in Fig.2-6

The initial contents of the stack depends on the initial state of the material undergoing the magnetisation process. Generally, the unmagnetised initial state (empty stack) is assumed at the beginning of the simulation. At time instant a (Fig.2-7(a)), the magnetic field strength reaches the maximum along the initial magnetisation curve, and the operating point (H_a,M_a) is kept in the stack afterwards. After reversal point a, the magnetic field strength decreases, and the magnetisation process follows the downward trajectory of the major hysteresis loop until time instant b when the field strength starts increasing. After the magnetisation M_b for the given field strength H_b is evaluated by the Preisach model, the operating point (H_b,M_b) is pushed into the stack (Fig.2-7(b)). The magnetisation process then follows the upward trajectory of the minor loop. At time instant c, the applied magnetic field reaches another local extremum (or reversal point). The operating point (H_c,M_c) is again pushed into the stack after the calculation of the magnetisation (Fig.2-7(c)). After reversal point c, the magnetisation process follows the downward trajectory of the minor loop until the applied field strength is equal to or smaller than H_b, when the minor loop has been completed and the tip points of the minor loop (H_b,M_b) and (H_c,M_c) are popped out of stack. The magnetisation process then proceeds along the downward trajectory of the major loop again. At time instant d, the applied field reaches the minimum, the tip point (H_d,M_d) is kept together with (H_a,M_a) for the other half of the cycle (Fig.2-7(d)-(f)). When the applied magnetic field reaches the maximum point a again after a complete cycle of magnetisation, the major loop is completed and wiped out. Tip point (H_a,M_a) is reset into the stack after the calculation of the flux density (Fig.2-7(a)).

2.2.5 Comparisons with Experiments

2.2.5.1 Experimental Method

Fig.2-8 illustrates the experimental set-up for the measurements of hysteresis loops using annular ring samples. Two coils of the equal number of turns were wound on the ring sample. The primary coil was used for excitation, and the secondary for the pick-up of flux density signal. For the sampling of magnetic field strength, a calibrated resistor R_1=1.17 Ω was used. The calibration of the resistor was performed by Dr. R. Day, Commonwealth Scientific and Industrial Research Organisation (CSIRO), National Measurement Laboratory, Lindfield. The excitation voltage was supplied by a power amplifier Australian Monitor AM1600. The bandwidth of this power amplifier is 5 Hz - 90 kHz, and the output power is 470 W with an 8 Ω resistive load and 810 W with a 4 Ω resistive load. A differential amplifier was used for feedback control so that the emf waveform followed the specified signal from the function generator. The differential amplifier was designed and constructed by Mr. B. Kalan, CSIRO, Division of Applied Physics, Lindfield. The function generator used was a Hewlett Packard HP3314A. For measurements of major hysteresis loops at a very low frequency, feedback control of waveform is not necessary, but for measurements of hysteresis loops with local reversal points or minor loops, it is required so as to control the sizes and positions of the minor loops. For data acquisition, an Analogic Data Precision 6000 signal processing system was used. The collected data were stored in ASCII data files and processed later by a C-code program written by the author for hysteresis loops and losses.

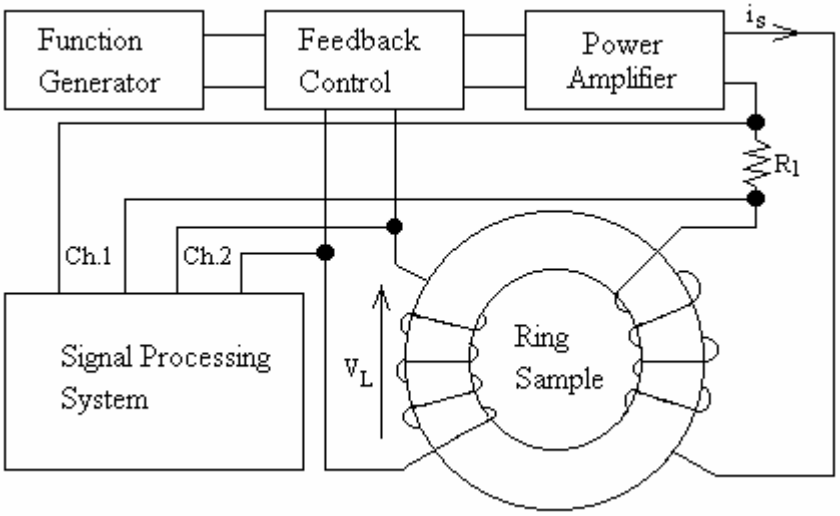

Fig.2-8 Experimental set-up for measuring hysteresis loops

The magnetic field strength H was calculated from the excitation current in the primary coil (which was measured from the voltage across the resistor R_1), by

$$H(t) = \frac{N i_s(t)}{l_m} \tag{2.24}$$

where N is the number of turns of the excitation coil, i_s the excitation current, and l_m the mean length of the annular ring sample ($\frac{\text{Outer diameter} - \text{Inner diameter}}{\text{Mean diameter}}$ of the ring not sufficient to cause distortion of results due to saturation near the inner diameter).

The flux density B was calculated by time integration of the voltage signal across the secondary coil since the current in this coil was zero, by

$$B(t) = \frac{1}{NA}\int V_L(t)dt \tag{2.25}$$

where A is the effective cross sectional area of the ring sample, V_L the terminal voltage of the secondary coil.

Hysteresis loss is defined as the area enclosed by the hysteresis loop and can be calculated by

$$P_h = \frac{1}{T\rho_m}\int_0^T H\frac{dB}{dt}dt \tag{2.26}$$

where T=1/f is the time period, f the frequency of magnetisation, and ρ_m the mass density of the material.

This system can also be used for alternating core loss measurements at different frequencies using ring samples. Then, the magnetic field strength calculated by (2.24) is the value at the surface of the sample. The flux density calculated by (2.25) gives the average value over the cross sectional area, and the power loss obtained by (2.26) is the total alternating core loss [197], including hysteresis, eddy current, and anomalous losses, as will be discussed in chapter 3, section 3.2.2.3.

2.2.5.2 Comparison of Major and Minor loops of Non-Oriented Silicon Steel Lycore-140

Hysteresis loops of a ring sample (wire cut and no further heat treatment) of non-oriented silicon steel Lycore-140 0.35 mm lamination were simulated and compared with the measured loops using an annular ring sample. The dimensions of the sample and the parameters of the excitation and flux density coils are listed in Table 2-1.

Table 2-1 Dimensions and coil parameters of Lycore-140 ring sample

Quantity	Value
Outer diameter (mm)	36.48
Inner diameter (mm)	28.96
Total thickness (mm), (15×0.35 mm sheets)	5.45
Stacking factor	0.98
Mass density (kg/m^3)	7650
Resistivity of lamination sheet (Ωm)	0.5×10^{-6}
Number of turns of coils	53
Coil resistance (Ω)	0.48

Fig.2-9 shows the largest major hysteresis loop of Lycore-140 measured on the annular ring sample with a sinusoidal flux density at 0.5 Hz using the system outlined in section 2.2.5.1. The corresponding specific hysteresis loss is 4.22×10^{-2} W/kg/Hz. This loop was used as the input data of the limiting loop in the simulation although the very deep saturation was not reached.

Fig.2-10(a) compares the measured and calculated major hysteresis loops, where the measured results were obtained under the same condition as that for the limiting loop. Fig.2-10(b) plots the simulated initial curve together with the measured normal magnetisation curve, which consists of the tip points of major loops. In the Preisach simulation, as illustrated in section 2.2.4 by the software implementation, the initial curve was assumed to be the same as the normal magnetisation curve, and whenever the stack for keeping the magnetisation history was empty (or all previous reversal points were wiped out) the magnetisation process was assumed to follow the initial magnetisation curve. This is approximately correct.

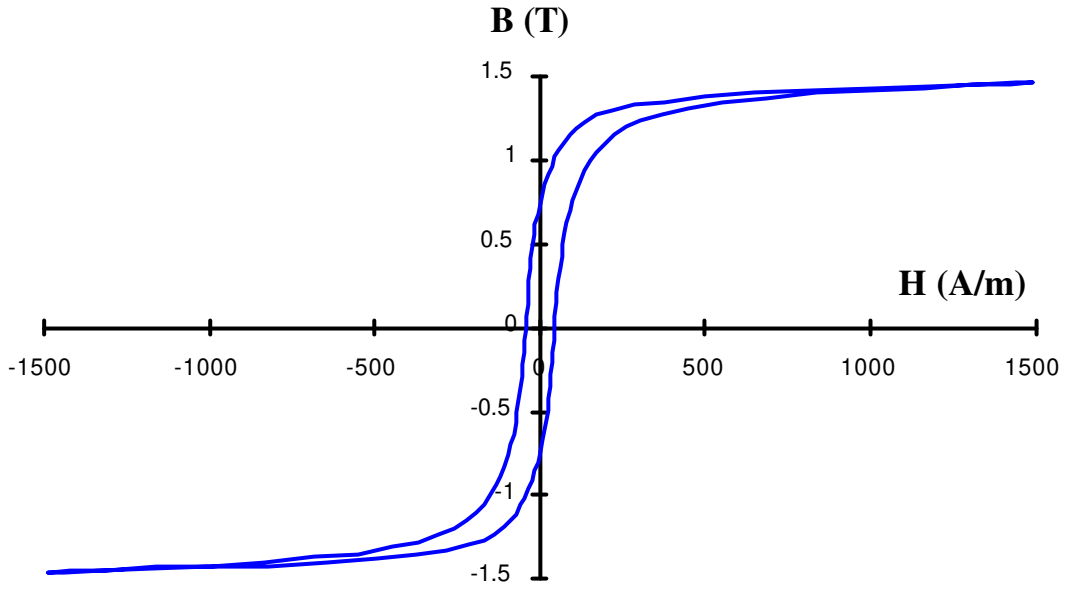

Fig.2-9 The measured limiting hysteresis loop of Lycore-140 used as the input data in the Preisach modelling

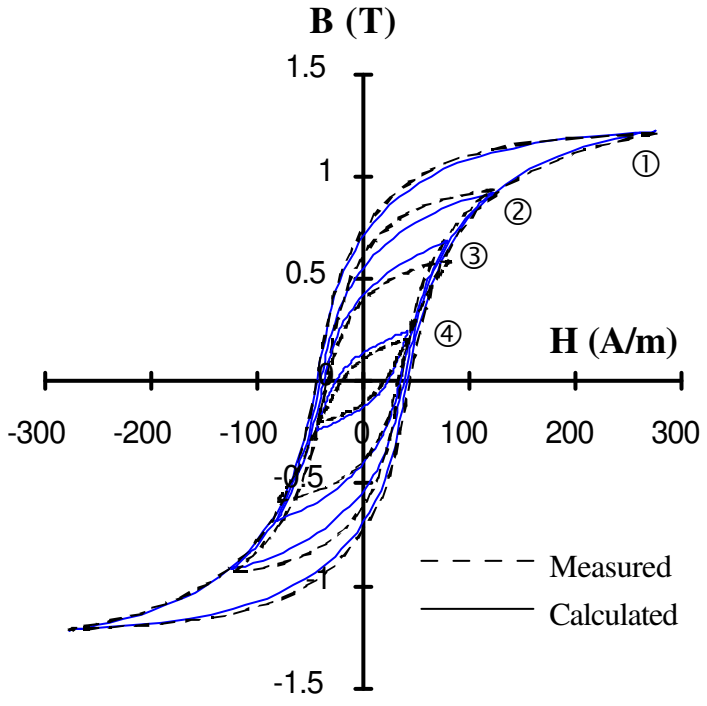

(a)

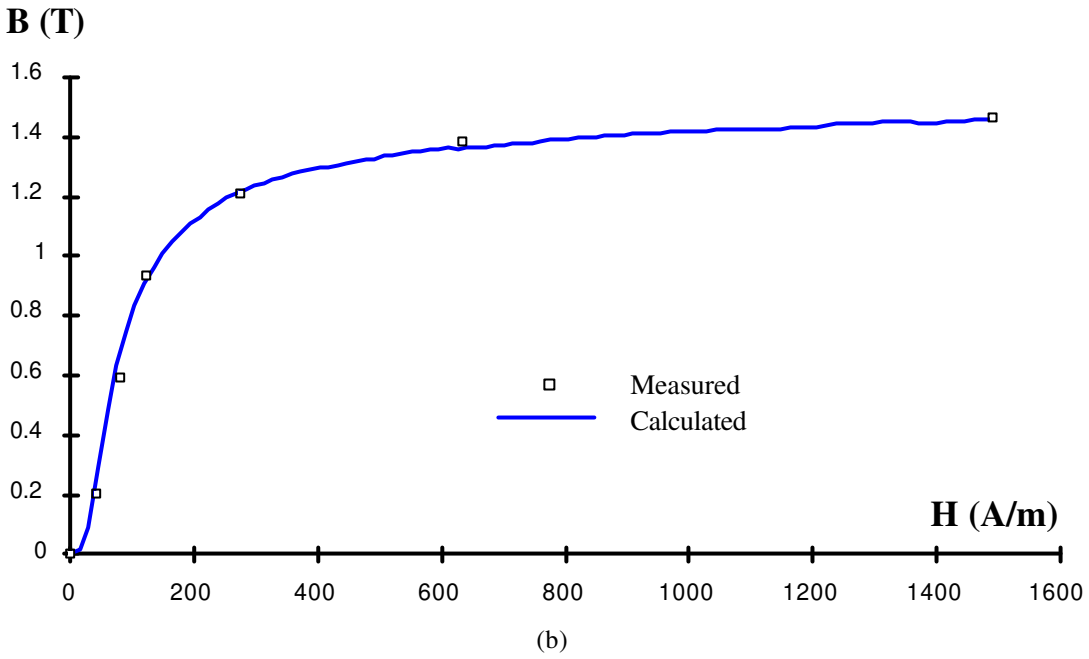

(b)

Fig.2-10 Preisach modelling of hysteresis of silicon steel Lycore-140
(a) major hysteresis loops, and (b) initial magnetisation curve

The calculated and measured hysteresis losses corresponding to the major hysteresis loops plotted in Fig.2-10(a) are listed in Table 2-2, where B_m and H_m are the magnitudes of the flux density and field strength of the major hysteresis loops. For the hysteresis loops of flux density magnitudes larger than 0.7 T, the percentage errors on hysteresis loss are equal to or less than about 10%. For smaller loops, the discrepancy between the calculated and the measured hysteresis losses increases rapidly, partly due to the rapid decrease of the hysteresis loss, but the calculated and measured hysteresis loops are still very close as can be seen in Fig.2-10(a).

Table 2-2 Comparison of calculated and measured hysteresis losses of Lycore-140 ring sample

Loop No.	①	②	③	④
B_m (T)	1.22	0.92	0.69	0.24
H_m (A/m)	276	123	81	43
$P_{h(Test)}$ (W/kg/Hz)	2.83×10^{-2}	1.57×10^{-2}	8.62×10^{-3}	1.56×10^{-3}
$P_{h(Cal.)}$ (W/kg/Hz)	2.62×10^{-2}	1.53×10^{-2}	9.69×10^{-3}	2.13×10^{-3}
Error (%)	–7.42	–2.55	+12.41	+36.54

The theory has also been compared with the experimental results for minor loops. Fig.2-11 depicts the calculated and measured hysteresis loops of Lycore-140 on the annular ring sample when the flux density consists of a primary fundamental component (1 Hz) plus a third harmonic component (3 Hz). A pair of minor loops were caused by the third harmonic component in the flux density waveform. This increases the total hysteresis loss. For a peak flux density of 1.08 T, the measured hysteresis loss was 2.13×10^{-2} (W/kg/Hz), and the calculated hysteresis loss is 2.25×10^{-2} (W/kg/Hz). The error on hysteresis loss is 5.55%.

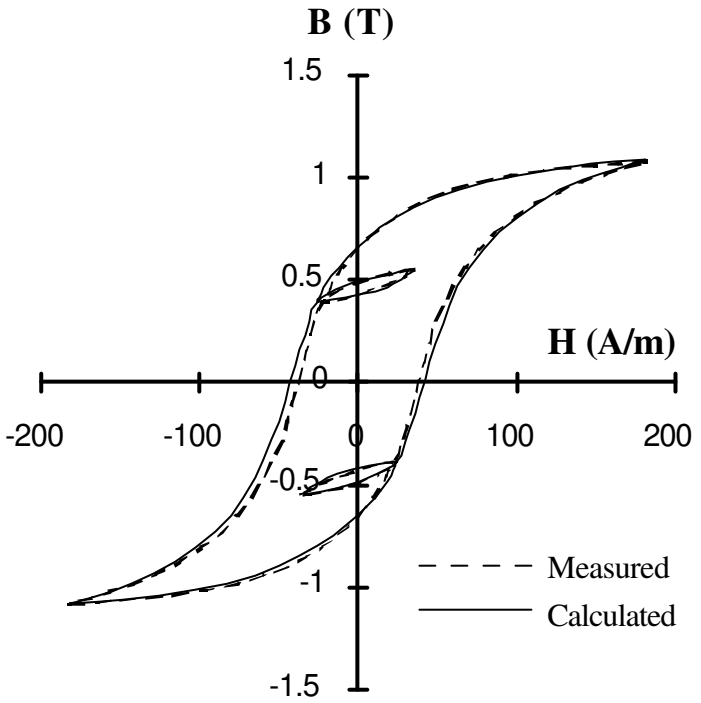

Fig.2-11 Preisach modelling of hysteresis loop of Lycore-140 with a flux density consisting of a primary fundamental component and a third harmonic component

2.2.5.3 Comparison of Major Loops of Soft Ferrite N47

Another test was carried out on a Siemens/Matsushita N47 soft ferrite toroid with a pure sinusoidal voltage excitation across the primary coil. Table 2-3 lists the dimensions and parameters of the ring sample and the excitation and flux density coils.

Fig.2-12 depicts the largest major hysteresis loop measured with a sinusoidal flux density at 1 Hz using the testing system described in section 2.2.5.1. This loop was used as the limiting loop in the simulation. The corresponding specific hysteresis loss is 4.30 W/kg/Hz.

Table 2-3 Dimensions and parameters of N47 soft ferrite R16 toroid core and windings

Quantity	Value
Outer diameter of the core (mm)	16.33
Inner diameter of the core (mm)	8.94
Thickness of the core (mm)	6.63
Resistivity of the core (Ωm)	4.00
Number of turns of each coil	20
Wire diameter of the coils (mm)	0.20
Winding resistance (Ω)	0.23

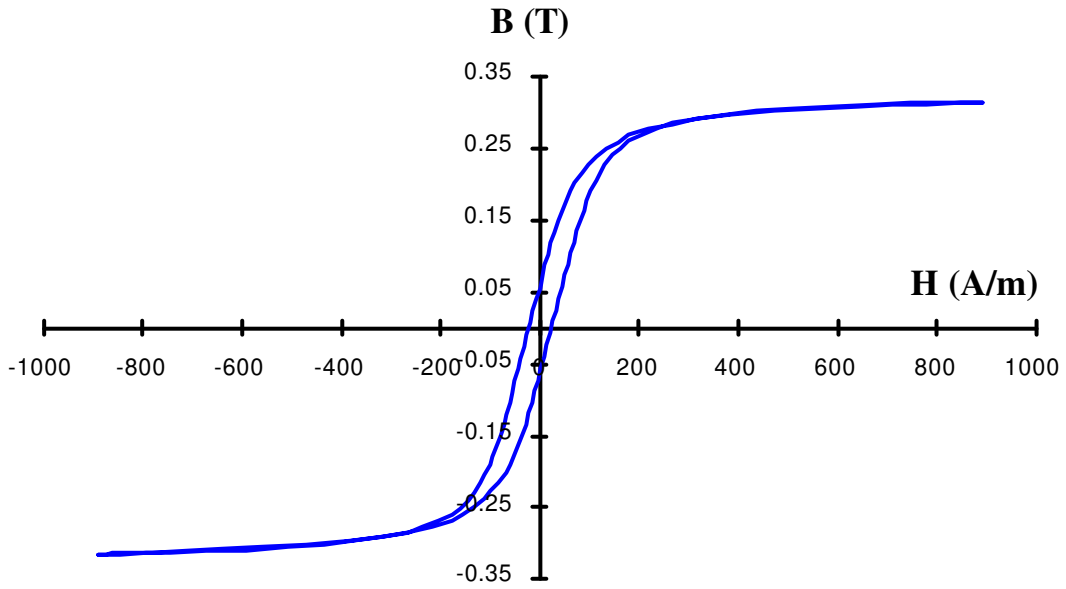

Fig.2-12 The limiting hysteresis loop of soft ferrite N47

The measured and predicted B-H loops and initial magnetisation curves at 1 Hz are shown in Figs.2-13(a) and (b), respectively. The corresponding hysteresis losses are listed in Table 2-4. The error between the calculated and measured hysteresis losses is small when the hysteresis loop is close to the limiting loop, but increases when the magnitude of the peak flux density is smaller than about 1/2 of the saturation flux density. This is consistent with the results observed on non-oriented silicon steel Lycore-140, as reported in the previous section.

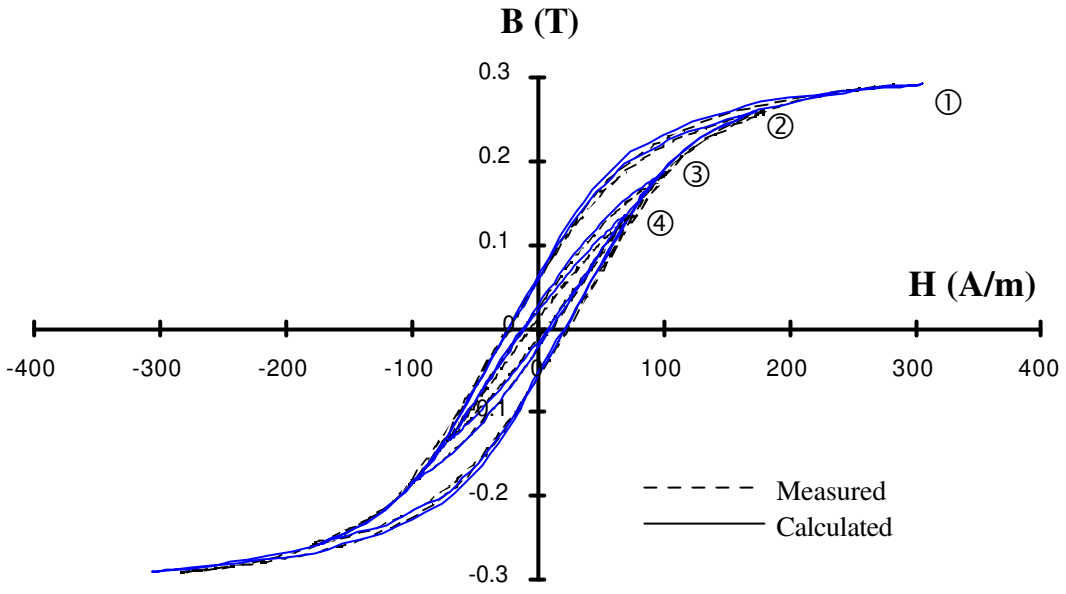

(a)

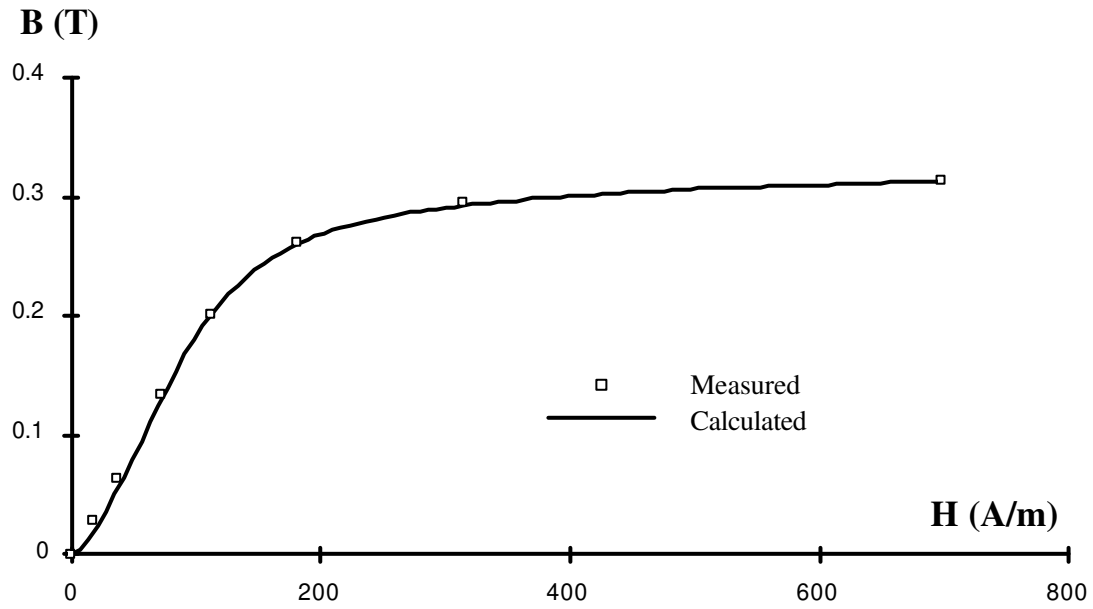

(b)

Fig.2-13 Preisach modelling of hysteresis of N47 soft ferrite core
(a) major hysteresis loops, and (b) initial magnetisation curve

Table 2-4 Comparison of calculated and measured hysteresis losses of N47 ring sample

Loop No.	①	②	③	④
B_m (T)	0.291	0.258	0.186	0.134
H_m (A/m)	283	180	103	72
$P_{h(Test)}$ (W/kg/Hz)	4.77×10^{-3}	3.99×10^{-2}	1.31×10^{-3}	4.73×10^{-4}
$P_{h(Cal.)}$ (W/kg/Hz)	4.98×10^{-3}	4.02×10^{-3}	1.34×10^{-3}	7.06×10^{-4}
Error (%)	4.40	0.75	+2.29	+49.17

2.2.5.4 Comparison of Major and DC Biased Incremental Loops of Mild Steel

The normal Preisach model has been used to simulate the major and DC biased incremental hysteresis loops of a solid mild steel ring specimen, EN1A grade 4 (B.S. 970) of chemical composition C 0.11%, S 0.25%, Mn 1.15%, measured by Ramsden in 1972 [198]. Table 2-5 lists the dimensions and parameters of the specimen and the flux and magnetising coils.

Table 2-5 Details of the specimen (from [198])

Quantity	Value
Outside diameter (cm)	18.97
Inside diameter (cm)	17.01
Thickness (cm)	1.004
Mean diameter (cm)	17.99
Mean magnetic path length (cm)	56.5
Cross-sectional area (cm^2)	0.791
Surface area (cm^2)	178.5
Volume (cm^3)	44.8
Number of turns of flux coil	1320
Number of turns of magnetising coil	2040

The major loops were measured by the uniformly-varying flux method, in which the magnetisation current is varied in such a way as to keep dB/dt constant, i.e. a uniform rate of change of flux density, and the biased loops by the slowly-varying flux method, in which the magnetising current is changed slowly. The circuits for measuring the major loops and the DC biased incremental loops are illustrated in Fig.2-14.

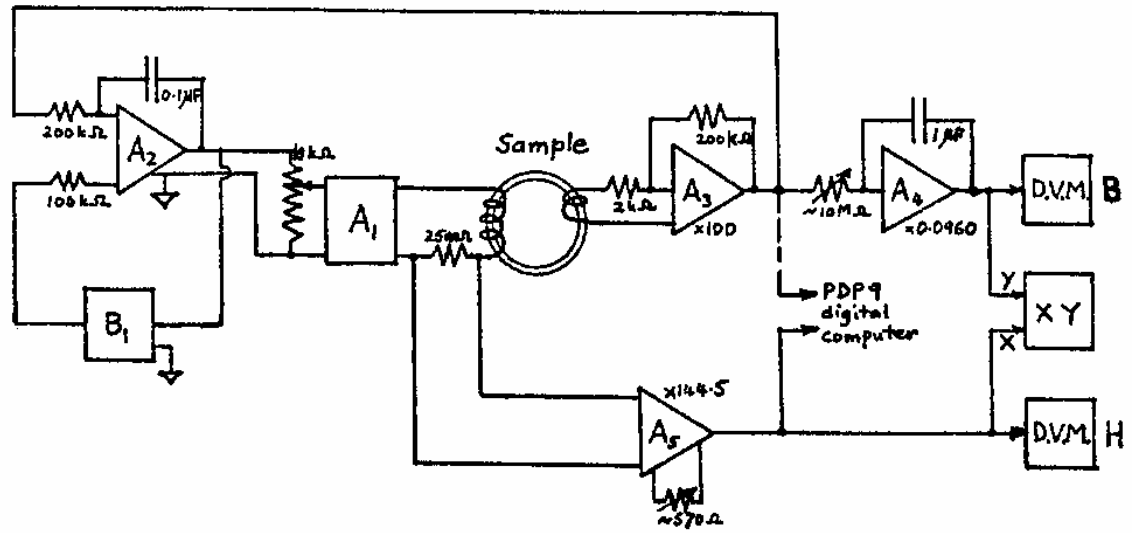

(a)

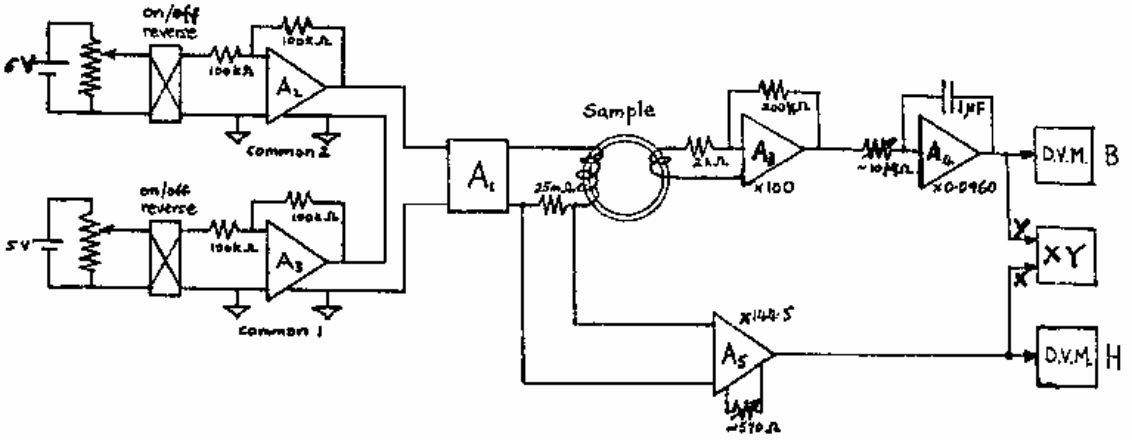

(b)

Fig.2-14 Circuits for measuring hysteresis loops (from [198])
(a) uniformly-varying flux method, and (b) slowly-varying flux method

A_1	Mazzetti and Soardo power amplifier
A_2	Burr Brown model 3010 chopper stabilised operational amplifier (low drift)
A_3,A_4	Burr Brown model 3071 chopper stabilised operational amplifier (low drift, low noise)
A_5	Burr Brown model 3061 instrumentation amplifier
B_1	Mazzetti and Soardo bistable
D.V.M.	Solartron digital voltmeter LM1402
XY	Houston Instrument model HR 92 X-Y recorder

Fig.2-15 is the limiting hysteresis loop used as the input data in the simulation. The measured and predicted major hysteresis loops are compared in Fig.2-16(a), while Fig.2-16(b) plots together the predicted initial magnetisation curve and the measured normal magnetisation curve.

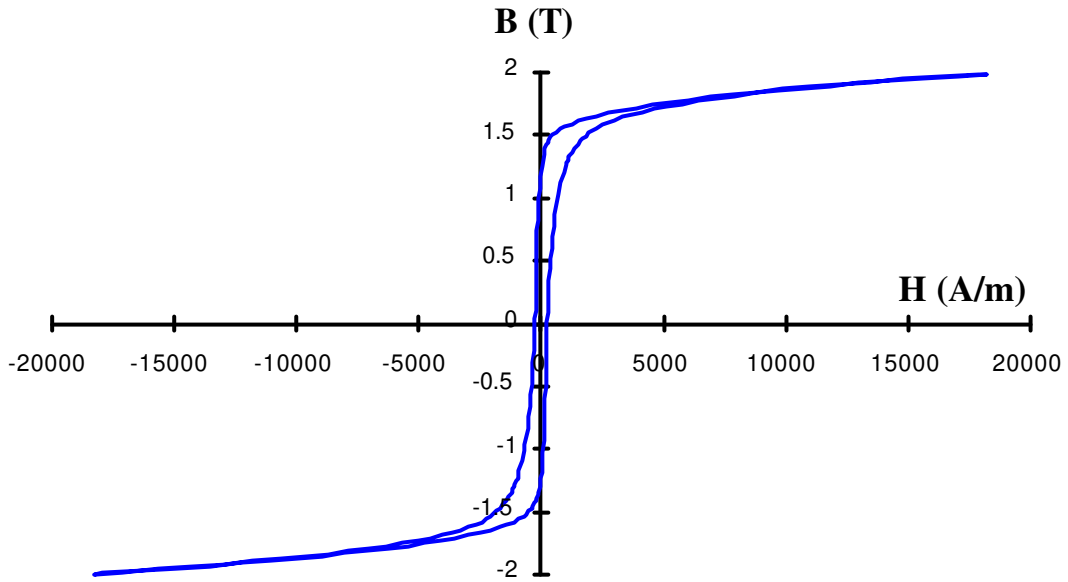

Fig.2-15 Limiting hysteresis loop of the ring specimen of mild steel (after [198])

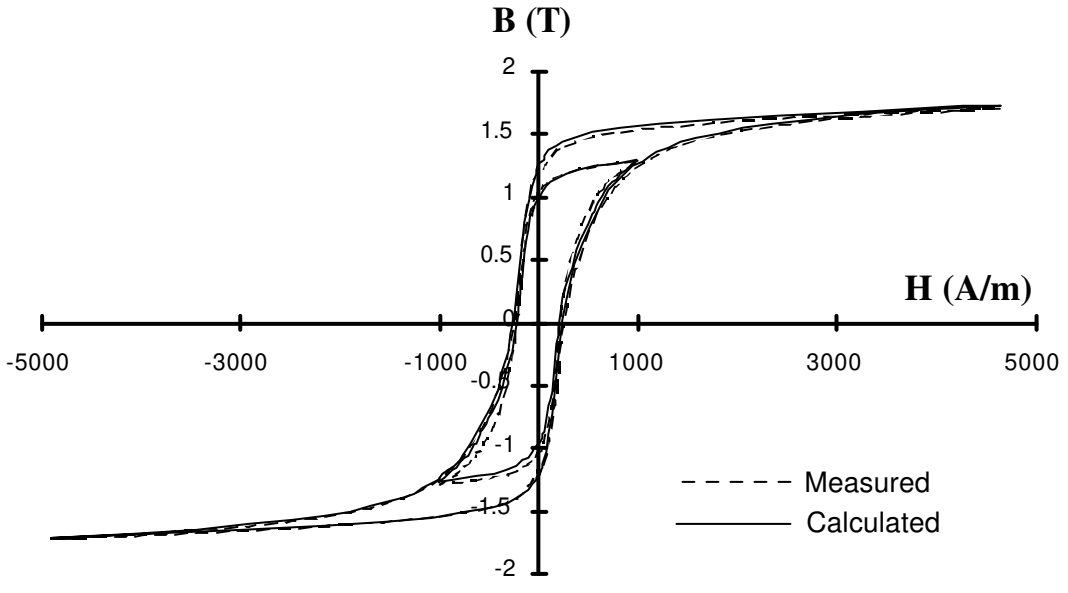

(a)

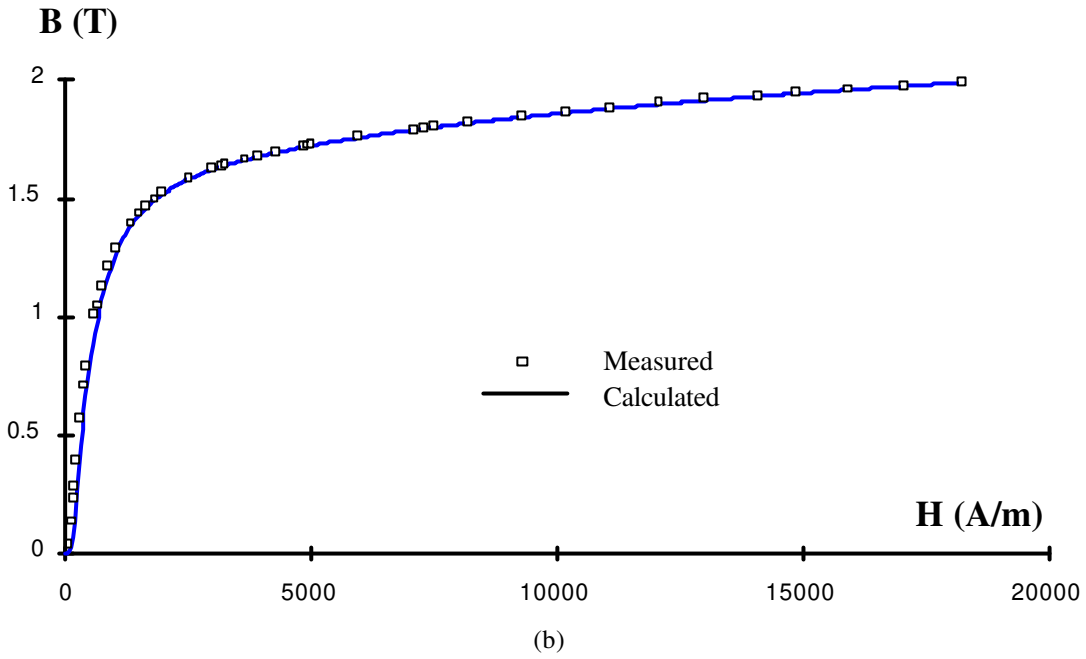

(b)

Fig.2-16 Preisach modelling of mild steel (measured data from [198])
(a) major hysteresis loops, and
(b) initial magnetisation curve

The incremental hysteresis loops were simulated in the same way as they were measured. In the simulation of each incremental loop, the magnetic field strength was first increased from zero to H_b+H_Δ, where H_b was the biasing magnetic field strength and H_Δ was the incremental magnetic field strength. The magnetisation process followed the initial magnetisation curve (curve segment O-a in Fig.2-17). The magnetic field strength was then reduced slowly, and the magnetisation process was performed along the downward trajectory of the incremental loop (curve segment a-b in Fig.2-17) until the next reversal point $H=H_b-H_\Delta$. After this reversal point, the magnetisation process followed the upward trajectory of the incremental loop (curve b-a in Fig.2-17) until the loop was completed when $H=H_b+H_\Delta$ again.

Fig.2-18(a) shows the incremental loops on the normal magnetisation curve recorded by a XY plotter using the slowly-varying flux method [198] for a biasing field strength H_b=900 A/m, and a range of incremental magnetic field strength H_Δ=100, 250, 500, 1000, 1500, and 2500 A/m, and Fig.2-18(b) depicts the predicted incremental loops. The measured and simulated incremental loops are similar.

Comparisons are also performed on the normal and incremental permeabilities. The incremental permeability is defined as

$$\mu_{\Delta} = \frac{1}{\mu_o}\frac{B_{\Delta}}{H_{\Delta}} \tag{2.27}$$

for a given biasing field strength H_b, where B_{Δ} is the magnitude of incremental flux density corresponding to the incremental magnetic field strength H_{Δ}, as illustrated in Fig.2-17 [198]. When H_b=0, the incremental permeability μ_{Δ} reduces to the normal relative permeability $\mu_r = \frac{1}{\mu_o}\frac{B}{H}$.

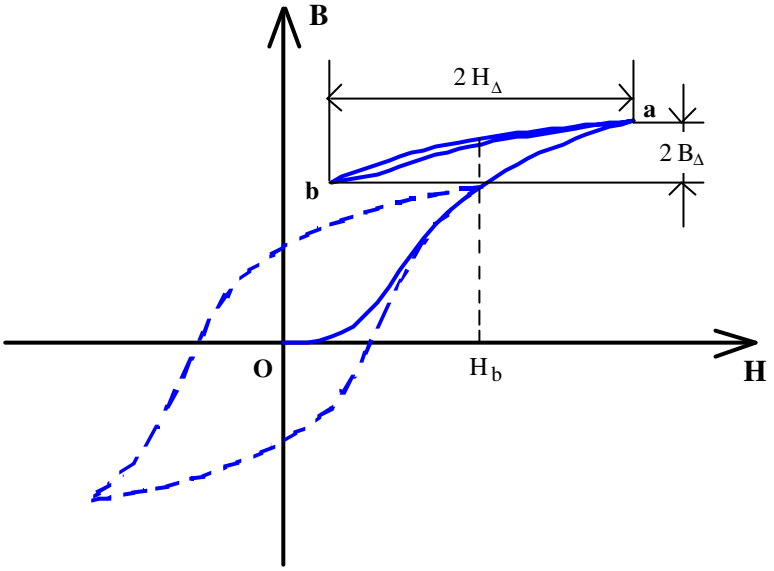

Fig.2-17 An incremental loop for a given biasing field strength

Fig.2-19 compares the calculated and measured incremental permeabilities for a range of DC biasing field strengths H_b=0, 112, 225, 450, 900, 1800, 3600, 7200, and 9000 A/m. Fig.2-19(a) plots the permeability in a linear scale. The calculation and measurement are in substantial agreement, but a large discrepancy occurs when the biasing field is small. To have a clearer view of the discrepancy, the permeability is replotted again to a logarithmic scale as shown in Fig.2-19(b). It is found that the normal Preisach model fails in predicting the normal and incremental permeabilities for $H_b \leq 225$ A/m and $H_{\Delta} \leq 300$ A/m. The possible cause of this phenomenon is discussed in the next section.

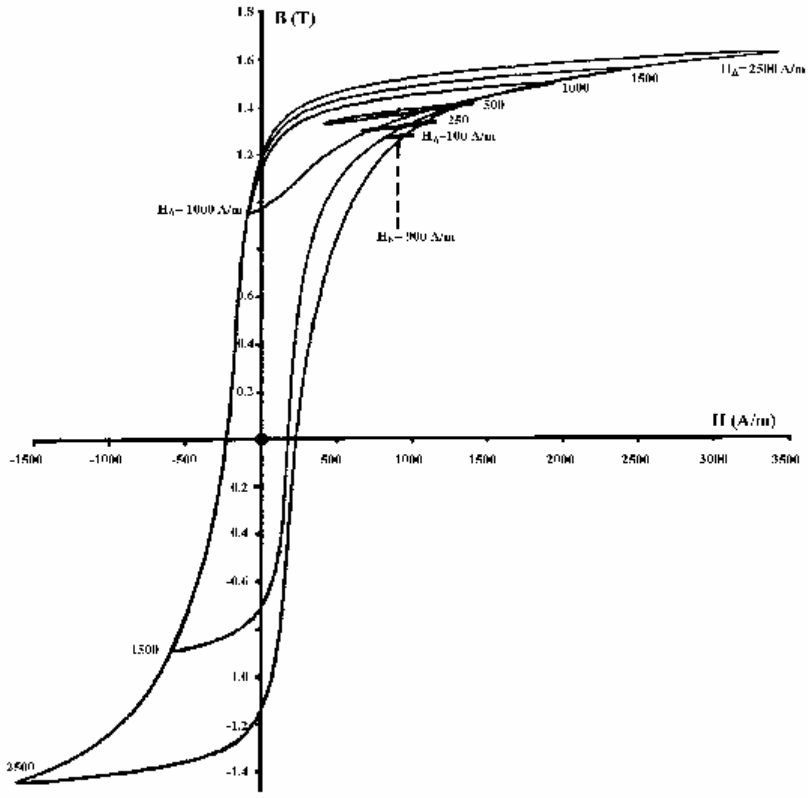

(a)

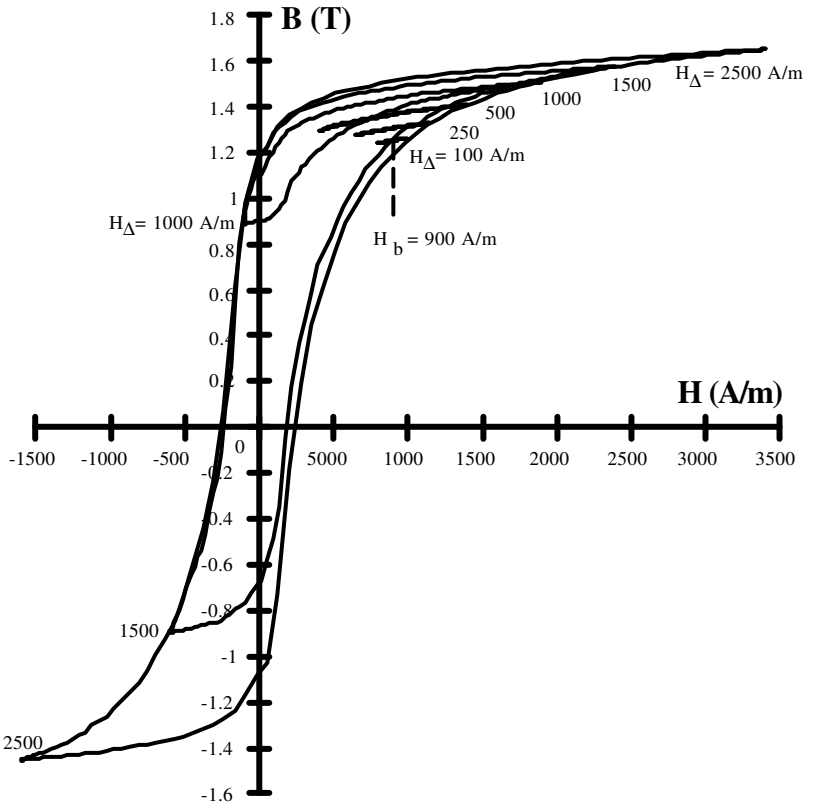

(b)

Fig.2-18 Preisach modelling of incremental loops on the normal magnetisation curve of mild steel, (a) measured loops (after [198]), and (b) predicted loops

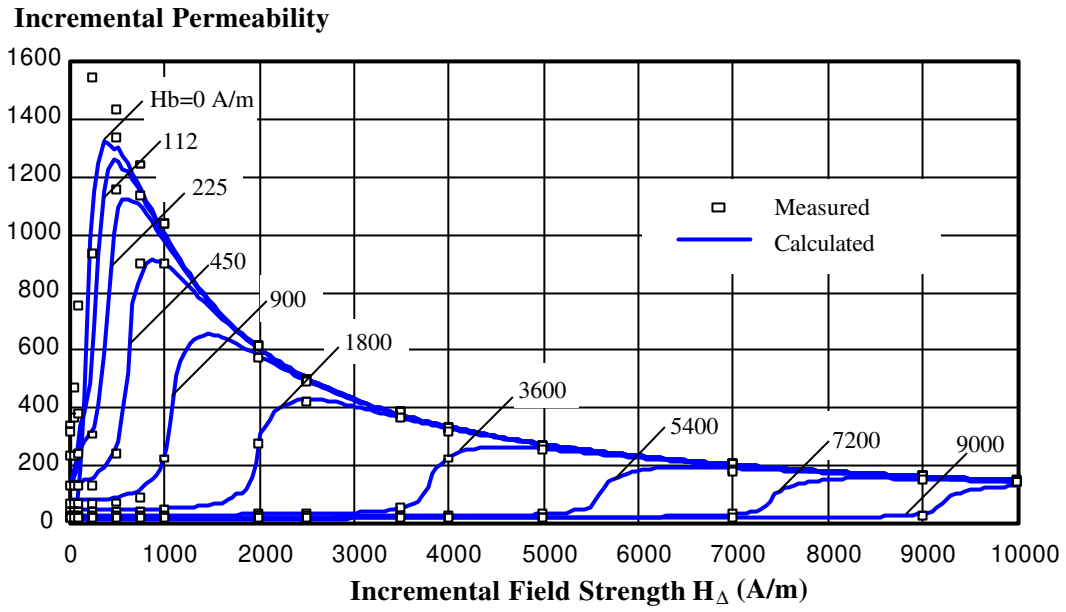

(a)

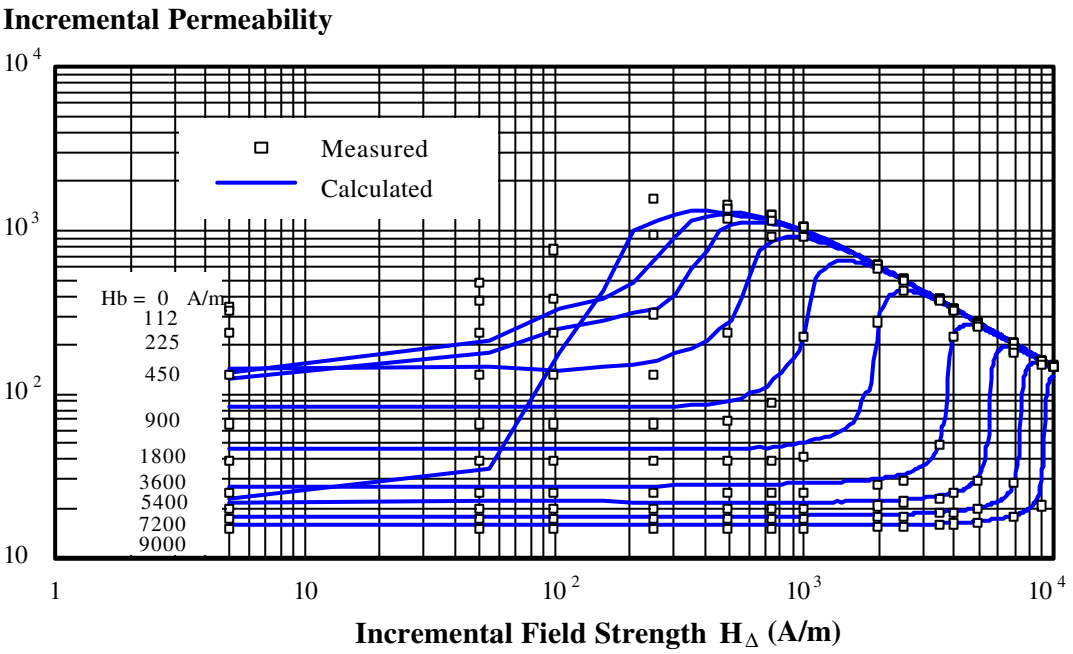

(b)

Fig.2-19 Comparison of calculated and measured incremental permeabilities for different biasing magnetic field strengths

2.2.6 Intrinsic Defects of the Normal Preisach Model

From the experimental verification of the Preisach theory, it can be seen that the normal Preisach model can predict correctly most major and minor hysteresis loops, but the model fails when it is used to predict the hysteresis loss and the normal and incremental permeabilities

of small loops far away from the limiting hysteresis loop. This may be attributed to some intrinsic defects of the model.

2.2.6.1 Zero Initial Magnetic Susceptibility

One of the intrinsic properties of the normal Preisach model, that is contrary to experimental observations is that the initial susceptibility (defined as the susceptibility of the initial magnetisation curve at the origin) predicted by the model is zero, as pointed out by various researchers [30,51,52]. This can also be shown mathematically. From (2.21), the initial susceptibility can be calculated as

$$\begin{aligned}\chi_{io} &= \left.\frac{dM_i}{dH}\right|_{H=0} \\ &= \left\{2\left[F(-H)-F(H)\right]\left[\frac{dF(-H)}{dH}-\frac{dF(H)}{dH}\right]\right\}_{H=0}\end{aligned} \tag{2.28}$$

At the origin, when H=0, functions F(−H) and F(H) and their derivatives can be calculated from (2.22) and (2.23) as following

$$\begin{aligned}F(H)\big|_{H=0} &= \frac{M_d(0)-M_u(0)}{2\sqrt{M_d(0)}} \\ &= \sqrt{M_d(0)} \\ &= F(-H)\big|_{H=0}\end{aligned} \tag{2.29}$$

and

$$\begin{aligned}\left.\frac{dF(H)}{dH}\right|_{H=0} &= \left\{\frac{\left[\frac{dM_d(H)}{dH}-\frac{dM_u(H)}{dH}\right]\sqrt{M_d(H)}-\frac{1}{2\sqrt{M_d(H)}}\frac{dM_d(H)}{dH}\left[M_d(H)-M_u(H)\right]}{2M_d(H)}\right\}_{H=0} \\ &= \frac{-1}{2\sqrt{M_d(0)}}\left.\frac{dM_d(H)}{dH}\right|_{H=0} \\ &= -\left.\frac{dF(-H)}{dH}\right|_{H=0}\end{aligned} \tag{2.30}$$

Notice that

$$M_u(0) = -M_d(0)$$

and

$$\left.\frac{dM_d(H)}{dH}\right|_{H=0} = \left.\frac{dM_u(H)}{dH}\right|_{H=0}$$

for a symmetric limiting hysteresis loop.

Therefore, the initial susceptibility

$$\chi_{io} = 0 \tag{2.31}$$

and the initial permeability is μ_o.

The effect of the zero initial susceptibility is that the predicted initial magnetisation curve is lower than the actual one for a small magnetic field strength. This in turn causes a large discrepancy in predicting major loops when the amplitude of the magnetic field strength is small. This can be illustrated by plotting the predicted and measured initial magnetisation curves of Fig.2-16 into a larger scale over a range from 0 to 2000 A/m in Fig.2-20. This is also believed to be the reason why the predicted normal and incremental permeabilities in Fig.2-19 are much smaller than the experimental data when H_b and H_Δ are small.

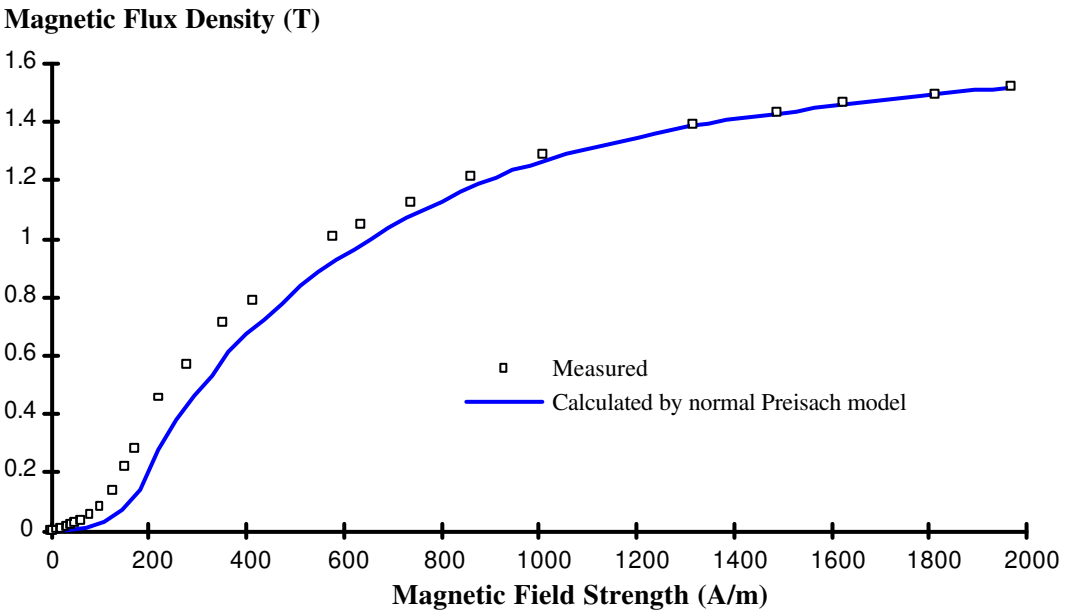

Fig.2-20 A larger scale view of predicted and measured initial magnetisation curves in Fig.2-16

This zero initial susceptibility may be attributed to the fact that the reversible magnetisation process is not properly accounted for by the rectangular hysteresis loop of the elementary magnetic dipoles shown in Fig.2-1(a). This rectangular hysteresis loop can describe the irreversible magnetisation process correctly by a switching of magnetisation, but the magnetisation is assumed constant ($\gamma_{\alpha\beta}(H)=-1$ or $+1$) before a switching point (α or β) has been reached. This is untrue. As discussed in section 2.1, before a domain wall breaks away from a pinning site to make a Barkhausen jump (or an elementary dipole in the normal Preisach model switches to an opposite direction of magnetisation), the domain wall movement takes place in the form of domain wall bowing. This domain wall bowing effect contributes a reversible component to the over all magnetisation.

To have the reversible magnetisation component accounted for properly, the elementary hysteresis loop of the normal Preisach model should be modified to allow the variation of magnetisation before a switching point is reached. This is done in section 2.3 in a generalised Preisach model.

2.2.6.2 Congruent Minor Loops

Congruency is another intrinsic property of the normal Preisach model, that does not agree with observed behaviour [29,32,41,48,49,53-59]. The normal Preisach model predicts that minor loops are identical or congruent if they are aligned vertically in the B-H plane (have the same H_b and H_Δ).

Fig.2-21(a) illustrates two identical minor loops (① and ②) predicted by the normal Preisach model for a given H_b and H_Δ. Figs.2-21(b)-(i) are the Preisach diagrams corresponding to the magnetisation process along curve O-a-b-a-c-d-e-d shown in Fig.2-21(a).

When predicted by the normal Preisach model, the vertical position of a minor loop is determined by the flux density of the last reversal point, while the shape and size are determined by the area integration over a right triangle bounded by the magnetic field strength of the last reversal point and the current field strength in the corresponding Preisach diagram. The calculation of the downward trajectory of minor loop ① (segment a-b in Fig.2-21(a)) is shown graphically in Figs.2-21(c)-(d). For an applied field strength $H<H_2$, the variation of flux density can be calculated by (2.10) as

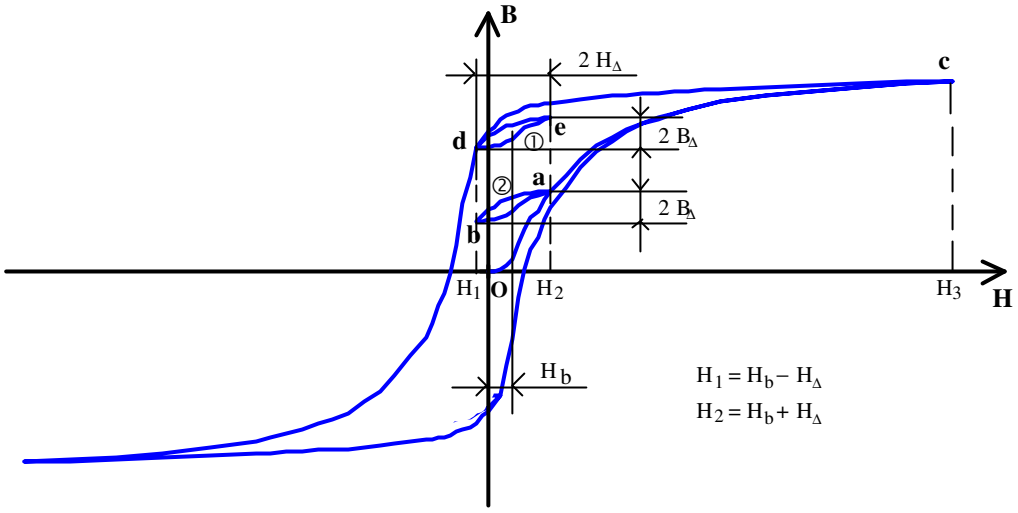
B
2 H_Δ
c
d
e
①
2 B_Δ
②
a
2 B_Δ
b
H_1
O
H_2
H_3
H
H_b
H_1 = H_b − H_Δ
H_2 = H_b + H_Δ

(a)

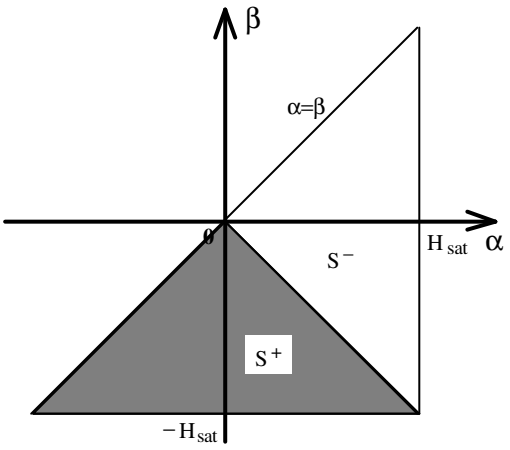
β
α=β
S⁻
H sat
α
S⁺
−H sat

(b)

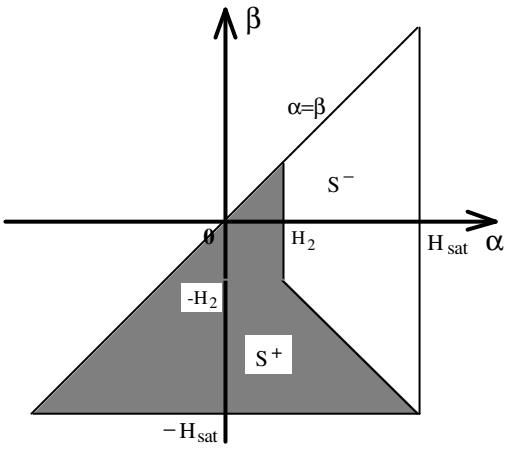
β
α=β
S⁻
H_2
H sat
α
-H_2
S⁺
−H sat

(c)

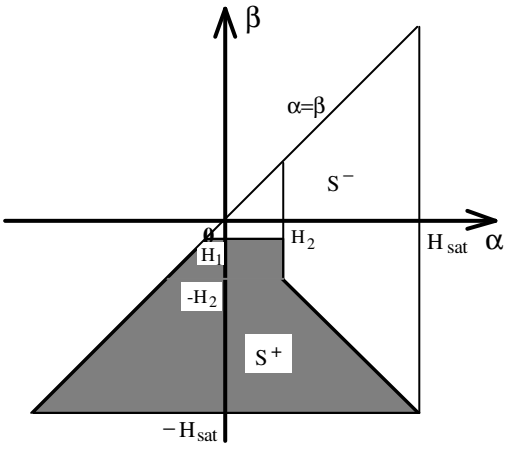
β
α=β
S⁻
H_2
H sat
α
H_1
-H_2
S⁺
−H sat

(d)

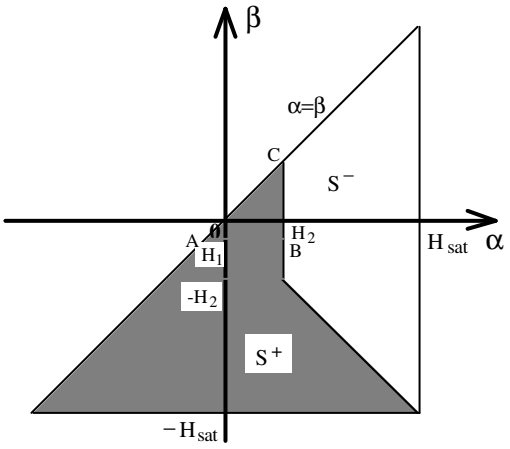
β
α=β
C
S⁻
A
H_2
B
H sat
α
H_1
-H_2
S⁺
−H sat

(e)

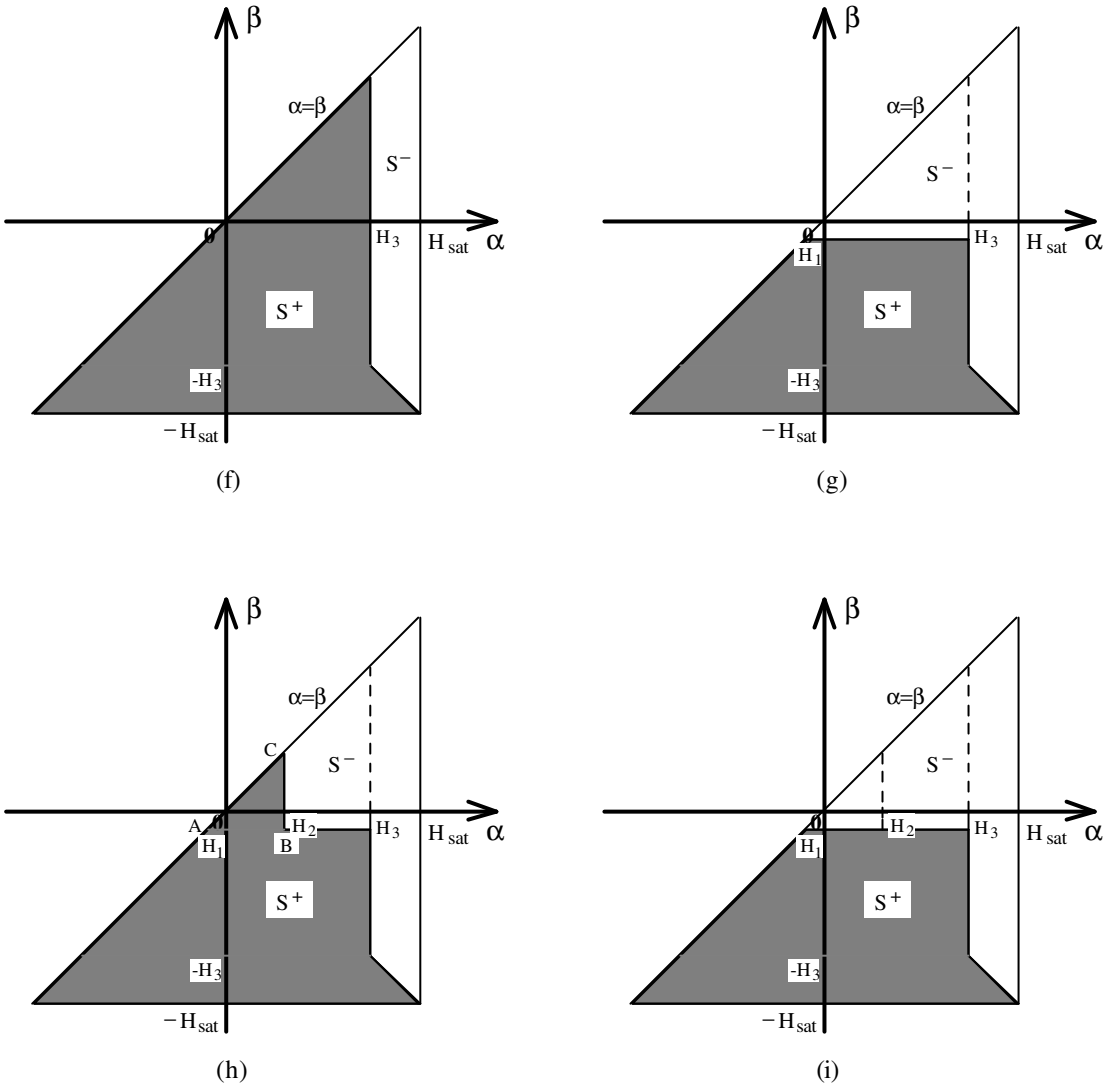

Fig.2-21 Congruent minor loops predicted by the normal Preisach model
(a) minor loops, and (b) - (i) Preisach diagrams corresponding to the magnetisation process O-a-b-a-c-d-e-d shown in (a)

$$\begin{aligned} B_{1d} - B_a &= \mu_o\big(H + M(H)\big) - \mu_o\big(H_2 + M(H_2)\big) \\ &= \mu_o(H - H_2) - 2\mu_o T(H_2, H) \end{aligned} \tag{2.32}$$

where B_{1d} is the flux density on the downward trajectory of loop ① for a given H, and B_a is the flux density at point a (last reversal point) in Fig.2-21(a).

The calculation of the downward trajectory of minor loop ② (segment e-d in Fig.2-21(a)) is illustrated in Figs.2-21(h)-(i). For an applied field strength $H<H_2$, the variation of flux density can be calculated by (2.10) as

$$\begin{aligned} B_{2d} - B_e &= \mu_o(H + M(H)) - \mu_o(H_2 + M(H_2)) \\ &= \mu_o(H - H_2) - 2\mu_o T(H_2, H) \end{aligned} \tag{2.33}$$

where B_{2d} is the flux density on the downward trajectory of loop ② for a given H, and B_e is the flux density at point e (last reversal point) in Fig.2-21(a).

Hence, for any given $H<H_2$, we have

$$B_{1d} - B_a = B_{2d} - B_e \tag{2.34}$$

that is, the downward trajectory of minor loop ① is identical to that of minor loop ②, although the vertical positions of these two minor loops are different.

Similarly, from Figs.2-21(d)-(e) and (g)-(h), it can also be shown that the upward trajectories of the two minor loops are the same, using (2.11).

Therefore, the two minor loops are congruent. The incremental permeability of the two minor loops for a given H_b and H_Δ is

$$\begin{aligned} \mu_\Delta &= \frac{B_\Delta}{\mu_o H_\Delta} \\ &= 1 + \frac{2T(H_2, H_1)}{H_2 - H_1} \end{aligned} \tag{2.35}$$

where $H_\Delta = (H_2 - H_1)/2$, $B_\Delta = (B_e - B_d)/2$, and B_d is the flux density at point d in Fig.2-21(a).

By comparing the Preisach diagrams shown in Figs.2-21(c)-(e) for minor loop ① with those shown in Figs.2-21(g)-(i) for minor loop ②, it can be seen that the congruency of these two minor loops is due to the fact that the distribution function of the elementary magnetic dipoles is independent of the previous and current magnetisation states and hence, the area integrations of the distribution function, which gives the incremental magnetisation for a given incremental field strength, for both minor loops are performed over the same right triangle (ΔABC in Figs.2-21(e) and (h)).

Errors, though small, will be caused by this congruency property when the normal Preisach model is used to predict minor hysteresis loops and incremental permeabilities.

To relax this congruency property, the distribution function of the elementary dipoles must be made dependent on the magnetisation state such that the minor loops determined by the area

integrations of the distribution function over the same triangle will be different if they have different magnetisation histories. For this purpose, two types of magnetisation dependent Preisach models have been proposed by Mayergoyz, Torre, and other researchers: the product model [29,32,49,53,54,56,58,59] and the moving model [41,48-57,59].

2.2.7 Magnetisation Dependent Preisach Models

2.2.7.1 Product Model

In the product model, the magnetisation predicted by the normal Preisach model is modified by a magnetisation dependent modifying function S(N), where N is the magnetisation predicted by the normal Preisach diagram, as illustrated by the block diagram shown in Fig.2-22.

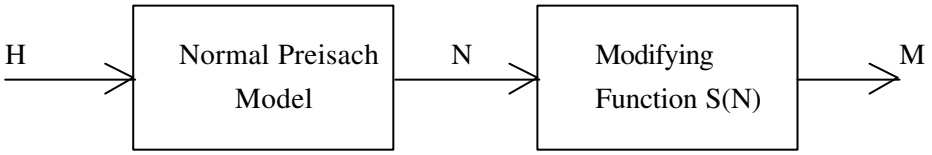

Fig.2-22 Block diagram representing the product model (after [49])

The modifying function S(N) is defined such that [29,32,49,53,58,59]

$$S^{-1}(M) = \int \frac{dM}{R(M)} \tag{2.36}$$

where R(M) is a non-congruency function.

Then

$$M = S(N) \tag{2.37}$$

The non-congruency function R(M) is an even function and may take a simple form such as [29,32]

$$R(M) = 1 - M^2 \tag{2.38}$$

Hence S(N) is an odd function which has properties such as

$$S(-\infty) = -M_s \tag{2.39}$$

and

$$S(+\infty) = M_s \tag{2.40}$$

where M_S is the saturation magnetisation.

The vertically aligned minor loops of the same H_b and H_Δ are predicted non-congruent by the product model. The product model has the property of nonlinear-congruency as determined by the non-congruency function R(M) [49], that is, the congruent minor loops are distributed by a nonlinear function.

2.2.7.2 Moving Model

The moving model relaxes the congruency property of the normal Preisach model using a magnetisation feedback as shown in Fig.2-23, where K is a constant feedback coefficient [41,48-57,59].

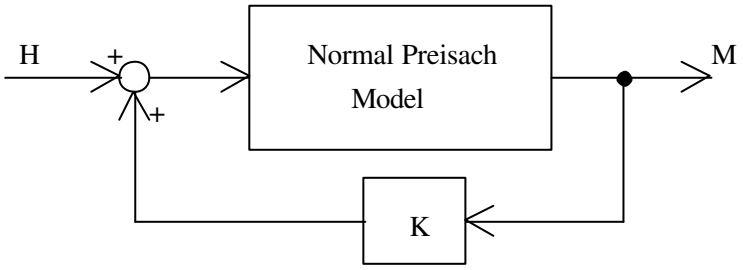

Fig.2-23 Block diagram representing the moving model (after [49])

In numerical calculation, the magnetic field strengths in the increasingly positive and negative directions α and β are replaced by α+KM and β+KM respectively. The resultant magnetisation M is then solved iteratively.

Using the magnetisation feedback, the moving model replaces the congruency property of the normal Preisach model with the skew-congruency property, by which the minor loops connected by lines of slope $-1/K$ are congruent, as illustrated in Fig.2-24. According to the study of Vajda and Torre [55,59], the skew-congruency property agrees better with the experimental data obtained for a variety of commercial recording media than the nonlinear-congruency property of the product model. Unfortunately, applications of this model to electrical steel sheets were not found in the literature.

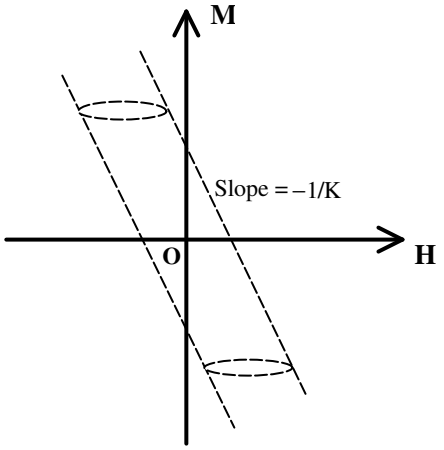

Fig.2-24 Skew-congruency of the moving Preisach model (after [49])

2.3 GENERALISED PREISACH MODEL

2.3.1 Formulation

In order to obtain a complete description of magnetic hysteresis, as discussed in section 2.2.6.1, the reversible component of magnetisation must be included in the model. Fig.2-25(a) shows an elementary hysteresis loop proposed by Vajda and Torre [50,51,52,55], which consists of both the irreversible switching action (Fig.2-25(b)) and the reversible variation (Fig.2-25(c)) of magnetisation process. As a matter of fact, this elementary loop has long been adopted in the development of various models of magnetic hysteresis, such as the Stoner-Wohlfarth model [17,18], and the Jiles-Atherton model [5,19-21].

For the relaxation of the congruency property of the normal Preisach model, the idea of the moving model is employed since it agrees better with experiments than the product model [55,59]. To make it more general, a novel nonlinear magnetisation feedback is used.

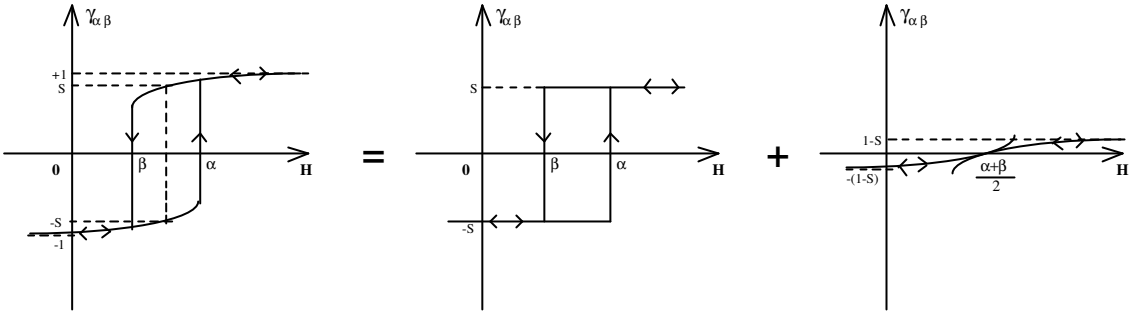

(a) (b) (c)

Fig.2-25 Elementary hysteresis loop for generalised Preisach model
(a) elementary hysteresis loop
(b) irreversible magnetisation component, and
(c) reversible magnetisation component.

Therefore, the magnetisation M and flux density B for a given applied magnetic field strength H can be expressed as

$$M(H) = M_{irr}(H + f(M)) + M_{rev}(H + f(M)) \tag{2.41}$$

and

$$B = \mu_o (H + M(H)) \tag{2.42}$$

where $M_{irr}(H+f(M))$ and $M_{rev}(H+f(M))$ are the irreversible and reversible magnetisation components, which are functions of both the applied field strength and the magnetisation, and f(M) is a nonlinear feedback function, which accounts for the effect of magnetisation on the distribution function of the elementary magnetic dipoles.

The irreversible component of magnetisation can be calculated by the normal Preisach model represented in section 2.2, since the irreversible switching action can be correctly accounted for by the rectangular elementary hysteresis loop, shown in Fig.2-25(b).

The reversible component of magnetisation, however, requires more consideration. An exponential function was used by Torre and Vajda [50-52,55]. As pointed out in section 2.1, however, there is not a single analytic function which fits the magnetisation characteristics of different magnetic materials. For describing the magnetisation process in terms of the reversible and irreversible domain wall motions, the theory of the Jiles-Atherton model [5,19-21] is most helpful. According to this theory, the reversible component of magnetisation is proportional to

the difference of the anhysteretic magnetisation and the irreversible magnetisation component, namely

$$M_{rev} = C(M_{anh} - M_{irr}) \tag{2.43}$$

where C is a constant, and M_{anh} is the anhysteretic magnetisation, which is defined as the magnetisation without hysteresis or when all the pinning sites in the material are removed.

Substituting (2.43) into (2.41), one obtains

$$\begin{aligned} M(H) &= M_{irr}(H + f(M)) + C\left[M_{anh}(H + f(M)) - M_{irr}(H + f(M))\right] \\ &= (1 - C)M_{irr}(H + f(M)) + CM_{anh}(H + f(M)) \end{aligned} \tag{2.44}$$

Defining S=1−C as the squareness of the elementary loop as shown in Figs.2-25(a) and (b) yields the magnetisation for a given applied magnetic field strength as following

$$M(H) = SM_{irr}(H + f(M)) + (1 - S)M_{anh}(H + f(M)) \tag{2.45}$$

Fig.2-26 gives a graphical expression of the generalised Preisach model, where

$$H_{eff} = H + f(M) \tag{2.46}$$

is the effective magnetic field strength when the feedback of magnetisation is considered, and

$$K(M) = \frac{f(M)}{M} \qquad (K(0)=0) \tag{2.47}$$

is a nonlinear feedback coefficient.

2.3.2 The Anhysteretic Magnetisation Curve

Hysteretic magnetisation represents processes where magnetic domains are in a local minimum energy configuration, while the anhysteretic magnetisation curve of a magnetic material represents the global minimum energy configuration. Experimentally, it can be measured by superimposing an AC field whose amplitude decays slowly from saturation to zero on a DC field at each point.

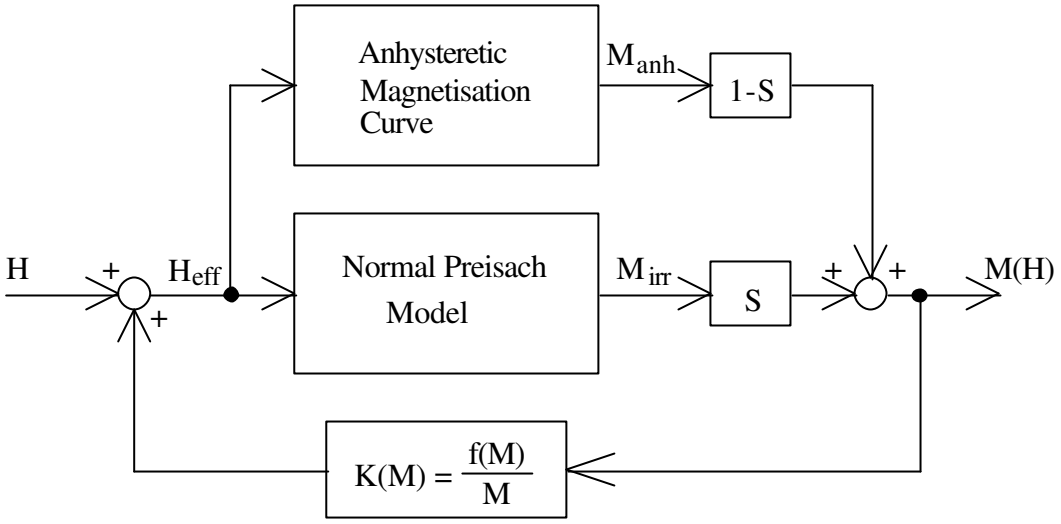

Fig.2-26 Block diagram representing the generalised Preisach model

In their model of hysteresis, Jiles and Atherton [5,19-21] used a modified Langevin function

$$M_{anh}(H) = M_s\left[\coth\left(\frac{H}{a}\right) - \frac{a}{H}\right] \tag{2.48}$$

where M_s is the saturation magnetisation and a is a parameter with dimensions of magnetic field strength which characterises the shape of the anhysteretic magnetisation curve, as the expression of the anhysteretic magnetisation curve. The general validity of this expression for different magnetic materials, however, was not found in the literature.

In 1987, Atherton, *et al* [30] proposed the calculation of anhysteretic magnetisation curves using the normal Preisach model by simulating the procedure of experimental measurement. It was found that the calculated anhysteretic magnetisation was dependent on the decreasing procedure of the superimposed AC magnetic field.

Fig.2-27 illustrates schematically two methods of reducing the superimposed AC field strength to zero in five steps. The reduction of field strength in each step is $(H_{sat}-H_{DC})/5$. Figs.2-27(a),(c), and (e) illustrate the first method. In this method, the initial magnitude of the superimposed AC field is $H_{sat}-H_{DC}$ and it is reduced by $(H_{sat}-H_{DC})/5$ when the magnetisation process is reversed after an upward trajectory as shown by 1,2,...,5 in Fig.2-27(c) and (e). This method gives a lower value of anhysteretic magnetisation (M_{anh}^- in Fig.2-27(a)).

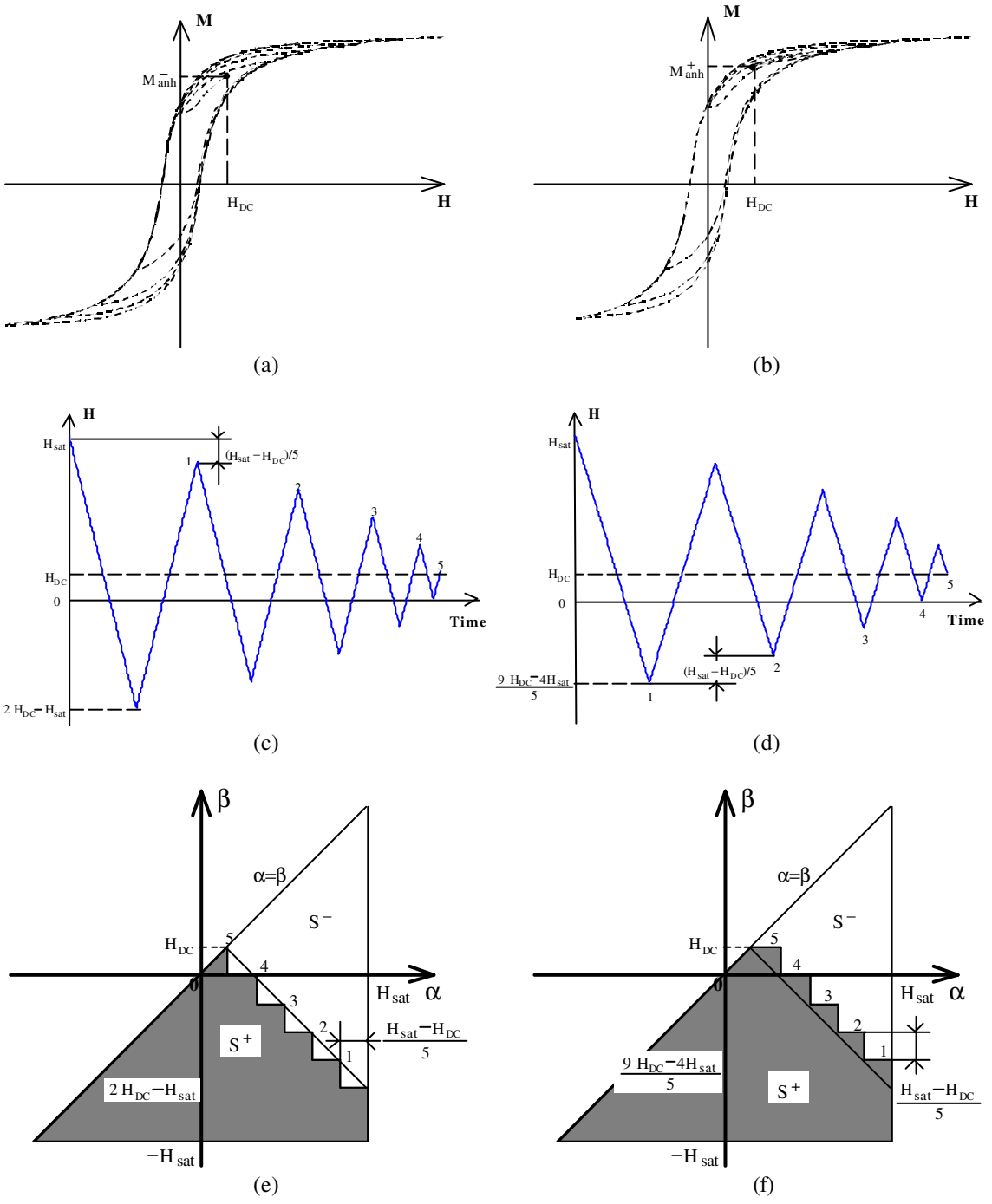

Fig.2-27 Prediction of anhysteretic magnetisation curve using the normal Preisach model
(a) and (b) magnetisation processes,
(c) and (d) variations of magnetic field strength with time, and
(e) and (f) corresponding Preisach diagrams,
for the lower and upper values of anhysteretic magnetisation, respectively.

The second method, as illustrated in Figs.2-17(b), (d), and (f), the magnitude of the superimposed AC field also starts from $H_{sat}-H_{DC}$, but it is reduced when the magnetisation process is reversed after a downward trajectory as indicated by 1,2,...,5 in Figs.2-27(d) and (f). A higher value (M_{anh}^{+} in Fig.2-27(b)) is obtained by this method.

From Figs.2-27(e) and (f), it can be found that the calculated anhysteretic magnetisation also depends on the number of steps in which the superimposed AC field is reduced to zero. When the number of steps approaches infinity, both the higher and lower values obtained by the different field reduction methods converge to the same answer. When a limited number of steps is used, more accurate results can be obtained by averaging the two values of anhysteretic magnetisation predicted by these two methods.

Figs.2-28(a) and (b) depict the calculated anhysteretic magnetisation curves of the mild steel ring sample mentioned in section 2.2.5.4, using the normal Preisach model when the superimposed AC field was reduced to zero in 100 and 500 steps respectively. With the increase of the number of steps, the difference between the higher and lower values decreases.

Fig.2-29 is the anhysteretic magnetisation curve of the mild steel ring sample calculated when the superimposed AC field was reduced to zero in 1000 steps. This curve will be used in the generalised Preisach modelling for the mild steel ring sample.

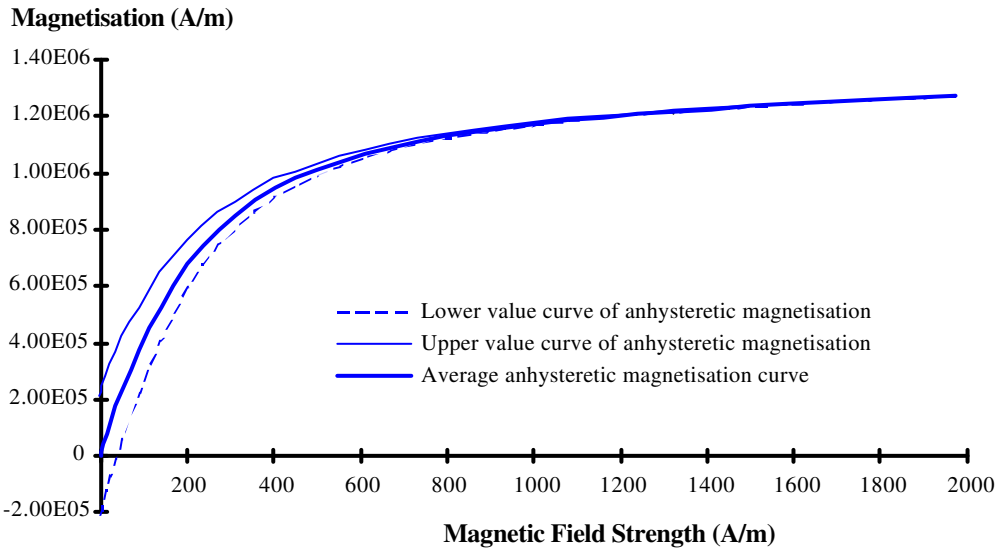

(a)

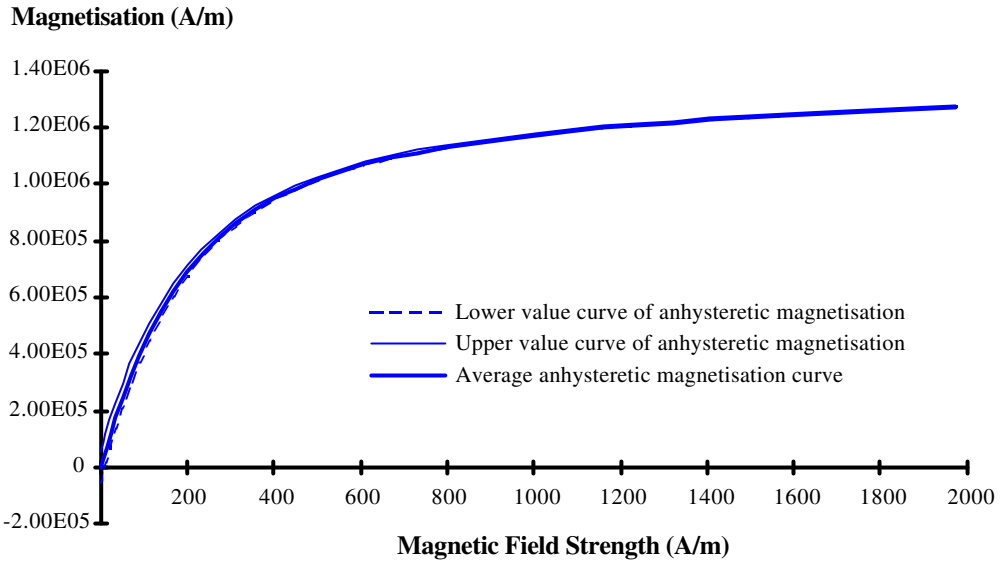

(b)

Fig.2-28 Calculated anhysteretic magnetisation curves of mild steel using the normal Preisach model, when the superimposed field is reduced to zero in (a) 100, and (b) 500 steps.

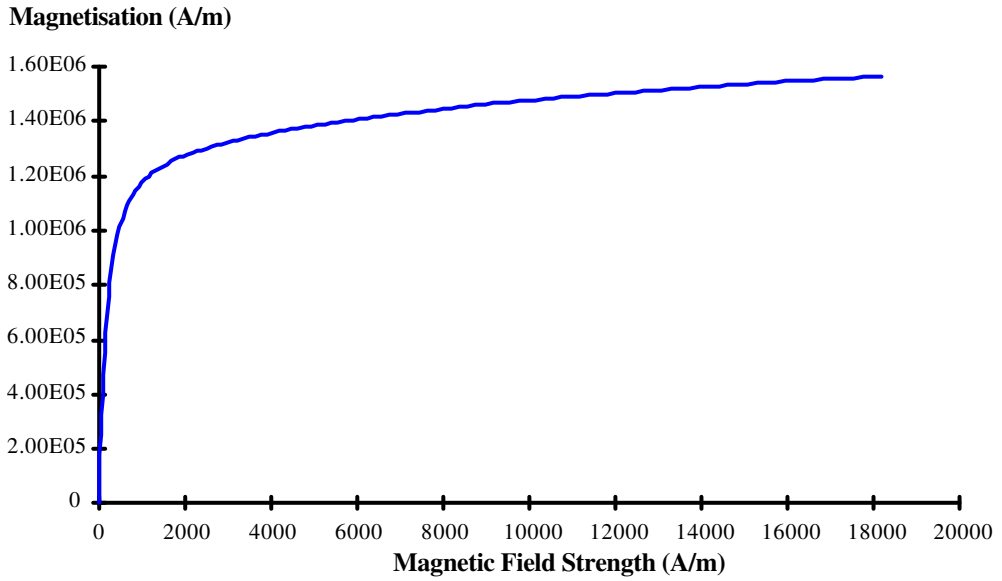

Fig.2-29 Anhysteretic magnetisation curve of mild steel calculated by the normal Preisach model when the superimposed AC field is reduced to zero in 1000 steps

2.3.3 Parameter Identification

The parameters to be identified are the squareness of the elementary hysteresis loop S and the nonlinear feedback coefficient K(M). The methods of identification and the information required are studied in this section.

2.3.3.1 The Squareness

When the generalised Preisach model (2.45) is used to predict the initial magnetisation curve, the susceptibility can be calculated as

$$\begin{aligned}\chi_i &= \frac{dM_i(H)}{dH} \\ &= \left[S\frac{dM_{irr}(H_{eff})}{dH_{eff}} + (1-S)\frac{dM_{anh}(H_{eff})}{dH_{eff}} \right]\left(\frac{dH_{eff}}{dH} \right) \\ &= \left[S\frac{dM_{irr}(H_{eff})}{dH_{eff}} + (1-S)\frac{dM_{anh}(H_{eff})}{dH_{eff}} \right]\left(1 + \frac{df(M_i)}{dM_i}\frac{dM_i(H)}{dH} \right)\end{aligned} \tag{2.49}$$

Hence,

$$\chi_i = \frac{S\frac{dM_{irr}(H_{eff})}{dH_{eff}} + (1-S)\frac{dM_{anh}(H_{eff})}{dH_{eff}}}{1-\left[S\frac{dM_{irr}(H_{eff})}{dH_{eff}} + (1-S)\frac{dM_{anh}(H_{eff})}{dH_{eff}} \right]\frac{df(M_i)}{dM_i}} \tag{2.50}$$

At the origin, when H=0, M_i=0, the magnetisation feedback function $f(M_i)$=0, and hence H_{eff}=0, while the derivative of the feedback function against the initial magnetisation $\left.\frac{df(M_i)}{dM_i}\right|_{M_i=0} = K(0) = 0$. Because the irreversible magnetisation component $M_{irr}(H_{eff})$ is predicted by the normal Preisach model, we have $\left.\frac{dM_{irr}(H_{eff})}{dH_{eff}}\right|_{H_{eff}=0} = 0$, as discussed in section 2.2.6.1. From (2.50), the initial susceptibility can then be written as

$$\begin{aligned}\chi_{io} &= \left.\frac{dM_i(H)}{dH}\right|_{H=0} \\ &= (1-S)\left.\frac{dM_{anh}(H_{eff})}{dH_{eff}}\right|_{H_{eff}=0} \\ &= (1-S)\chi_{ano}\end{aligned} \tag{2.51}$$

Therefore, the squareness of the elementary hysteresis loop

$$S = 1 - \frac{\chi_{io}}{\chi_{ano}} \tag{2.52}$$

where $\chi_{ano} = \left.\frac{dM_{anh}(H_{eff})}{dH_{eff}}\right|_{H_{eff}=0}$ is the gradient or susceptibility of the anhysteretic magnetisation curve at the origin.

For the mild steel ring sample mentioned in section 2.2.5.4, the initial susceptibility obtained from the measured normal magnetisation curve [198] (Preisach modelling assumes the initial magnetisation curve identical to the normal magnetisation curve) is $\chi_{io} = 315$, and the gradient or susceptibility of the anhysteretic magnetisation curve, shown in Fig.2-29, at the origin is $\chi_{ano} = 12113$. Therefore, by (2.52), the squareness S = 0.97.

2.3.3.2 The Magnetisation Feedback Coefficient

Strictly speaking, a great amount of information from various minor loops at different positions is required in order to identify the magnetisation feedback coefficient since it is introduced into the model to account for the dependence of the distribution function of magnetic dipoles on the previous and current magnetisation states of the material. This is, however, inconvenient for both the identification of the coefficient and the practical application of the model. In 1991, Oti, Vajda, and Torre [48] proposed an approximate identification method from the susceptibility on major loops to deduce a constant feedback coefficient, but the determination of the feedback coefficient from the experimental data was very much empirical and inaccurate.

Because of the simplicity of the method, their idea is adapted here to determine the nonlinear feedback coefficient in the generalised Preisach model from the measured initial magnetisation curve.

On an initial magnetisation curve, the susceptibility can be approximately calculated as

$$\begin{aligned}\chi_i &= \frac{dM_i(H)}{dH} \\ &\approx \frac{M_i(H) - M_i(H - \Delta H)}{\Delta H}\end{aligned} \tag{2.53}$$

Let $f(M_i) = \Delta H$, and we have

$$\chi_i \approx \frac{M_i(H) - M_i(H - f(M_i))}{f(M_i)} \tag{2.54}$$

or

$$f(M_i) \approx \frac{M_i(H) - M_i(H - f(M_i))}{\chi_i} \tag{2.55}$$

When the generalised Preisach model is used to simulate the initial magnetisation curve, it is expected to agree with the experimental data, that is

$$\begin{aligned} M_i(H) &= SM_{irr}(H + f(M_i)) + (1-S)M_{anh}(H + f(M_i)) \\ &= M_{i(Test)}(H) \end{aligned} \tag{2.56}$$

where $M_{i(Test)}(H)$ is the measured initial magnetisation curve.

The second term in the numerator of (2.55)

$$M_i(H - f(M_i)) = SM_{irr}(H) + (1-S)M_{anh}(H) \tag{2.57}$$

stands for the initial magnetisation curve calculated when the magnetisation feedback is absent.

Fig.2-30 explains graphically the principle of this identification method for the magnetisation feedback function.

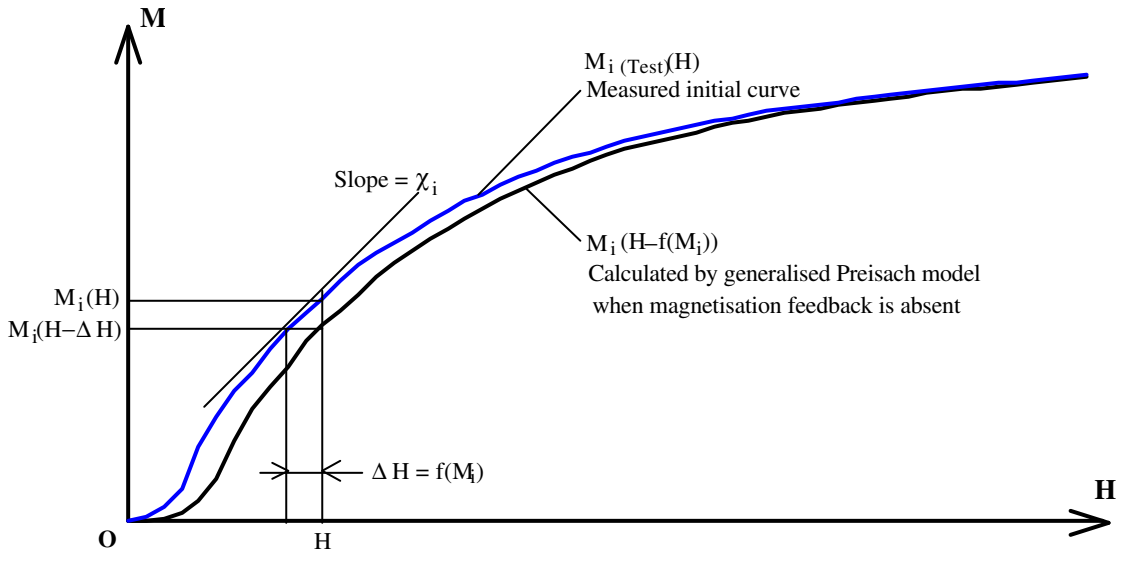

Fig.2-30 Graphical explanation of identification method for magnetisation feedback function

Physically, the feedback is introduced to account for the effect of domain interaction on the distribution function of the elementary dipoles or domains. It may be expected to have the following properties:

(1) It is an odd function of magnetisation, i.e. the effect of domain interaction is reversed if the over all magnetisation is reversed;

(2) It increases with the magnetisation and reaches a maximum in the region where the magnetisation process is dominated by domain expansion and shrinking;

(3) It dies out when the material is saturated and all domain walls disappear.

Finally, the feedback coefficient can be obtained by

$$K(M) = \frac{f(M_i)}{M_i}$$

$$\approx \frac{M_i(H) - M_i(H - f(M_i))}{\chi_i M_i} \tag{2.58}$$

Fig.2-31 illustrates the inferred profile of the magnetisation feedback coefficient for the mild steel ring sample mentioned in section 2.2.5.4. As can be seen from the plot, the profile deduced from the experimental data is jerky. Especially, when the sample is close to saturation, the deduced feedback coefficient jumps up and down because of the very small susceptibility. For the convenience of simulation, the curve is smoothed piecewisely by least square curve fitting using a straight line

$$K(M) = 2.94 \times 10^{-8} M \qquad (0 \le M < 2.19 \times 10^4 \ A/m) \tag{2.59}$$

and a combination of a straight line and an exponential curve

$$K(M) = \left(5.15 \times 10^{-4} + 8.11 \times 10^{-11} M\right) e^{0.187 - 8.56 \times 10^{-6} M} - 8.11 \times 10^{-11} M + 1.3 \times 10^{-4}$$
$$(2.19 \times 10^4 \ A/m \le M < \infty) \tag{2.60}$$

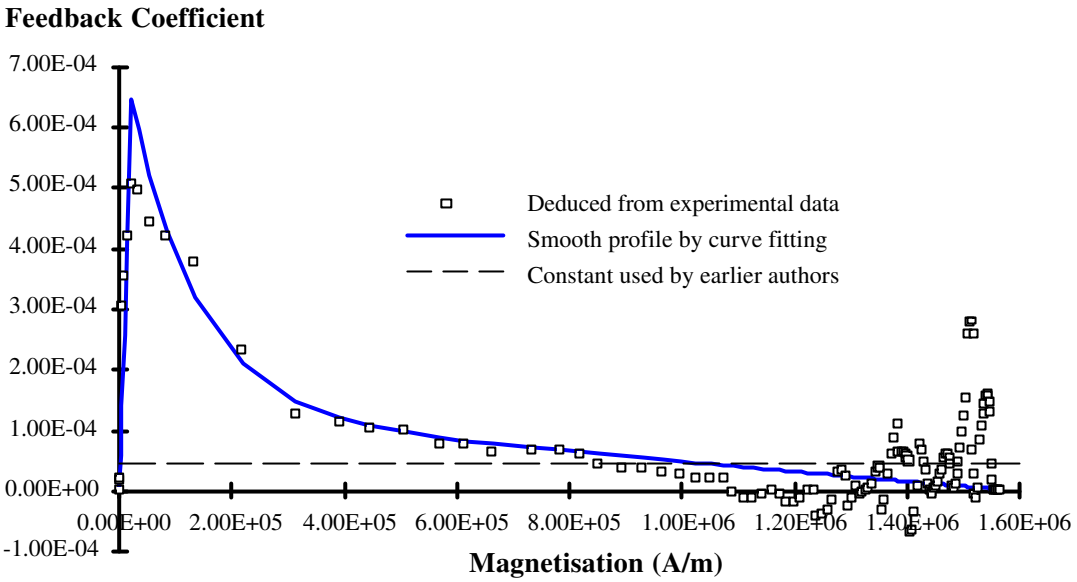

Fig.2-31 New nonlinear feedback coefficient of magnetisation for mild steel (Previous authors used a constant value which would be approximately 0.5×10^{-4} for mild steel)

2.3.4 Software Implementation

Fig.2-32 illustrates the flow chart of the subroutine for the generalised Preisach model. The input data required in the calculation are the limiting hysteresis loop (required by the normal Preisach model) with the upward and downward trajectories in $M_u(H)$ and $M_d(H)$ respectively, the anhysteretic magnetisation curve $M_{anh}(H)$, the squareness S, the nonlinear feedback coefficient K(M), a relaxation coefficient c, which is to be used in the solution of the nonlinear equation (2.45) for the resultant magnetisation by the successive relaxation method, and the convergence precision ε. These input data are transferred from the main program, and hence are not indicated in the flow chart of the subroutine.

In the calculation, the irreversible magnetisation component is calculated by the normal Preisach model. The anhysteretic magnetisation for a given field strength is obtained from the corresponding data table using a second order interpolation while the nonlinear feedback coefficient for a magnetisation is calculated by (2.59) and (2.60). The resultant magnetisation is obtained by solving the nonlinear equation (2.45) using the successive relaxation method. As a convergence criterion, the per unit variation of the magnetisation is adopted, namely

$$\left|\frac{M - M_o}{M_o}\right| \le \varepsilon \tag{2.61}$$

where M is the current value of magnetisation and M_o the old value of magnetisation obtained by the last iteration. After each iteration, if the convergence criterion is not satisfied, the magnetisation for the feedback is then modified by

$$M_o' = M_o + c(M - M_o) \tag{2.62}$$

where M_o' is the new value of the magnetisation used in the calculation of H_{eff}. In the flow chart, the new value M_o' is stored in M_o after the modification.

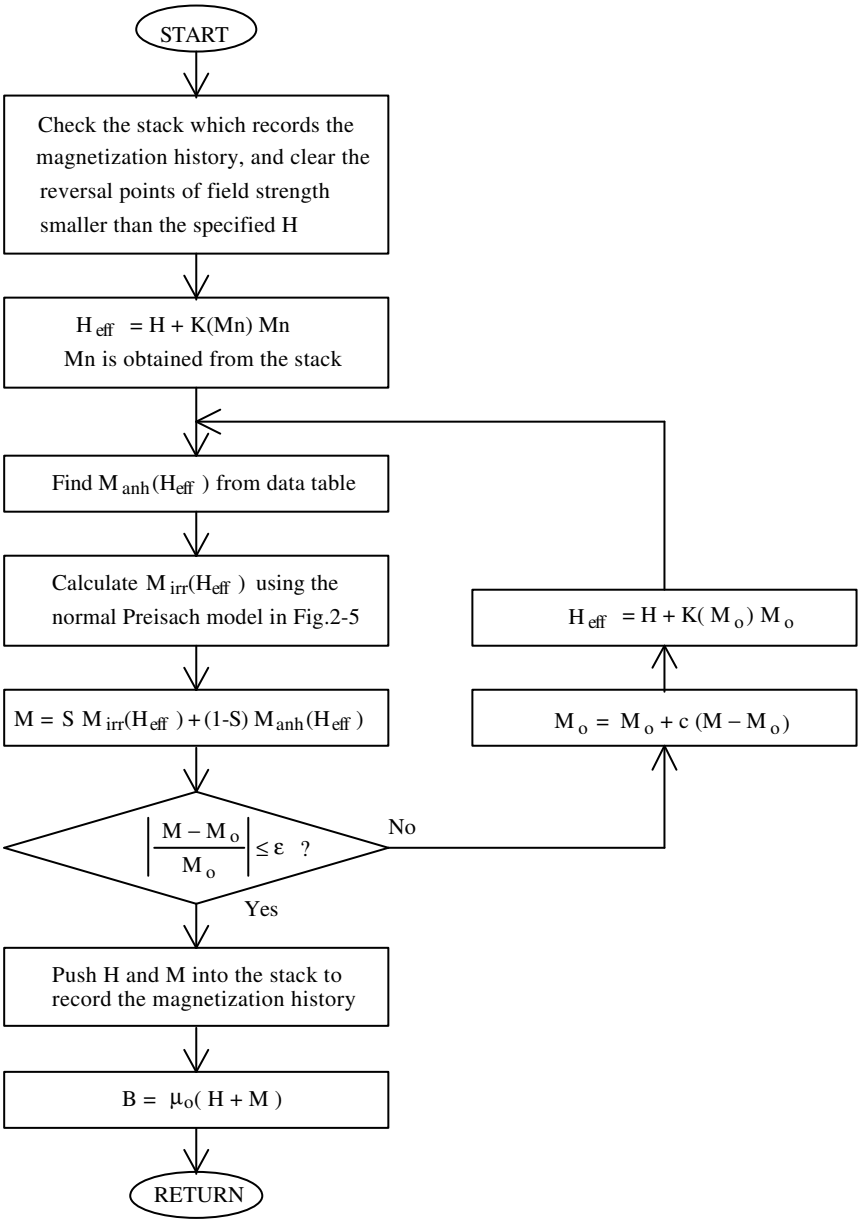

Fig.2-32 Flow chart of the subroutine for the generalised Preisach model

2.3.5 Verification

The experimental data of the mild steel ring sample mentioned in section 2.2.5.4 are again used here for the examination of the generalised Preisach model. The limiting hysteresis loop shown in Fig.2-15 was used as the input data for the normal Preisach model. The squareness and the magnetisation feedback coefficient are reported in sections 2.3.3.1 and 2.3.3.2, respectively. The relaxation coefficient used in the successive solution was 0.5, and the convergence accuracy was 10^{-5}.

2.3.5.1 Non-Congruent Minor Loops

A numerical experiment was conducted on the prediction of minor loops with the same H_b and H_Δ. Fig.2-33(a) shows two different minor loops (① and ②) with the same horizontal positions, and Fig.2-33(b) plots together the minor loops predicted by the normal and the generalised Preisach models. It can be seen that the congruency property of the normal Preisach model, as discussed in section 2.2.6.2, has been relaxed by the magnetisation feedback. Because the magnetisation feedback coefficient depends on the magnetisation state, the skew-congruency that the generalised Preisach model possesses is nonlinear, which is different from the skew-congruency property possessed by the moving model [55,59] (discussed in section 2.2.7.2), in which the magnetisation feedback coefficient is a constant.

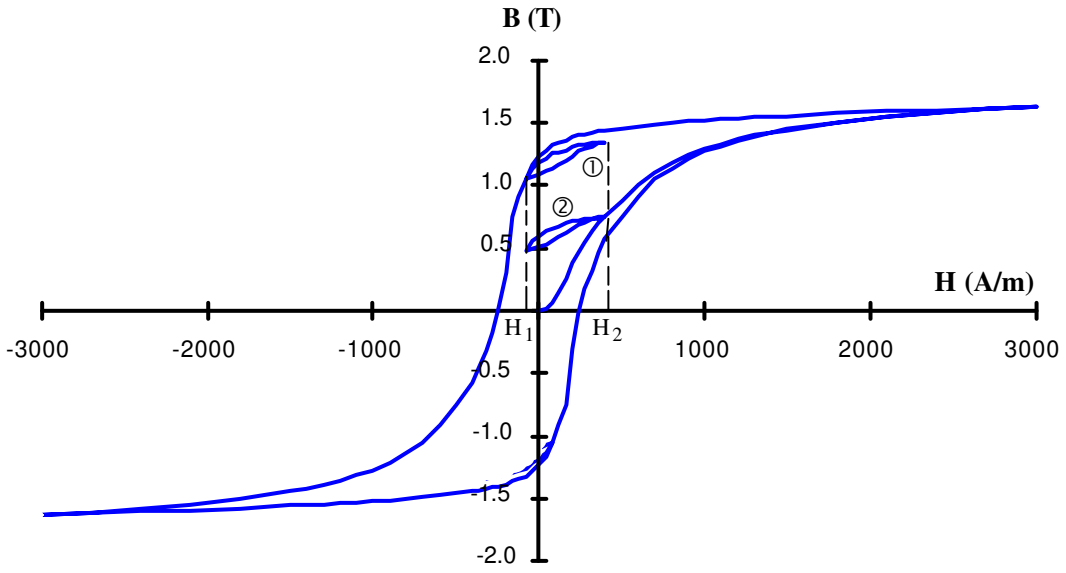

(a)

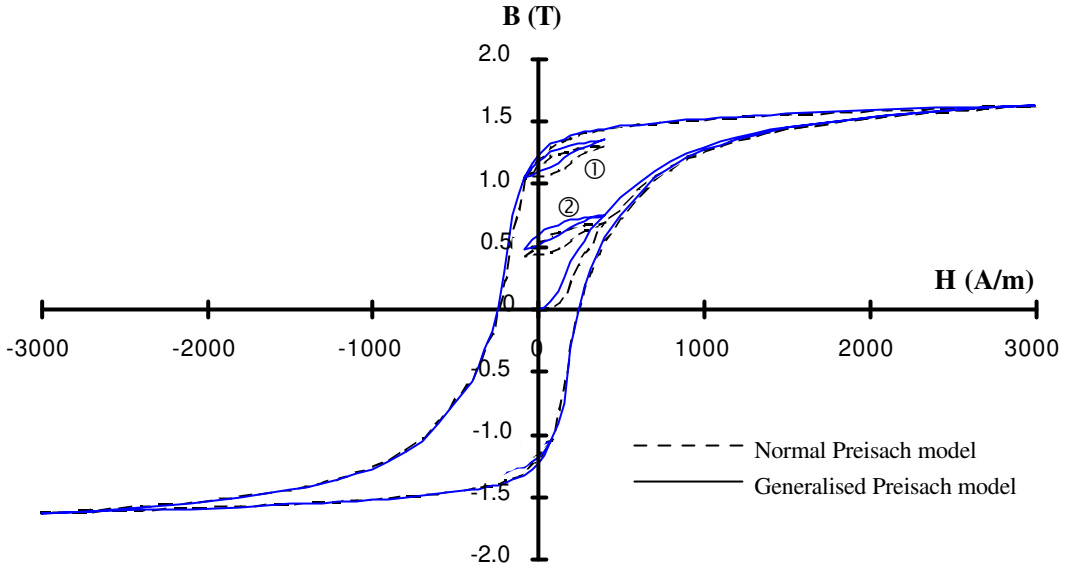

(b)

Fig.2-33 Verification of non-congruency property of the generalised Preisach model for minor loops with same H_b and H_Δ.
(a) Non-congruent minor loops predicted by the generalised Preisach model
(b) Comparison of minor loops predicted by the normal and generalised Preisach models

2.3.5.2 Major Loops

The major loops predicted by the normal and the generalised Preisach models are shown in Fig.2-34 together with the measured loop. The generalised Preisach model prediction is more accurate than the normal model.

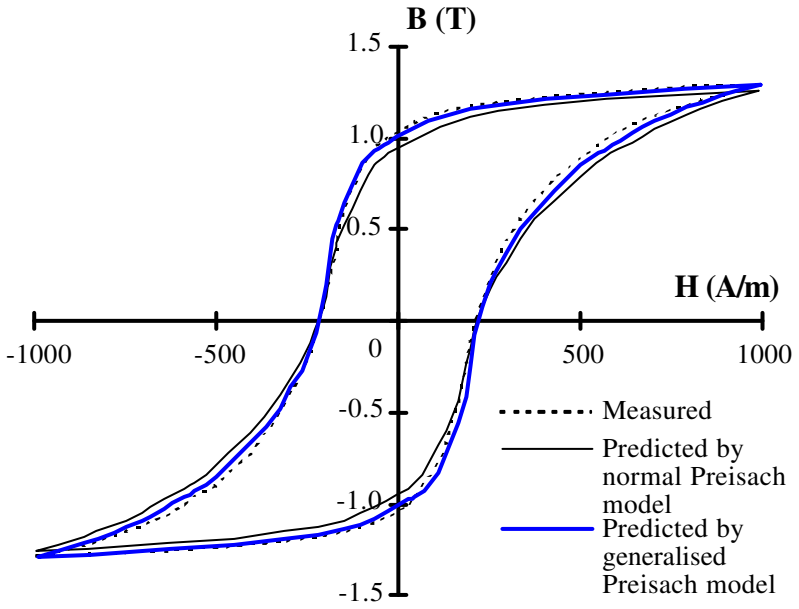

Fig.2-34 Comparison of measured and predicted major loops

2.3.5.3 Normal and Incremental Permeabilities

Finally, the generalised Preisach model was used to calculate the incremental permeabilities measured at different DC biasing magnetic field strengths. Figs.2-35(a) and (b) plot the measured and predicted permeabilities together in linear and logarithmic scales respectively. Much better agreement between the prediction and the measurement is shown.

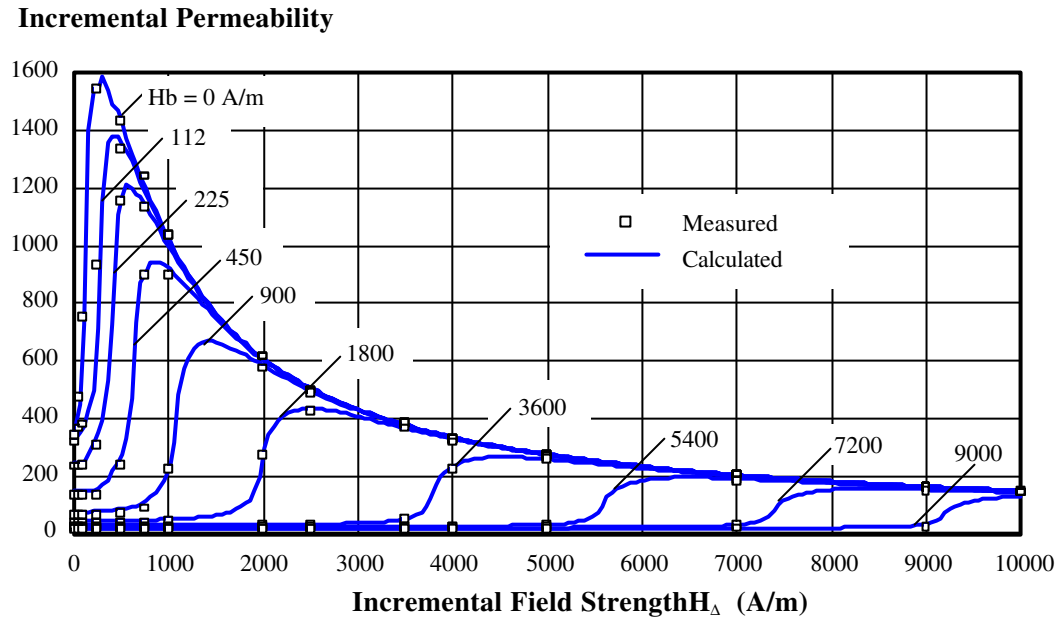

(a)

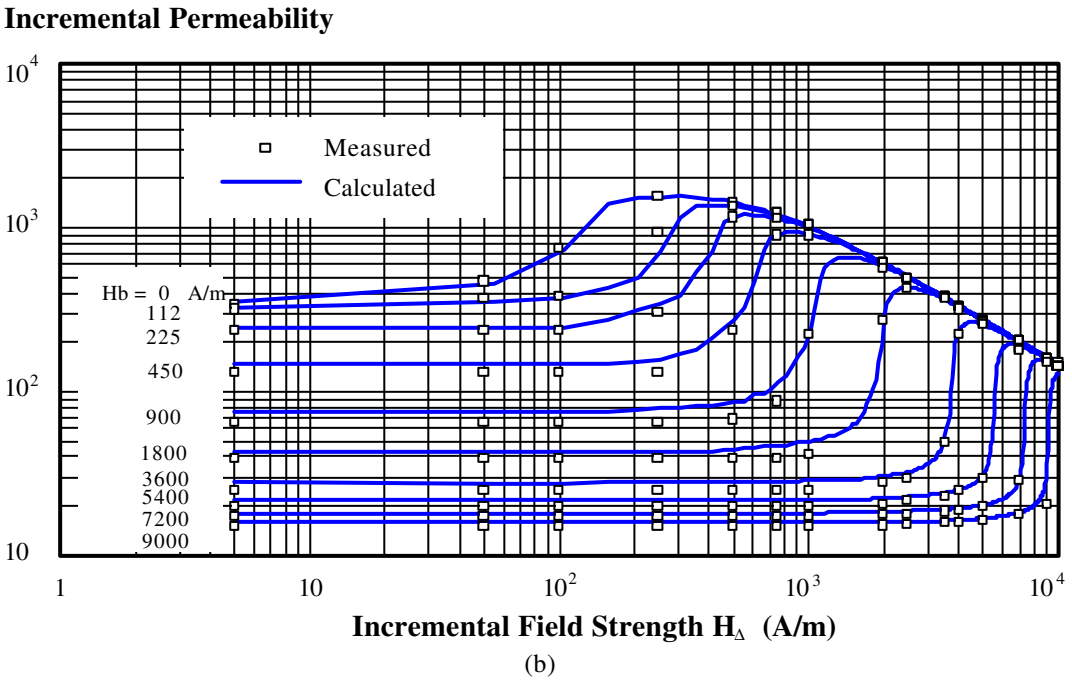

(b)

Fig.2-35 Normal and incremental permeabilities of mild steel plotted in (a) linear, and (b) logarithmic scales

2.4 CONCLUSION

Among various models of magnetic hysteresis, the Preisach model appears to be the most promising one for practical engineering applications. It is strongly related to the mechanisms of magnetic hysteresis, and can describe various macroscopic hysteretic phenomena. The final formulation is very simple for numerical implementation. The only difficulty is that it requires numerous experimental data of the first and second order transition curves for the identification of the elementary dipole distribution function.

In section 2.2, a new formulation of the normal Preisach model was derived based on a graphical description of the Preisach theory of magnetic hysteresis. With the help of the Preisach diagrams for the limiting hysteresis loop, the difficulty of identifying the elementary dipole distribution function was circumvented. The new parameter identification method requires only the limiting hysteresis loop as the input data. Therefore, the normal Preisach model developed here is much more suitable for practical engineering applications.

An experimental verification of the new normal Preisach model was given in section 2.2.5 using major and minor hysteresis loops, hysteresis losses, initial magnetisation curves, and normal and incremental permeabilities of different magnetic materials. The comparison showed that the normal Preisach model can provide correct results, but that errors occur when the hysteresis loop to be predicted is close to the origin of the B-H plane. It was suggested in section 2.2.6 that the discrepancies could be traced to intrinsic defects of the model, such as zero initial susceptibility and congruent minor loops.

To eliminate these incorrect properties of the normal Preisach model, a new generalised Preisach model was developed in section 2.3 by combining elements of the Stoner-Wohlfarth theory, Jiles-Atherton theory, and Vajda-Torre theory of magnetic hysteresis with the Preisach theory. A new nonlinear magnetisation feedback was used in the generalised model. The extra data required by the generalised Preisach model is the normal magnetisation curve, which is readily available from manufacturers' data sheets or simple measurements.

Verifications using minor loops of same H_b and H_Δ, major loops, and normal and incremental permeabilities showed that the new generalised Preisach model gives better accuracy than the normal Preisach model.

Further work is required on development of vector magnetic hysteresis models, i.e. the B-H relation when the magnetic field has a rotational component. Although the Preisach model has

been extended to cover rotational hysteresis [72-79], the method for parameter identification is impractical for engineering applications, and experimental verification was not reported.

CHAPTER 3. DYNAMIC CIRCUIT MODEL OF MAGNETIC CORES

3.1 INTRODUCTION

This chapter concerns the core losses of inductors, transformers, and similar devices with purely alternating magnetic flux. The core losses of devices where the flux has a rotational component will be considered later.

In steady state with sinusoidal and/or non-sinusoidal excitations, the total alternating core loss can generally be separated into hysteresis, eddy current, and anomalous losses [3,81-103]. The Steinmetz law is commonly used for the calculation of hysteresis loss without minor loops [3,90,92,98]. When minor loops appear, the total hysteresis loss can be corrected by multiplying a correction factor based on the amplitudes of minor loops [104-106]. With a non-sinusoidal magnetic flux, the eddy current loss is normally calculated by summing up the contributions from all harmonics [99,100,104-108], while the anomalous loss, which is caused by the effects of magnetic domain wall movement, can only be calculated by integrating the time derivative waveform of flux density [99,100].

Dynamic modelling of magnetic cores, however, has long been a difficult task owing to the non-linear characteristics of magnetic materials and the complicated mechanisms of core losses. Accurate prediction of the instantaneous B-H operating point is important because magnetic cores are often excited with non-sinusoidal waveforms and at high frequency. It would be useful if a simple but accurate magnetic core model could be developed for both low and high frequency applications. The model should be simple to use, easy to formulate, based on data supplied by manufacturers and/or obtained from simple measurements, and able to predict all types of core losses, including hysteresis, eddy current, and anomalous losses, to a good degree of accuracy. In order to satisfy these criteria, a circuit model of magnetic cores is preferred because of its simplicity and time efficiency in simulation.

The conventional core model, which consists of a resistor, standing for the core loss, including the hysteresis and eddy current losses, in parallel or in series with an ideal inductor, which is assumed lossless, standing for the magnetisation, has been widely used in the circuit modelling of inductors and transformers [109-112]. This core model, however, does not account for effects of non-linear magnetisation, hysteresis, and anomalous loss, and hence, is not appropriate to be used for dynamic simulation.

A sampled data model has been used to simulate power electronic circuits containing non-linear inductances [113], but unfortunately, only a non-linear magnetisation curve without hysteresis was used in the model. To account for magnetic hysteresis, PSPICE [114] incorporates the Jiles-Atherton model of hysteresis to model non-linear magnetic cores in transient circuit analysis, but the core loss is not included. Besides, the parameters, such as the pinning energy per unit volume, of the Jiles-Atherton model are not convenient to identify.

Among different hysteresis modelling methods, as discussed in chapter 2, the normal Preisach model seems to be a practical and easy-to-use technique because it can be readily implemented using a simple graphical approach without the use of the complicated mathematics in the full Preisach theory. Details of such a graphical approach were illustrated in chapter 2.

The modelling of core loss needs more investigation. For dynamic simulation, the steady state models mentioned above can not be adopted directly. Firstly, the B-H relationship and the hysteresis loss should be determined by the hysteresis model, instead of the normal magnetisation curve and the Steinmetz law. Secondly, the eddy current and anomalous losses should be calculated instantaneously. O'Kelly [199,200] studied flux penetration and losses in a steel plate with nonsinusoidal magnetisation using an exponential model for hysteresis and a multilayer approach for eddy currents. Burais [201] and Naidu [202] calculated the core loss in thin laminations with hysteresis and eddy current losses included using the Preisach model for hysteresis and the finite element method and finite differential method, respectively, for eddy currents. However, the anomalous loss can not be calculated by these methods.

In this chapter, dynamic circuit models of magnetic cores for low and high frequency operation are developed, discussed, and verified with experiments. All components of core loss are considered.

Section 3.2 presents a dynamic circuit model of laminated magnetic cores for low frequency operation. In this circuit model, eddy current loss is modelled by a constant resistor and anomalous loss by a non-linear resistor, while a non-ideal inductor is used to account for the effects of hysteresis and magnetisation. The normal Preisach model of hysteresis outlined in chapter 2 is used to trace the trajectory of magnetisation. A recently developed discrete transform technique [203-205] is applied to the model for easy and quick numerical solution of non-linear state equations. The model is compared with experiments on a laminated annular ring of non-oriented electrical steel Lycore-140 under sinusoidal and square wave voltage excitations at 100 Hz. Skin effect, models of eddy current loss, and computing time and precision are discussed.

Section 3.3 generalises the above circuit model for high frequency operation. The cross section of a solid core or laminated core at high frequency can be divided into a few slices according to the size of the core and the excitation frequency. A ladder network model is developed to account for the skin effect. This model reduces to the simple one outlined in section 3.2 when only one stage of the ladder network is used. A comparison with measurements on a laminated annular ring of Lycore-140 under square wave 1 kHz voltage excitation and on a Siemens/Matsushita N47 soft ferrite R16 toroid core under 100 kHz square wave voltage excitation is made. The results show that this model is suitable for engineering applications.

3.2 A DYNAMIC CIRCUIT MODEL OF LAMINATED CORES

3.2.1 Dynamic Circuit Model

The total energy dissipated in a magnetic core can be separated into hysteresis loss P_h, eddy current loss P_e, and anomalous loss P_a [3,81-103]. For dynamic calculations, the eddy current and anomalous losses can be represented by two resistors, R_e and R_a, respectively, as shown in Fig.3-1, but it is not adequate to define an equivalent resistor for hysteresis loss, since it can not be explicitly related to the instantaneous flux density. The hysteresis loss per cycle is defined as the area enclosed by the hysteresis loop for a whole cycle of extremely low frequency excitation, and the loss is incorporated in the model by a non-ideal inductor L(i), which includes both the hysteresis and the core non-linearity. The circuit equations can be written as

$$V_s = R_w i_s + V_L \tag{3.1}$$

$$V_L = \frac{d\lambda}{dt} = L(i)\frac{di_L}{dt} \tag{3.2}$$

$$i_e = \frac{V_L}{R_e} \tag{3.3}$$

$$i_a = \frac{V_L}{R_a} \tag{3.4}$$

$$i_s = i_e + i_a + i_L \tag{3.5}$$

where R_w is the resistance of the excitation coil, λ is the flux linkage of the coil, and $L(i) = \frac{d\lambda}{di_L}$ the differential inductance.

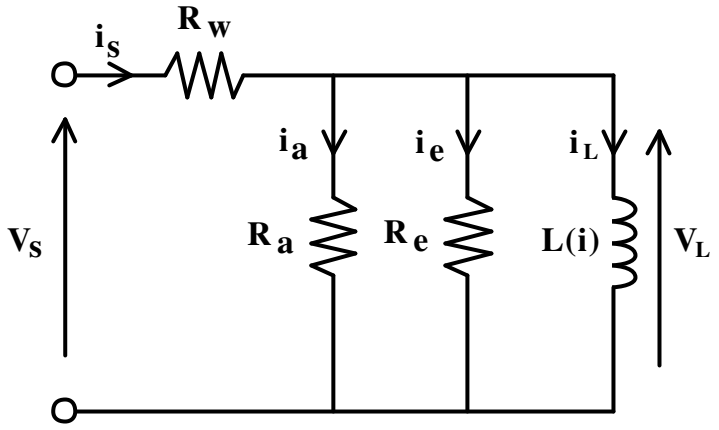

Fig.3-1 Dynamic equivalent circuit of a magnetic core

For computer simulation, a discrete circuit model can be readily derived using the TLM-based discrete transform technique [203-205]. The TLM discrete transform technique expresses $\frac{di}{dt}$ as $\frac{di}{dt} = V_U = Z_U i + 2V_U^i$, where $Z_U = 2/T_p$, T_p the propagation time (which equals the time step used in the numerical solution), V_U^i is the incident voltage pulse used in the TLM method, and V_U is equal to the magnitude of di/dt or numerically the voltage across an inductor of 1 Henry with the same di/dt. Equation (3.2) can be rewritten as

$$V_L = L(i)\,(Z_U i_L + 2V_U^i) \tag{3.6}$$

Therefore, the discrete form of the dynamic circuit model of magnetic cores can be readily obtained as depicted in Fig.3-2.

With the help of the TLM discrete transform technique, the circuit equations have been reduced from a non-linear differential equation system to a non-linear algebraic equation system, which can be solved iteratively. In iterations,

$$V_{U(m)} = Z_{U(m)} i_{L(m)} + 2V_U^i{}_{(m)} \tag{3.7}$$

and

$$V_U^i{}_{(m+1)} = V_U^i{}_{(m)} - V_{U(m)} \tag{3.8}$$

where the bracketed subscript (m) denotes the *m*-th iteration.

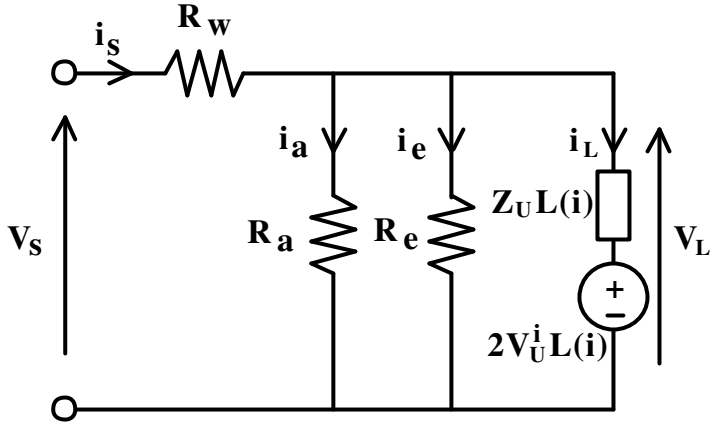

Fig.3-2 Discrete core model

3.2.2 Core Losses and Circuit Parameters

3.2.2.1 Core Losses in the Equivalent Circuit

The energy of the model should be conserved, when all sources of loss are considered. The total average power fed into the core can be obtained by multiplying the instantaneous voltage $V_L(t)$ with the instantaneous current $i_s(t)$ and then averaging over a cycle, i.e.

$$\begin{aligned}\frac{1}{T}\int_0^T V_L i_s dt &= \frac{1}{T}\int_0^T V_L (i_a + i_e + i_L) dt \\ &= \frac{1}{T}\int_0^T R_e i_e^2 dt + \frac{1}{T}\int_0^T R_a i_a^2 dt + \frac{1}{T}\int_0^T i_L \frac{d\lambda}{dt} dt \end{aligned} \qquad (3.9)$$

The first and the second terms on the right hand side of (3.9) represent the power losses dissipated in the equivalent resistors for the eddy current loss and the anomalous loss, while the last term gives the hysteresis loss when hysteresis is considered in the flux linkage calculation.

3.2.2.2 Equivalent Resistors

According to the classical calculation for thin laminations, the instantaneous eddy current loss

$$P_e(t) = C_e\left(\frac{dB}{dt}\right)^2 \rho_m A l_m \tag{3.10}$$

where C_e is the eddy current loss coefficient, B the instantaneous flux density, ρ_m the mass density, A the cross sectional area, and l_m the mean length of the flux path in the core. Hence, the equivalent eddy current resistance

$$\begin{aligned} R_e &= \frac{V_L(t)^2}{P_e(t)} \\ &= \frac{N^2 A}{C_e\ \rho_m l_m} \end{aligned} \tag{3.11}$$

where N is the number of turns of the excitation coil wound on the core, and it is assumed that λ=NAB, so $V_L = NA\frac{dB}{dt}$.

The anomalous loss is generally considered to be caused by the motion of domain walls. In addition to the eddy currents generated in the vicinity of the moving walls [81], anomalous hysteresis loss is caused by the wall interaction with lattice inhomogeneities [95]. The dependence

$$P_a(t) = C_a\left|\frac{dB}{dt}\right|^{3/2} \rho_m A l_m \tag{3.12}$$

where C_a is a constant coefficient, has been corroborated experimentally [95,99,101], and will be assumed here. Thus

$$\begin{aligned} R_a &= \frac{V_L(t)^2}{P_a(t)} \\ &= \frac{N^{3/2}}{C_a\ \rho_m l_m}\sqrt{A\left|V_L(t)\right|} \end{aligned} \tag{3.13}$$

Here, R_a is a non-linear resistor.

3.2.2.3 Identification of Loss Coefficients

The loss coefficients, C_e and C_a, are identified experimentally by the classical alternating core loss separation procedure [82,92,101] from the loss curves obtained either from the manufacturers' data sheets or by measurements with a sinusoidal flux density.

The experimental set-up for measuring hysteresis loops and losses presented in chapter 2, section 2.2.5.1 can also be used here for alternating core loss measurement. The alternating core loss can be calculated from the measured excitation current $i_s(t)$ and induced emf $V_L(t)$ by

$$\begin{aligned} P_c &= \frac{1}{T}\int_0^T V_L(t) i_s(t) dt \\ &= \frac{Al_m}{T}\int_0^T H_s \frac{dB}{dt} dt \end{aligned} \tag{3.14}$$

where $\frac{dB}{dt} = \frac{V_L(t)}{NA}$, $H_s = Ni_s(t)/l_m$ is the surface magnetic field strength, and $\int_0^T H_s \frac{dB}{dt} dt$ is the area enclosed by the B-H_s loop. At a very low frequency, eddy currents can be ignored and (3.14) gives pure hysteresis loss.

In the measurement, the flux density waveform should be kept sinusoidal, as required by the international standard of alternating core loss measurement [208]. This can be done by a negative feedback of the voltage across the secondary coil (flux density coil) on the ring sample, as illustrated in Fig.2-8. Therefore, loss contributions from higher harmonics of flux density, such as hysteresis losses due to minor loops and higher harmonic eddy current losses, are excluded, and accurate loss separation can be achieved.

Fig.3-3 shows the alternating core losses of Lycore-140 0.35mm sheet (wire cut and no further heat treatment) measured using an annular ring sample with a sinusoidal flux density at different frequencies. The dimensions and parameters of the annular ring sample and the excitation and flux density coils were given in section 2.2.5.2, Table 2-1.

Fig.3-4 illustrates the alternating core loss separation procedure at B = 0.1, 0.3, 0.5, 1.0, and 1.3 T. The specific core loss per cycle p_c/f (in W/kg/Hz) was separated into the specific hysteresis loss per cycle p_h/f, the specific eddy current loss per cycle p_e/f, and the specific anomalous loss per cycle p_a/f, where lowercase p is used to denote average loss over a cycle. The specific hysteresis loss per cycle p_h/f was measured at 0.5 Hz. The specific eddy current

loss per cycle p_e/f was calculated analytically, under the assumption of sinusoidal flux density and thin laminations, by

$$p_e / f = \frac{\sigma \pi^2 b^2}{6\rho_m} f B_p^2 \tag{3.15}$$

where f is the magnetisation frequency, σ the conductivity, b the thickness of the steel sheet, and B_p the peak value of flux density.

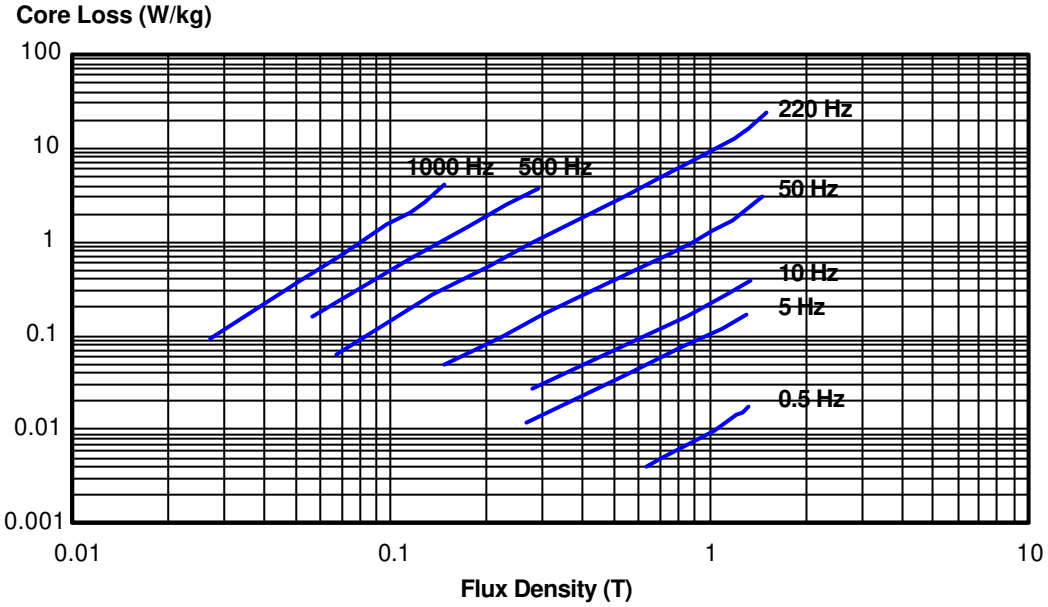

Fig.3-3 Alternating core losses of Lycore-140 measured using an annular ring sample with a sinusoidal flux density at different frequencies

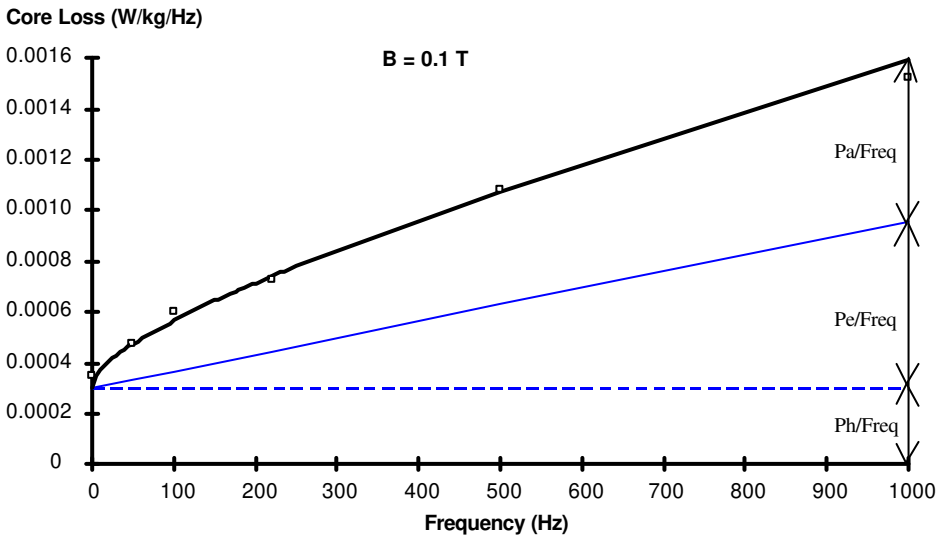

(a)

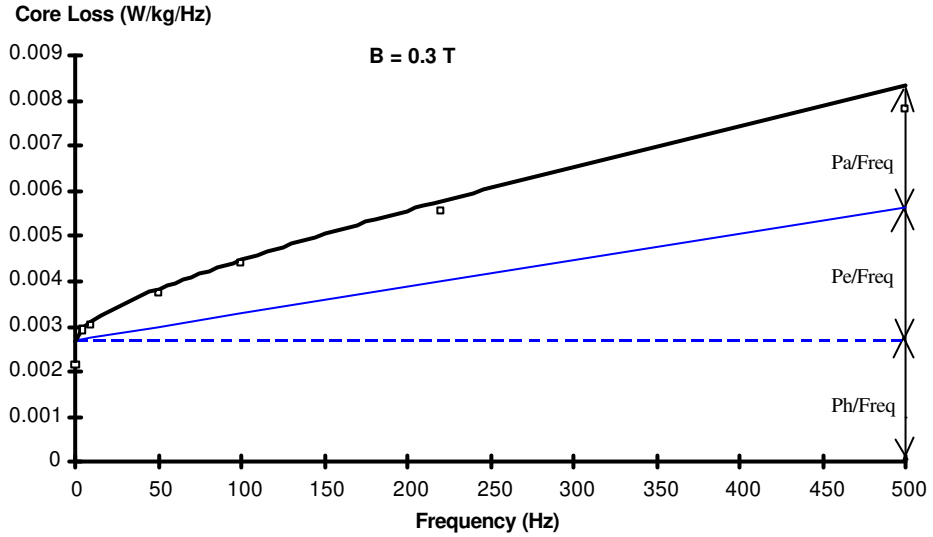
Core Loss (W/kg/Hz)
B = 0.3 T
0.009
0.008
0.007
0.006
0.005
0.004
0.003
0.002
0.001
0
Pa/Freq
Pe/Freq
Ph/Freq
0
50
100
150
200
250
300
350
400
450
500
Frequency (Hz)

(b)

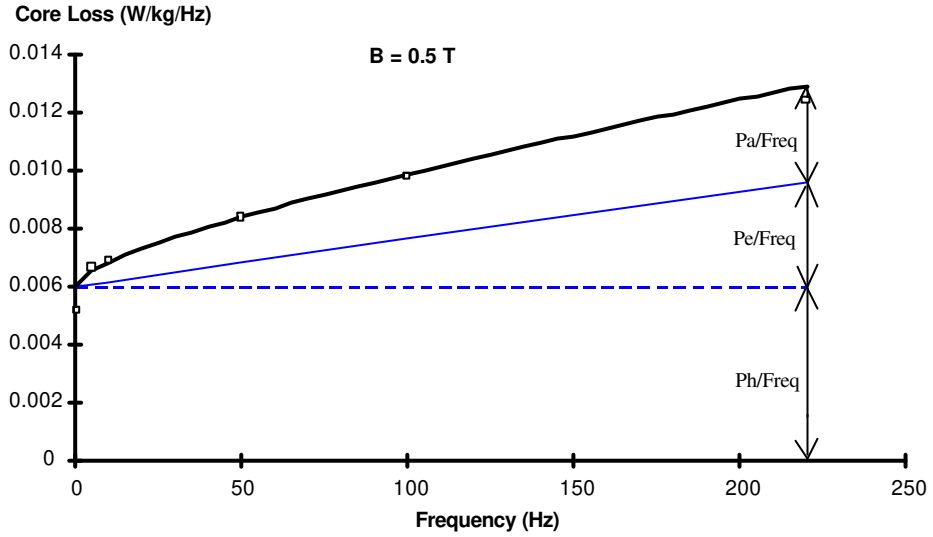
Core Loss (W/kg/Hz)
B = 0.5 T
0.014
0.012
0.010
0.008
0.006
0.004
0.002
0
Pa/Freq
Pe/Freq
Ph/Freq
0
50
100
150
200
250
Frequency (Hz)

(c)

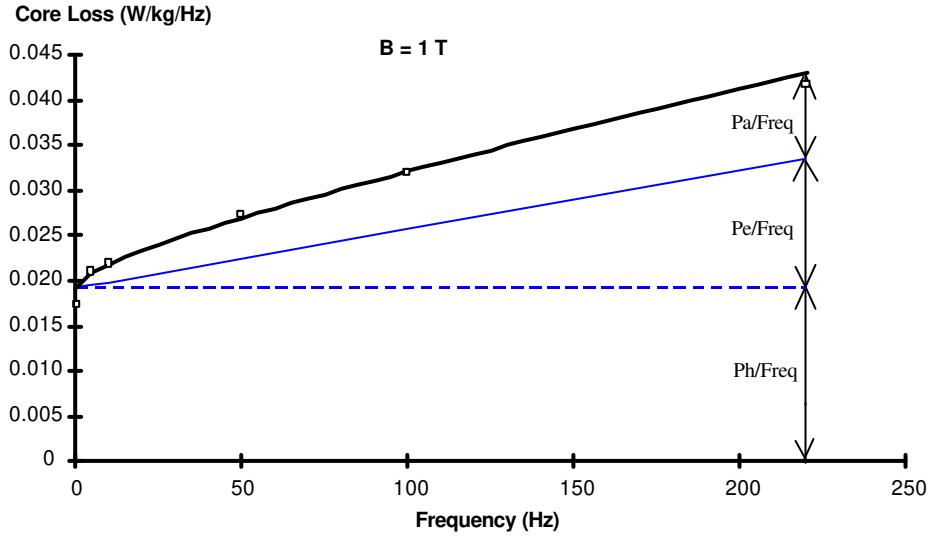
Core Loss (W/kg/Hz)
B = 1 T
0.045
0.040
0.035
0.030
0.025
0.020
0.015
0.010
0.005
0
Pa/Freq
Pe/Freq
Ph/Freq
0
50
100
150
200
250
Frequency (Hz)

(d)

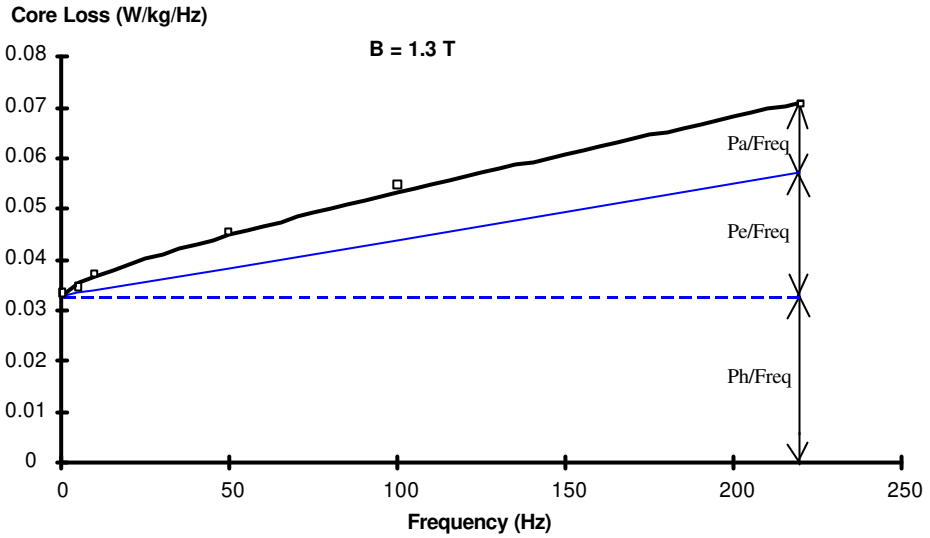

(e)

Fig.3-4 Core loss separation of Lycore-140
▫ Measured, and
——— , ——, and – – – Calculated

When calculated from (3.10),

$$p_e/f = \frac{1}{T}\int_0^T \frac{P_e(t)}{\rho_m A l_m f}\,dt = 2\pi^2 C_e f B_p^2 \qquad (3.16)$$

Therefore, $C_e = \frac{\sigma b^2}{12\rho_m}$.

The specific anomalous loss per cycle p_a/f was obtained by subtracting p_h/f and p_e/f from the total specific core loss per cycle p_c/f. For a sinusoidal flux density,

$$p_a/f = \frac{1}{T}\int_0^T \frac{P_a(t)}{\rho_m A l_m f}\,dt = 8.764 C_a f^{1/2} B_p^{3/2} \qquad (3.17)$$

where coefficient $8.764 = \sqrt{2\pi}\int_0^{2\pi} \left|\cos(\omega t)\right|^{3/2} d\omega t$ is corrected from 8.67 in [99]. C_a can, therefore, be determined by fitting the p_a/f curve with (3.17).

For the core loss of Lycore-140 0.35mm sheet reported in Fig.3-3 and Fig.3-4, the deduced core loss coefficients are $C_e = 0.3314\times10^{-5}$, and $C_a = 0.7280\times10^{-4}$. The curve fitting process used was least squares curve fitting.

3.2.2.4 Hysteresis Model and Differential Inductance

Among the hysteresis models available, as discussed in chapter 2, the Preisach model appears to be the most practical one due to easy parameter identification and good accuracy. The normal Preisach model of magnetic hysteresis is thus employed to trace the history of magnetisation in the magnetic core to be modelled.

When the flux densities in two consecutive time steps are obtained by the Preisach hysteresis model, the differential inductance can be calculated as

$$L(i) = \frac{d\lambda}{di_L} = NA\frac{B_m - B_{m-1}}{i_{L(m)} - i_{L(m-1)}} \tag{3.18}$$

where the subscript m denotes the *m*-th time step.

3.2.3 Experimental Verification

To confirm the validity of the proposed discrete circuit model, the current and emf waveforms and the core loss of the annular ring sample used in the alternating core loss measurement in section 3.2.2.3 were measured and simulated under sinusoidal and square wave voltage excitations at 100 Hz.

3.2.3.1 Experimental Method

Fig.3-5 illustrates the experimental set-up for the measurements. The annular ring was the same one (Lycore-140) used in the alternating core loss measurement reported in section 3.2.2.3. The current i_s signal was obtained from the voltage across the resistor R_1 (1.17 Ω), and the voltage V_L in the core model was measured from the secondary coil voltage because the current was zero. The total core loss was calculated by (3.14).

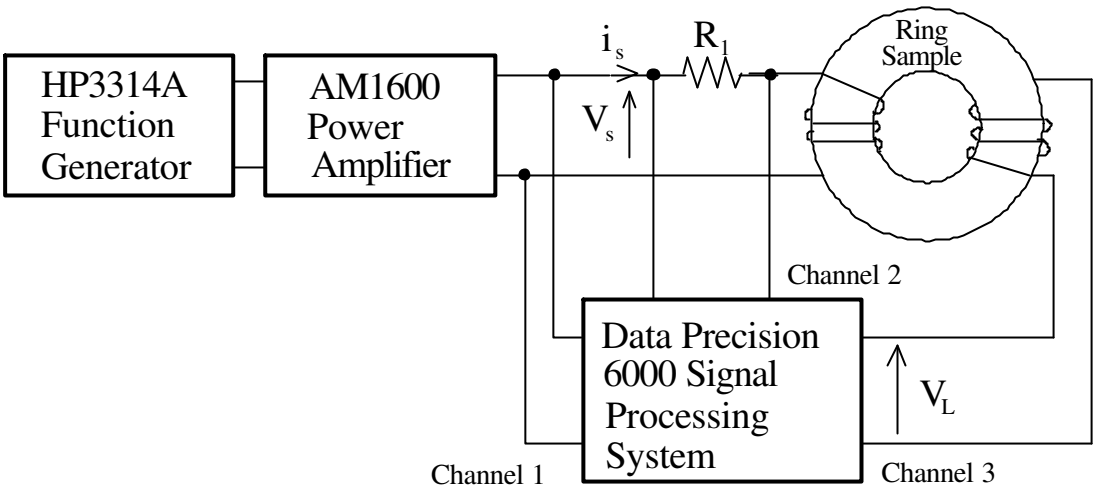

Fig.3-5 Experimental set-up of annular ring example

3.2.3.2 Calculation

The equivalent circuit in Fig.3-2 was used in the simulation with R_1 in series with R_w. The core losses were calculated by (3.9), where the hysteresis loss was calculated by the numerical integration of the pure hysteresis loop obtained from the normal Preisach model in chapter 2.

3.2.3.3 Comparison of Results

Fig.3-6(a) and Fig.3-7(a) show the simulated and the measured voltage and current waveforms under both sinusoidal and square wave excitation. Fig.3-6(b) and Fig.3-7(b) give the variation of the anomalous loss equivalent resistance and the differential inductance against time. The anomalous loss equivalent resistances in Fig.3-6(b) and Fig.3-7(b) should have become zero when V_L=0. Due to the big change of V_L about zero, very small time steps are required to achieve this point. For the time steps used, the R_a curves did not reach zero, because the exact point was not calculated. Fig.3-6(c) and Fig.3-7(c) are various B-H loops. Among these loops, the innermost is the pure hysteresis loop obtained by plotting B against $H=Ni_L/l_m$. The Hyst.+Eddy Loop was obtained by plotting B against $H_{eh}=N(i_L+i_e)/l_m$, and the Hyst.+Eddy+Anom. Loop by plotting B against $H_s=Ni_s/l_m$. The predicted outermost loops are quite close to the measurements. This shows the agreement between the predicted and the measured core losses. Table 3-1 lists the calculated and the measured core losses in each case.

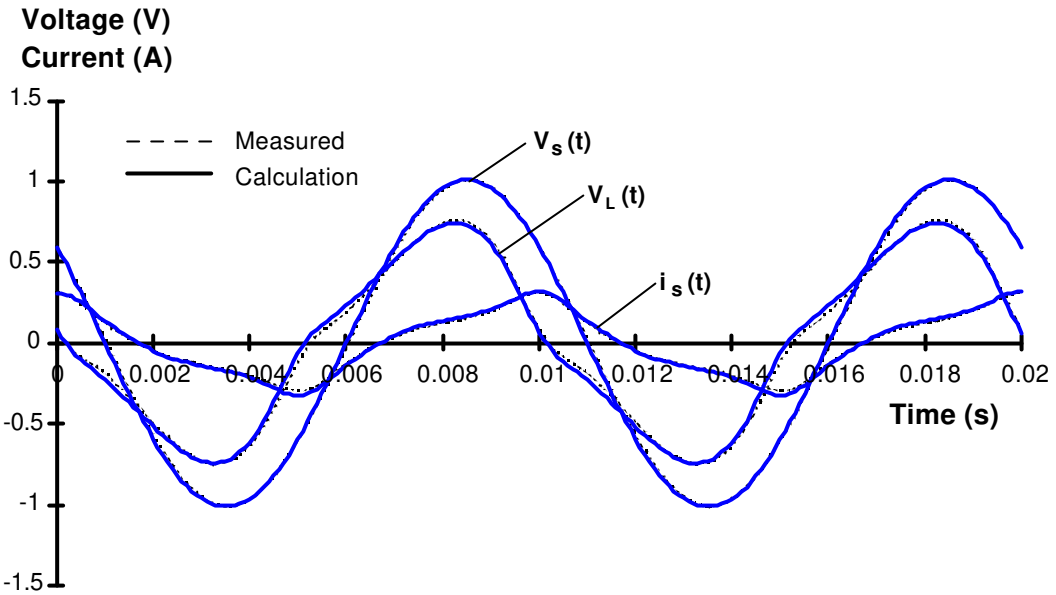

Note: The ideal value of V_S used in the calculation is slightly different from the actual signal due to the non-ideal characteristics of the power amplifier.

(a)

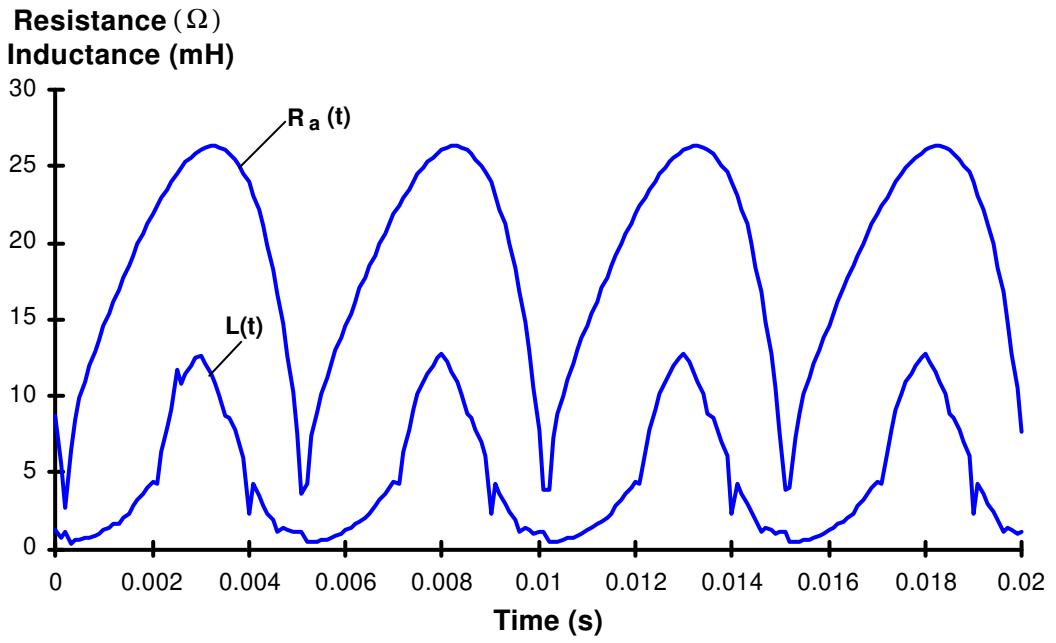

(b)

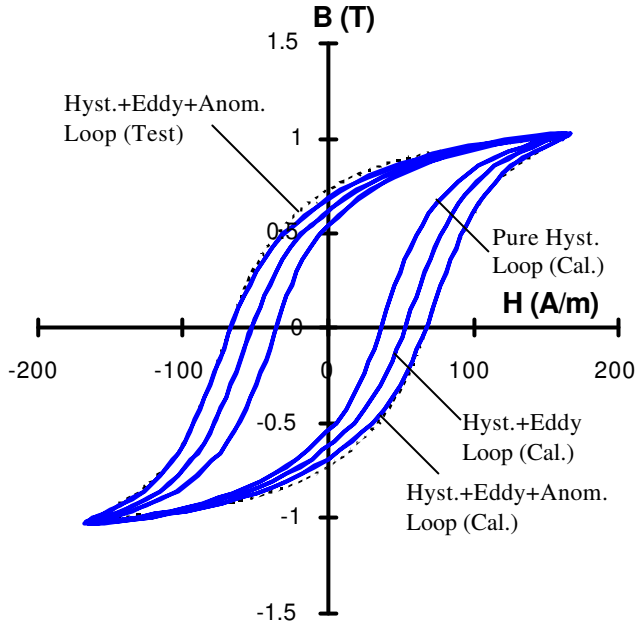

(c)

Fig.3-6 Results of discrete modelling under 100 Hz sine wave voltage excitation
(a) comparison of voltage and current waveforms,
(b) time variation of anomalous loss equivalent resistance and differential inductance, and
(c) comparison of B-H loops

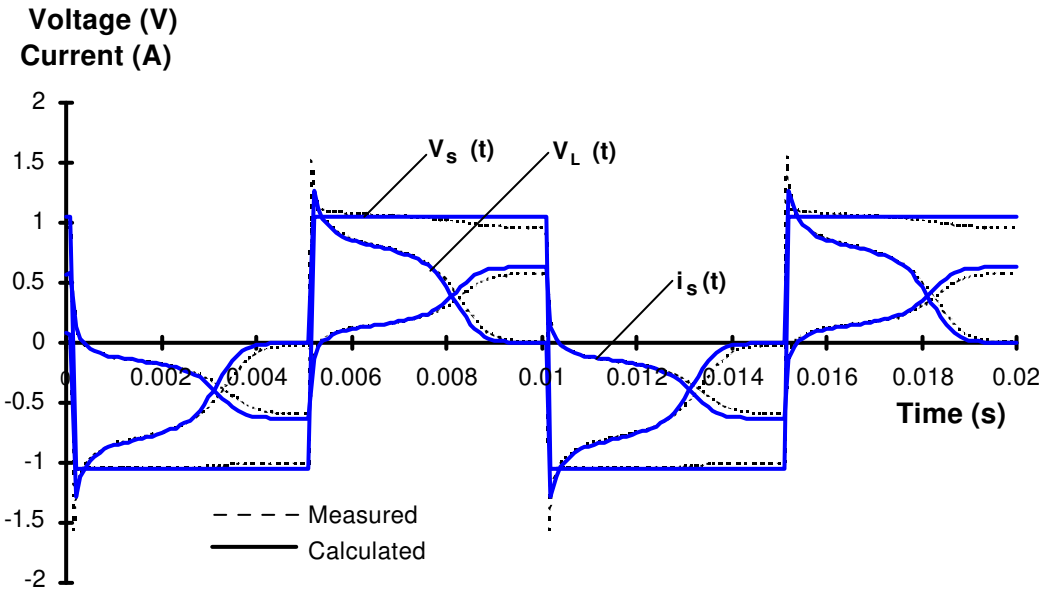

Note: The ideal value of V_S used in the calculation is slightly different from the actual signal due to the non-ideal characteristics of the power amplifier.

(a)

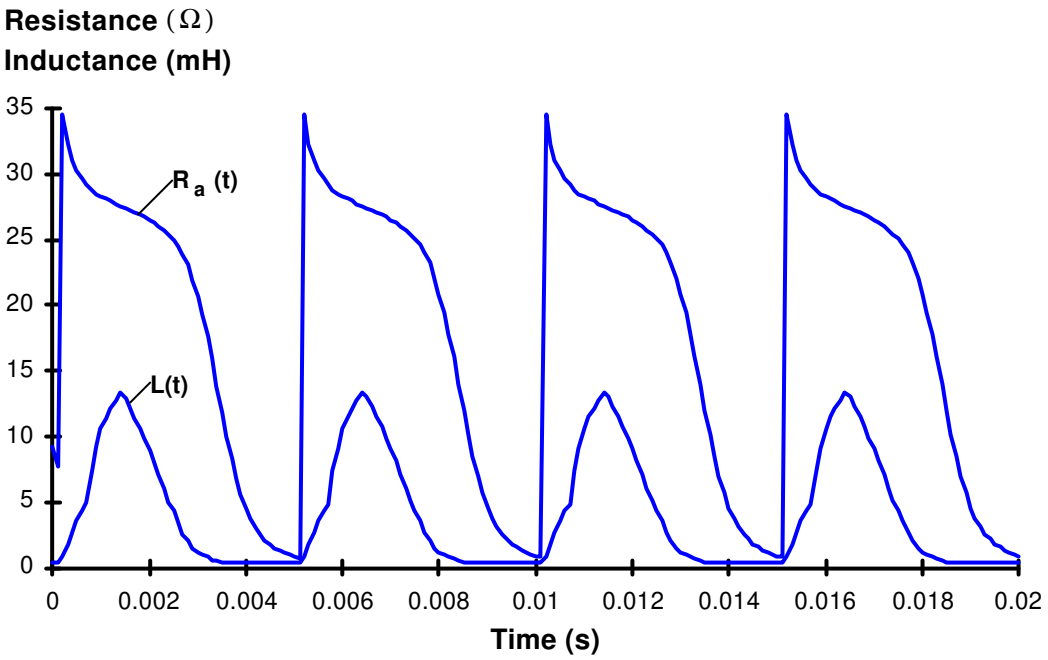

(b)

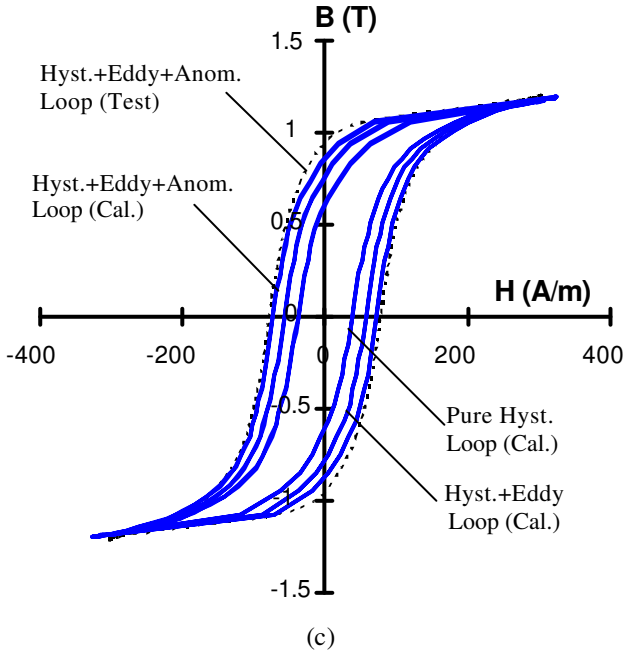

(c)

Fig.3-7 Results of discrete modelling under 100 Hz square wave voltage excitation
(a) comparison of voltage and current waveforms,
(b) time variation of anomalous loss equivalent resistance and differential inductance, and
(c) comparison of B-H loops

Table 3-1 Comparison of calculated and measured core losses

Excitation	$P_{c(Cal.)}$ (W)	$P_{c(Test)}$ (W)	Error (%)
Sine Wave	0.0474	0.0488	2.87
Square Wave	0.0691	0.0726	4.82

The time step used to achieve these results was 50 μs or 200 steps per cycle for sinusoidal excitation, and 10 μs or 1000 steps per cycle for square wave. A smaller time step was required for the second due to the sudden change in voltage.

3.2.4 Discussion

3.2.4.1 Skin Effect

Although the loss coefficients C_e and C_a used to obtain the equivalent resistors in the model are identified from sinusoidal alternating core loss measurements, this model gives reasonable results for the dynamic simulation of non-sinusoidal flux densities. However, it is important to notice that the expression for the classical eddy current loss (3.10) neglects the reaction of eddy currents on the distribution of magnetic field, i.e. the magnetic flux density is assumed to be uniform over the cross sectional area of the lamination. This is approximately correct only when the lamination is effectively thin (i.e. skin depth > one lamination thickness) [206]. Hence, one can anticipate that this model is limited to the modelling of magnetic cores of effectively thin laminations. When the frequency increases, or laminations are thick, errors may appear. This may explain why the difference between predicted and measured results in Table 3-1 is higher under square wave than under sine wave voltage excitation.

For effectively thick laminations, the cross sectional area of a lamination sheet can be discretised into a few slices, or 'thin sheets', where symmetrically opposite slices are paired, as illustrated in Fig.3-8. The flux density can be considered uniform in each slice, but the field couples with other slices, which can be accounted for by mutual inductance. The discrete transform technique can be easily applied to networks with mutual inductance [203]. The losses occurring in each pair of slices can be calculated with the method outlined in the preceding sections. Thus the discrete model can be extended to include cores with thick laminations.

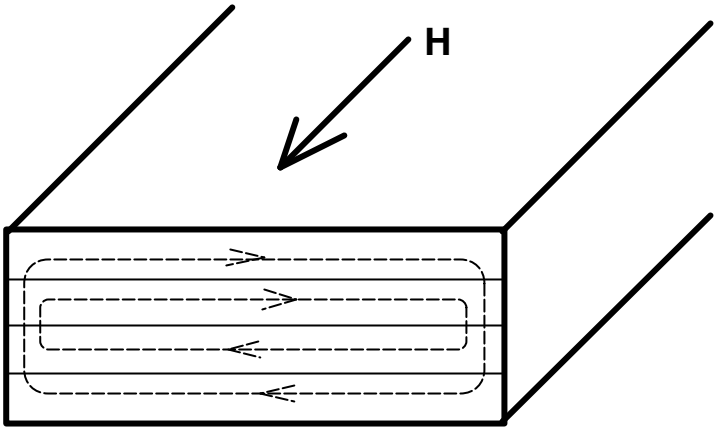

Fig.3-8 Subdivision of an effectively thick lamination

3.2.4.2 Eddy Current Loss Models

As discussed in section 3.2.2.2, the eddy current losses are classified as the classical eddy current loss and the anomalous eddy current loss. This is not the true representation of what happens during the magnetisation of the materials. The eddy currents are induced in the magnetisation process by the movement of magnetic domain walls [3,81-103]. Fig.3-9 illustrates the eddy current paths with and without the presence of domain walls. Hence, it is obvious that the actual eddy current loss is different from that calculated by the classical method, which does not consider the domain wall motion effects. Although great efforts have been made to calculate the eddy current losses in ferromagnetic cores with domain wall motion effects included [81,87,88,94,95,99], there has only been limited success because of the complexity of domain patterns and domain wall movements. Equations (3.10) and (3.12) provide a relatively simple and approximate approach based on the macroscopic measurement with reasonable precision [95,99]. To build a unified model of eddy current losses, a much better understanding of the mechanisms is still required.

3.2.4.3 Computing Time and Precision

For applications of the model in the analysis and design of electrical and electronic systems containing electromagnetic devices, the computing time to achieve a precision which is acceptable in practice has to be kept as short as possible.

Due to its simplicity, the discrete circuit model is fast. The results in this section have shown that this model is sufficiently precise for most engineering purposes.

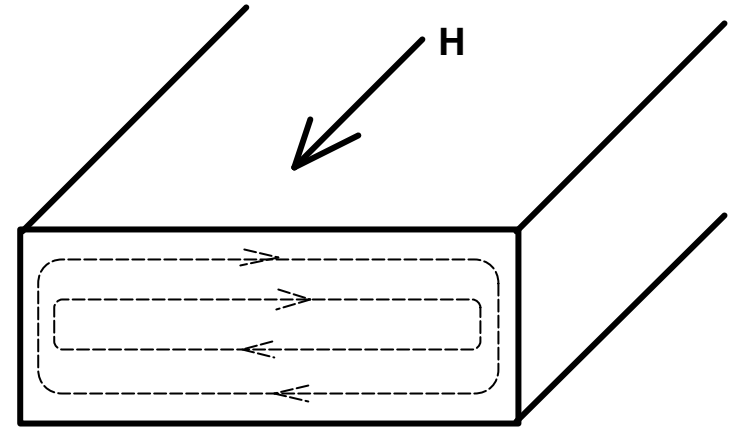

(a)

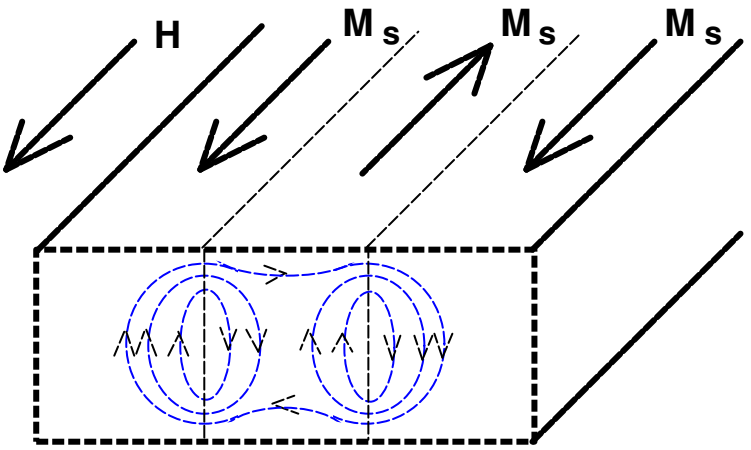

(b)

Fig.3-9 Eddy currents, (a) classical model, and (b) domain model

The discrete transform technique reported in [203,204] was used to develop the discrete model for the core material. This transform has been compared with other numerical methods and has been shown to offer advantages which include: unconditional stability, good efficiency and accuracy, similarity with Laplace transforms, and ease of handling non-linearities. For the modelling of hysteresis loops, the Preisach theory presented in chapter 2 was incorporated into the circuit model. Although constant time steps were used in the present simulations, a further reduction in computing time could have been achieved if the variable-time-step technique [205] was employed.

3.3 A GENERALISED DYNAMIC CIRCUIT MODEL OF MAGNETIC CORES

As pointed out in section 3.2.4.1, the dynamic circuit model outlined in section 3.2 is limited to magnetic cores of effectively thin laminations because the skin effect is not considered. For high frequency operation, the cross sectional area of the core lamination should be divided into a number of paired slices to account for the non-uniform distribution of flux density due to the eddy current reaction or the skin effect. In this section, the equivalent circuit model is extended into a flexible ladder network model of magnetic cores for both low and high frequency operation taking the skin effect into consideration. The number of ladder network stages is determined by the size of the core, the excitation frequency, and the resistivity and permeability. In fact, it will be shown that even for low frequency operation, a ladder network can provide better accuracy than the single-stage circuit.

3.3.1 Ladder Network Model of Magnetic Cores

Cross sections of laminated and solid magnetic cores can be divided into a few segments for magnetic circuit analysis. To calculate eddy currents, eddy current paths and their associated magnetic flux paths are assumed in each segment, as shown in Fig.3-10.

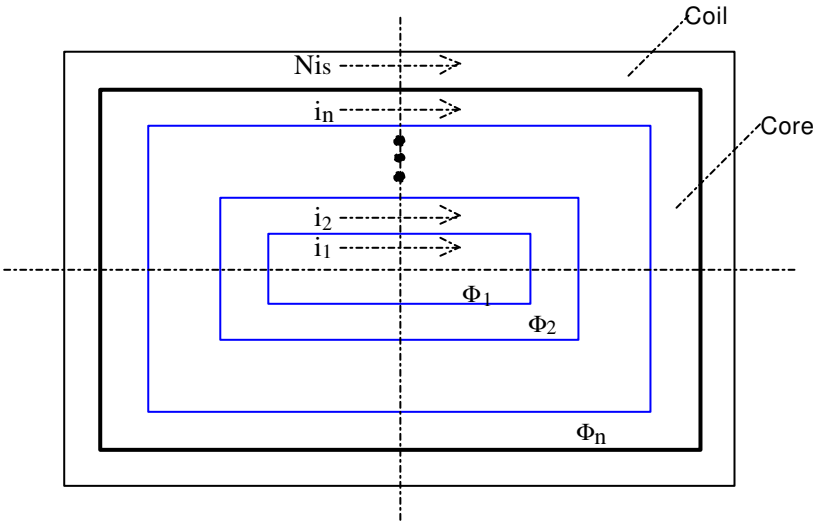

Fig.3-10 Cross section of a solid magnetic core with assumed eddy current paths

These eddy current paths are divided so that the reaction of eddy currents on the distribution of flux density is negligible, that is, the flux density in each path is assumed uniform. In general, assume that there are n eddy current loops in the core. The generalised circuit equations are

Coil:

$$\frac{R_w}{N^2}(Ni_s) + \frac{d(\Phi_1 + \Phi_2 + \ \dots \ + \Phi_n)}{dt} = \frac{V_s}{N} \tag{3.19}$$

Core:

$$R_n i_n + \frac{d(\Phi_1 + \Phi_2 + \ \dots \ + \Phi_n)}{dt} = 0 \tag{3.20}$$

.....

$$R_2 i_2 + \frac{d(\Phi_1 + \Phi_2)}{dt} = 0 \tag{3.21}$$

$$R_1 i_1 + \frac{d\Phi_1}{dt} = 0 \tag{3.22}$$

where R_w is the winding AC resistance, N the number of turns of the winding, i_s the current in the winding, Φ_k (k=1,2,...,n) the flux within each path, V_s the terminal voltage across the winding, and R_k (k=1,2,...,n) the equivalent resistance of each assumed eddy current path representing eddy current and anomalous losses.

The generalised set of equations (3.19-3.22) can be represented as an equivalent circuit in the form of a ladder network as shown in Fig.3-11.

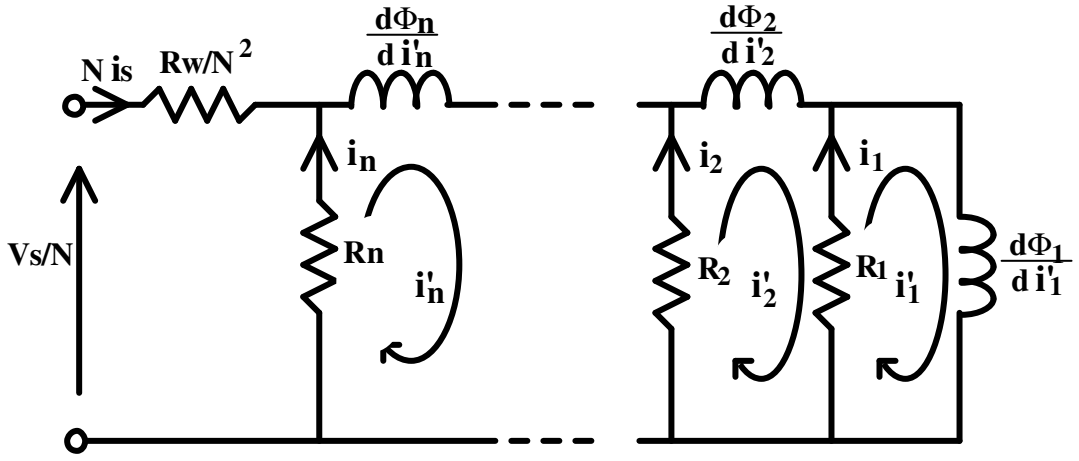

Fig.3-11 Equivalent circuit of a generalised magnetic core model

3.3.2 Discrete Mathematical Description of Dynamic Magnetic Core Model

In terms of the mesh currents, these circuit equations can be written in matrix form as

$$\begin{pmatrix} R_1 & -R_1 & 0 & 0 & \dots & 0 \\ -R_1 & R_1+R_2 & -R_2 & 0 & \dots & 0 \\ \dots\dots & & & & & \\ 0 & \dots & & 0 & -R_{n-1} & R_{n-1}+R_n' \end{pmatrix} \begin{pmatrix} i_1' \\ i_2' \\ \dots \\ i_n' \end{pmatrix} + \begin{pmatrix} \frac{d\Phi_1}{di_1'} & 0 & 0 & \dots & 0 \\ 0 & \frac{d\Phi_2}{di_2'} & 0 & \dots & 0 \\ \dots\dots & & & & \\ 0 & \dots\dots & & & \frac{d\Phi_n}{di_n'} \end{pmatrix} \begin{pmatrix} \frac{di_1'}{dt} \\ \frac{di_2'}{dt} \\ \dots \\ \frac{di_n'}{dt} \end{pmatrix} = \begin{pmatrix} 0 \\ 0 \\ \dots \\ V_n' \end{pmatrix} \tag{3.23a}$$

where $R_n' = \dfrac{R_n(R_w/N^2)}{(R_w/N^2)+R_n}$, and $V_n' = \dfrac{R_n}{(R_w/N^2)+R_n}\left(\dfrac{V_s}{N}\right)$, or in a symbolic matrix form as

$$[\mathbf{R}][\mathbf{i'}] + \left[\frac{\mathbf{dF}}{\mathbf{di'}}\right]\left[\frac{\mathbf{di'}}{\mathbf{dt}}\right] = [\mathbf{V}] \tag{3.23b}$$

The relationship between the assumed eddy currents i_k (k=1,2,...,n) in Fig.3-11 and the mesh currents i_k' (k=1,2,...,n) in the ladder network (Fig.3-12) is as follows

$$\begin{pmatrix} i_1 \\ i_2 \\ \dots \\ i_n + Ni_s \end{pmatrix} = \begin{pmatrix} 1 & -1 & 0 & 0 & \dots & 0 \\ 0 & 1 & -1 & 0 & \dots & 0 \\ \dots\dots & & & & & \\ 0 & \dots & & & & 1 \end{pmatrix} \begin{pmatrix} i_1' \\ i_2' \\ \dots \\ i_n' \end{pmatrix} \tag{3.24}$$

Equations (3.23) and (3.24) give the mathematical description of the generalised magnetic core model in a continuous form. In the ladder network, while resistor R_k represents the core loss equivalent resistance in the *k*-th eddy current path, the hysteresis effects can be included in the $\dfrac{d\Phi_k}{di_k'}$ terms in equation (3.23).

For computer simulation, a discrete circuit model is derived using the TLM-based discrete transform technique [203,204]. First, $\dfrac{d\Phi_k}{di_k'}$ is replaced by the corresponding differential inductance $L(i_k')$ in the *k*-th loop, where

$$L(i_k') = \frac{d\Phi_k}{di_k'} \tag{3.25}$$

These differential inductances at any time instant are determined by the normal Preisach model of hysteresis as described in chapter 2. Second, express the $\frac{di_k'}{dt}$ (k=1,2,...,n) terms in (3.23) as

$$\frac{di_k'}{dt} = V_U^k = Z_U i_k' + 2V_U^{ik'} \qquad (k=1,2,...,n) \tag{3.26}$$

using the TLM-based discrete transform technique, where $Z_U = 2/T_p$, T_p the propagation time (which equals the time step used in the numerical solution), $V_U^{ik'}$ is the incident voltage pulse on inductor $L(i_k')$ used in the TLM method, and V_U^k is equal to the magnitude of di_k'/dt or numerically the voltage across an inductor of 1 Henry with the same di_k'/dt.

Hence, using equations (3.25) and (3.26), matrix equation (3.23) can be rewritten as

$$\begin{pmatrix} R_1 + Z_U L(i_1') & -R_1 & 0 & \dots & 0 \\ -R_1 & R_1 + R_2 + Z_U L(i_2') & -R_2 & 0 \dots & 0 \\ \dots\dots & & & & \\ 0 & \dots & & -R_{n-1} & R_{n-1} + R_n' + Z_U L(i_n') \end{pmatrix} \begin{pmatrix} i_1' \\ i_2' \\ \dots \\ i_n' \end{pmatrix} = \begin{pmatrix} -2V_U^{i1'} L(i_1') \\ -2V_U^{i2'} L(i_2') \\ \dots \\ V_n' - 2V_U^{in'} L(i_n') \end{pmatrix} \tag{3.27a}$$

or

$$\mathbf{[Z][i']} = \mathbf{[V^{i'}]} \tag{3.27b}$$

where $L(i_k')$ (k=1,2,...,n), are non-ideal differential inductors when magnetic hysteresis is considered and $\mathbf{[V^{i'}]}$ is the voltage vector containing the incident pulses. Equation (3.27) is the generalised discrete-time model of magnetic cores and is suitable for direct implementation on digital computers.

At the beginning of each time stepping procedure, incident pulses $V_U^{ik'}$ and the instantaneous differential inductances $L(i_k')$ calculated from the i_k' (k=1,2,...n) in the previous time step are substituted into (3.27) in order to determine the new current vector $\mathbf{[i']}$. The differential inductances $L(i_k')$ can then be updated according to the new i_k' and the history of magnetisation using the Preisach theory.

According to the TLM discrete transform, it can be shown that the incident pulses for the next time step can be obtained as follows:

$$V^{ik'}_{U(m+1)} = -\left[Z_U i_k{}'_{(m)} + V^{ik'}_{U(m)}\right] \tag{3.28}$$

where $i_k' = i_1', i_2', ...,$ and i_n', and the bracketed subscripts (m) and (m+1) denote the *m*-th and *(m+1)*-th time steps, respectively. From (3.27) and (3.28), it can be seen that the discrete algorithms of the dynamic core model are recursive, and that the discrete transform technique allows simple discrete circuit formulation, and easy handling of non-linearities. Therefore, a non-linear magnetic core can be modelled by a tridiagonal system of non-linear algebraic equations which can be easily solved.

3.3.3 A Criterion for the Size of the Ladder Network for Low and High Frequency Applications

For solid or laminated cores, the flux distribution within the core becomes less uniform as the operating frequency increases. The number of stages of the ladder network (which represents the number of assumed eddy current paths) depends on the operating frequency, conductivity and permeability of the core materials. Generally, the width of each eddy current path (w_e) should be smaller than the skin depth δ at the fundamental excitation frequency f, i.e.

$$w_e \le \delta = \sqrt{\frac{2}{\sigma\omega\mu_r\mu_o}} \tag{3.29}$$

where σ is the conductivity, $\omega=2\pi f$ the angular frequency, $\mu_o=4\pi\times10^{-7}$ the permeability of a vacuum in SI units, and μ_r the relative permeability. Equation (3.29) shows that the skin depth decreases with increasing frequency. Thus more stages are required in the ladder network for a high frequency model. For low frequency applications, the flux distribution within the core is fairly uniform so that only one or two eddy current paths are required. The generalised model reduces to the low frequency model developed in section 3.2 when only one stage of the ladder network is used. However, it should be noted that (3.29) gives the minimum criterion in choosing the size (i.e. the number of stages) of the ladder network. In general, a larger ladder network would give more accurate results.

3.3.4 Core Losses and Circuit Parameters

3.3.4.1 Approximate Eddy Current Distribution in a Thick Lamination Sheet

Figs.3-12(a) and (b) show the cross section of a thick lamination sheet of length l_z, thickness b and width a. The applied magnetic field is in the Z direction. If a>>b>>δ and l_z>>b>>δ, where δ is the skin depth of the fundamental excitation of frequency f, the reaction of the eddy currents on the distribution of magnetic field can not be neglected. When the cross section is divided into several slice pairs (Fig.3-12(b)), the flux density in each slice pair can however be considered as uniformly distributed.

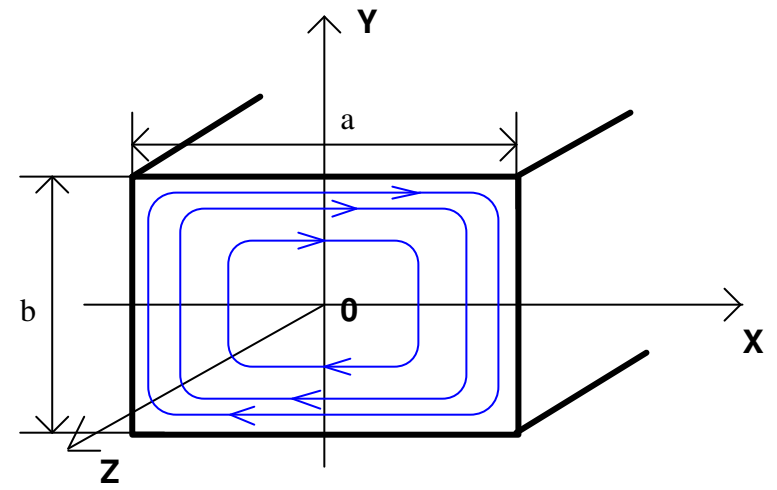

(a)

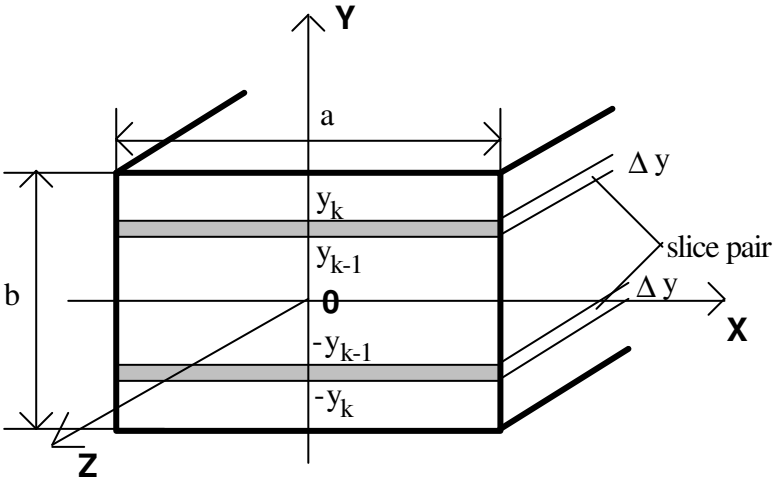

(b)

Fig.3-12 Diagram of a cross section of a thick lamination sheet
(a) with assumed eddy current paths shown
(b) with typical slice pair shown

In the *k*-th slice pair, let the flux density be

$$\mathbf{B}_k = B_{zk}\,\mathbf{k} \tag{3.30}$$

where the bold symbols denote that they are vectors, **k** is the unity vector in the z direction in Fig.3-12, subscript k refers to the *k*-th slice pair (k=1,2,...,n), and the subscript z refers to the Z component. Since a>>b, the eddy current density in the *k*-th slice pair is

$$\mathbf{J}_k = J_{xk}\,\mathbf{i} \tag{3.31}$$

where the subscript x denotes the X component, and **i** is the unity vector in the X direction in Fig.3-12.

Substituting (3.30) and (3.31) into

$$\mathbf{J} = \sigma\mathbf{E} \tag{3.32}$$

and

$$\nabla \times \mathbf{E} = -\frac{\partial \mathbf{B}}{\partial t} \tag{3.33}$$

where **E** is electric field strength, one obtains

$$\frac{\partial J_{xk}}{\partial y} = \sigma\left(\frac{dB_z}{dt}\right)_k \tag{3.34}$$

where the index k=1,2,...,n.

From (3.34),

$$\int_{J_{k-1}}^{J_k} dJ_{xi} = \int_{y_{k-1}}^{y_k} \sigma\left(\frac{dB_z}{dt}\right)_k dy \tag{3.35}$$

where J_k and J_{k-1} are the eddy current densities at $y=y_k$ and $y=y_{k-1}$ respectively.

Therefore,

$$J_k = \sigma\left(\frac{dB_z}{dt}\right)_k \Delta y + J_{k-1} \tag{3.36}$$

where $\left(\frac{dB_z}{dt}\right)_k$ is assumed to be independent of y in the *k*-th slice pair and $\Delta y = y_k - y_{k-1}$.

3.3.4.2 Classical Eddy Current Loss

The classical eddy current loss in the *k*-th slice pair P_{ek} can be expressed as the resistive loss of the eddy current path in the *k*-th slice pair. Since the classical eddy current loss $P_e = \frac{1}{\sigma} J^2$ per unit volume, the instantaneous power loss P_{ek} is

$$P_{ek} = \frac{2al_z}{\sigma} \int_{y_{k-1}}^{y_k} J_{xk}^{\,2} dy \tag{3.37}$$

From (3.34), we have

$$dy = \frac{1}{\sigma\left(\frac{dB_z}{dt}\right)_k} dJ_{xk} \tag{3.38}$$

Therefore,

$$P_{ek} = \frac{2al_z}{\sigma^2\left(\frac{dB_z}{dt}\right)_k} \frac{J_k^{\,3} - J_{k-1}^{\,3}}{3} \tag{3.39}$$

Resistance in the current paths along the Y axis is ignored because the thickness b is assumed to be very small when compared with width a and length l_z. From (3.35), one obtains

$$\left(\frac{dB_z}{dt}\right)_k = \frac{J_k - J_{k-1}}{\sigma \Delta y} \tag{3.40}$$

Therefore, the classical eddy current loss in the *k*-th slice pair becomes

$$\begin{aligned} P_{ek} &= \left(\frac{2al_z\Delta y}{\sigma}\right)\left[\frac{1}{3}\left(\frac{J_k^{\,3} - J_{k-1}^{\,3}}{J_k - J_{k-1}}\right)\right] \\ &= \left(\frac{2al_z\Delta y}{\sigma}\right) J_k^{\,2}\left\{\frac{1}{3}\left[1 + \left(1 + \frac{J_{k-1}}{J_k}\right)\frac{J_{k-1}}{J_k}\right]\right\} \end{aligned}$$

$$= \left(\frac{2al_z \Delta y}{\sigma} \right) J_k^{\,2} r_{Jk} \tag{3.41}$$

where

$$r_{Jk} = \frac{1}{3}\left[1 + \left(1 + \frac{J_{k-1}}{J_k} \right) \frac{J_{k-1}}{J_k} \right] \tag{3.42}$$

is a correction factor which takes into account the variation of eddy current density J_x with y. If current densities are assumed to be uniform, i.e. $J_k = J_{k-1}$, r_{Jk} becomes one.

3.3.4.3 Consideration of Anomalous Loss

It has been pointed out in section 3.2 that the eddy current loss P_e and the anomalous loss P_a expressions (in W/kg) in a thin sheet are given by

$$P_e = C_e \left(\frac{dB_z}{dt} \right)^2 \tag{3.43}$$

and

$$P_a = C_a \left| \frac{dB_z}{dt} \right|^{3/2} \tag{3.44}$$

where C_e and C_a are the coefficients of the classical eddy current loss and the anomalous loss respectively, and B is assumed uniform within the depth. The sum of the classical eddy current loss and the anomalous loss is

$$P_{ea} = P_e + P_a$$

$$= C_e \left(\frac{dB_z}{dt} \right)^2 + C_a \left| \frac{dB_z}{dt} \right|^{3/2}$$

$$= C_e \left(\frac{dB_z}{dt} \right)^2 \left[1 + \frac{C_a}{C_e \sqrt{\left| \frac{dB_z}{dt} \right|}} \right]$$

$$= C_e \left(\frac{dB_z}{dt} \right)^2 r_c \tag{3.45}$$

where

$$r_c = 1 + \frac{C_a}{C_e \sqrt{\left|\frac{dB_z}{dt}\right|}} \tag{3.46}$$

is a correction factor if the anomalous loss (the effects of domain wall movement) is included in the calculation of the eddy current loss.

Therefore, the sum of the eddy current and anomalous losses in the *k*-th slice pair P_{eak} from (3.41) is

$$P_{eak} = \left(\frac{2al_z\Delta y}{\sigma}\right) J_k{}^2 r_{Jk} r_{ck} \tag{3.47}$$

where

$$r_{ck} = 1 + \frac{C_a}{C_e \sqrt{\left|\frac{dB_z}{dt}\right|_k}}$$

is the correction factor for the *k*-th slice pair. For the time instant at which $\left|\frac{dB_z}{dt}\right|_k = 0$, $P_{eak}=0$, and r_{ck} approaches infinity. Numerically, a large number, for example 10^{20}, is assigned to r_{ck} in this case.

3.3.4.4 Equivalent Core Loss Resistance

Since a>>b, the induced emf V_k in the *k*-th slice pair at $y=y_k$ is

$$V_k = 2aE_k \tag{3.48}$$

Since $J_k = \sigma E_k$, then

$$V_k = \frac{2a}{\sigma} J_k \tag{3.49}$$

for the *k*-th slice pair.

Because the equivalent resistance for the eddy current and anomalous losses is in parallel with the differential inductance in the model (Fig.3-11), the equivalent core loss resistance R_k for the *k*-th slice pair can be calculated by

$$R_k = \frac{V_k^2}{P_{eak}} \tag{3.50}$$

Thus, from (3.47) and (3.49), one obtains

$$R_k = \frac{\left(\frac{2a}{\sigma} J_k\right)^2}{\left(\frac{2al_z\Delta y}{\sigma}\right) J_k^{\,2} r_{Jk} r_{ck}}$$

$$= \frac{\left(\frac{2a}{\sigma l_z \Delta y}\right)}{r_{Jk} r_{ck}}$$

$$= \frac{R_{DCk}}{r_{Jk} r_{ck}} \tag{3.51}$$

where $R_{DCk} = \frac{2a}{\sigma l_z \Delta y}$ is the DC resistance of the *k*-th slice pair.

The DC resistance R_{DCk} changes to $\frac{R_{DCk}}{r_{Jk}}$ if the eddy current density variation is considered. The resistance expression changes to the form in (3.51) if the anomalous loss is also included.

Equation (3.51) provides a simple general expression for the equivalent eddy current and anomalous loss resistance for each eddy current loop in the magnetic core. It is important to note that R_k is expressed in terms of the DC resistance which can be easily determined.

The coefficients of the classical eddy current and anomalous losses used in (3.46) for correction factor r_c can be obtained by the alternating core loss separation procedure described in section 3.2.2.3.

3.3.4.5 Hysteresis and Differential Inductance

The normal Preisach model of magnetic hysteresis outlined in chapter 2 is used to trace the history of magnetisation in each slice pair in the magnetic core. At a time instant, the mesh currents i_k', (k=1,2,...,n), can be obtained by solving the tridiagonal non-linear algebraic equation system (3.27). The magnetic field strength in the *k*-th segment of the magnetic core can be calculated by

$$H_{k(m)} = \frac{i_k{}'_{(m)}}{l_z} \tag{3.52}$$

where bracketed subscript (m) denotes the *m*-th time step. The magnetic flux density in the *k*-th segment of the magnetic core for the *m*-th time step $B_{k(m)}$ can then be determined according to the magnetic field strength $H_{k(m)}$ and the previous magnetisation state ($H_{k(m-1)}$, $B_{k(m-1)}$) by the normal Preisach model.

When the flux densities in each segment in two consecutive time steps are obtained, the differential inductance in the *k*-th segment can be calculated as following

$$L(i_k') = \frac{d\Phi_k}{di_k'} = A_k \left[\frac{B_{k(m)} - B_{k(m-1)}}{i_k'_{(m)} - i_k'_{(m-1)}} \right] \tag{3.53}$$

where A_k is the cross sectional area of the *k*-th segment.

When the effect of hysteresis is considered, the differential inductance $L(i_k')$ is non-ideal. The average hysteresis loss dissipated in the *k*-th inductor can be calculated by

$$P_{hk} = \frac{1}{T}\int_0^T i_k' L(i_k') \frac{di_k'}{dt} dt \tag{3.54}$$

The total average hysteresis loss P_h is therefore equal to

$$P_h = \sum_{k=1}^{n} P_{hk} = \sum_{k=1}^{n} \frac{1}{T}\int_0^T i_k' L(i_k') \frac{di_k'}{dt} dt \tag{3.55}$$

3.3.4.6 Total Core Loss Calculation in the Ladder Network Model

The general core loss expression of the magnetic core model can be described, based on the law of energy conservation, as

$$\frac{1}{T}\int_0^T V_{R_n}(Ni_s)dt = \sum_{k=1}^{n}\frac{1}{T}\int_0^T R_k i_k{}^2 dt + \sum_{k=1}^{n}\frac{1}{T}\int_0^T i_k'L(i_k')\left(\frac{di_k'}{dt}\right)dt$$
$$= P_{ea} + P_h \qquad (3.56)$$

where $V_{Rn} = V_s/N - R_w(Ni_s)$ is the voltage across resistor R_n, and P_{ea} and P_h are the sum of the eddy current and anomalous losses and the hysteresis loss, respectively. The term on the left hand side of (3.56) is the total power fed into the core loss model (i.e. total input power less the copper loss of the winding). The first term on the right hand side of (3.56) is sum of the classical eddy current and anomalous losses, and the second term on the right hand side is the total hysteresis loss dissipated in the non-ideal inductors $L(i_k')$, (k=1,2,...n), for an *n*-stage ladder network.

3.3.5 Software Implementation

Fig.3-13 shows the flow chart of the operation of the magnetic core model. The program can be used to run the core model routine N_c times. A user chosen N_s points can be obtained within each switching period. A variable time step TLM technique [205] can be selected in the routine so that any non-linear excitation waveforms with transients can be incorporated without losing transient information. This is particularly important in the study of magnetic core behaviour in many modern switched mode power supplies because the excitation waveforms are normally highly non-sinusoidal with rapidly changing edges.

3.3.6 Experimental Verification

3.3.6.1 Annular Ring of Silicon Iron with Square Wave Voltage Excitation

The experimental apparatus shown in Fig.3-5 was again used for measuring the response of an annular ring of silicon iron Lycore-140 0.35mm laminations under square wave voltage excitation at 1 kHz. The dimensions and winding parameters of the ring inductor were given in chapter 2, section 2.2.5.2, Table 2-1.

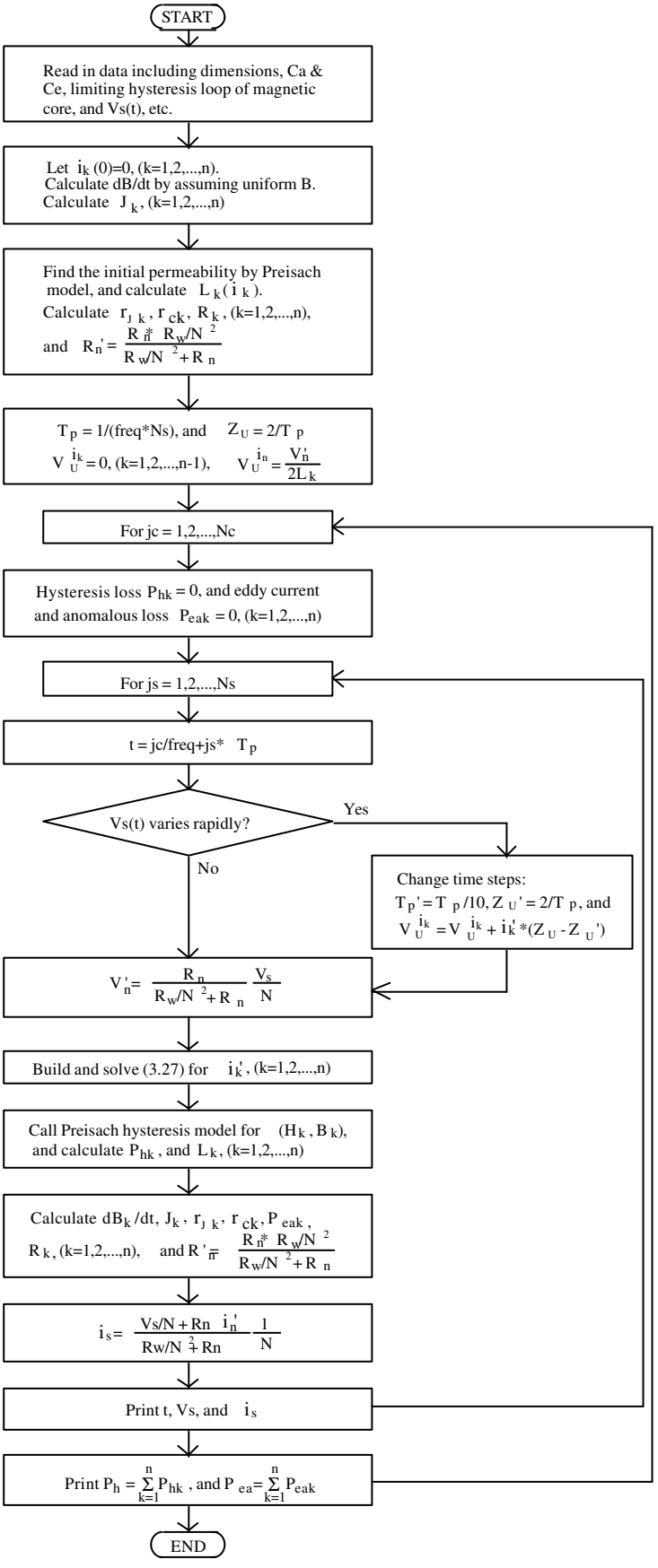

Fig.3-13 Flow chart of dynamic circuit model calculation

(1) Simulation with width of eddy current path larger than skin depth

Fig.3-14 shows the simulated and measured results of Lycore-140 core at 1 kHz excitation, assuming only one eddy current loop. At this frequency, the skin depth (δ) for the core is 0.134 mm. The width of each lamination in the core is 0.35 mm, giving the width of each eddy current path (w_e) to be 0.175 mm. This means that the condition set in (3.29) is not satisfied. It can be seen that the calculated excitation current is lower and flatter than measured. The calculated specific core loss per Hertz is 0.036 W/kg/Hz, and the measured core loss was 0.0336 W/kg/Hz. The percentage error is 7.2%. This inaccuracy can be attributed to the reaction of eddy currents on the distribution of flux density in the core as discussed in section 3.2.4.1.

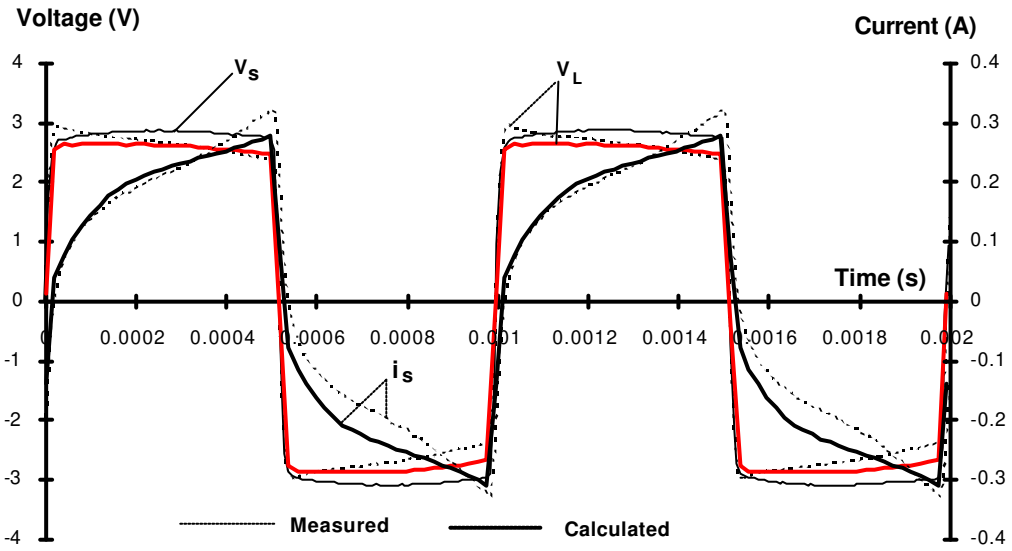

Fig.3-14 Simulated and measured results of Lycore-140 ring sample at 1 kHz with a one-stage ladder network model

(2) Simulation with width of eddy current path smaller than skin depth

Applying the condition set in (3.29), the cross section of the core is divided into two layers of eddy current paths, resulting in the width of each layer being 0.0875 mm. The width of the eddy current path (w_e) is now smaller than the skin depth (δ). The core model with two assumed eddy current paths is represented by a two-stage ladder network (i.e. n=2). Fig.3-15 shows the simulated results using a two-stage ladder network. The simulated current has better agreement with the measured excitation current than that in Fig.3-14. The calculated specific core loss per Hertz is 0.0346 W/kg/Hz, and the percentage error is reduced to 2.98%.

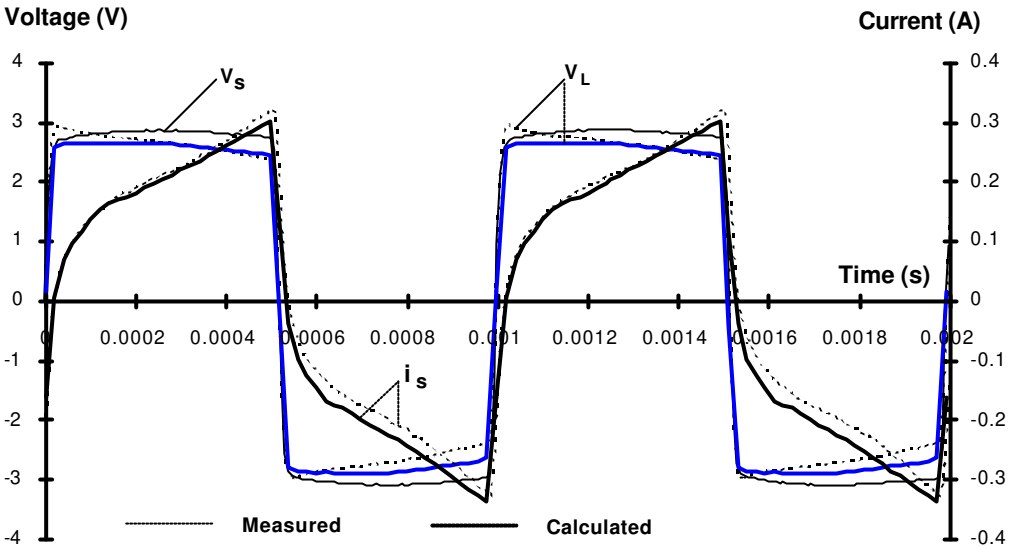

Fig.3-15 Simulated and measured results of Lycore-140 ring sample at 1kHz with a two-stage ladder network model

3.3.6.2 A Ferrite Toroid in a Switching Circuit

A Siemens/Matsushita N47 soft ferrite R16 toroid core with high frequency excitation (provided by a switching circuit as shown in Fig.3-16) was also simulated. The dimensions and parameters of the core and the excitation and flux density coils were given in chapter 2, section 2.2.5.3, Table 2-3.

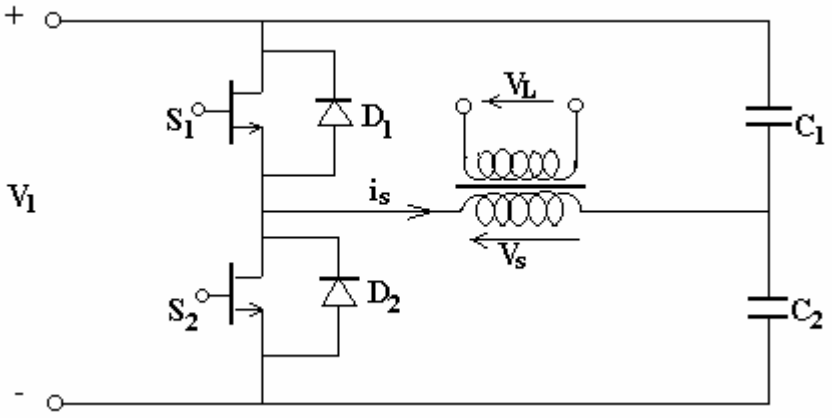

Fig.3-16 Schematic of a high frequency switching circuit

For the measurements of voltage and current in high frequency switching mode, a YOKOGAWA DL-1200A 4 channel digital oscilloscope was used. The sampling frequency of the oscilloscope is 100 MHz. Because the reactance of the winding is much higher than the

resistance, there was hardly any difference between the measured signals of V_s and V_L. Therefore, V_L was not compared with the simulation. The current signal in the primary winding was picked up by a Tektronix current probe, PS042. The bandwidth of the current probe is from DC to 50 MHz.

The AC resistance of the winding R_w is higher than the DC resistance, since the skin effect and the proximity effect [4] in the wire are significant when the switching frequency is high. The winding in this example was constructed with thin (diameter = 0.2 mm) wire, with only a few turns, so the difference between the DC resistance and the AC resistance at the frequency used was ignored.

The magnetisation of ferrites is very sensitive to the ambient temperature [4,207]. In order to account for this effect, various hysteresis loops at different temperatures should be incorporated in the model. In this example, the limiting hysteresis loop used in the simulation was measured immediately after the switching mode measurements, and reported in chapter 2, Fig.2-12. Hence, the temperature effect was not specially treated.

For identification of core loss coefficients, an alternating core loss separation procedure described in section 3.2.2.3 was performed on the specific core loss per Hertz of N47 ferrite obtained from the manufacturer's data sheet. Fig.3-17 shows the specific core loss at different frequencies provided by the manufacturer [207]. Fig.3-18 depicts the specific hysteresis loss per cycle measured at 1 Hz using the testing system reported in chapter 2, section 2.2.5.1, Fig.2-8. The alternating core loss separation is illustrated in Fig.3-19 for flux density B=0.025, 0.05, and 0.1 T. For N47 soft ferrite, the deduced core loss coefficients are $C_e = 9.12\times10^{-10}$, and $C_a = 7.53\times10^{-7}$ SI units.

Fig.3-20 shows the simulated and measured current waveforms and the B-H loops of the core at 100 kHz switching frequency. The cross section of the core was divided into five paths. The time step was 50 ns or 200 steps/cycle. The calculated specific core loss per Hz, corresponding to the area enclosed by the calculated B-H loop in Fig.3-20(b), is 2.592×10^{-3} W/kg/Hz, and the measured specific core loss, corresponding to the area enclosed by the measured B-H loop in Fig.3-20(b), is 2.566×10^{-3} W/kg/Hz. The percentage error is about 1%.

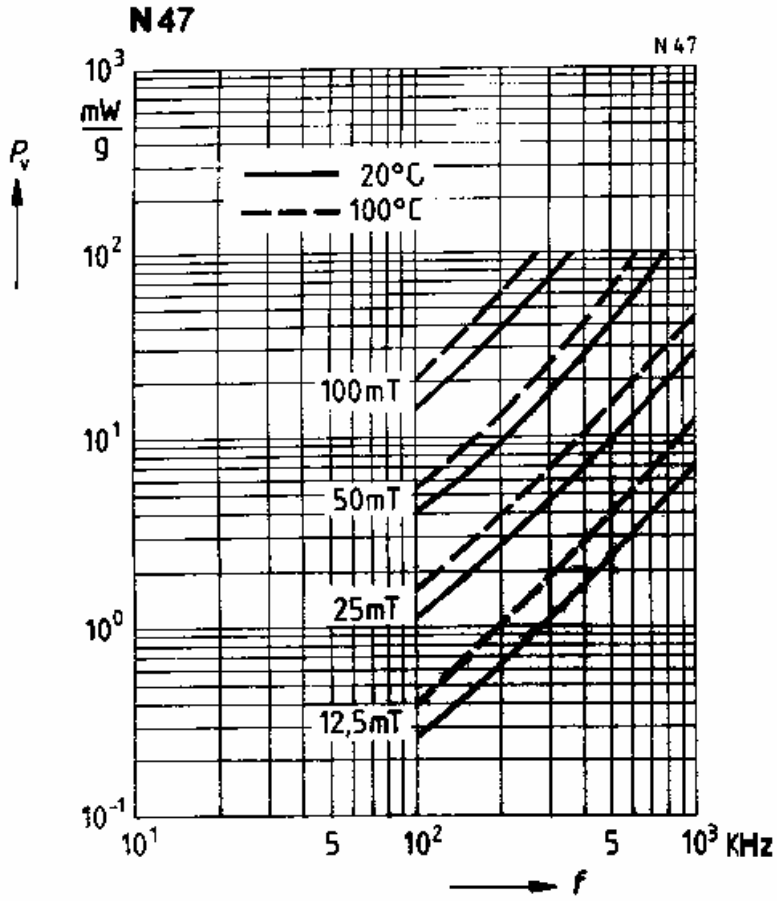

Fig.3-17 Core loss of N47 ferrite at different frequencies (from [207])

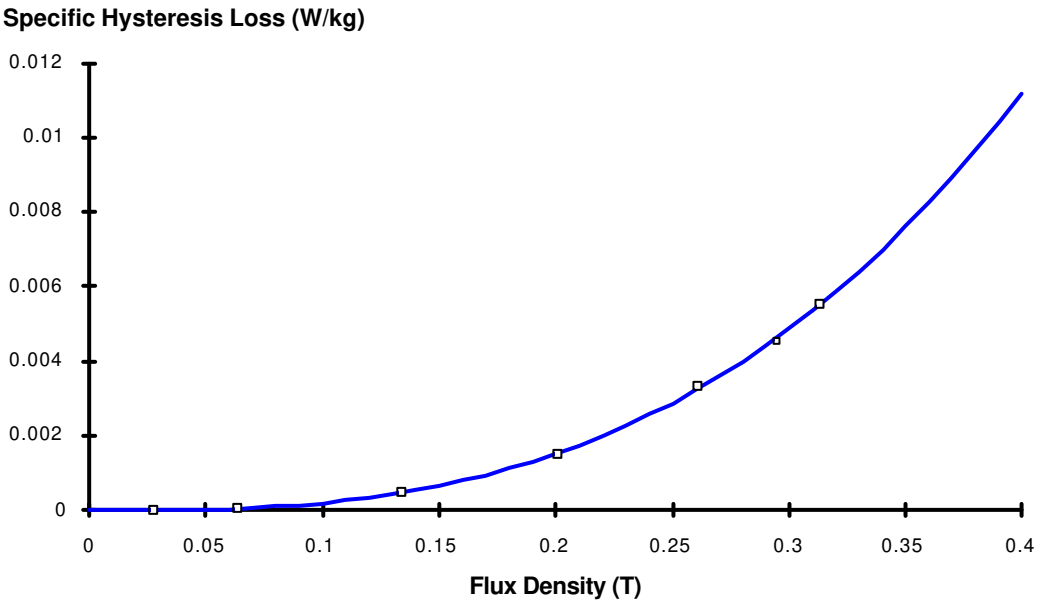

Fig.3-18 Alternating hysteresis loss of N47 soft ferrite measured at 1 Hz

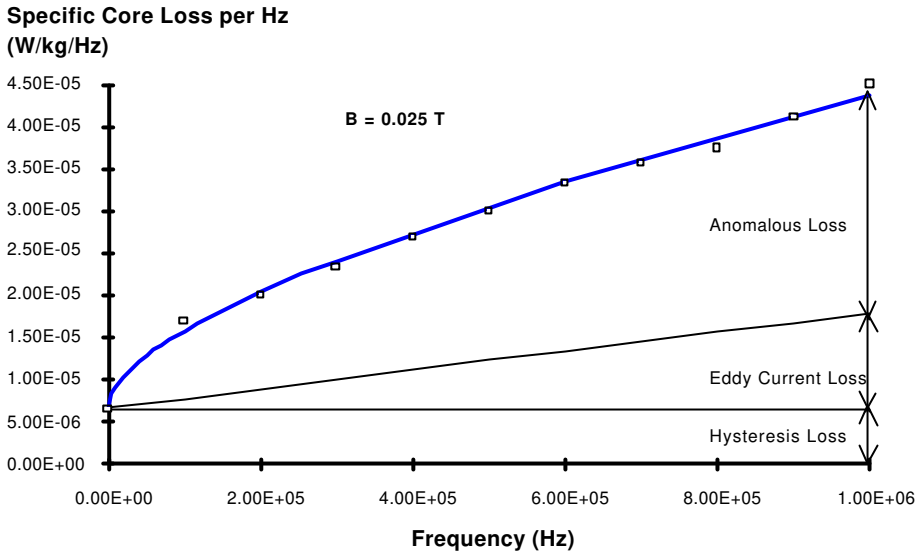

(a)

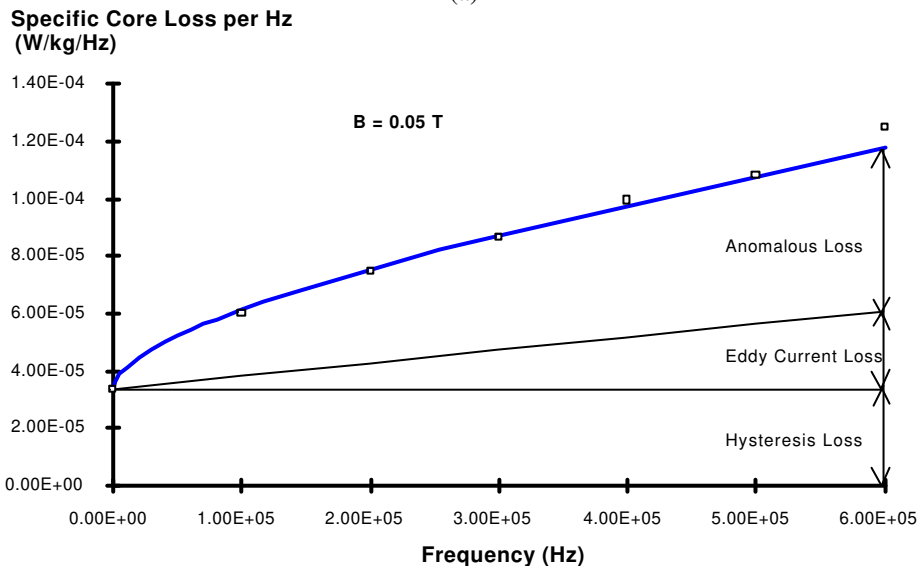

(b)

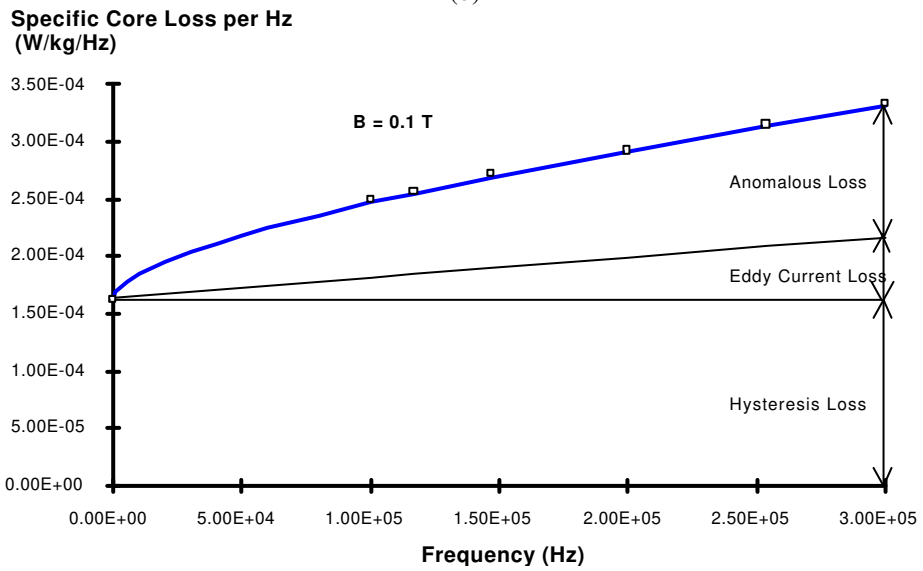

(c)

Fig.3-19 Core loss separation of N47 soft ferrite for (a) B=0.025 T, (b) B=0.05 T, and (c) B=0.1 T

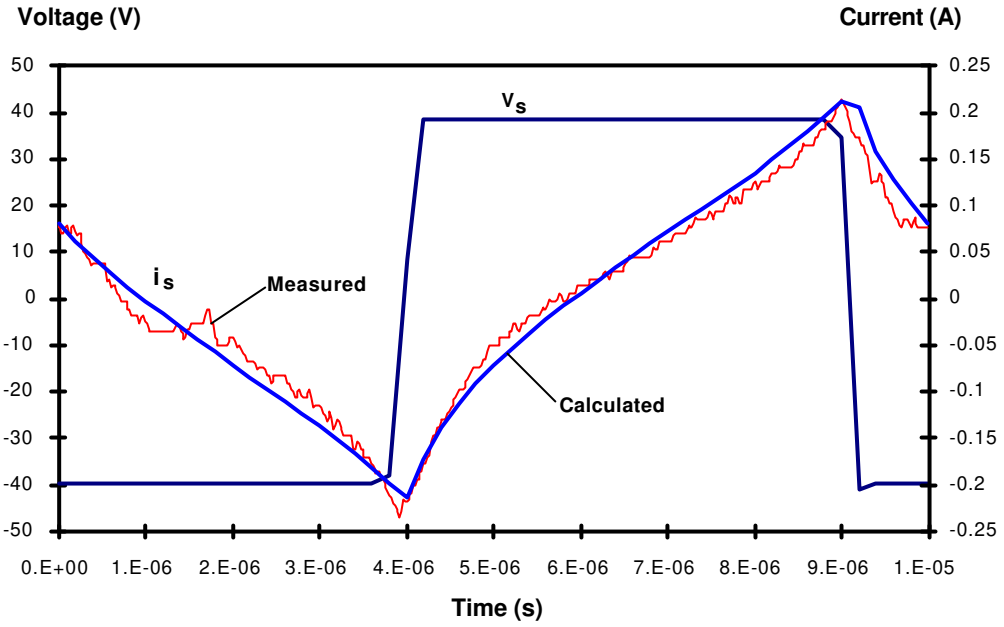

(a)

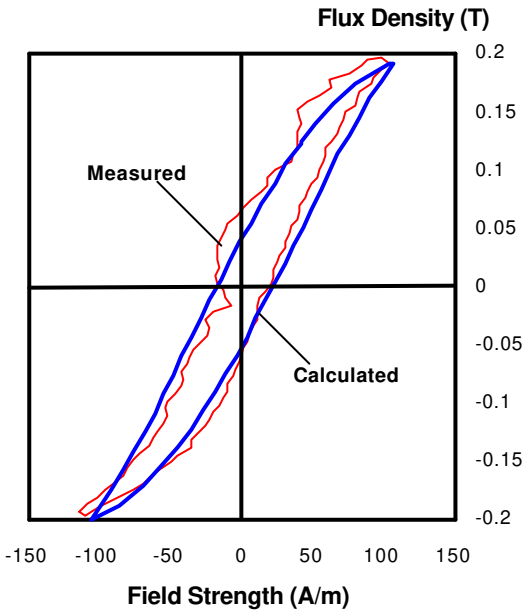

(b)

Fig.3-20 Comparison of simulated and measured
(a) current waveforms and (b) B-H loops

3.4 CONCLUSION

The dynamic discrete circuit model proposed in section 3.2 takes magnetic non-linearity and all kinds of core losses into consideration and has shown satisfactory accuracy. Since the Preisach model is used to keep trace of the magnetisation process, this model can simulate the performance of a magnetic core under arbitrary excitation. The discrete transform technique

provides a simple, fast, and accurate means for non-linear transient analysis. This model is limited to simulations of magnetic cores which are effectively thin at the excitation frequency.

A generalised dynamic discrete circuit model of magnetic cores for both low and high frequency applications was presented in section 3.3. Skin effect was included by using a ladder network. This model reduces to the simple model for low frequency applications outlined in section 3.2, when only one stage of the ladder network is used. The criterion for choosing the number of stages of the ladder network was $w_e < \delta$.

The non-linear B-H loop and the hysteresis loss were incorporated in the distributed non-ideal inductors, and calculated by the normal Preisach model of hysteresis. The classical eddy current and anomalous losses were included in the distributed non-linear resistors based on an approximate analysis of the magnetic field and eddy current distribution. A new expression for the effective core loss resistance, which includes both the classical eddy current and anomalous losses, was derived and explained.

All information required for identifying the model parameters, such as limiting hysteresis loop and specific core losses with sinusoidal flux densities at different frequencies, can be obtained from the manufacturers' data sheets or through simple measurements.

The anomalous loss coefficient used in the identification of effective resistors was determined by a standard alternating core loss separation procedure. This procedure was illustrated for two different magnetic materials. Although the core loss coefficients were identified from the core loss curves measured with a sinusoidal flux density, they could be used to evaluate the core losses with non-sinusoidal flux densities.

The discrete transform technique together with the Preisach hysteresis model provides a useful means to handle hysteresis non-linearity. The resultant tridiagonal non-linear algebraic equation system features easy programming and fast computation. Comparisons of the simulations with the experimental results for two types of magnetic cores and at different frequencies confirmed the accuracy of the generalised model.

CHAPTER 4. A REVIEW OF ROTATIONAL CORE LOSS MEASUREMENT AND MODELLING

4.1 INTRODUCTION

Rotational core loss is the power dissipated in a magnetic core subjected to a rotating magnetic field, including rotational hysteresis, eddy current, and anomalous losses. Practically, it occurs in the regions of electrical machines where the direction of magnetic flux varies in the plane of laminations, such as the T joints of a three phase transformer and the stator yoke of a rotating electrical machine.

In a rotating machine stator core, it can account for up to 50% of the total core loss [119]. It would be very advantageous if the rotational core loss is considered properly in electrical machine design. For various reasons, however, the study in this area is still at an early stage, although a considerable amount of work has been done [119-196]. So far, the techniques for measuring rotational core loss have not been fully developed, and there is no model bearing a strong physical background for predicting the core losses with practical accuracy, since the mechanisms of rotational core losses have not been well understood.

For core loss analysis in rotating electrical machines, models for alternating core losses are generally used. When the magnetic flux density waveforms in all motor core parts are assumed sinusoidal, the loss values obtained by this procedure are always lower than the experimental ones, from 20 to 50% in standard motors operating at 50 or 60 Hz, and even more in motors operating at higher frequencies [192]. Since 1991, a phenomenological approach generalised directly from the corresponding model for alternating core losses has been employed by several researchers for rotational core loss analysis in rotating electrical machines, but the comparison between the theoretical and experimental results showed that further improvement was required [192-196].

In this chapter, a literature survey on rotational core loss measurement and modelling is reported. Section 4.2 is a review of the development of measuring techniques and apparatus in the last hundred years, including the measuring techniques of magnetic field and flux density, evaluation of rotational core loss, and rotational core loss testers, while the important results of measurement, understanding, and modelling of rotational core losses in electrical sheet steels are discussed in section 4.3. In section 4.4, the current status of core loss modelling in rotating electrical machines is presented.

4.2 DEVELOPMENT OF TECHNIQUES AND APPARATUS FOR ROTATIONAL CORE LOSS MEASUREMENT

The first experimental work upon the hysteresis of ferromagnetic materials in a rotating magnetic field was carried out by Ferraris in 1888, but he was not able to measure the hysteresis loss because of his rough apparatus. The rotational hysteresis loss was first quantitatively determined by Baily in 1896 [120]. Fig.4-1 illustrates the apparatus used by Baily. The specimen was made up of a stack of laminations. The magnetic field was generated by an electromagnet, which could rotate around the specimen. The power loss was measured via the torque which is proportional to the angle of rotation of the specimen.

Since then, in the last a hundred years, various measuring techniques and systems have been developed [121-180]. Mainly, they fall into two categories:

(1) rotating a disk sample in a static magnetic field [125-134];

(2) rotating the magnetic field while keeping the sample stationary [120,135-180].

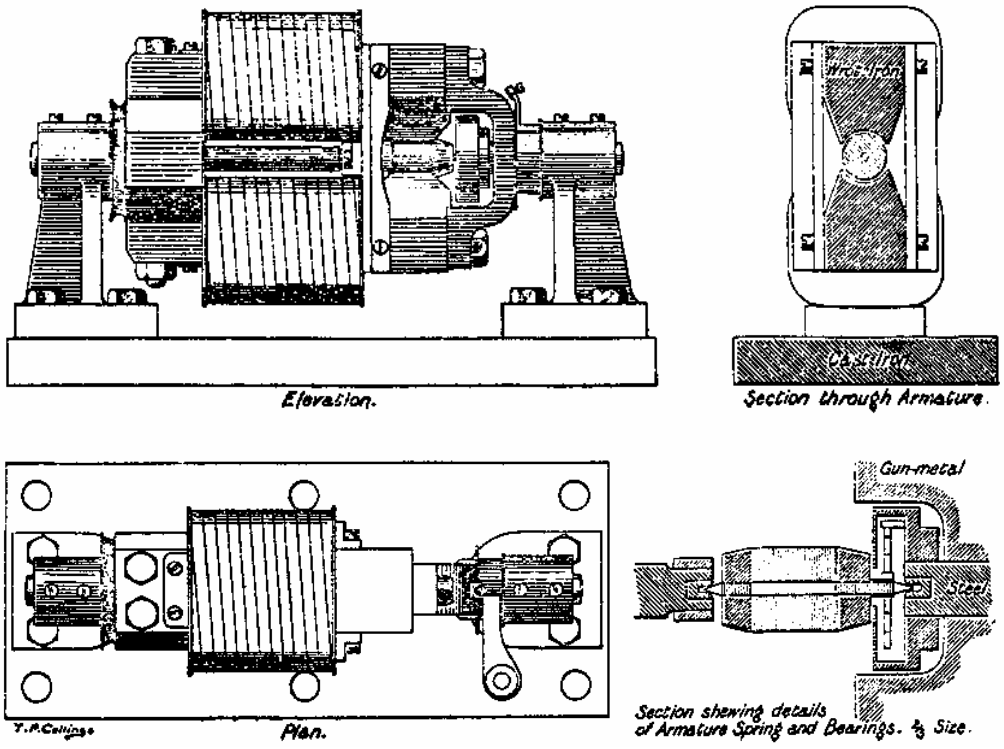

Fig.4-1 Rotational hysteresis measuring apparatus used by Baily (from [120])

In the second category, the sample can be a disk [137,162,170] (or a stack of disks [120,147,168,179]), a stack of annular rings [146], a cross [136,139-142,170], an Epstein strip [145,164,170], a square [138,143,144,148-157,160,161,163,165-167,169-173,177,178,180] (or a stack of squares [135]), or a large sheet [158,159,169,174,175].

In core loss testers, magnetic field strength H and flux density B are two basic quantities to be measured. Generally, there are four methods available: the magnetisation current method [3,123,135,137,139,174,208], the sensing coil method [3,125-132,135-152,155-157,160-165,167-173,176-181,210,211], the Hall element method [3,133,134], and the B tip method [136,143,144,152,166,209-211].

As to the power loss evaluation, four methods have been used. They are the torque-metric method [120,125-127,130,131,146], the thermometric method [135,137,138,140, 141,146,147,168,170,181], the field-metric method [128,129,132-134,136,142-145,147-149,151,152,155,157,161,163-166,168-176,178,180], and the watt-metric method [139,174].

4.2.1 Measuring Techniques for Magnetic Field Strength and Flux Density

4.2.1.1 Magnetisation Current Method

When the magnetic circuit of a core loss tester satisfies the following conditions:

(1) the magnetic flux path inside the sample is well defined,

(2) there are no dissipative processes outside the sample, and

(3) there is no magnetic potential drop outside the sample, then

the magnetic field strength H can be determined from the magnetisation current I by applying Ampere's law:

$$H = \frac{NI}{l_m} \tag{4.1}$$

where N is the number of turns of the excitation winding, and l_m the mean length of magnetic flux path.

This method is widely used in apparatus for alternating core loss measurement, such as annular rings, Epstein frames, and single sheet testers [208]. If used in rotational core loss testers, however, this method is not accurate, since the magnetic flux paths in the specimen are vague [174].

4.2.1.2 Sensing Coil Method

(1) Conventional H Coil

The tangential component of magnetic field strength at the specimen surface can be measured by a thin search coil placed on the surface, as illustrated in Fig.4-2. When the magnetic field is parallel to the surface of the specimen, the magnetic field strength can be calculated by

$$H = \frac{1}{\mu_o K_H} \int V_H dt \tag{4.2}$$

where $\mu_o = 4\pi \times 10^{-7}$ is the permeability of a vacuum, K_H the coil coefficient determined by calibration, and V_H the terminal voltage of the H sensing coil.

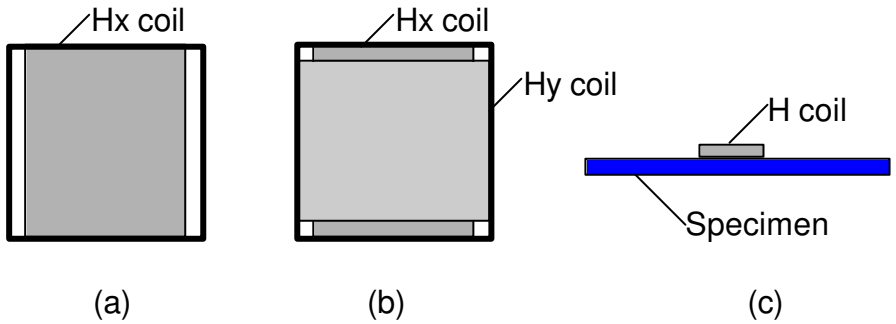

Fig.4-2 (a) One dimensional H coil, (b) two dimensional H coil, and (c) position of H coil.

This method is commonly used in both alternating and rotational core loss testers, and can yield accurate results if the magnetic field on the specimen surface is uniform. In square specimen rotational core loss testers with horizontal yokes, however, the magnetic field varies significantly with the distance between the specimen surface and the **H** coils, as observed by several researchers [149,153,154,180,211]. In order to reduce error, the sensing coils must be made extremely thin and installed as close to the specimen surface as possible, but this is often very difficult.

(2) Two H Coil Arrangement

To reduce the error caused by the variation of magnetic field with the distance above the specimen surface, a two H coil arrangement, as shown in Fig.4-3, can be used [164,212]. The magnetic field strength at the specimen surface can be calculated by

$$H = \frac{d_2 H_1 - d_1 H_2}{d_2 - d_1} \tag{4.3}$$

where H_1 and H_2 are the magnetic field strength measured by H coil #1 and #2, d_1 and d_2 the distances of two H coils away from the specimen surface.

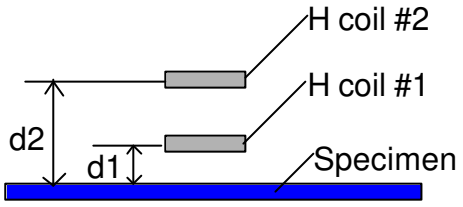

Fig.4-3 Two H coil arrangement

Both numerical analysis [149,153,154] and experimental measurement [164,180] have shown that the linear extrapolation of (4.3) is a reasonable approximation, when two H coils are placed not far away from the specimen.

(3) The Rogowski-Chattock Coil

Another choice of higher accuracy than the conventional H coil is the Rogowski-Chattock coil (also known as magnetic potentiometer) [3,148,210,211], as depicted in Fig.4-4, the principle of which is based on the existence of the scalar magnetic potential V_m in the absence of currents. The magnetic potential difference between two points A and B can be determined by

$$\begin{aligned} V_{mA} - V_{mB} &= \int_{C1} \mathbf{H} \bullet d\mathbf{l} \\ &= \int_{C2} \mathbf{H} \bullet d\mathbf{l} \end{aligned} \tag{4.4}$$

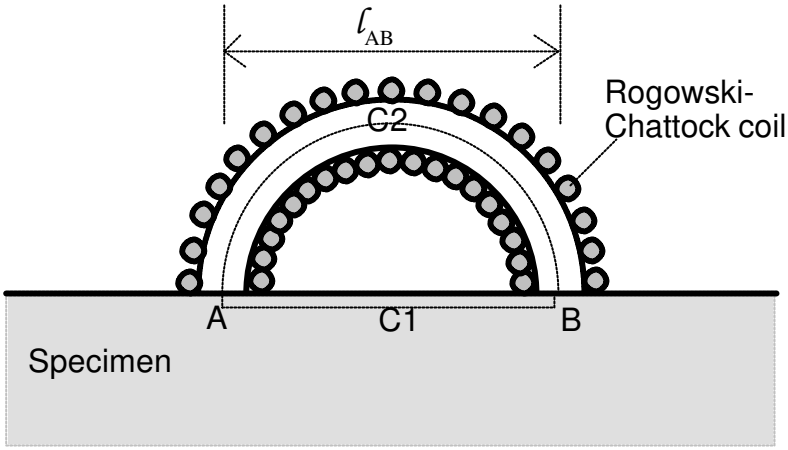

Fig.4-4 The Rogowski-Chattock coil (magnetic potentiometer)

If the magnetic field is uniform between point A and B, the line integral of **H** along path C1 can be calculated as

$$\int_{C1} \mathbf{H} \bullet d\mathbf{l} = H\, l_{AB} \tag{4.5}$$

where l_{AB} is the distance between point A and B. When the magnetic field varies with time, the induced terminal voltage of the coil is

$$\begin{aligned} V_H &= \frac{d\lambda}{dt} \\ &= \mu_o A_H n \frac{d}{dt} \int_{C2} \mathbf{H} \bullet d\mathbf{l} \end{aligned} \tag{4.6}$$

where λ is the total flux linkage, A_H the cross sectional area, and n the number of turns per unit length of the coil. Substituting (4.4) and (4.5) into (4.6) yields

$$\begin{aligned} V_H &= \mu_o A_H n \frac{d(H\, l_{AB})}{dt} \\ &= \mu_o K_H \frac{dH}{dt} \end{aligned} \tag{4.7}$$

where $K_H = A_H n l_{AB}$ is the coil coefficient, which can be determined by calibration. Therefore, the magnetic field on the specimen surface can also be obtained by the time integral of V_H.

Because both ends of the coil can be installed very close to the specimen surface, correct H can be detected, and higher sensitivity can be achieved by a larger coil coefficient K_H, which is proportional to the number of turns per unit length of the coil.

(4) B Coils

Magnetic flux density in core loss testers can also be measured by sensing coils [3,125-132,135,137-151,155-157,160-165,167-173,176-181]. When magnetic flux density is uniformly distributed over the cross section of a sample, the sensing coil can be wound around the whole sample, as illustrated in Fig.4-5(a). If the flux density is non-uniform over the cross section of a sample, the sensing coil can then be threaded through small holes at the position of interest, as shown in Fig.4-5(b). The magnetic flux density in the sample is calculated by

$$B = \frac{1}{NA_B}\int V_B dt \tag{4.8}$$

where N is the number of turns, A_B the cross sectional area, and V_B the induced terminal voltage of the B coil.

This method gives accurate results, but it is not advantageous when a great number of specimens are to be measured.

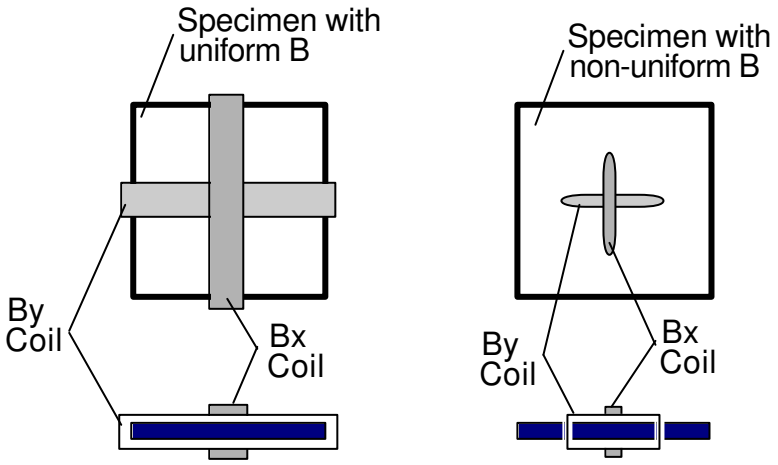

(a) (b)

Fig.4-5 B coil settings for specimens with (a) uniform B, and (b) non-uniform B

4.2.1.3 Hall Elements

This method makes use of the Hall effect, which occurs in any conductor carrying a current in the presence of a transverse magnetic field. In semiconductors, this effect is much larger than in metals. If there is a current *i* in a plate-shaped semiconductor, as shown in Fig.4-6, then two opposite points *a* and *b* will be at the same potential in the absence of a magnetic field. When a field H acts at right angles to the plate, the current path is distorted, and an emf e_H is developed between *a* and *b*. The magnitude of this Hall emf is proportional to the product of the current and the field, and hence, the magnetic field strength can be determined as

$$H = \frac{e_H t}{R_H i} \tag{4.9}$$

where t is the thickness of the plate, and R_H, the Hall constant, which is a property of the material.

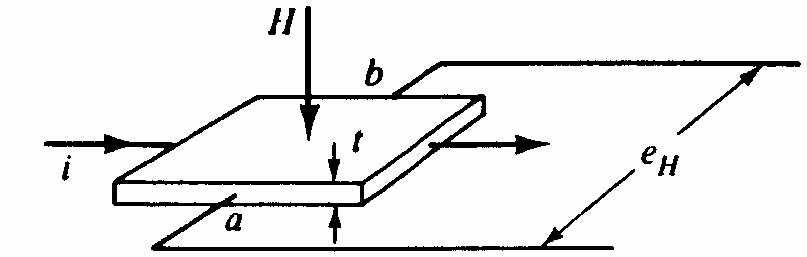

Fig.4-6 Relationship between magnetic field, current, and emf in the Hall effect

Because of the difficulties of installation, this method is not commonly used in rotational core loss testers, except the one using a rotating disk sample developed by Flanders in 1985 [133,134].

4.2.1.4 B Tips

This method was first developed by Werner in 1949 [209], and used for rotational core loss measurement by Kaplan in 1961 [136,210], Brix in 1983 [143,144], and Sievert in 1990 [152,166].

As illustrated in Fig.4-7, the induced electromotive force V is measured between two needle tips placed a certain distance apart in contact with the specimen surface. If the specimen is a thin lamination, by Maxwell's equations, the measured voltage can be approximately calculated by

$$V = \frac{bd}{2}\frac{dB_y}{dt} \qquad (d << b) \tag{4.10}$$

where d is the thickness of the sample, b the distance between two potential tips, and B_y the Y component of magnetic flux density in the specimen. Therefore,

$$B_y = \frac{2}{bd}\int V dt \tag{4.11}$$

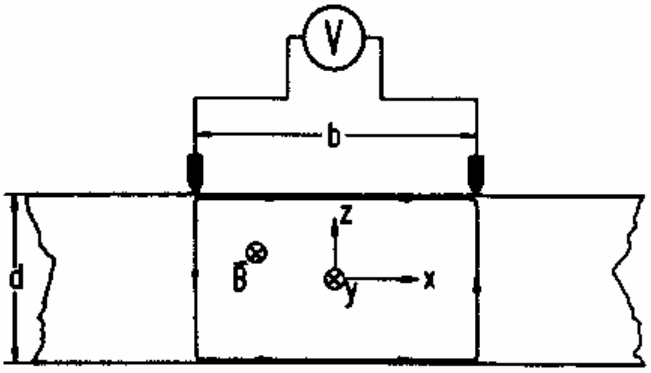

Fig.4-7 Principle of measuring one component of **B** using tips (from [143])

Compared with the B sensing coils, B tips are more suitable for batch measurements, but limited to conducting materials. Essentially, this method is equivalent to a one turn search coil. In practical measurement, high quality preamplifiers are required, since the voltage signal obtained from the tips is very weak. It is also very difficult to exclude stray fluxes through the air, which may become significant when the specimen size is small. Therefore, the sensitivity of this method is lower than that of the B search coil.

4.2.2 Methods for Measuring Rotational Core Loss

4.2.2.1 Torque-metric Method

This method is usually used in apparatus using disk or ring samples, as will be described in section 4.2.3.1. The torque due to rotational core loss occurring in the sample is measured by using mechanical torque meters [120,125-127,130,146], or calculated from the variation of sample angular speed [131].

The advantages of this method are the direct reading of the torque corresponding to rotational core loss from the torque meter, and the ability to measure rotational core loss with high flux density.

The disadvantage is the difficulty of torque meter construction owing to the complicated mechanics.

4.2.2.2 Thermometric Method

In the thermometric method, the temperature of the sample is determined by thermocouples, thermistors, or thermoviewers [135,137,138,140,141,146,147,168,170, 171]. The rotational core loss is proportional to the initial rate of the sample temperature rise if no cooling process is involved, namely,

$$P_r = C\frac{d\theta}{dt} \tag{4.12}$$

where P_r is the specific rotational core loss in W/kg, C the specific heat of the sample material, θ the temperature of the sample, and t the time instant.

This is a very versatile method, which has been widely used in apparatus using various types of samples, such as disc [137,147,168], ring [146], cross [140,141], and square [135,138], with various types of rotating magnetic field. It is also able to measure localised core loss at the T joints of a 3-phase transformer core [170,181].

The major short-comings of this method are the difficulties of installation and calibration of thermosensors, and isolation against the surrounding. It is, therefore, being more and more replaced by the field-metric method.

4.2.2.3 Field-metric Method

In the field-metric method, rotational core loss is calculated from the measured magnetic field strength **H** at the sample surface and flux density **B** inside the sample. This method features high accuracy and great versatility. Moreover, the set of measured instantaneous **H** and **B** values can yield more desirable information, such as various loss contributions, the loci of **H** and **B** vectors, and harmonics etc. The main disadvantages are the difficulties of manufacture, calibration, and installation of **B** and **H** sensors, and the sensitivity to preamplifier phase angle errors.

For the evaluation of rotational core loss, there exist two formulas, which are here called as the field-metric method type one and type two, respectively. The field-metric method type one [136,142-145,147-149,151,152,155,157,161,163-166,168-176,178,180] calculates the total specific core loss P_t in W/kg as

$$\begin{aligned} P_t &= \frac{1}{T\rho_m}\int_0^T (\mathbf{H}\bullet\frac{d\mathbf{B}}{dt})dt \\ &= \frac{1}{T\rho_m}\int_0^T (H_x\frac{dB_x}{dt}+H_y\frac{dB_y}{dt})dt \end{aligned} \tag{4.13}$$

where T=1/f is the time period, f the frequency of magnetisation, ρ_m the sample material mass density, and H_x, H_y, B_x, and B_y are the X and Y components of **H** and **B**.

In the field-metric method type two [128,129,132-134], the torque per unit volume due to the rotational core loss in the sample is calculated by

$$\begin{aligned} T_r &= \mu_o|\mathbf{H}\times\mathbf{M}| \\ &= \mu_o HM\sin\alpha \\ &= \mu_o HM_\perp \end{aligned} \tag{4.14}$$

where M is the magnetisation, α the angle between **H** and **M** vectors, and $M_\perp$ the component of **M** perpendicular to **H**.

For the rotational specific core loss corresponding to the torque T_r calculated by (4.14), Enokizono and Sievert [121,149,151] proposed a formula as following

$$P_r = \frac{\omega}{T\rho_m}\int_0^T |\mathbf{H}\times\mathbf{B}|\,dt \tag{4.15}$$

where $\omega=2\pi f$ is the angular speed of magnetisation.

According to Enokizono and Sievert [121,149,151], (4.13) can be classified as the total loss, while (4.15) as rotational loss, since it is related to the rotational component of the magnetic flux. In measurements on both grain oriented and non-oriented electrical sheet steels with purely circular rotating magnetic flux, (4.13) and (4.15) gave identical results, whilst with elliptically rotating magnetic flux, contradictory results were obtained [151].

About (4.15), there are still some open questions, and they will be further discussed and clarified in chapter 5, section 5.3, and 5.4.

4.2.2.4 Watt-metric Method

This method differs from the field-metric method in that the magnetic field strength H is determined from the magnetisation current [123], and is widely used in the Epstein frames and single sheet testers for alternating core loss measurement [208]. Initially, magnetic field strength, flux density, and core loss were measured by ammeters, voltmeters, and wattmeters [139,208], respectively. That is why this method is known as the watt-metric method. With the development of digital techniques, H and B waves can be readily obtained in numerical form, and core losses can then be calculated by (4.13) and (4.15) [174]. An outstanding advantage of this method is the simplicity of the H determination.

In apparatuses for rotational core loss measurement, this method can only be applied to the vertical yoke single sheet tester (to be described in section 4.2.3.4) [139,174], because of the absence of air gaps between the sample and the yokes. Compared with alternating core loss testers, the magnetic flux paths in the sample and the yoke system of the rotational core loss testers are not well defined. This causes excessive systematic error in magnetic field strength measurement by applying Ampere's law. Since the flux density is not uniformly distributed in the sample, the magnetic flux density is measured in the centre of the sample by sensing coils wound through small holes, or B tips.

The accuracy of measurement strongly depends on the structure of the yoke and the shape of the sample, which define the path of the magnetic flux. When a 500×500 mm^2 square sheet

sample was used, the systematic error reached up to 27% at B=1 T, 50 Hz, with yokes of wound C-core lamination (Fig.4-8(a)) and was reduced to 17%, with yokes of stacked lamination (Fig.4-8(b)) [174].

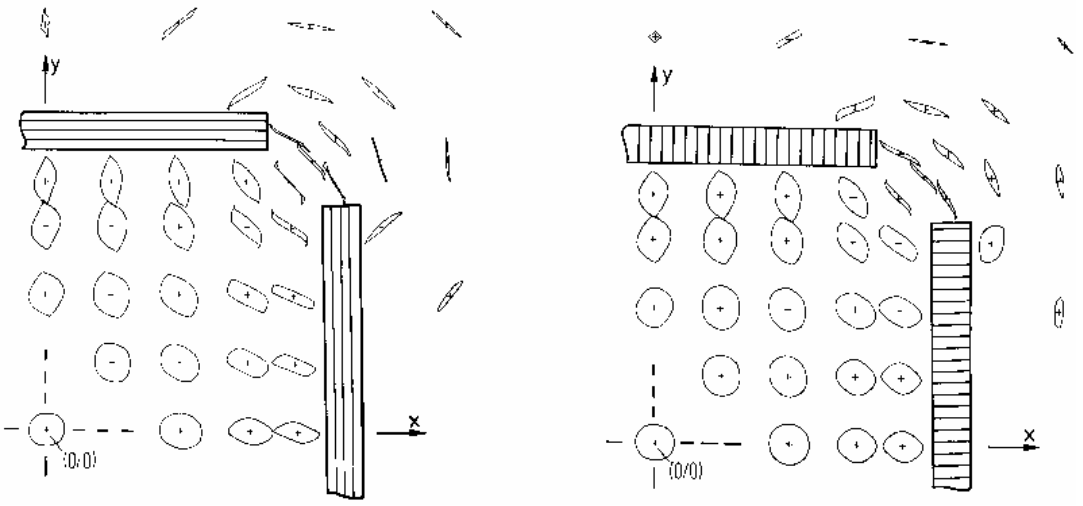

Fig.4-8 Loci of **B** vector in the sample of a vertical yoke single sheet tester, two phase excitation, isotropic sample, and B=1T in the centre; (a) wound C-core yokes; and (b) yokes with stacked lamination (from [174]).

4.2.3 Development of Measuring Apparatus

4.2.3.1 Disk and Ring Samples

In earlier measurements, disk samples were commonly used. A typical set up, developed by Brailsford in 1938 [125], is shown in Fig.4-9. The rotational hysteresis loss was determined by measuring the torque due to rotational hysteresis, and hence known as torque magnetometer. To eliminate the torque caused by anisotropic effect, a stack of several disks with the easy directions uniformly oriented was adopted, and the sample was rotated both clockwise and anticlockwise. The average torque curve of these two rotating directions would be the torque curve only due to the rotational hysteresis loss. For accurate torque measurement, the friction of the mechanical system should be kept as small as possible.

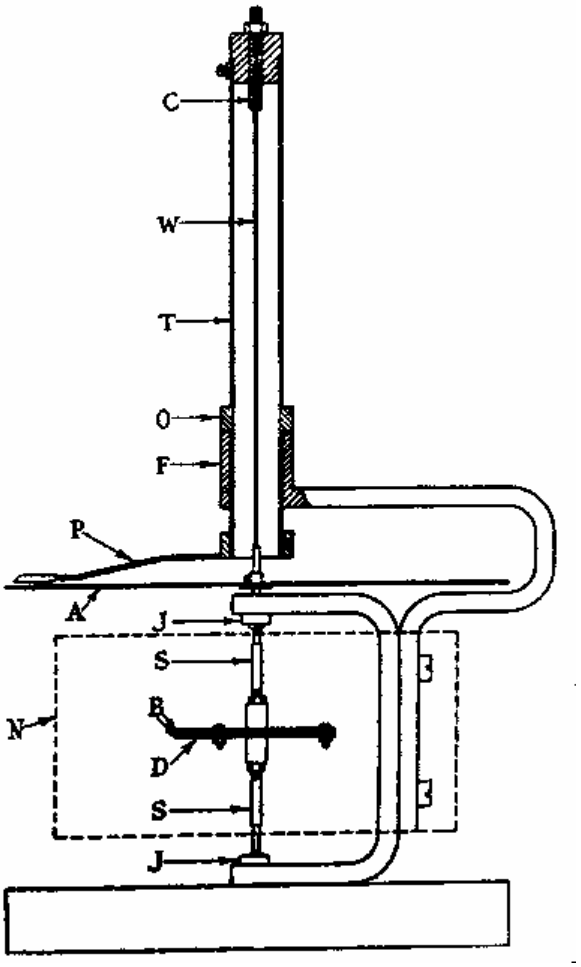

Fig.4-9 Torque magnetometer built by Brailsford (from [125])
A -- graduated aluminium disk
B -- brass disks to clamp the sample
D -- sample
N -- pole faces of an electromagnet to generate the applied field
P -- pointer

In 1967, Flanders developed a rotating sample magnetometer [128,129] as shown in Fig.4-10, which could be used for multiple purposes, such as the measurements of magnetic moment, rotational hysteresis, spin flop, and properties related to anisotropic energy, i.e. anisotropic constants, anisotropic susceptibility, and anisotropic spontaneous magnetisation. The measurements were performed on a single piece rotating sample. Sensing coils were used to detect the magnetisation perpendicular to the applied magnetic field. The field metric method type two (4.14) was used to evaluate the torque due to rotational hysteresis.

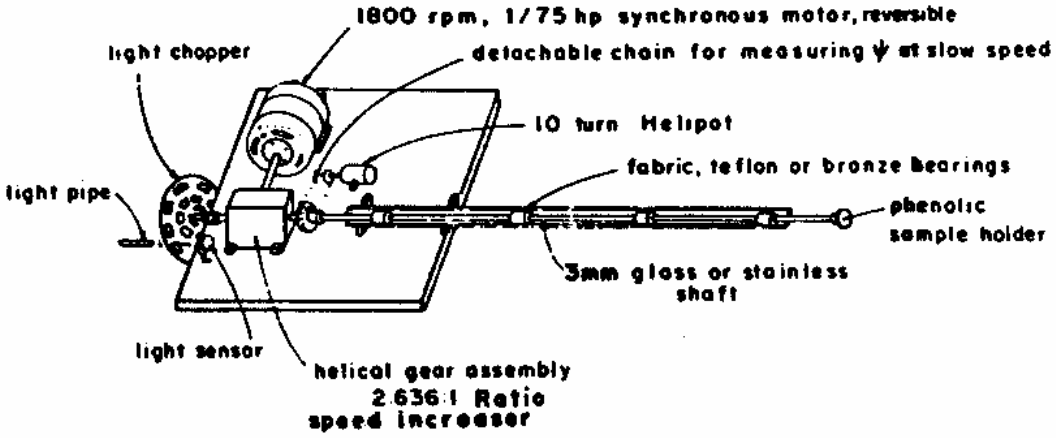

(a)

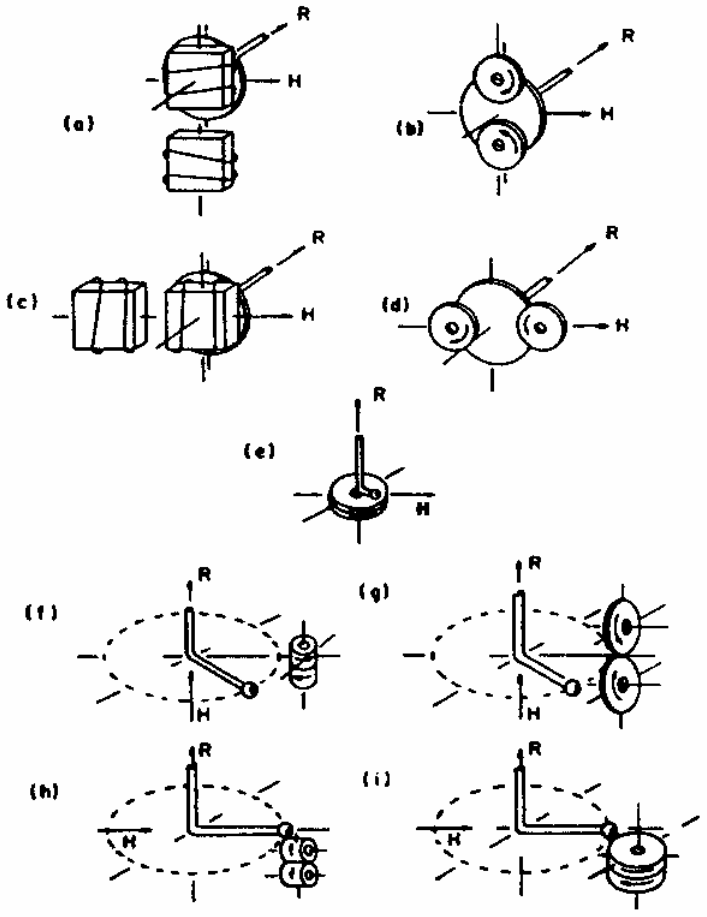

(b)

Fig.4-10 Rotating sample magnetometer developed by Flanders (from [129])
(a) Mechanical details, and
(b) Samples and sensing coil configurations.

To minimise the pickup due to variations in magnetic field or to coil motion relative to H, a set up of two coils connected in series opposition was employed. This method gives better results than the torque magnetometer illustrated in Fig.4-9, since the effect of mechanical friction has been removed. This magnetometer was further improved by replacing the sensing coils with Hall elements in 1985 [133].

Besides the rotating disk samples, a fixed disk sample was used by Fiorillo and Reitto [147,168] in 1988. Fig.4-11 is the layout of the equipment and the cross sectional view of a sample, which consists of a number of disks (from two to six) of scaled diameters, cut from the same lamination, and superposed to emulate an oblate ellipsoid. The sample was placed in a cylindrical plexiglass chamber, which could be evacuated to emulate the adiabatic conditions for measuring the temperature variation of a sample required in the thermometric method. The rotating field was generated by a three phase motor stator. Both the thermometric and field-metric type one methods were used for rotational core loss determination. The results obtained by both methods were in excellent agreement as illustrated in Fig.4-12.

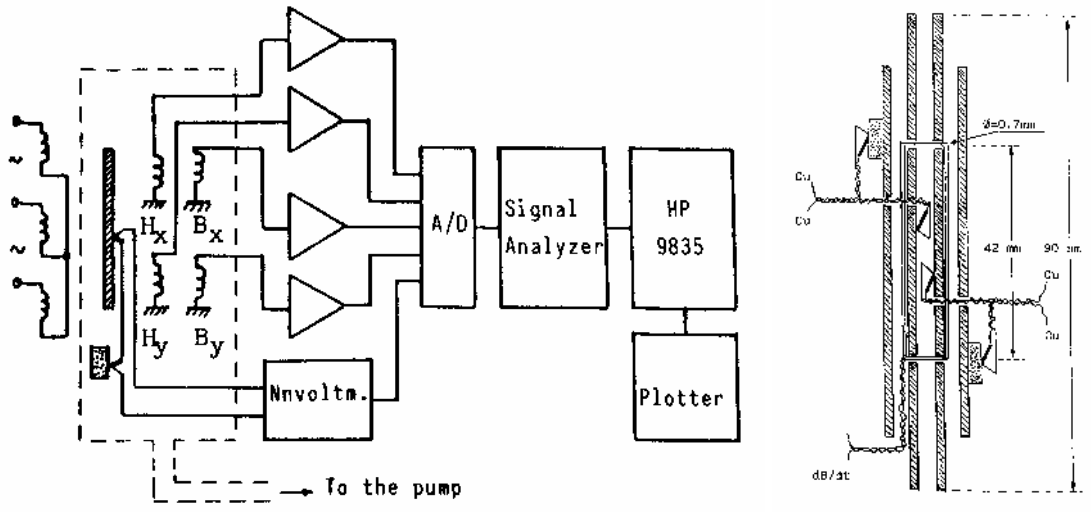

(a) (b)

Fig.4-11 (a) Layout of the equipment built by Fiorillo and Reitto (from [147]);
(b) Cross sectional view of a sample (from [168]).

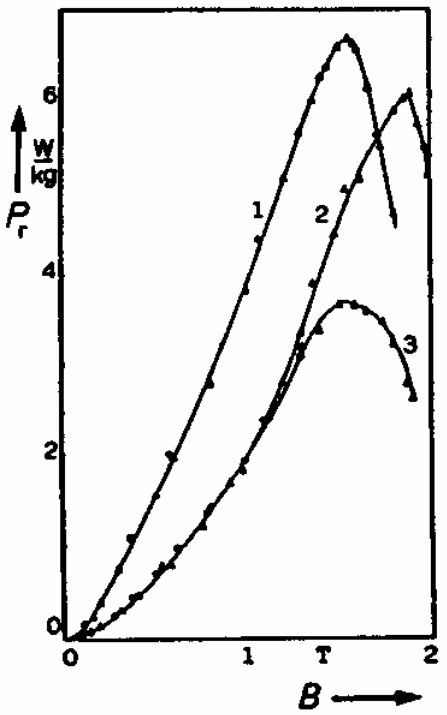

Fig.4-12 Rotational core loss vs. flux density, measured by two methods: ▵ thermometric method, • field-metric method, in three different materials: (1) soft iron (0.20 mm), (2) grain oriented silicon iron (0.35 mm), and (3) non-oriented silicon iron (0.35 mm), at 50 Hz (from [147])

In 1987, Reisinger [146] developed an apparatus using a stack of ring samples as shown in Fig.4-13. The torque-metric and thermometric methods were adopted. Essentially, this apparatus has the same features as those using disk samples described above. In addition, the sample preparation and the flux control are not convenient.

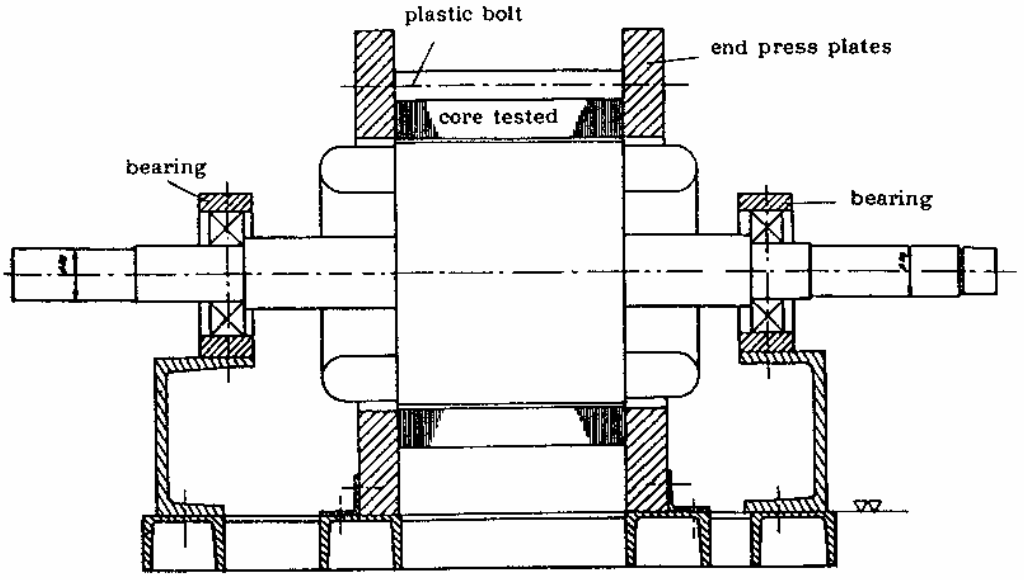

(a)

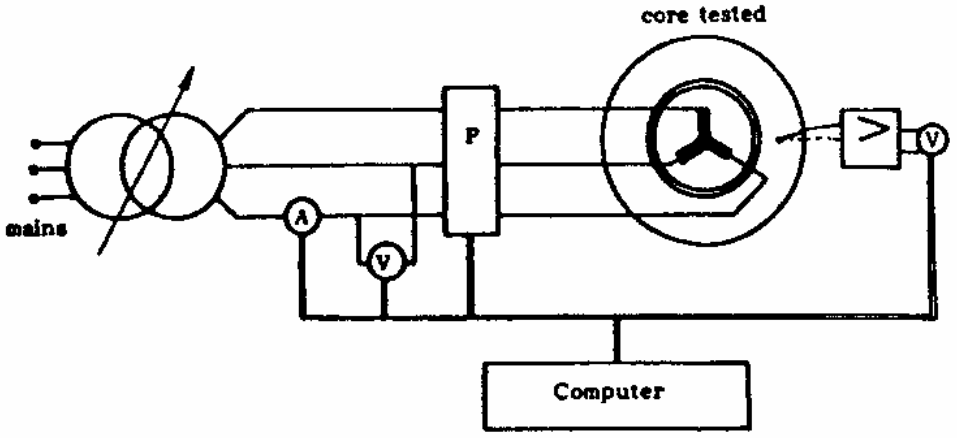

(b)

Fig.4-13 Rotational power loss measuring system using a stack of ring samples built by Reisinger (a) set-up, and (b) circuit diagram, (from [146])

The major disadvantages of these disk sample methods are:

(1) Since the magnetic flux density is not controlled by feedback, the flux density fluctuates according to the anisotropic permeability of the sample. This is particularly serious when grain oriented materials are under test.

(2) The magnetic field is not uniform within the sample. This will affect the precision of the measurement.

(3) Disk samples can not be conveniently used for testing under various flux conditions, such as elliptically rotating magnetic fields. In practice, it is often required to study the core loss under a rotating field of variable magnitude.

4.2.3.2 Cross and Strip Samples

On the other hand, cross samples do not have these problems. In 1973, Moses and Thomas [140] measured the rotating magnetic flux and the rotational core loss in silicon iron laminations with cross samples as shown in Fig.4-14. The two dimensional magnetic field was generated by the excitation windings wound on the cross sample. The rotational core loss was measured by the thermometric method, and the magnetic flux density by the sensing coils wound through very small holes in the centre of the cross, while the magnetic field strength was determined

from the magnetisation current. In this set-up, there was no flux density feedback control. Therefore, in grain oriented samples, the magnitude of flux density was not kept constant.

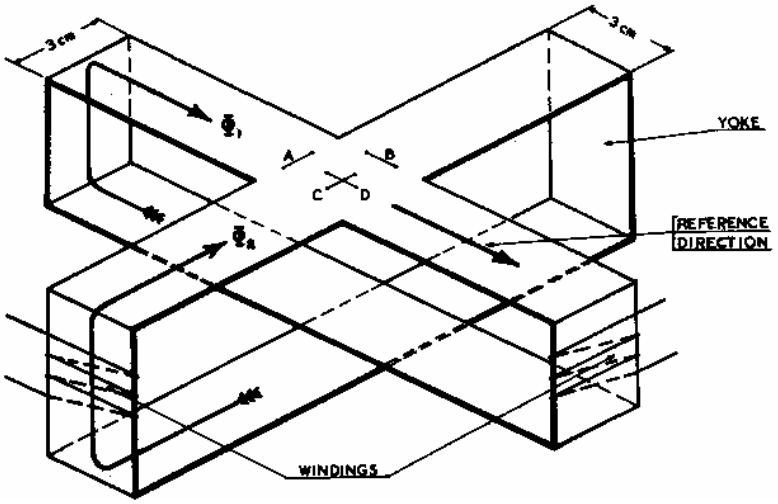

Fig.4-14 Cross sample used by Moses and Thomas (from [140])

In 1978, Basak and Moses [141] studied the sensitivity to mechanical stress of rotational power loss in silicon iron with cross samples and magnetic flux density feedback. Fig.4-15 shows their system.

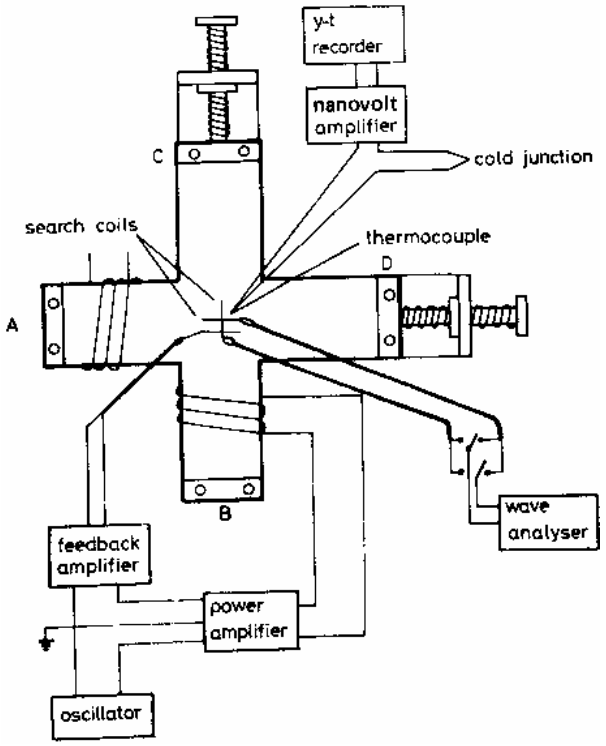

Fig.4-15 Apparatus for measuring rotational core loss under complex stress developed by Basak and Moses, where A and B are fixed ends, and C and D spring loaded ends (from [141])

In 1982, Brix, Hempel, and Schroeder [142] built a fully computerised control and measurement system with cross samples as depicted in Fig.4-16. In this system both magnetic field strength **H** and flux density **B** were obtained by the sensing coils, and the power loss was determined by the field-metric method type one.

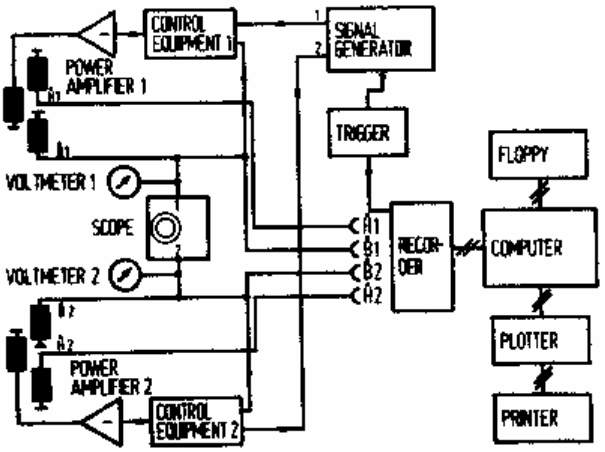

(a)

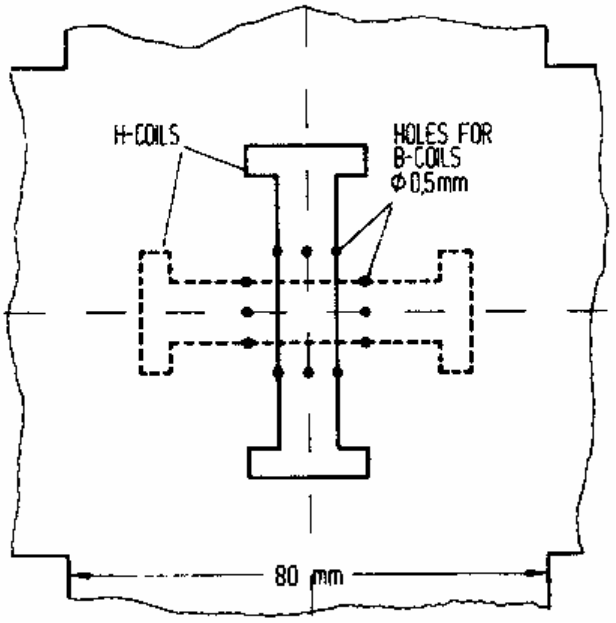

(b)

Fig.4-16 Rotational core loss measuring system using cross samples built by Brix, Hempel, and Schulte, (from [142])
(a) block diagram of the system, and
(b) arrangement of **B** and **H** sensing coils

In 1985, Sasaki, Imamura, Takada, and Suzuki [145,164] built a measuring system using a single Epstein strip. Sensing coils were used to measure magnetic field strength and flux density, and the core loss was calculated by the field-metric method type one. The configuration and the block diagram are illustrated in Fig.4-17. This system is quite similar to those using cross samples.

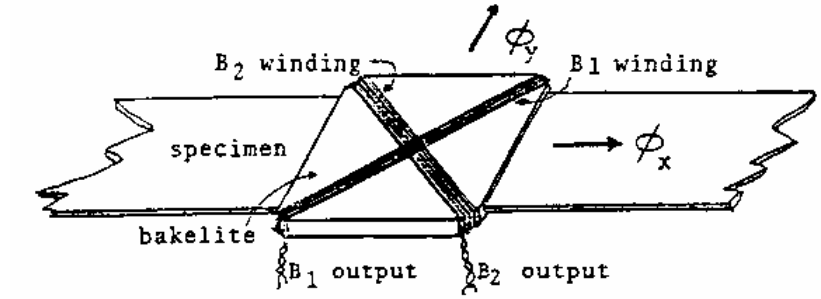

(a)

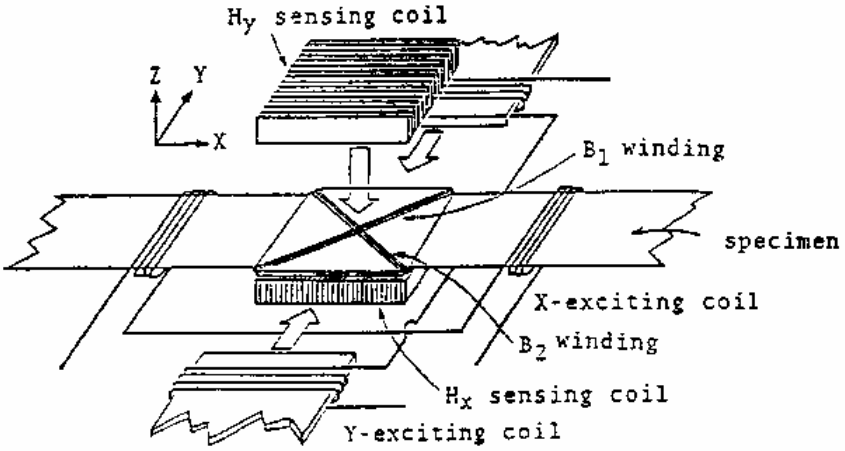

(b)

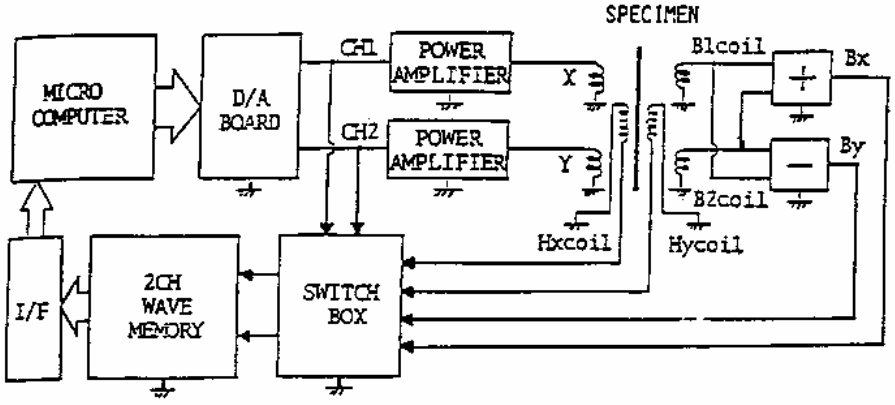

(c)

Fig.4-17 Rotational core loss tester using an Epstein strip built by Sasaki, Imamura, Takada, and Suzuki, (from [145,164])
(a) magnetic flux search coils, (b) configuration, and (c) block diagram.

4.2.3.3 Square Samples

In 1983, Brix, Hempel, and Schulte [143,144] found that the magnetic field was more uniform in a square sample than in a cross sample, and developed a tester using square samples. Fig.4-18 illustrates the whole arrangement, and the sensor. In this system, B tips were exploited for detecting magnetic flux density.

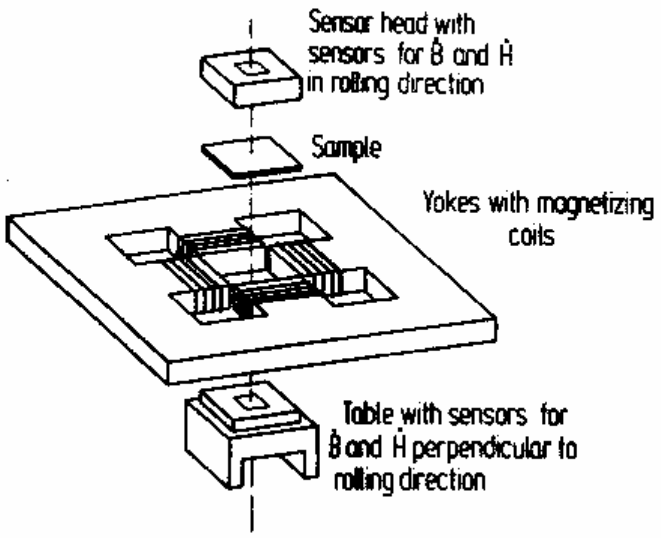

(a)

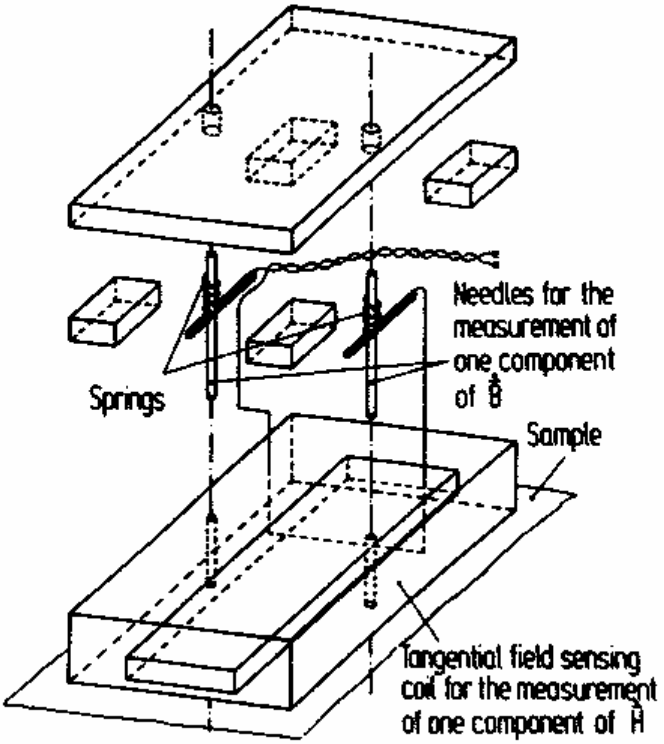

(b)

Fig.4-18 Rotational core loss tester using square samples built by Brix, Hempel, and Schulte,
(a) arrangement of yoke, sample, and sensors, and
(b) details of sensor head for one component of **H** and **B**. (from [143,144])

In 1989, Enokizono and Sievert [149-155,165-167] developed a very flexible system consisting of a horizontal magnetic circuit with a square single sheet sample and adjustable air gaps, an analog electronic circuit for flux density feedback control, and a computer which performed function generation and data acquisition in rotational core loss measurement. Fig.4-19 illustrates the configuration and the circuit diagram. The magnetic field strength was picked up by conventional surface H sensing coils. For flux density measurement, **B** sensing coils threaded through small holes in the centre of square sample were adopted by Enokizono [151,165], while B tips were used by Sievert [152,166], which is more convenient for batch measurements.

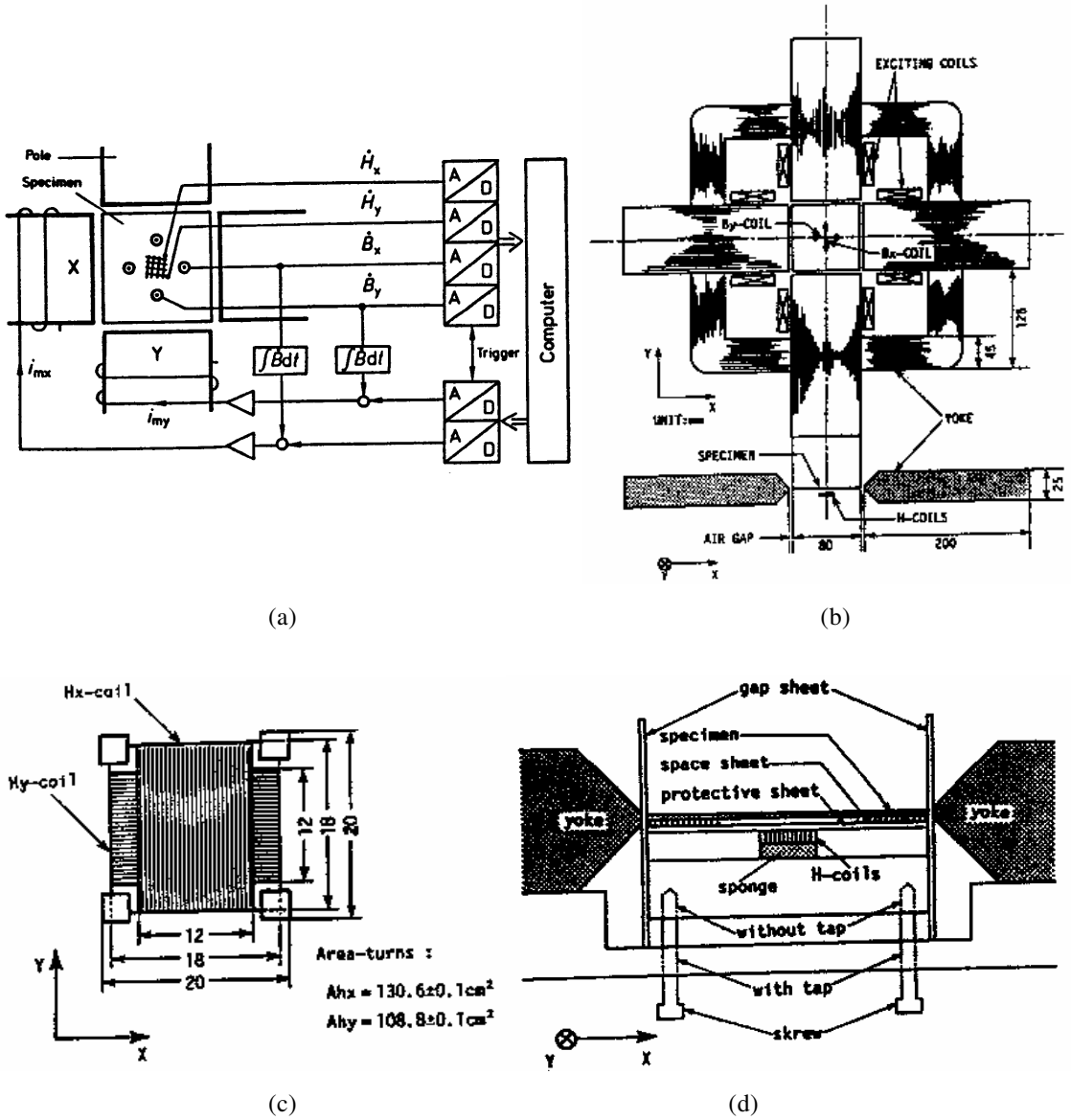

(a) (b)

(c) (d)

Fig.4-19 Rotational core loss measuring system built by Enokizono and Sievert (from [151,152])
(a) outline of system and **B** tips (b) magnetic circuit and **B** sensing coils
(c) **H** sensing coils (d) setting of **H** coils

According to the analysis by Enokizono and Sievert [154], the optimum performance in **H** measurement can be obtained when the yoke laminations are arranged vertically and the magnetisation poles are shaped in wedges, as illustrated by Type D in Fig.4-20.

This system can be used to examine the behaviour of ferromagnetic materials under either rotational or alternating magnetic field. Measurements on rotational core losses of various electrical steels [151,155,157,160,173] and dynamic magnetostriction under rotational field have been performed with this system [150,156,167].

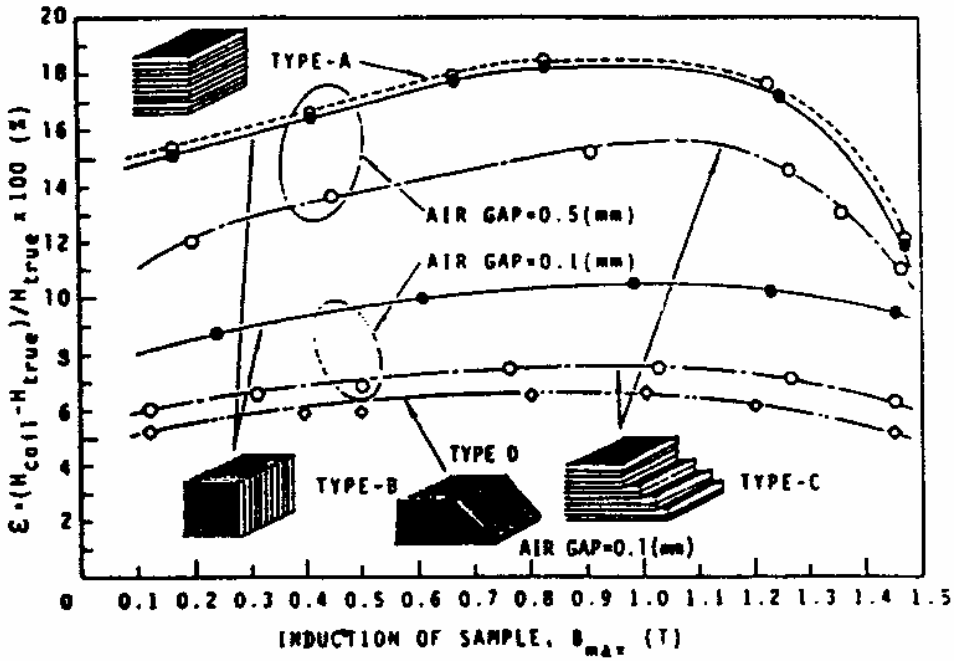

Fig.4-20 Effect of yoke construction (from [154])

In 1990, Nakata, Nakano, and Fujii [170,185] developed a square specimen tester with complicated auxiliary yokes. Fig.4-21 illustrates the measuring system, the tester, the specimen, **B** and **H** search coils, and the principle of the auxiliary yokes. It was believed that the single sheet auxiliary yoke could help to control the magnetic flux deviated from the rolling direction, as shown in Fig.4-21(c), while the double layer laminated auxiliary yokes, which formed a symmetric flux path, could make the magnetic flux distribution in the specimen more uniform, as shown in Fig.4-21(d). The two H coil method described in section 4.2.1.2 was adopted. This testing system is much more sophisticated than those developed by other researchers, but the performance was not reported in detail.

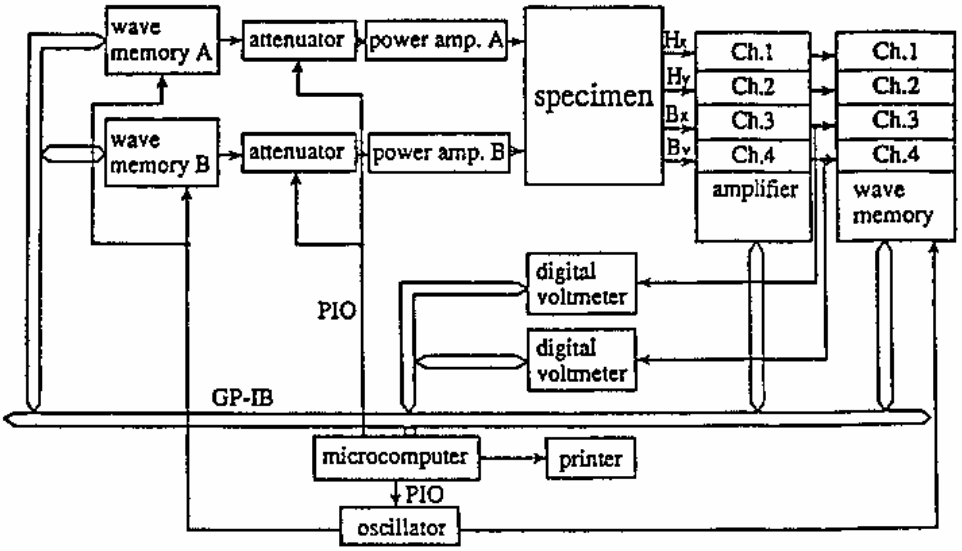

H_x: waveform of H coil for transverse direction
H_y: waveform of H coil for rolling direction
B_x : waveform of B coil for transverse direction
B_y : waveform of B coil for rolling direction

(a)

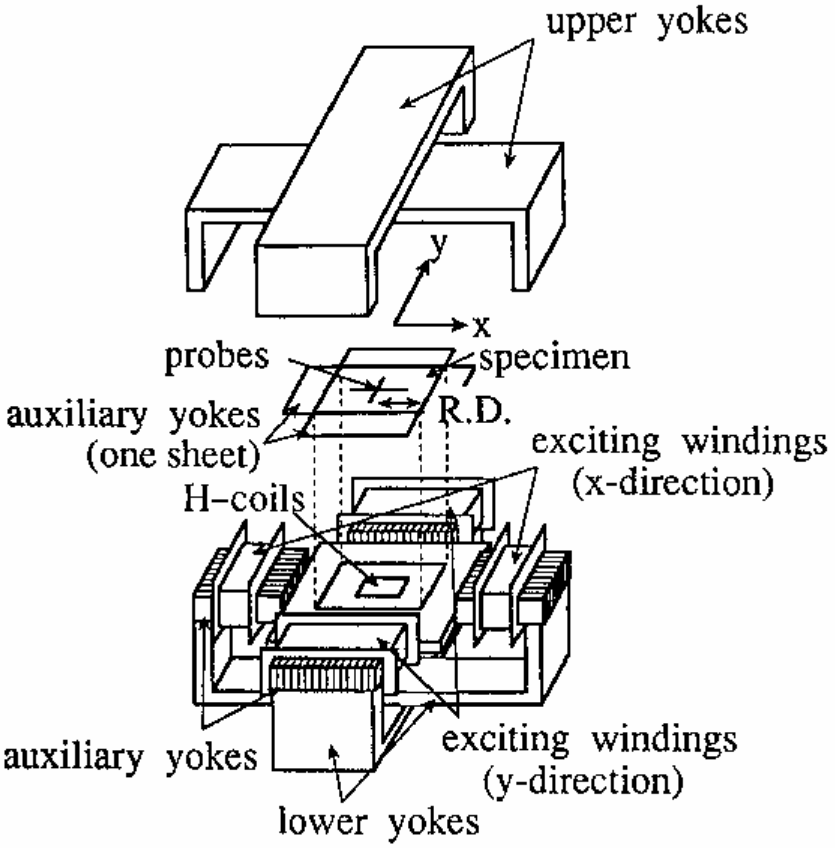

(b)

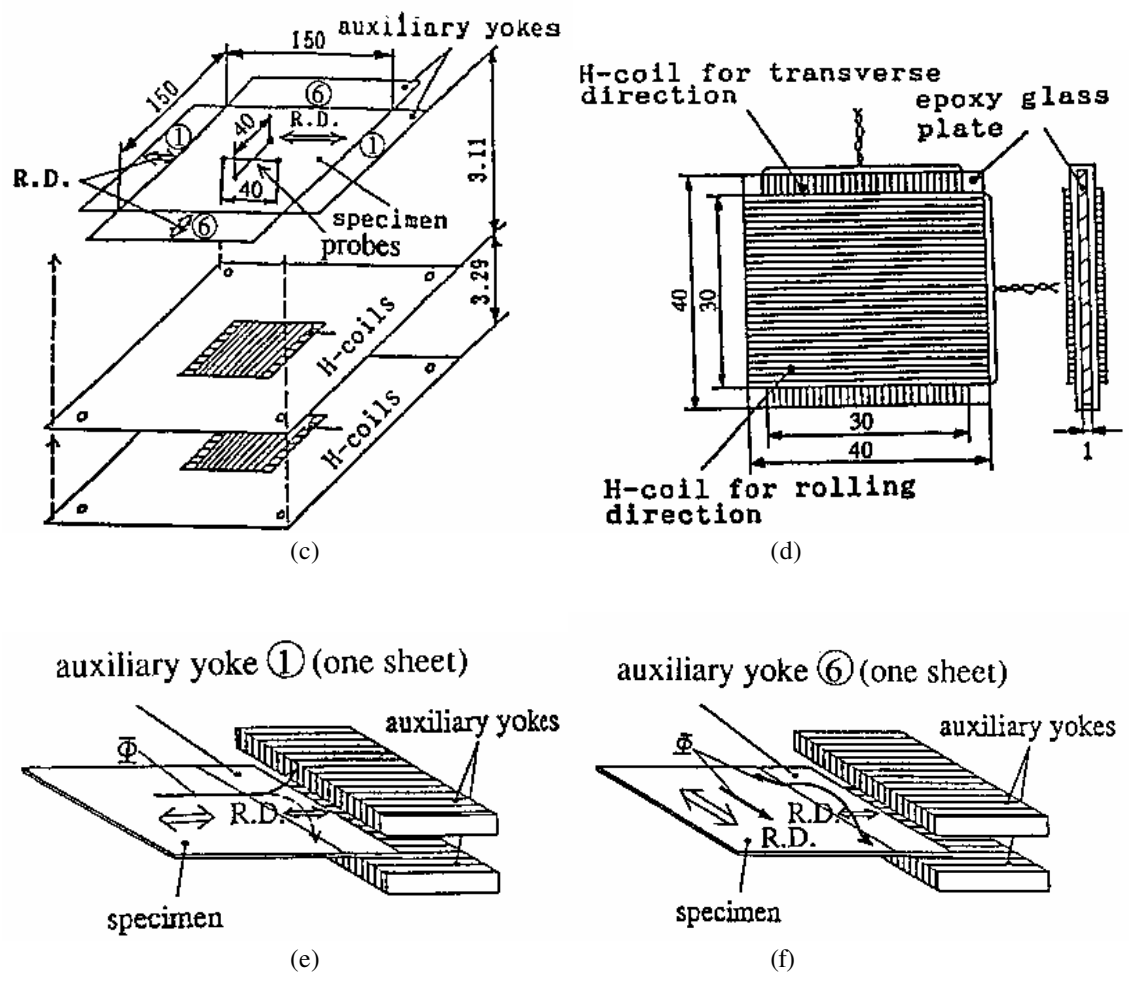

Fig.4-21 Rotational core loss measuring system developed by Nakata, Nakano, and Fujii (from [170])
(a) block diagram of the system, (b) square specimen tester,
(c) position of specimen, B and H coils, (d) dimension of H coils,
(e) flux flow parallel to auxiliary yoke, and (f) flux flow perpendicular to auxiliary yoke.

In 1991, Gumaidh, Mahadi, Alinejad-Beromi, Moses, and Meydan [169,176] also built a testing system for rotational core loss in square samples, as illustrated in Fig.4-22. Essentially, it is almost the same as that described above (Fig.4-21) in all aspects.

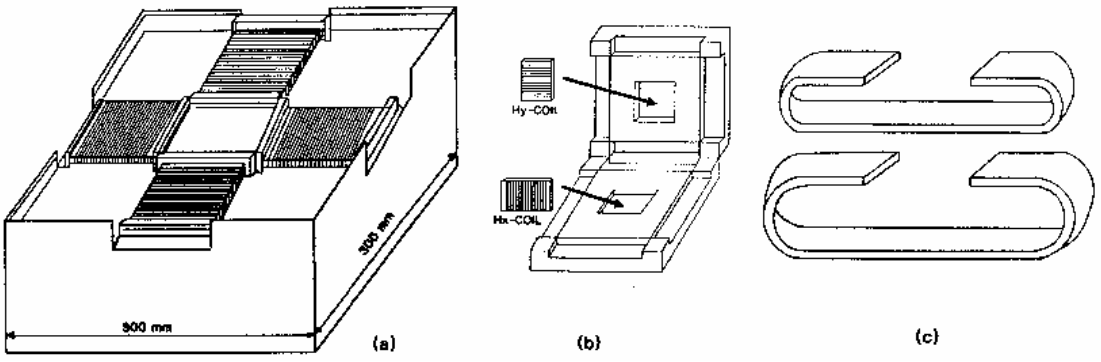

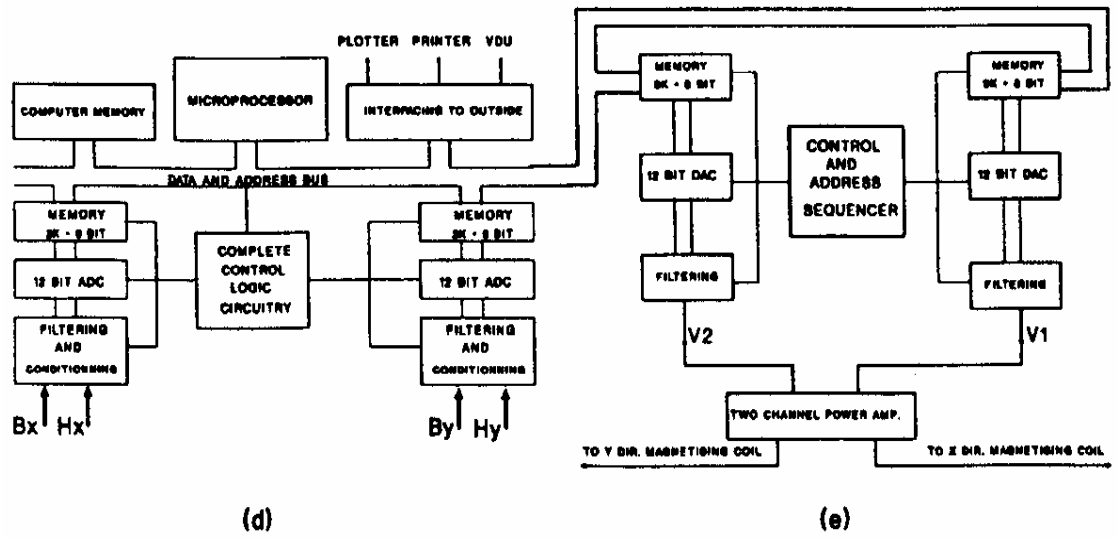

Fig.4-22 Rotational core loss testing system built by Gumaidh, Mahadi, Alinejad-Beromi, Moses, and Meydan (from [176]). (a) Tester, (b) sample and sensor holder, (c) yokes, (d) 4-channel magnetic signals digitiser board, and (e) 2-channel waveform generating board.

In the same year, Kedous-Lebouc, Zouzou, and Brissonneau built a square specimen tester with double vertical yokes [163,178]. The tester and the B and H search coils are illustrated in Fig.4-23. The size of the specimen is exactly the same as that used by Enokizono and Sievert. The performance is also similar.

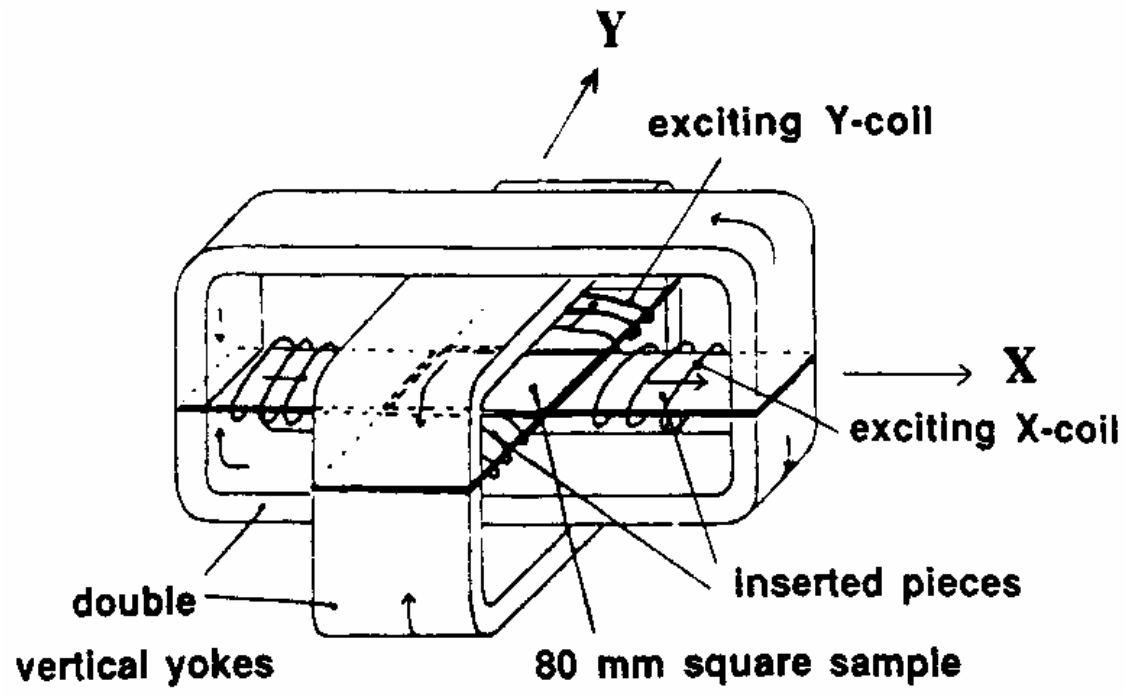

(a)

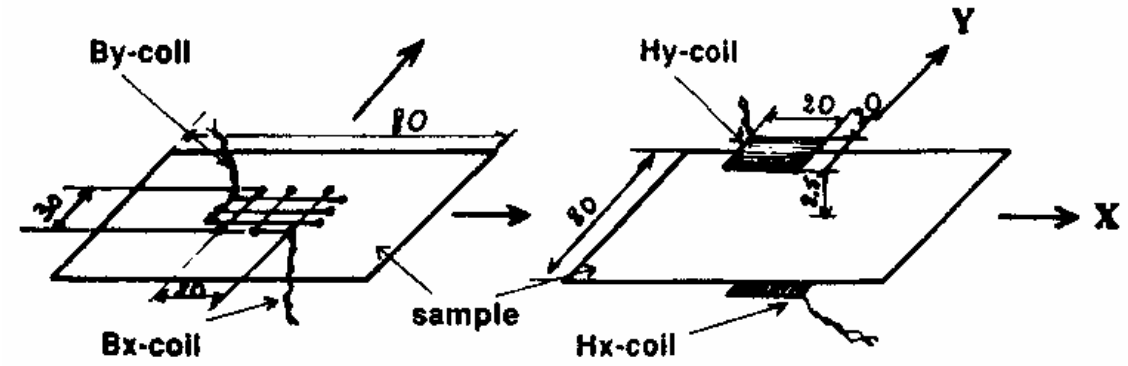

(b)

Fig.4-23 Rotational core loss tester built by Kedous-Lebouc, Zouzou, and Brissonneau (from [163]), (a) tester, and (b) **B** and **H** search coils.

The system using square samples is superior to those using disk and cross samples in the following aspects:

(1) Since the magnetic fluxes in the two perpendicular directions are controlled by feedback, the system can generate magnetic field excitations of various complex magnetic flux patterns, and hence can be used to simulate the actual situation happening in electrical machines where the magnetic field is rotating with either constant or varying magnitude.

(2) The measurement is carried out in the centre of the specimen where the field appears to be the most uniform, which leads to more accurate results.

(3) More information can be obtained from the measured **B** and **H** curves, which helps in understanding the mechanisms of rotational core losses.

(4) Preparation of the specimen is much simpler.

(5) This system can be conveniently incorporated into a system for domain structure observation, which is very important for the understanding of the mechanisms of rotational core losses.

The major drawback of this system is that it is difficult to control the flux density waveforms on the X and Y axes to be sinusoidal when the sample is close to saturation. Generally, the highest flux density values are 1.6 T for non-oriented and 1.2 T for grain oriented electrical sheet steels [186,187].

4.2.3.4 Large Sheet Samples

In 1991, Sievert and Enokizono [159,166,174,175] developed a vertical yoke system, which allowed measurements on larger sheet samples, as illustrated in Fig.4-24. Both the field-metric and watt-metric methods were used for rotational core loss evaluation, but as discussed in section 4.2.2.4, the systematic error of the watt-metric method was high (up to 28% in the worst case [174]). The major problem, however, was the inability to reach high flux density values in the centre of the sample, where the rotational core loss was measured. It was stated [187] that the highest flux density that could be reached in the sample was normally about 0.2 T lower than that achieved by the horizontal arrangement using square samples described in section 4.2.3.3. According to Dr. Sievert [166,187], this was due to the heavy leakage and stray magnetic fluxes between the yokes of the X and Y axes.

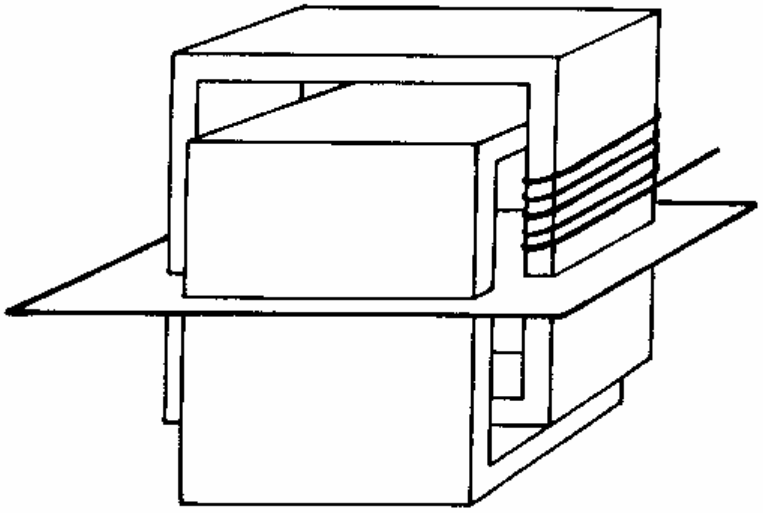

Fig.4-24 Apparatus for two dimensional excitation and measurements with vertical yokes (from [174])

4.3 INTERNATIONAL STANDARDISATION AND INTER-COMPARISON OF ROTATIONAL CORE LOSS MEASUREMENT TECHNIQUES AND APPARATUS

In June 1990, the Central Office of the International Electrotechnical Commission (IEC) circulated a questionnaire, "Questionnaire on the standardization of methods of measurement of rotational power loss", under No. 68(Secretariat)70. According to the results of this inquiry, the need for such a standard is generally accepted [212]. However, discussions among experts active in the field of rotational core loss measurement revealed that it was still too early to lay down one method in a standard of mandatory character. Since the existing formulas

(4.13) and (4.15) yielded contradictory results in the case of elliptically rotating magnetic fluxes [151,155,157,160,173,180], comprehensive and clear definitions would be desirable before drafting a standard touching this problem.

Although core losses of various electrical sheet steels with rotating magnetic fluxes have been measured and reported by various laboratories in Australia [180], Austria [146], France [163,178], Germany [151,152,155,157,160,161,166,172-174], Italy [131,147, 168,179], Japan [130,139,145,151,152,155,157,160,164,165,173,174], U.K. [120,125-127,132,138,141,169,176], and U.S.A. [134,136,137], with different principles and setup designs, the measured results have never been compared with each other. For the standardisation, the Magnetic Measurement Techniques Laboratory, Physikalisch-Technische Bundesanstalt (PTB), Braunschweig, Germany, is currently organising an European intercomparison of rotational core loss measurements [186,187]. Several sets of grain oriented and non-oriented specimens have been distributed among the participant laboratories, and are to be measured with various different testers.

4.4 MEASUREMENT, UNDERSTANDING, AND MODELLING OF ROTATIONAL CORE LOSSES IN ELECTRICAL SHEET STEELS

During the last hundred years, a great amount of study has been done on the measurement, understanding, and modelling of rotational core losses in electrical sheet steels. Early research work in this field dealt more with rotational hysteresis loss with purely circular rotating magnetic field. From 1960's, total rotational core loss with both purely circular and elliptically rotating magnetic fields at different excitation frequencies have been investigated. Important results are summarised and discussed in this section.

4.4.1 Rotational Hysteresis Loss

(1) In 1888, Ferraris concluded that the rotational hysteresis is independent of the rotating speed of a disk sample, although he did not obtain quantitative experimental results.

(2) In 1896, Baily [120] measured the rotational hysteresis loss of hard steel and soft iron using the apparatus shown in Fig.4-1, and confirmed the conclusion of Ferraris. Fig.4-25 illustrates his results obtained under rotating and alternating magnetic fields. For a range of flux density up to about 70% of the saturation flux density, the rotational hysteresis losses in both hard steel and soft iron are larger than the alternating hysteresis losses, but when the flux

density further increases, the rotational hysteresis losses drop quickly and vanish when the flux density reaches the saturation value, while the alternating hysteresis losses continue to increase. This indicates that the mechanisms of rotational hysteresis loss are different from that of alternating hysteresis loss.

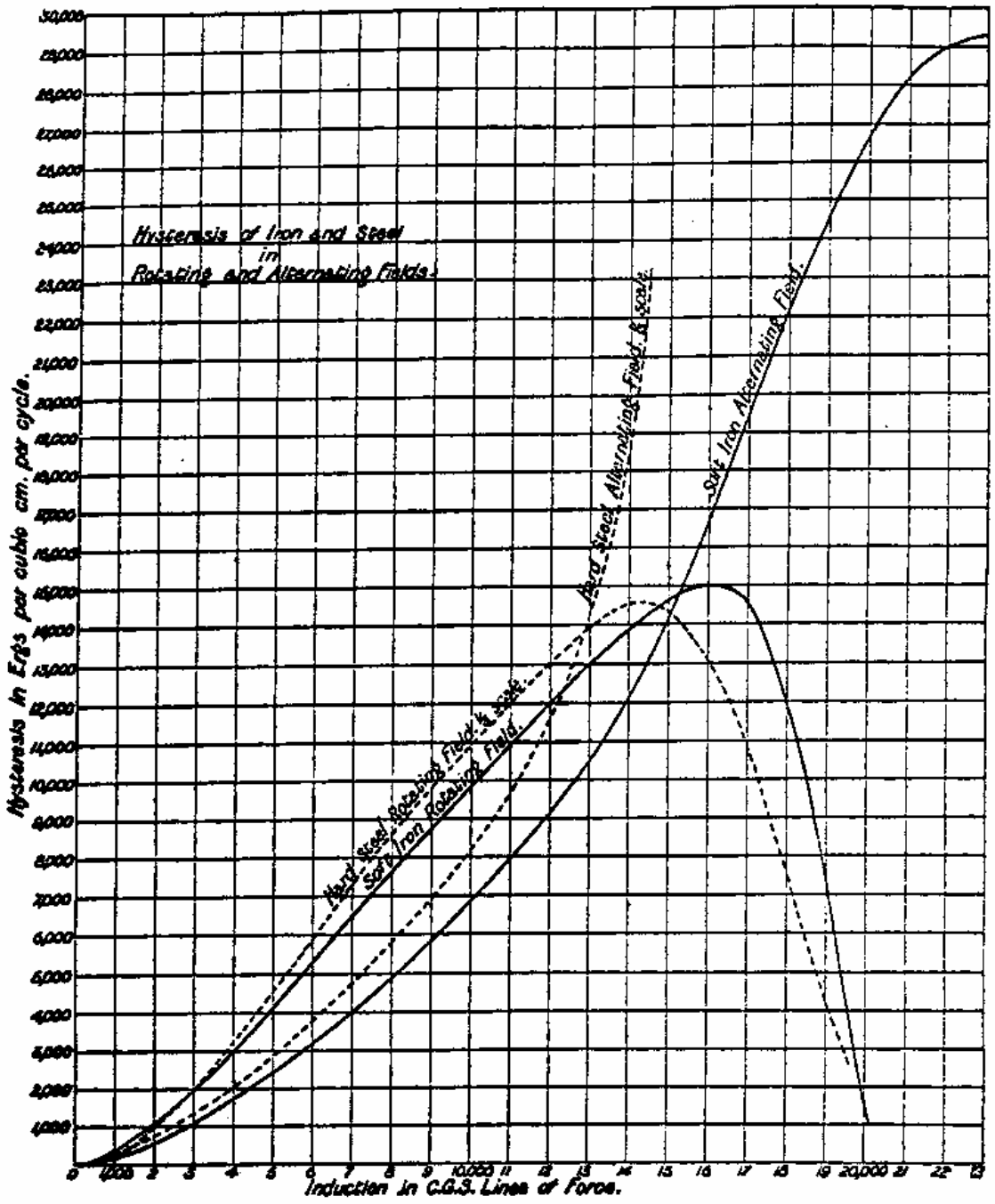

Fig.4-25 Rotational hysteresis loss of iron and steel obtained by Baily (from [120])

(3) In 1938, Brailsford [125] measured rotational hysteresis losses of four materials: ordinary electrical dynamo sheet, high quality dynamo sheet, ordinary transformer silicon steel, and cold rolled transformer silicon steel, using the torque magnetometer illustrated in Fig.4-9, and observed a sharp increase in loss at about 0.7 of the saturation value of B-H for all four materials. Fig.4-26 shows the rotational hysteresis loss and magnetisation curve of cold-rolled transformer silicon steel. When the flux density is close to the saturation value, the rotational hysteresis loss decreases quickly to zero. A qualitative explanation of this phenomenon and of the general form of the loss curves was given on the basis of the domain theory of ferromagnetism.

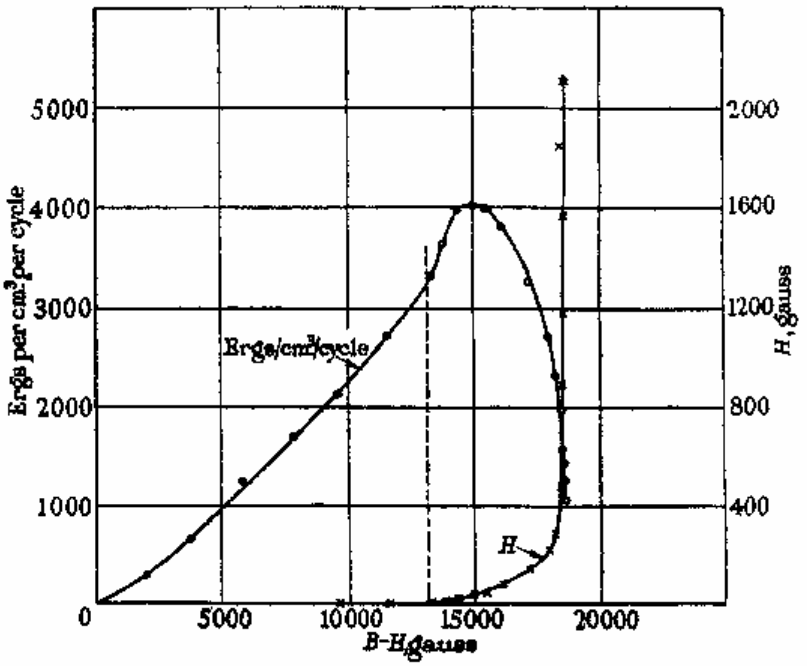

Fig.4-26 Rotational hysteresis loss and magnetisation curve of cold-rolled silicon steel (from [125])

According to this theory, magnetisation below the knee proceeds in steps, corresponding to the Barkhausen discontinuities, each step representing a reversal or sudden change in direction through 90° of the spontaneous saturation in a domain. There may be, in addition, a parallel reversible process, involving no hysteresis loss. For any particular domain, the sudden change in direction may be expected when a certain value of the field acting on it in the final direction of its magnetisation has been reached. The total change in energy involved in this discontinuous change is then dissipated as hysteresis loss, a function of the volume of the domain, the saturation magnetisation and the effective field strength.

At the knee of the magnetisation curve, the field required to produce the discontinuous rotation has already been reached or exceeded for most of the domains, and these domains contribute further to the total magnetisation on a further large increase of H, by a rotation of the spontaneous magnetisation in the domains from the easy direction towards the direction of the applied field. There are some domains remaining, however, which are not acted upon until H has increased beyond its value at the knee. The contribution to the magnetisation due to these domains is only that corresponding to their volume, but the contribution to the loss is high on account of the high value of H at which the sudden change in direction of the magnetisation occurs. The loss will therefore rise steeply with increase of magnetisation.

Similar ideas may be applied to the portion of the loss curve near saturation. For a very high field, the spontaneous magnetisation is always in the direction of the field, and as the field is rotated, it rotates smoothly and without the discontinuities which result in hysteresis loss. Hence, the hysteresis loss may then be expected to be zero.

(4) In 1960, Archenhold, Sandham, and Thompson [126] measured the rotational hysteresis loss in grain oriented silicon iron for various orientations and thicknesses with rotating disk samples (Fig.4-27). The experimental results were discussed in terms of multi-domain concepts and of the Stoner-Wohlfarth single-domain particle, of which the rotational hysteresis behaviour had been evaluated.

The basic Stoner-Wohlfarth model is of a particle sufficiently small that it acts as a single domain with an angular dependence of the energy on the direction of the applied field caused either by strain, by crystal anisotropy, or by shape anisotropy. The variable part of the energy W is

$$W = -\frac{1}{4}\cos 2\psi - h\cos\phi \tag{4.16}$$

where $h = HI_s/2K$ for crystalline anisotropy, H is the effective field strength acting on the particle, I_s the intensity of magnetisation, K the first anisotropy constant, ϕ the angle between the intensity and field vectors, and ψ the angle between the direction of easy magnetisation and the intensity vector.

For rotational hysteresis, the H vector is taken as a constant and is rotated from an initial position aligned with the intensity vector, when there occurs a discrete energy jump for certain values of the field. This was derived and given by

$$-\Delta W = \left(\frac{h^2+2}{3}\right)^{3/2} - \frac{7-h^2}{6}\left(\frac{4h^2-1}{3}\right)^{1/2} \qquad (4.17)$$

The value of h must lie within the range of 0.5-1.0, the energy change being a maximum at h=0.5 and zero at h=1.0. As shown in Fig.4-27, there exists a significant discrepancy between the experimental results and the model.

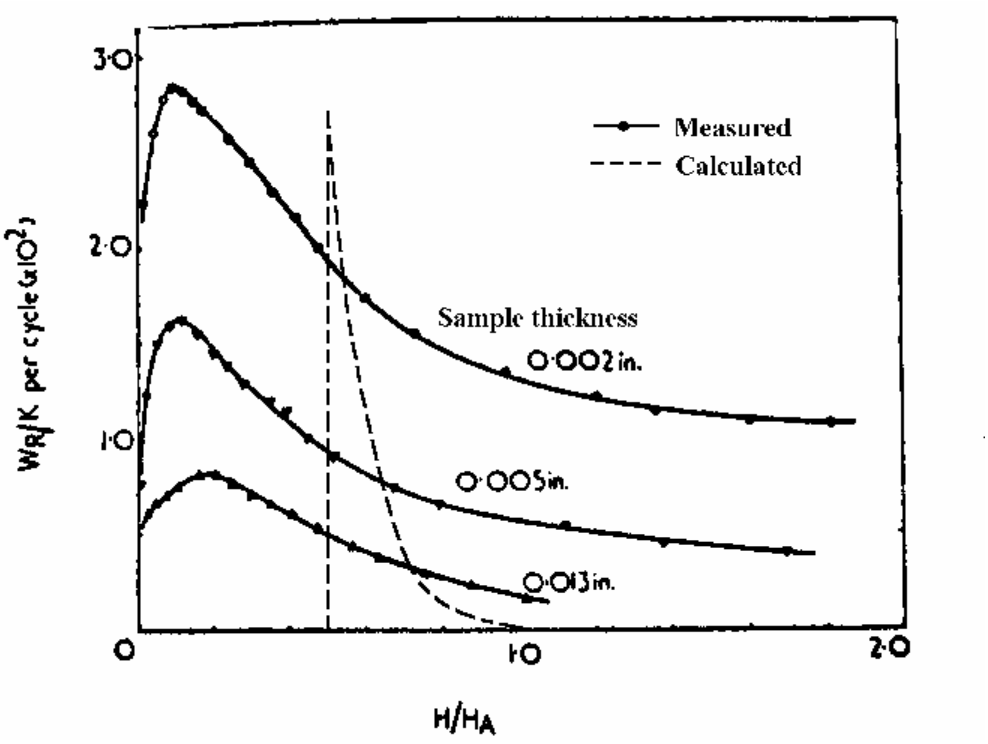

Fig.4-27 Graph of W_R/K and H/H_A, where W_R the rotational hysteresis loss, and $H_A=2K/I_S$ (after [126])

(5) In 1964, Boon and Thompson [127] used a torque magnetometer to measure the rotational hysteresis loss in 3% (nominal-weight) silicon iron disks cut from single crystals with the planar orientations (100), (110) and (111) versus magnetic flux density. The variation of the hysteresis loss with magnetic flux density was obtained for the three principal crystal directions [100], [110], and [111], from normal B-H loop measurements on single-crystal picture frames. Variation in the magnitude and direction of the field both took place slowly, so that essentially static results were obtained.

The manner in which the ratio of rotational hysteresis loss to alternating hysteresis loss depends on the magnetic flux density B for the three planes and directions was considered in terms of an existing theoretical model of the magnetic domain changes that took place during the

rotational hysteresis and alternating hysteresis loss cycles. The rotational hysteresis loss was discussed in terms of the energy required for the creation and annihilation of various domain configurations. For the (100) plane, there are two equivalent easy directions of magnetisation in the plane, and as the field rotates there is a gradual and continuous change in the amount of material magnetised along these two directions, by simple domain-wall movements. The experimental value of the ratio of rotational hysteresis and alternating hysteresis losses is about 2:1 for the (100) plane and [100] direction, except for high and low degrees of saturation, but it is 8:1 for the other two planes and directions.

(6) In 1974, Narita and Yamaguchi [130] measured rotational hysteresis loss on small disks of approximately 4% silicon iron single crystal with (001) surfaces, and explained the results on the basis of the changes in domain structure observed under a rotating magnetic field. It was confirmed that in the high magnetisation region a considerable part of the loss could be attributed to the energy dissipation which takes place at the time of the annihilation of domain walls. The rapid fall of the rotational hysteresis loss near saturation magnetisation was explained in terms of the decrease of the surface energy of domain walls. The loss measurements were carried out on a composite specimen consisting of three identical disks using a torque magnetometer proposed by Brailsford [125]. The domain structure was observed by the Bitter technique.

(7) In 1978, Grimwood, Cambell, and Evetts [132] studied the rotational hysteresis at very low rotational speeds in nearly isotropic polycrystalline materials. Measurements were made on disk shaped samples of pure iron, 1.2% carbon steel and mild steel. The results were explained in terms of two models, one appropriate to low fields, below the maximum in the rotational loss curve, and the other to the high field region. At low fields the losses are due to domain wall motion, and the model predicted that the ratio of rotational loss to alternating loss was $\pi/\sqrt{2}$. At high fields the loss was thought to be due to a mechanism not present in alternating fields. This is the unstable rotation of the magnetisation in each grain past its direction of difficult magnetisation.

Their observation that the ratio between the rotational and alternating hysteresis losses is $\pi/\sqrt{2}$ at low fields appears to be consistent with the experimental results observed by Boon and Thompson [127], but not with the experimental results reported by Baily [120]. The experimental value of 2:1 reported by Boon and Thompson was measured in the (100) plane and [100] direction of a single crystal sample where exists only two easy axis and a medium axis. In a practical silicon steel sheet, the iron crystals are randomly distributed, and the actual ratio could possibly be a little higher due to the existence of the hard axis of magnetisation. The experimental results reported by Baily [120] in Fig.4-25, however, shows that the ratio

between the rotational and alternating hysteresis losses is smaller than 2:1 for both hard steel and soft iron at low fields. This may suggest that the ratio of rotational hysteresis loss to alternating hysteresis loss at low fields is material dependent.

(8) In 1988, Fiorillo and Reitto [147] measured rotational hysteresis loss of soft iron laminations in a very large induction range using the fixed samples described in section 4.2.3.1. The ratio between the rotational hysteresis loss P_{rh} and the corresponding alternating hysteresis loss P_{ah}, measured in soft iron, exhibited a monotonic dependence on magnetic flux density and attained a maximum value $P_{rh}/P_{ah} \leq 4$ at about $B=10^{-4}$ T.

(9) In 1990, Fiorillo and Reitto [184] explained the rotational hysteresis loss with the domain theory, and it was concluded that the ratio of rotational and alternating hysteresis losses was between 1 and 2 at intermediate flux densities, say ≤1.5 T, in non-oriented SiFe laminations.

(10) In 1991, Radley [162] performed dynamic domain observations and domain wall velocity measurements on disk samples of grain oriented SiFe sheets subject to rotating magnetic flux at 0.2 Hz by the Kerr effect. Domain photographs at several points in the cycle were included in the paper. These images implied that the flux took selective routes through a polycrystalline material, and these routes were at the scale of grains rather than individual domains. High velocity of domain wall movement was observed. It was suggested that this could be the dominant mechanism for rotational core loss, with contributions also from bar wall motion.

4.4.2 Total Rotational Loss (Hysteresis + Eddy Current)

(1) In 1961, Kaplan [136] measured core losses of grain oriented (M-7) and non-grain oriented (M-19) silicon iron using cross samples under various flux conditions ranging from a pure alternating flux (only the magnitude of flux varies with time) to a pure rotating flux (only the direction of flux varies with time) with a magnetic probe [210], in which the Rogowski-Chattock coils and B tips were exploited, as shown in Fig.4-28. The field metric method type one was used, and it was found that the grain oriented iron was still the lower loss material under all flux conditions. This is not always true. As will be further discussed later in chapter 5, the rotational core loss in grain oriented steel sheets can be higher than that in non-oriented steel sheets, since grain oriented steel sheets have stronger magnetic anisotropy due to the textures, which causes higher hysteresis loss.

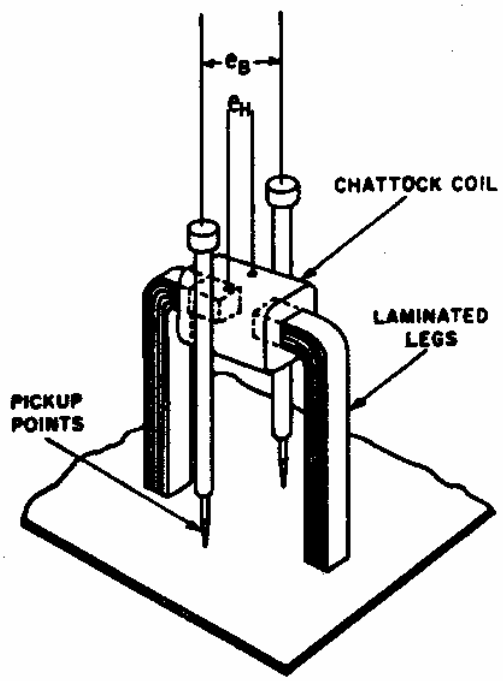

Fig.4-28 Magnetic probe developed by Tompkins, Stauffer, and Kaplan (from [210])

(2) In 1962, Strattant and Young [137] studied the power frequency losses in silicon iron alloys due to an elliptically rotating magnetic field with disk samples placed in the centre of two perpendicular pairs of rectangular Helmholtz-type air-cored coils, and predicted the losses approximately using a simple model

$$P = P_{hyst} + P_{eddy} \tag{4.18}$$

$$P_{hyst} = P_1\left[\frac{B_1}{B_s}-\left(\frac{B_1}{B_s}\right)^2\right] + P_2\left[\frac{B_2}{B_s}-\left(\frac{B_2}{B_s}\right)^2\right] \tag{4.19}$$

and

$$P_{eddy} = P_3\left[\left(\frac{B_1}{B_s}\right)^2+\left(\frac{B_2}{B_s}\right)^2\right] \tag{4.20}$$

where B_1 and B_2 are the major and minor axis flux densities, B_s is the saturation flux density, P_1 and P_2 are the alternating hysteresis losses in the major and minor axes for peak flux densities of B_s, respectively, and P_3 is the eddy current loss for a peak flux density of B_s.

As indicated in the paper, this model only simulates the core loss with elliptically rotating magnetic fields, while the basic physical phenomena were not described. The calculated losses

were compared to the measured losses for the (100) plane single crystal material as shown in Fig.4-29. Although there are sizeable differences in the calculated and measured losses, especially for circular fields, the general field dependence is similar.

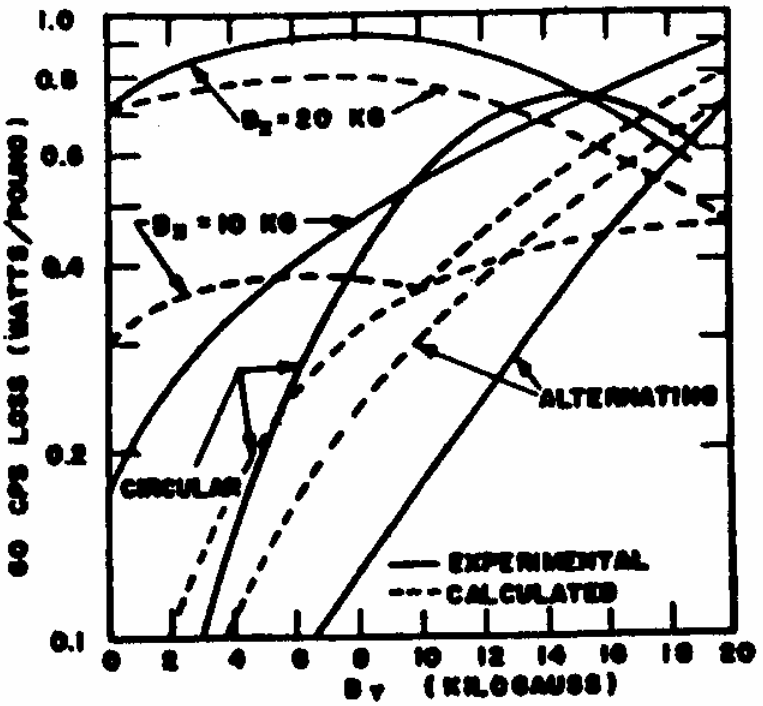

Fig.4-29 Comparison of experimental data and losses calculated using the proposed model for (100) plane single-crystal 0.0075 inch thick material. The parameters used for the calculation are $P_1=P_2=0.48$ W/lb, $P_3=0.22$ W/lb, and $B_S=20$ kGauss, (from [137])

(3) In 1965, Boon and Thompson [138] measured alternating and rotational core losses at 50 Hz under various flux densities for hot-rolled and cold rolled 3% silicon iron in a square sample of 0.013 inch laminations, using an improved thermometric method, and found that the ratio of rotational loss to alternating loss at 50 Hz in four-square silicon iron was about 2:1 over a wide range of flux densities (except at a high flux density), as illustrated in Fig.4-30.

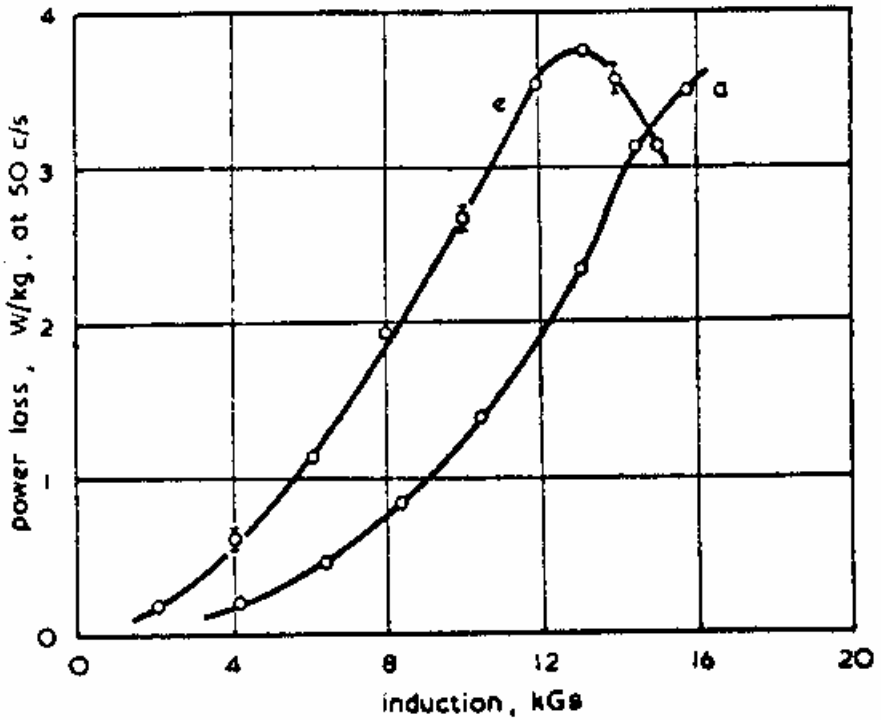

Fig.4-30 Rotational and alternating core losses in 0.013 inch hot-rolled 3% silicon iron sheet at 50 Hz, a ---- alternating, and e ---- rotational. (from [138])

(4) In 1973, Moses and Thomas [181] studied the localised power loss in the T-joints of three phase transformers. The power loss was measured by 220 miniature thermocouples placed 1.5 cm apart in arrays, and the flux density by an array of 600 search coils threaded through small holes on the laminations. Rotational flux was found in those T-joints, and it caused areas of high localised loss. A combination of normal flux between adjacent layers of laminations, rotating flux, and circulating third-harmonic fluxes caused the localised loss to rise to double the average core loss in some regions of the T-joints.

(5) In 1974, Phillips and Overshott [183] measured core losses of individual grains in polycrystalline specimens of commercial 3% grain oriented silicon iron under longitudinal and transverse AC magnetisation and rotational flux conditions, and observed the corresponding domain configurations using a stroboscopic Kerr magnetic-optic apparatus. The effect of longitudinal stress and dc bias fields on the domain patterns and core loss under these AC magnetisation conditions was also investigated. It was concluded that the highest core loss occurred under pure rotational flux conditions and that the application of longitudinal compressive stress increased the core loss, but to a lesser extent when a transverse AC flux was present. The application of a longitudinal dc field increased the core loss for all AC magnetising conditions, and it was observed that a longitudinal tensile stress had the opposite effect on the domain configuration to the application of a transverse dc field.

(6) In 1978, Basak and Moses [141] investigated the stress sensitivity of rotational power loss in silicon iron, using cross samples, and made the following discoveries: The loss increases with tensile stress applied parallel to the rolling direction and decreases with compression. The opposite occurs when the stress is applied perpendicular to the rolling direction. Increasing the frequency causes the loss to rise drastically and also increases its stress sensitivity. It was also proved theoretically that the angle of lag of the flux density behind the applied field increases with stress and varies during the magnetising cycle.

(7) In 1978, Cecchitti, Ferrari, Masoli, and Soardo [131] measured rotational power loss per cycle P_r/f as a function of rotational frequency f, between about 0 and 25 Hz, on grain oriented and non-oriented 3% SiFe, under different magnetisation conditions, up to almost complete saturation, using disk samples. Maximum losses were found to occur for a relative magnetisation M/M_S, which is of the order of 0.8 for all rotational frequencies. The results showed that the behaviour of P_r/f vs. f was characterised by large excess anomalous loss with respect to classical eddy current loss, except for M/M_S close to 1.0. On the other hand, the nonlinear anomalous loss, typical of alternating loss curves, was absent since the rotational core losses per cycle were found to increase linearly with f for all M/M_S values.

(8) In 1985, Tan, Datta, Flanders, and Graham, Jr. [134] determined the rotational core losses in several thin gauge ferromagnetic materials as a function of frequency and magnetisation, using a Hall effect probe rotating disk sample magnetometer developed by Flanders [133]. The results, as illustrated in Fig.4-31, showed that the rotational core losses in Fe-based amorphous alloys are at least a factor of ten lower than non-oriented SiFe at very low frequencies. Furthermore, the rotational core loss in the thin high resistivity amorphous alloy is independent of frequency up to their measurement limit of 80 Hz, while SiFe alloys show a significant increase in loss with increasing frequency. The rotational core loss in planar oriented 6.5% SiFe is less than half of that in the best non-oriented 3% SiFe.

(9) In 1988, Fiorillo and Reitto [147] measured rotational losses of soft Fe, 3% non-oriented SiFe and 3% grain oriented SiFe in a very large induction range using the fixed samples described in section 4.2.3.1. The measurements of total rotational core loss at 50 Hz (Fig.4-12) showed that the total rotational core loss in 3% grain oriented silicon iron was higher than that in 3% non-oriented silicon iron.

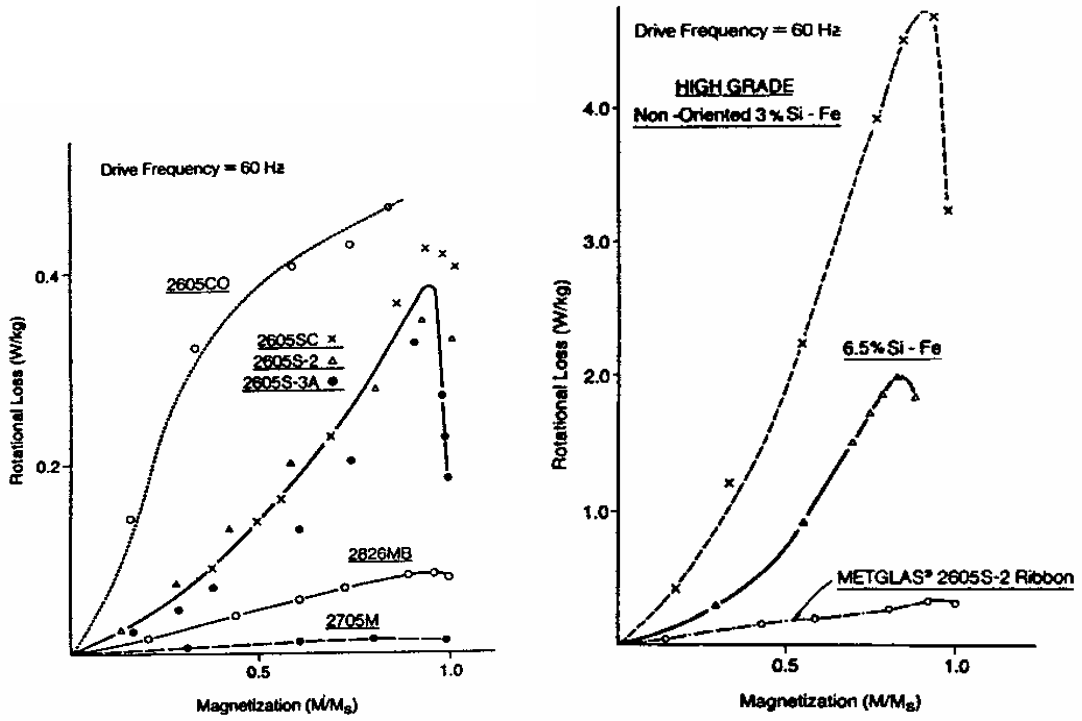

Fig.4-31 Rotational core losses measured by rotating sample magnetometer (from [134])
(a) rotational core loss for various METGLAS® Alloys, and
(b) comparison of rotational core loss of METGLAS® Alloy 2605S-2 to those of SiFe.

(10) In 1990, Enokizono, Suzuki, Shirakawa, Sievert, and Xu [151,155,157] measured rotational core losses in non-oriented and grain oriented steel sheets using the system described in section 4.2.3.3. They defined (4.15) as the rotational loss P_r, while taking (4.13) as total loss P_t. According to their measurements, in circularly rotating magnetic flux, $P_t = P_r$ for both grain oriented and non-oriented electrical steel sheets, while in elliptically rotating magnetic flux, $P_t \geq P_r$ for non-oriented materials, and $P_t \leq P_r$ for grain oriented materials, as shown in Fig.4-32. But the reason for this phenomenon was unknown. (This is questionable. Theoretically speaking, the rotational loss is just a component of the total loss, and hence, it should never exceeds the total loss.) It was also found that P_r reached minimum values when the major axis of an elliptically rotating magnetic flux was applied to 45° from the rolling direction in non-oriented electrical steel sheets.

(11) In 1990, Fiorillo and Rietto [168,179,184] reported the experimental results of rotational core loss in 3.2% non-oriented SiFe at different magnetisation frequencies up to 50 Hz, as depicted in Fig.4-33, measured by their tester using fixed disk samples. By plotting the losses against frequency (Fig.4-34), it was shown that the rotational core loss could also be separated into rotational hysteresis, classical eddy current, and anomalous losses, similar to the case of alternating core loss.

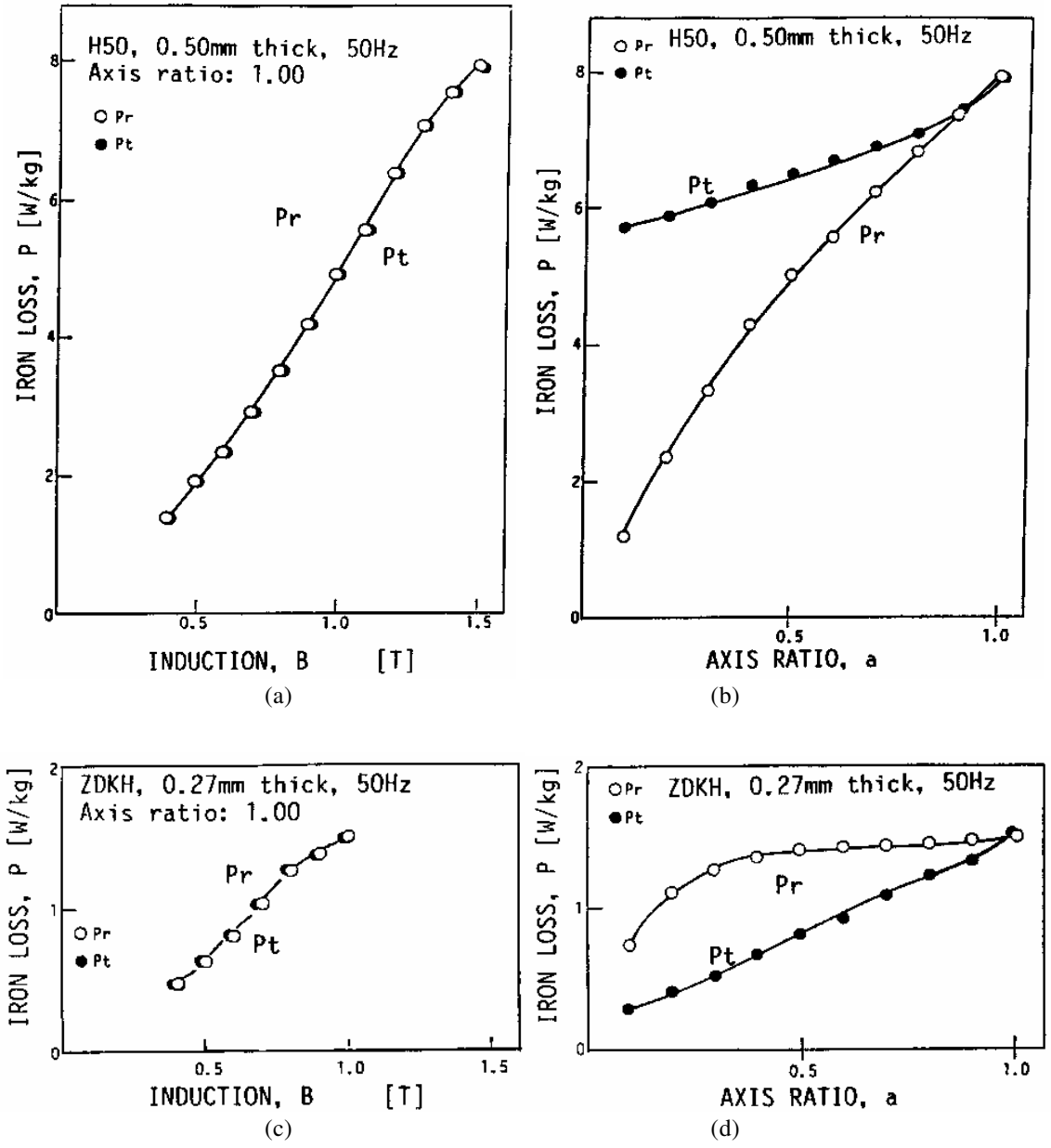

Fig.4-32 Specific total core loss P_t and specific rotational core loss P_r in grain oriented (ZDKH, 0.27 mm thick) and non-oriented (H50, 0.50 mm thick) electrical steel sheets with purely circular and elliptical magnetic fluxes at 50 Hz.
(a) P_t and P_r in non-oriented sheet with circular flux,
(b) P_t and P_r in non-oriented sheet with elliptical flux, the major axis (B_{max}=1.5T) on the X axis (rolling direction),
(c) P_t and P_r in grain-oriented sheet with circular flux, and
(d) P_t and P_r in grain-oriented sheet with elliptical flux, the major axis (B_{max}=1.0T) on the X axis (rolling direction). (from [151])

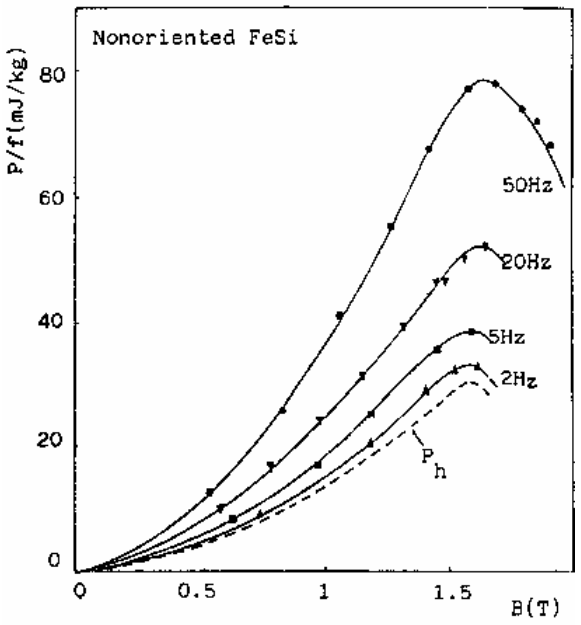

Fig.4-33 Specific rotational core loss per cycle vs. peak flux density in a 3.2% SiFe non-oriented sheet, 0.637 mm thick, at different frequencies. Ph is the rotational hysteresis loss obtained by extrapolating the specific rotational core loss vs. frequency curves to zero frequency (Fig.4-34). (from [168])

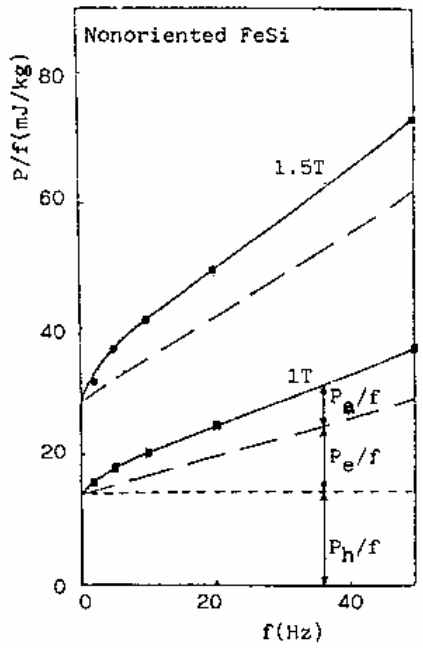

Fig.4-34 Specific rotational core loss vs. frequency in a 3.2% non-oriented sheet at 1T and 1.5T. P_h is the rotational hysteresis, P_e the eddy current, and P_a the anomalous losses. (from [168])

A phenomenological approach to the rotational anomalous loss P_a was proposed in [179] as following

$$P_{ar} = C_{ar} (f B)^{3/2} \tag{4.21}$$

where C_{ar} is the anomalous loss coefficient, f the magnetisation frequency, and B the magnitude of flux density. This formula is essentially the same as the one for alternating anomalous loss described in chapter 3, except that the rotational anomalous loss coefficient C_{ar} is a function of flux density B, while the one for alternating anomalous loss is a constant, and it was also agreed by Dr. Fiorillo that C_{ar} would eventually drop to zero when the material was saturated and all domains disappeared [219].

(12) In 1991, Kedous-Lebouc, Zouzou, and Brissonneau [163,178] measured the magnetic properties of cubic textured NiFe using a square sample under alternating and rotational magnetic fields at 50 Hz. The experimental results of alternating and rotational core losses are illustrated in Fig.4-35. It was realised that the rotational core loss would decrease to the value of classical eddy current loss when the sample was saturated.

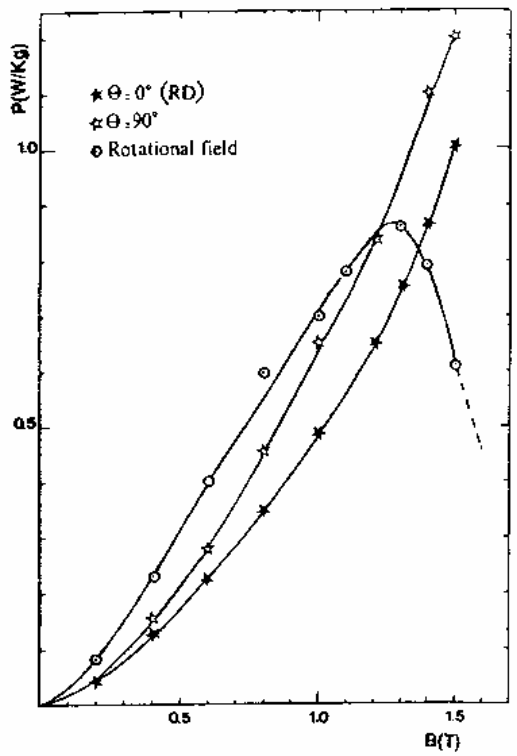

Fig.4-35 Alternating and rotational core losses of NiFe (from [178])

(13) In 1992, Salz and Hempel [172] measured various magnetic properties, including magnetic polarisation, permeability, and core losses, of the (100) [001] textured steels T1-50 (nominal thickness 0.5 mm) and T1-65 (nominal thickness 0.65 mm) under rotational and alternating magnetic field excitations at various frequencies, using the square specimen core loss tester described in section 4.2.3.3. It was concluded that the rotational hysteresis loss was independent of the sample thickness, while the rotational eddy current loss increased with the sample thickness.

4.5 MODELLING OF CORE LOSSES IN ROTATING MACHINES

Although it has long been realised that a considerable amount of the total core loss in the stator core of a rotating electrical machine is caused by the rotating magnetic field, alternating core loss models were generally employed [188-191] due to the lack of a model and data for rotational core losses.

In 1991, Bertotti *et al* [192] calculated the core loss of an induction motor with a three term model developed by Fiorillo and Rietto [168,179,184], which consisted of rotational hysteresis, classical eddy current, and anomalous losses, as described in section 4.4.2. For rotational hysteresis loss with an elliptically rotating magnetic flux, a linear interpolation between purely circular and alternating core losses was used. Due to various reasons, however, the calculated core losses were about 20% lower than the measured.

In 1992, Atallah, Zhu, and Howe [193,194] predicted the core loss of two permanent magnet brushless dc motors of different types of laminations under different operating modes with the three term model for alternating core losses proposed by Bertotti [97] and Fiorillo [99], but the rotational effects were not included. Instead, the core bss was calculated from the loss deduced for each of the two equivalent orthogonal alternating flux density components. The finite element method was adopted to obtain the loci of rotating flux density vectors. Unfortunately, the theoretical results were not compared with measurements, and the accuracy of prediction was not reported.

Also in 1992, Zhu, Ramsden, and Watterson [195] calculated the core loss of a permanent magnet motor using the finite element method and the three term model. The loss terms for classical eddy current and anomalous losses were modified to include the rotational effects, but owing to the lack of rotational hysteresis loss data of the material, the alternating hysteresis was calculated. The calculated results were about 15% lower than the measured. In 1993, the

model was improved by including the rotational hysteresis loss, and the discrepancy was reduced to less than 10% [196].

4.6 CONCLUSION

The computer controlled square sample testing system appears to be the most advantageous in all aspects among the rotational core loss measuring systems available, and the horizontal yokes are superior to vertical yokes due to easier construction, and better performance.

The field-metric method has higher accuracy, contains more information, and gives greater versatility than the other methods for rotational core loss evaluation, but equation (4.15) requires to be further clarified since it yields contradictory results in the case of elliptical magnetic flux excitation.

Although quite a few rotational core loss measurements and domain structure observations have been carried out on various ferromagnetic materials, the mechanisms of rotational core loss are still far from being fully understood.

Because of the very complicated mechanisms, it is not practical to develop a model of strong physical background at the current stage. On the other hand, a phenomenological approach, such as the three term model generalised by Fiorillo from the corresponding alternating core loss model, appears to be useful for core loss analysis in rotating electrical machines.

Similar to the case of alternating core loss, the total rotational core loss can generally be separated into three components: rotational hysteresis, eddy current, and anomalous losses. The ratio of rotational hysteresis loss to alternating hysteresis loss at low fields veries from one to two for different materials as reported by various researchers. With a circular field, the rotational eddy current loss is twice as much as alternating eddy current loss. The rotational anomalous loss can be modelled using the same formula as for alternating anomalous loss, but the coefficient of rotational anomalous loss is generally a function of flux density, and eventually reduces to zero when the material is saturated and all domain walls disappear.

CHAPTER 5. ROTATIONAL CORE LOSS MEASUREMENT

5.1 INTRODUCTION

This chapter deals with the development of rotational core loss measuring system and the measurement of rotational core loss in electrical sheet steels, whilst the modelling problem is left for chapter 6.

As discussed in chapter 4, the rotational core loss tester using a single sheet square specimen is very flexible and suitable for measurements under various complex magnetic flux conditions. Hence, an apparatus using square specimens was designed, and constructed at the Commonwealth Scientific and Industrial Research Organisation (CSIRO), Division of Applied Physics, Lindfield. The whole system was finally installed and calibrated at the School of Electrical Engineering, University of Technology, Sydney (UTS).

The design and construction of the measuring system, including the system outline, tester structure, feedback control, and the digital signal processing system for the specification of flux density waveforms (function generation) and the data acquisition, is presented in section 5.2. A novel sandwich arrangement of magnetic field strength **H** sensing coils was used to improve the accuracy of measurement.

For high precision and more information, the field-metric method was adopted to evaluate the core losses from the measured magnetic field strength and flux density. The total core loss P_t was derived from Poynting's theorem, and the rotational core loss P_r was obtained by calculating the torque on the magnetic dipoles in the specimen. The derivation showed that (4.15) for calculating P_r was incorrect for measurements with magnetic fluxes other than purely circular rotating flux. Core losses in a square specimen of 0.35 mm electrical steel sheet Lycore-130 (a non-oriented silicon iron with alternating core loss of 1.30 W/kg at 1.0 T, 50 Hz, chosen for its applications in rotational machines, which is our main field of interest) were measured with purely circular and elliptically rotating magnetic fluxes over a range of excitation frequencies from 1 to 200 Hz. The measured results are illustrated and discussed in section 5.3.

From December 8, 1993 to February 24, 1994, the author was invited to visit the Physikalisch-Technische Bundesanstalt (PTB), Braunschweig, Germany, as a guest scientist for a bilateral cooperative research project on rotational core loss measurement, which was funded by PTB and the Department of Industry, Technology and Regional Development

(DITARD), Australia. As part of the project, it was agreed to carry out an inter-comparison between the testers at PTB and UTS. This comparison will follow all the regulations used in the European Inter-Comparison of Rotational Core Loss Measurements, which is currently organised by PTB. The rotational core losses in four specimens of grain oriented (ORSI-100) and non-oriented (V270-35A) electrical steel sheets (part of the specimen set used for the European inter-comparison) will be used and compared. Core losses of these specimens have been measured with various magnetic flux patterns using the tester at PTB, and will be reported in section 5.4. Because of insufficient time, however, measurements using the tester at UTS have not been completed for this thesis.

In section 5.5, discussions are given on the effects of material texture and crystal anisotropy, and the clarification of the relationship between P_t and P_r. A possible explanation of P_r is presented.

5.2 DEVELOPMENT OF A ROTATIONAL CORE LOSS MEASURING SYSTEM USING A SQUARE SPECIMEN

5.2.1 Outline of the System

The core loss was measured by the field-metric method with an apparatus capable of generating arbitrary two dimensional magnetic flux patterns. Fig.5-1 is a photograph of the testing system, and Fig.5-2 illustrates the system schematically.

Fig.5-1 A photograph of the rotational core loss measuring system developed at UTS

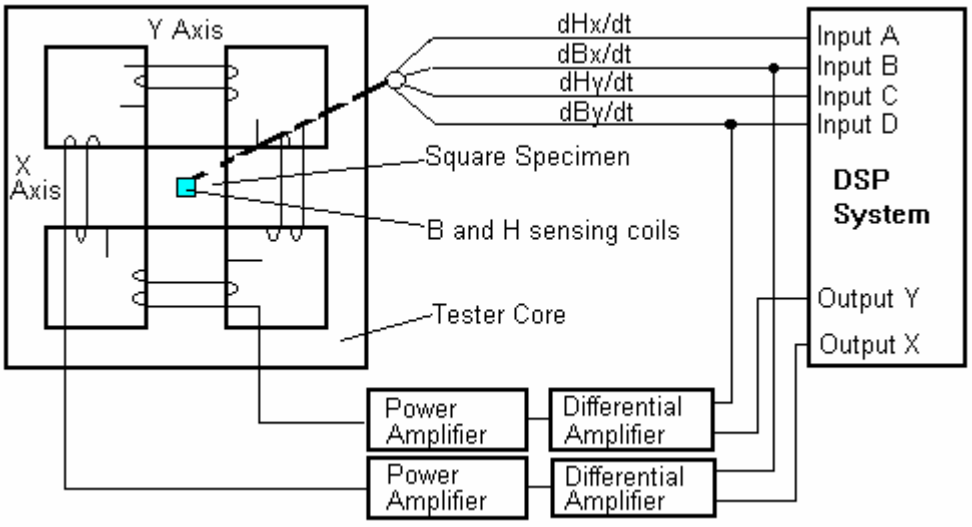

Fig.5-2 Schematic diagram of the square specimen testing system developed at UTS

The magnetic field is generated by two groups of excitation coils arranged on the X and Y axes, respectively. The excitation voltages and currents are supplied by two identical power amplifiers. By controlling the waveforms, magnitudes, and phase angles of the excitation voltages on the X and Y axes, any complex one or two dimensional magnetic flux density vector, such as an alternating magnetic flux density inclined at a specified angle from the X or Y axis, a purely circular or elliptically rotating magnetic flux density, and a rotating magnetic flux density of any specified locus, can be generated. Two specially designed differential amplifiers were used in the feedback control of the magnetic flux density components on the X and Y axes.

An IBM/PC-386 based digital signal processing (DSP) system was used for both function generation and data acquisition. This DSP system is a commercial system, AMLAB, supplied by an Australian company, Associative Measurement Pty. Ltd, Specified voltage waveforms for the X and Y components of magnetic flux density were generated by the software, and exported through two isolated channels of analog output (X and Y). Voltage signals from the sensing coils of magnetic field strength and flux density on the X and Y axes were collected by four independent input channels (A, B, C, and D) with high precision preamplifiers, and recorded into an ASCII data file. The software project for both function generation and data acquisition was written by the author in a graphic form and compiled by the graphic compiler provided together with the hardware by the manufacturer.

The recorded data was then processed by a C code for calculating rotational core losses, plotting the component waveforms and loci of **B** and **H** vectors, and other analyses for better understanding and modelling.

5.2.2 Square Specimen Tester (SST)

Fig.5-3(a) is a photograph of the square specimen tester, and Fig.5-3(b) a drawing of the assembly, while the dimensions of the yoke and the specimen are illustrated in Fig.5-3(c). The horizontal yoke arrangement was employed. For high precision measurement, the power loss in the yoke and the excitation poles should be kept as low as possible, and hence, low core loss ORIENTCORE.HI-B, grade M-0H grain oriented silicon steel sheet [213] manufactured by Nippon Steel Corporation, Japan, was chosen as the yoke material. The yoke laminations were arranged vertically and the magnetisation poles were shaped in wedges, since this type of structure, according to the analysis by Enokizono and Sievert [154], gave better results in **H** measurement, as discussed in section 4.2.3.3.

Four excitation coils were placed on the magnetisation poles, and every two on the same coordinate axis were connected in series to contribute aiding magnetomotive forces. Each coil was wound with 300 turns of 1.6 mm enamel insulated copper wire.

The size of the specimen was chosen as 50×50 mm^2 according to the possible minimum width of electrical steel sheets to be measured, which was found to be 50 mm for MetGlas 2605S-2, an amorphous material.

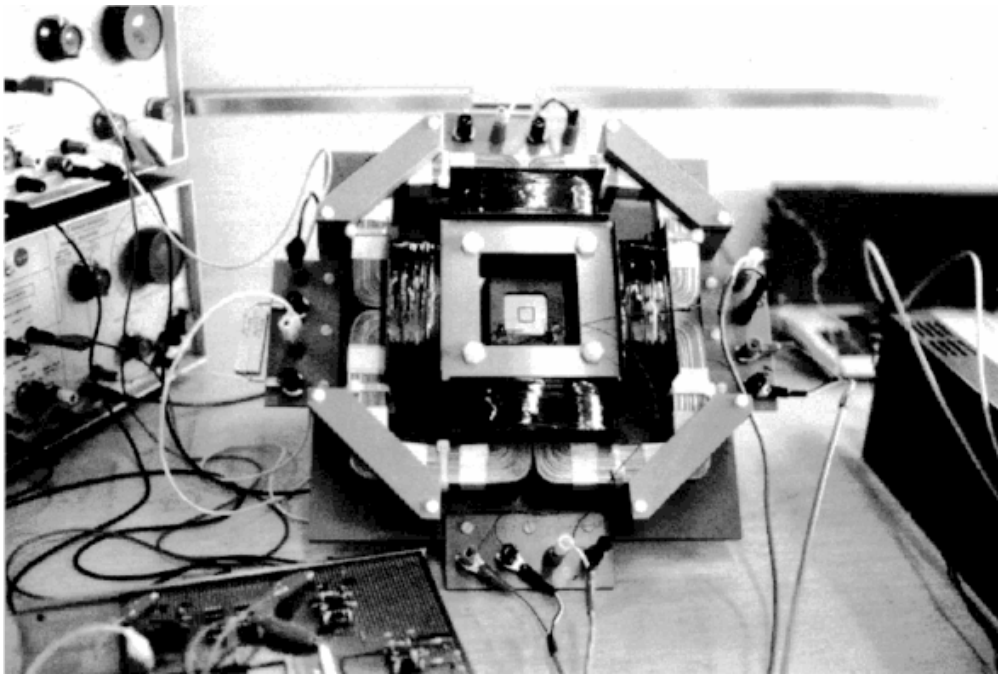

(a)

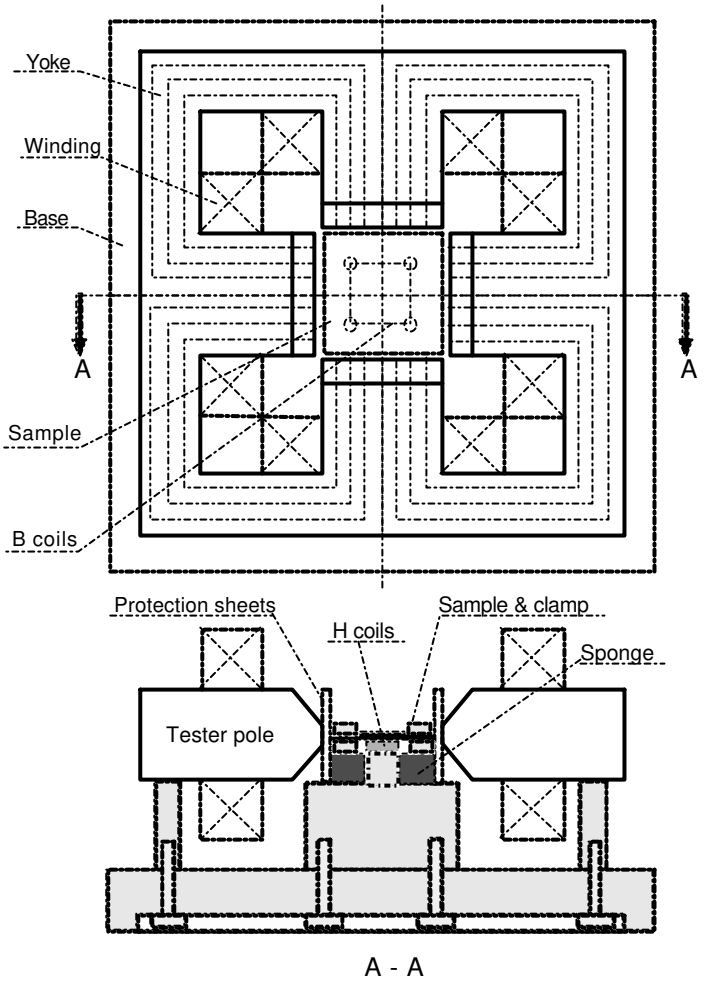

(b)

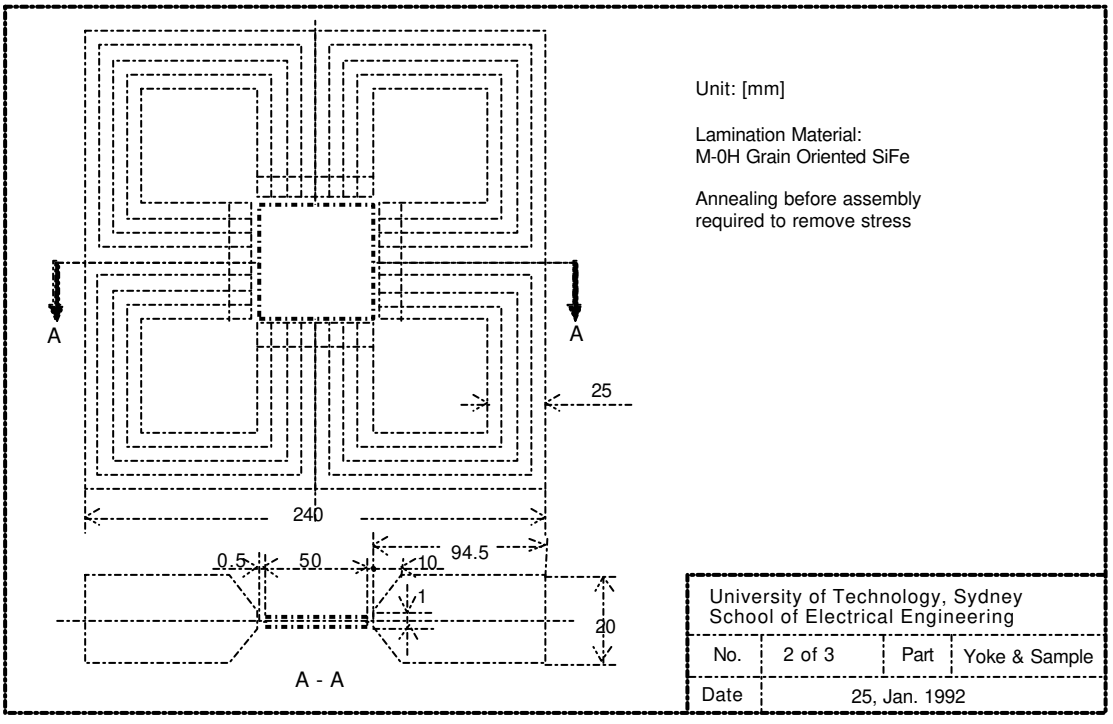

(c)

Fig.5-3 Square specimen tester (a) photograph, (b) assembly, and (c) dimensions of yoke and specimen

The magnetic circuit design and the calculation of temperature rise in the excitation coils, the yokes, and the poles, are given in Appendix B. An equivalent heat transfer network was employed for thermal modelling.

Fig.5-4 illustrates the magnetic field distributions in the middle area of the tester, measured with and without a specimen when the X axis was excited. It can be seen that the field in the centre area of the specimen is close to uniform (±5%).

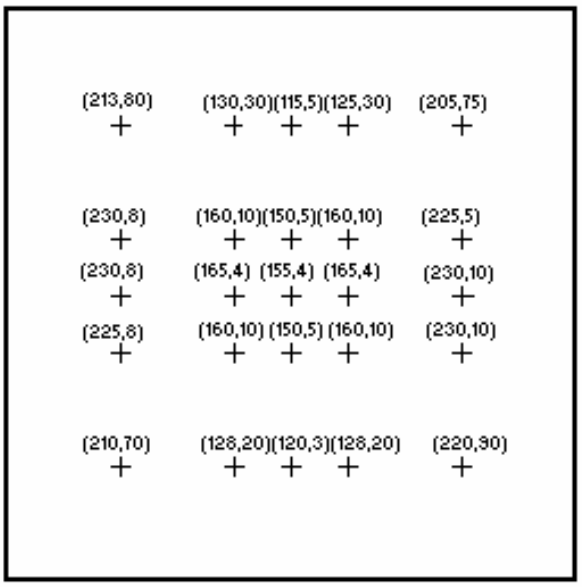

Note:
1. Two exciting coils on X axis are in series.
   Terminal Voltage V = 50 [V]
   Current I = 2 [A]
   Frequency f = 50 [Hz]
2. At each point +, the flux density is expressed as (Bx, By) [Gs].
3. The Gauss meter used in the measurement is Bell 610 Gauss meter.
4. The measured area is the middle of the SST without specimen.

(a)

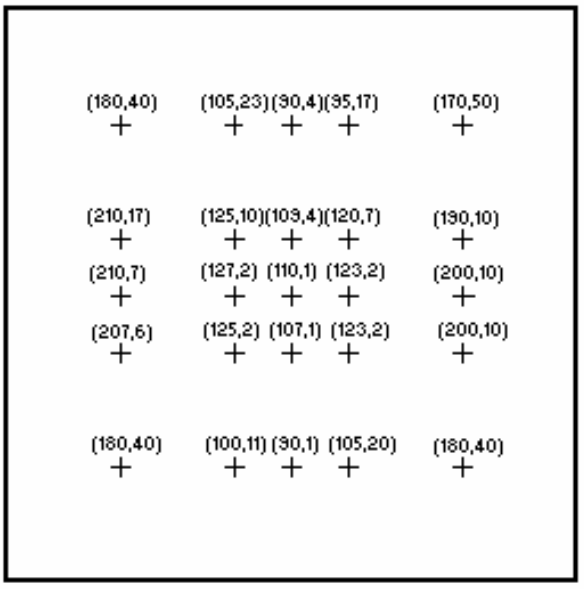

Note:
1. Two exciting coils on X axis are in series.
   Terminal Voltage V = 53 [V]
   Current I = 2 [A]
   Frequency f = 50 [Hz]
2. At each point +, the flux density is expressed as (Bx, By) [Gs].
3. The Gauss meter used in the measurement is Bell 610 Gauss meter.
4. The measured area is the middle of the SST 3 mm above the surface of the specimen Lycore-130, 0.35 mm thick.

(b)

Fig.5-4 Field distribution in the middle of SST (a) without, and (b) with a specimen

5.2.3 Measurement of Two Dimensional Magnetic Field Strength and Flux Density

5.2.3.1 Sensors for Measuring Magnetic Field and Flux Density

As discussed in section 4.2.1, both sensing coil method and Hall element method can be used to measure magnetic field strength **H**. In a single sheet tester, sensing coils are generally preferred for surface magnetic field strength, because their response is linear, and they may be mounted very close to the surface of the specimen.

For the measurement of magnetic flux density **B**, two methods can be used. In one method, a sensing coil is wound through tiny holes in the specimen. This method gives very accurate results, but winding a coil through tiny holes in the specimen is tedious, especially when a batch of specimens is to be measured in a short time. Moreover, the tiny holes also affect the distribution of the magnetic field in the specimen. Another method for flux density measurement is to use B tips, which pick up the induced electromotive force on the specimen surface. This method is especially suitable for batch measurements, but is limited to thin sheets of conducting materials. The sensitivity of this method is also lower than that of sensing coils.

In our rotational core loss tester, sensing coils were used to measure magnetic field strength and magnetic flux density components on both the X and Y axes. Fig.5-5(a) illustrates the two dimensional magnetic field sensing coils used in the tester. The conventional surface **H** sensing coils were wound with 130 turns on each axis of 0.08 mm enamel insulated copper wire on a 1.0 mm plastic former. The sandwich **H** sensing coils, which will be described later in section 5.2.3.3, were wound with 1000 turns on each axis of 0.02 mm enamel insulated copper wire on a 0.35 mm thick plastic former, and then sealed in a plastic container. The total thickness of the sandwich H coils is about 1.2 mm. Fig.5-5(b) shows the magnetic flux density sensing coils. Each coil was threaded with 20 turns of 0.02 mm enamel insulated copper wire through small holes of 1.0 mm diameter. The two coils on each axis were connected in series, and the terminals were twisted to exclude stray magnetic flux. Fig.5-5(c) shows the conventional surface arrangement of **H** sensing coils, and Fig.5-5(d) the new sandwich arrangement of **H** sensing coils.

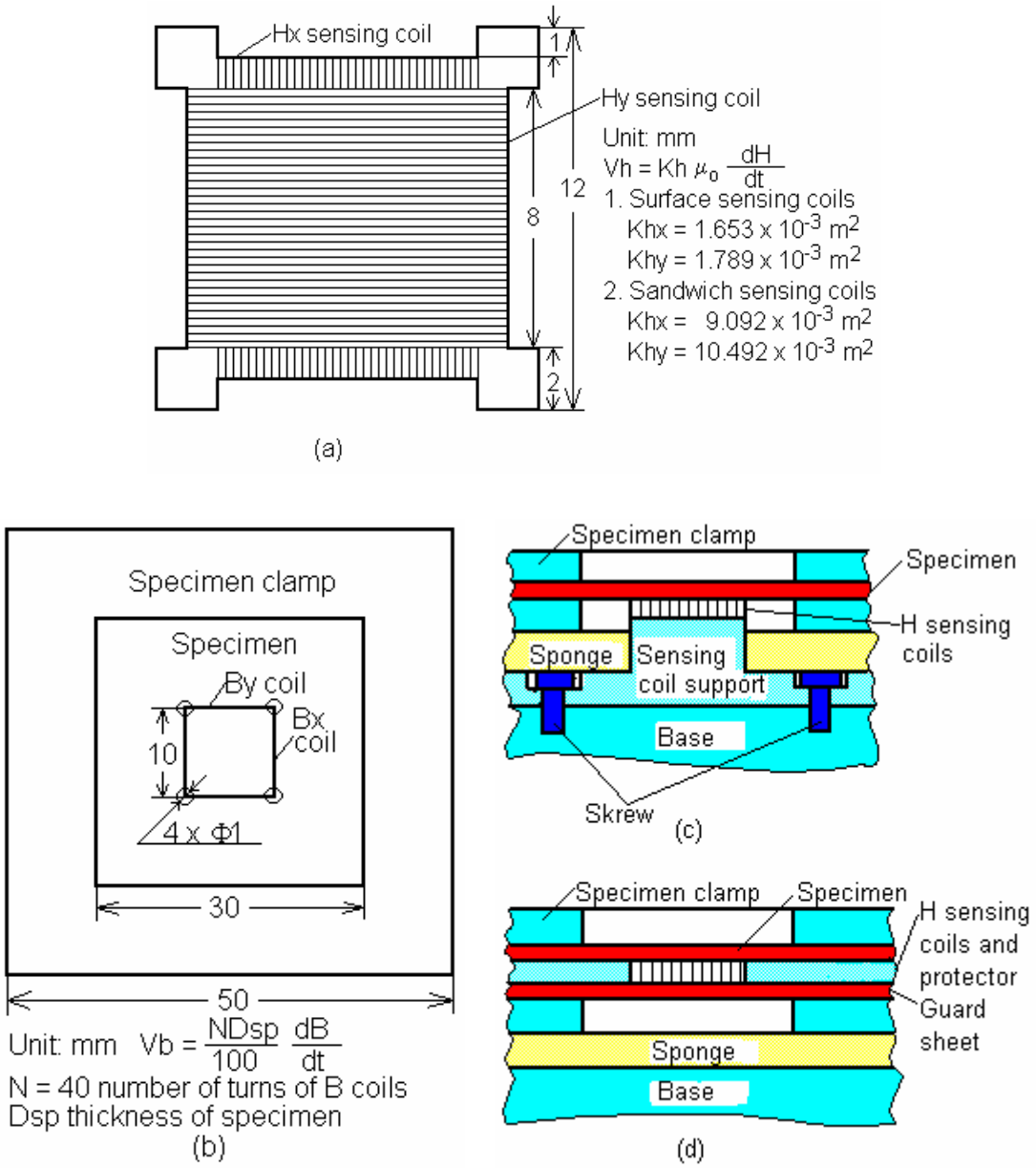

Fig.5-5 (a) Structure of **H** sensing coils,
(b) Structure of **B** sensing coils and specimen clamp,
(c) Conventional surface arrangement of **H** sensing coils, and
(d) New sandwich arrangement of **H** sensing coils.

The components of magnetic field strength **H** and flux density **B** on each coordinate axis can be calculated from the induced emf of the sensing coils by

$$B_i = \frac{1}{K_{Bi}} \int V_{Bi} dt \qquad (i=x,y) \qquad (5.1)$$

and

$$H_i = \frac{1}{\mu_0 K_{Hi}} \int V_{Hi} dt \qquad (i=x,y) \qquad (5.2)$$

where $K_{Bi} = N_{Bi}D_{sp}d_i$ is the **B** sensing coil coefficient, N_{Bi} the number of turns of the **B** sensing coil, D_{sp} the thickness of the specimen, d_i the distance between two holes, K_{Hi} the **H** sensing coil coefficient obtained by calibration, and V_{Bi} and V_{Hi} are terminal voltages of the **B** and **H** sensing coils.

5.2.3.2 Calibration of Magnetic Field Sensing Coils

The magnetic field sensing coils were calibrated in a solenoid as shown in Fig.5-6. The coils were mounted in the middle of the solenoid, where the magnetic field was uniform. The magnetic field strength was double checked by measuring both the excitation current and the magnetic flux density. By adjusting the orientation of the coil under calibration for the maximum induced emf, the coil coefficient is determined by

$$K_H = \frac{V_H}{\sqrt{2}\pi f \mu_o H_m} \tag{5.3}$$

where V_H is the rms value of the sensing coil terminal voltage when the coil axis is aligned with the field, f the frequency of excitation current, and H_m the magnitude of the magnetic field strength in the centre of the solenoid.

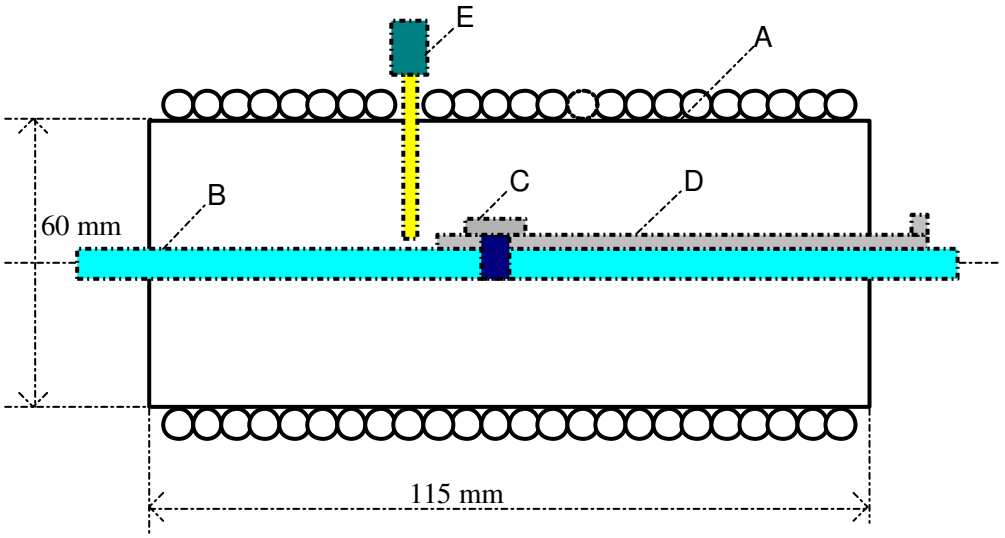

Solenoid: N = 281 (turns), and B/I = 0.002722 (T/A)

Fig.5-6 Solenoid for calibration of **H** sensing coils
A -- Solenoid
B -- Table supporting the sensing coils
C -- Sensing coils
D -- Handle for adjusting coil orientation
E -- Gaussmeter probe

The calibration results of the **H** sensing coils depicted in Fig.5-5 are listed in Table 5-1, where I is the rms value of the solenoid magnetisation current, B_I the rms value of the flux density in the centre of the solenoid calculated from the magnetisation current, B_{GM} the rms value of the flux density measured by a gaussmeter (Bell-610 with a Hall element probe), V_{Hx} and V_{Hy} are the rms values of the sensing coil terminal voltage measured by a digital millivoltmeter (SELFCAL-1271 made by DATRON INSTRUMENTS), and K_{Hx} and K_{Hy} are the coil coefficients of H_x and H_y sensing coils. The excitation frequency was 50 Hz.

Table 5-1. Calibration results of H sensing coils shown in Fig.5-5

(a) conventional surface $\mathbf{H_x}$ sensing coil

I (A)	**B_I (T)**	**B_{GM} (T)**	**H_m (A/m)**	**V_{Hx} (mV)**	**K_{Hx} (m^2)**
0.506	0.00138	0.00136	1530.538	0.716	0.001676
1.035	0.00282	0.00285	3207.377	1.457	0.001627
1.495	0.00407	0.00400	4501.582	2.091	0.001664
1.990	0.00542	0.00530	5964.596	2.783	0.001671
2.502	0.00681	0.00670	7540.149	3.476	0.001651
3.030	0.00825	0.00820	9228.242	4.200	0.001630
				Average K_{Hx}	0.001653

(b) conventional surface $\mathbf{H_y}$ sensing coil

I (A)	**B_I (T)**	**B_{GM} (T)**	**H_m (A/m)**	**V_{Hy} (mV)**	**K_{Hy} (m^2)**
0.501	0.00136	0.00135	1519.284	0.757	0.001785
1.019	0.00277	0.00280	3151.107	1.517	0.001725
1.506	0.00410	0.00400	4501.582	2.276	0.001811
2.001	0.00545	0.00530	5964.596	3.020	0.001814
2.505	0.00682	0.00680	7652.689	3.833	0.001794
3.070	0.00836	0.00830	9340.782	4.710	0.001806
				Average K_{Hy}	0.001789

(c) sandwich $\mathbf{H_x}$ sensing coil

I (A)	B_I (T)	B_{GM} (T)	H_m (A/m)	V_{Hx} (mV)	K_{Hx} (m^2)
0.504	0.00137	0.00136	1530.538	3.987	0.009332
1.010	0.00280	0.00280	3151.107	7.825	0.008896
1.502	0.00409	0.00400	4501.582	11.569	0.009206
2.008	0.00547	0.00540	6077.135	15.418	0.009088
2.508	0.00683	0.00675	7596.419	19.248	0.009077
3.008	0.00819	0.00820	9228.242	23.072	0.008956
				Average K_{Hx}	0.009092

(d) sandwich $\mathbf{H_y}$ sensing coil

I (A)	B_I (T)	B_{GM} (T)	H_m (A/m)	V_{Hy} (mV)	K_{Hy} (m^2)
0.510	0.00139	0.00137	1541.792	4.609	0.010709
1.030	0.00280	0.00282	3173.615	9.166	0.010346
1.501	0.00409	0.00400	4501.582	13.306	0.010589
2.020	0.00550	0.00540	6077.135	17.910	0.010557
2.515	0.00685	0.00680	7652.689	22.281	0.010430
3.004	0.00818	0.00820	9228.242	26.584	0.010319
				Average K_{Hy}	0.010492

5.2.3.3 Correction of Error due to Distance between H Sensing Coils and Specimen

At first, a conventional surface magnetic field sensing coil arrangement, as shown in Fig.5-5(c) was employed. It was found, however, that the measured value of magnetic field strength varied significantly with the distance between the specimen surface and the centre of the sensing coils, as observed by other researchers [149,154,211]. Only when this distance becomes very small, will the magnitude converge to the true value, but this distance is limited by the thickness of the coils.

This problem is mainly caused by the flux through the air near the specimen surfaces. Because of the small specimen size, the flux through the air is more than half of the total flux, as will be described in section 5.2.5.1 via the inductances with and without a specimen. If the specimen is large enough, as in the case of a single sheet tester for alternating core loss [121], this flux

through the air is negligible compared with the flux through the specimen, so that accurate field strength can be picked up by the surface field sensing coil. Unfortunately, this is not the case with rotational core loss testers.

As discussed in section 4.2.1 and 4.2.3, Enokizono and Sievert [154] reduced the error by using an optimum yoke structure, and Nakata [170] estimated the value of the surface magnetic field strength by extrapolating the measurements from the two H coil arrangement, whereas the Rogowski-Chattock coils were used by Salz and Hempel [211]. We used a novel sandwich sensing coil arrangement, as depicted in Fig.5-5(d). Fig.5-7 shows a photo of the **H** and **B** sensing coil assembly. The magnetic field sensing coils are sandwiched between the specimen and an identical guard sheet. With this structure, the effect of air flux is almost completely removed.

Fig.5-7 Photograph of magnetic field and flux density sensing coil assembly

Figs.5-8(a) and (b) illustrate the measured magnetic field strength and alternating specific core loss on the X axis (rolling direction) at different distances between the specimen surface and the sensing coil centre with and without the guard sheet. It can be seen that the sandwich arrangement yields less variation, although both results converge to the same value when the distance reduces to zero.

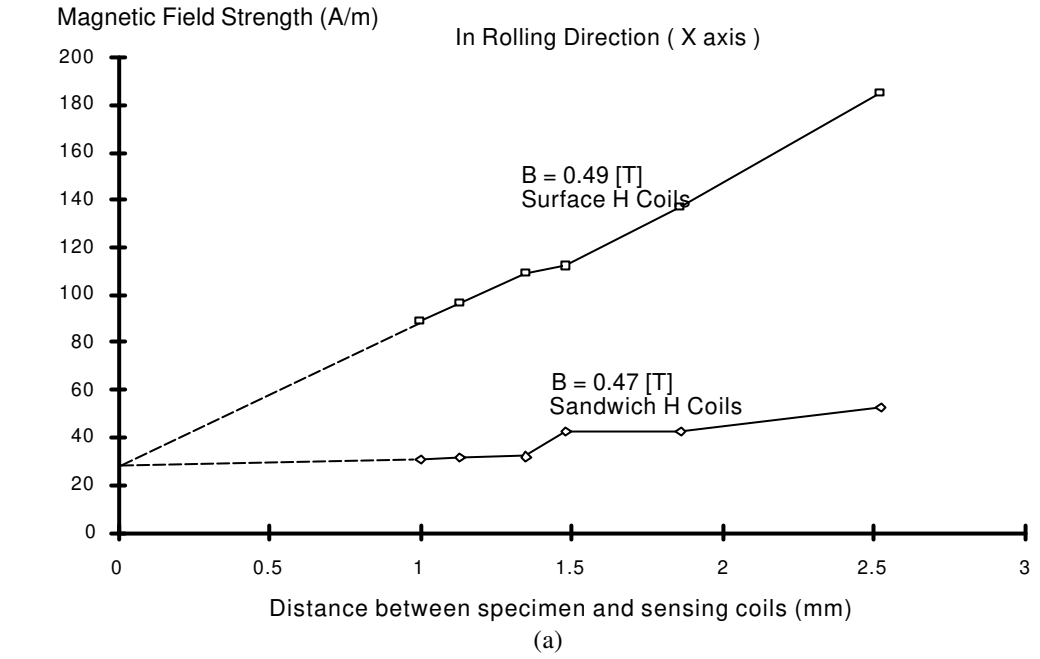

(a)

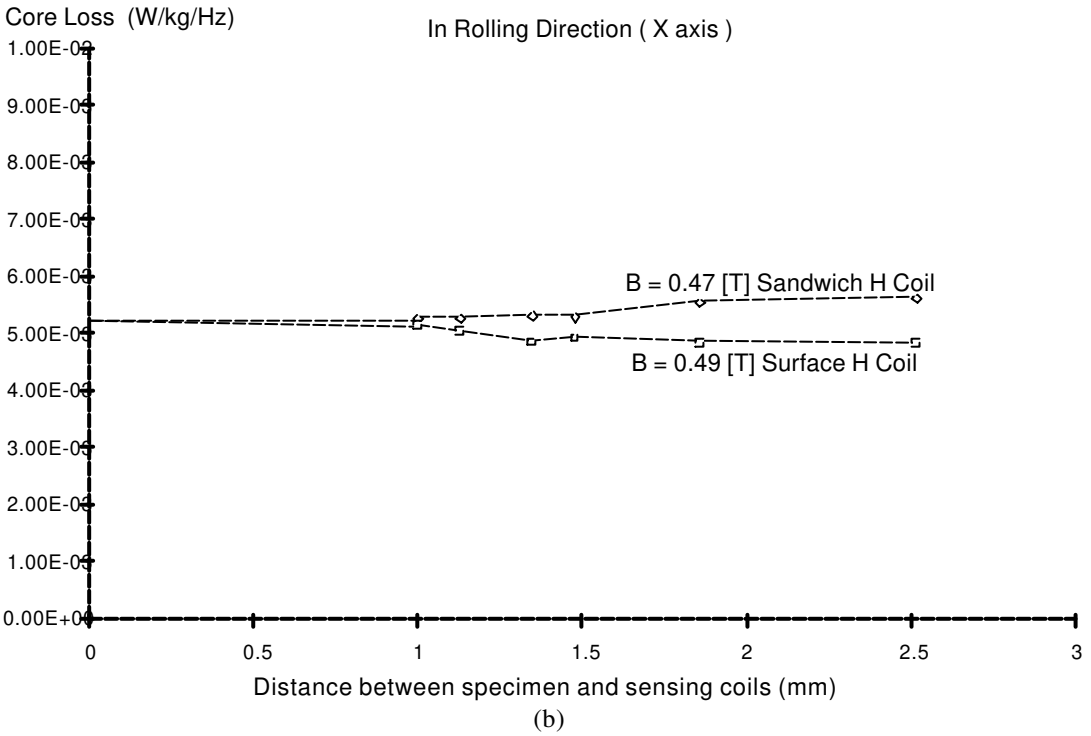

(b)

Fig.5-8 Variation of (a) magnetic field strength, and (b) alternating core loss with distance between specimen surface and coil centre

A comparison of B-H loops measured with an alternating magnetic field on a square specimen and on an annular ring specimen of 0.35 mm non-oriented electrical steel sheet Lycore-130 was made at 1 Hz and 40 Hz, as illustrated in Figs.5-9(a) and (b). Although this steel sheet is non-grain-oriented, the B-H loops on the rolling direction (X axis) and the transversal direction (Y axis) are different. Interestingly, the mean B-H loop, which was obtained by placing the

rolling directions of the specimen and the guard sheet perpendicular to each other, agrees with that measured on the annular ring specimen, as does the arithmetic mean of the B-H loops on the X and Y axes.

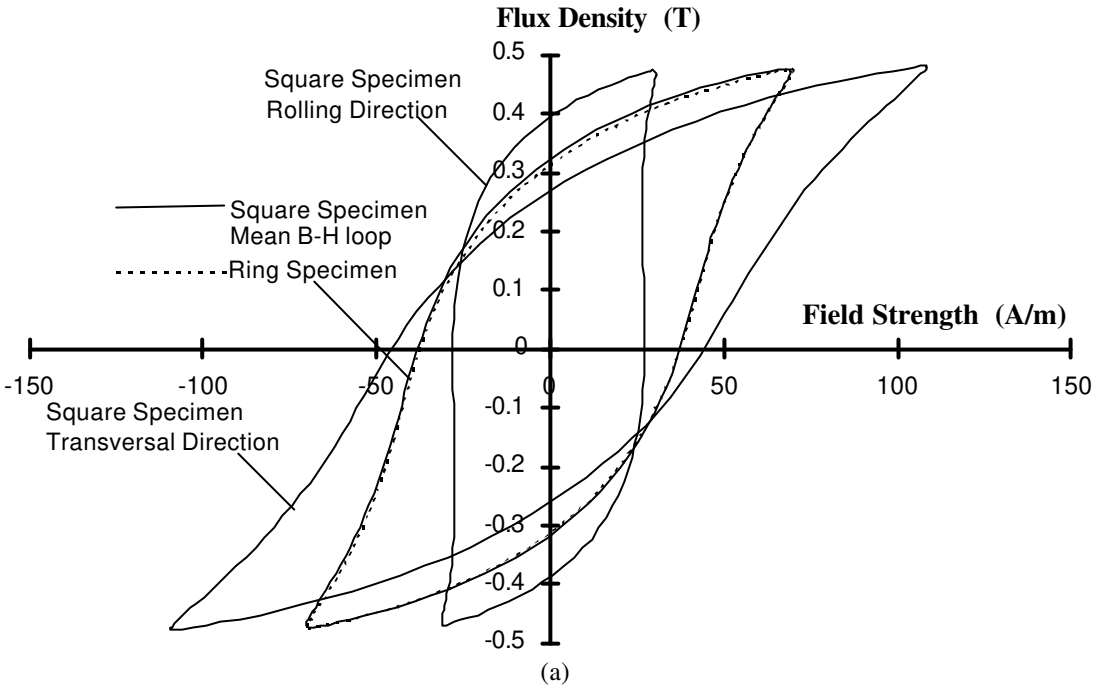

(a)

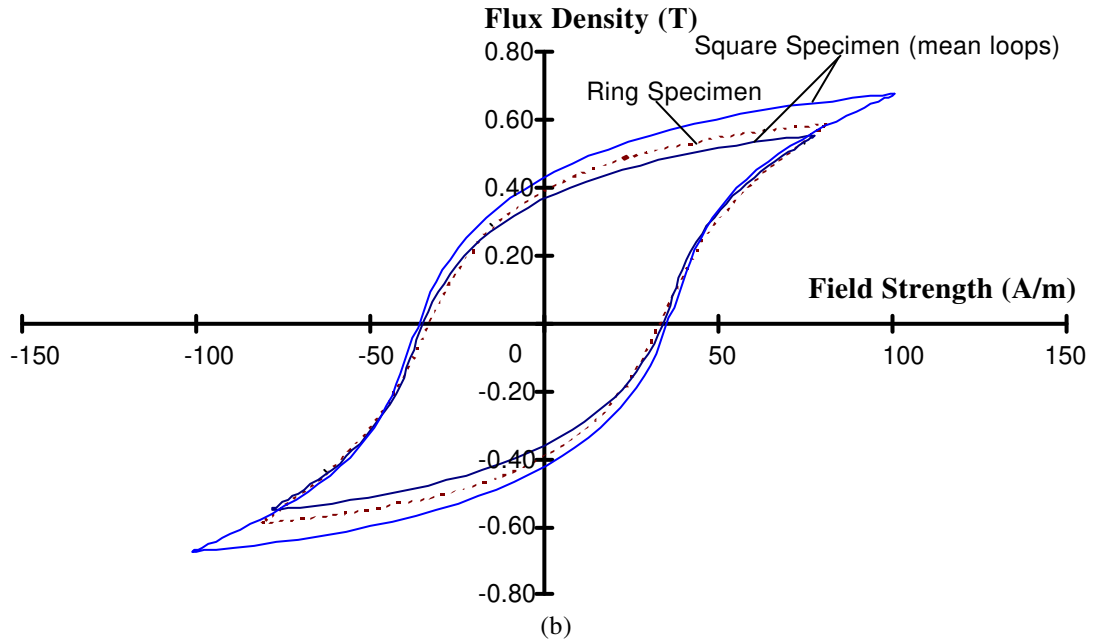

(b)

Fig.5-9 B-H loops of Lycore-130 measured on square and annular ring specimens at (a) 40 Hz, and (b) 1 Hz

5.2.3.4 Correction of Error due to Misalignment of Sensing Coils

If the axes of the sensing coils, either magnetic field or flux density, are possibly misaligned with the axes of excitation coils, the measured values will not be the true components on X and Y axes of the magnetic field or flux density. The error caused by this misalignment can be eliminated easily by a rotation of coordinate axes, by using the following transformation:

$$\begin{pmatrix} C_x \\ C_y \end{pmatrix} = \frac{1}{|\mathbf{C}|} \begin{pmatrix} \cos\alpha_y & -\sin\alpha_x \\ \sin\alpha_y & \cos\alpha_x \end{pmatrix} \begin{pmatrix} C_x' \\ C_y' \end{pmatrix} \tag{5.4}$$

where α_x and α_y are the angles of misalignment with the X and Y axes respectively, as shown in Fig.5-10(a), C_x and C_y are the true values of the X and Y components, C_x' and C_y' the measured values of the sensing coils, and $|\mathbf{C}| = \cos\alpha_x\cos\alpha_y+\sin\alpha_x\sin\alpha_y$. The angle α_x and α_y can be identified by a measurement of both sensing coils on the X and Y axes under one dimensional excitation. When only the X axis is excited, one has $C_y = 0$, and

$$A_x = \frac{C_x'}{C_y'} = \frac{\cos\alpha_x}{-\sin\alpha_y} \tag{5.5}$$

When only the Y axis is excited, $C_x = 0$, and

$$A_y = \frac{C_x'}{C_y'} = \frac{\sin\alpha_x}{\cos\alpha_y} \tag{5.6}$$

Solving (5.5) and (5.6) simultaneously, one obtains

$$\alpha_x = \arccos\left(\pm A_x \sqrt{\frac{1-A_y^2}{A_x^2 - A_y^2}} \right) \tag{5.7}$$

and

$$\alpha_y = \arccos\left(\frac{\sin\alpha_x}{A_y} \right) \tag{5.8}$$

Fig.5-10(b) illustrates the effect of this axis rotation on the results obtained by the sandwich field sensing coils when the X and the Y axes are excited separately, where the dotted lines and solid lines are the results before and after the rotation, $\alpha_x = -4.26^\circ$, and $\alpha_y = 8.29^\circ$. The results of the flux density sensing coils did not need to be corrected, because the angle of misalignment was very small.

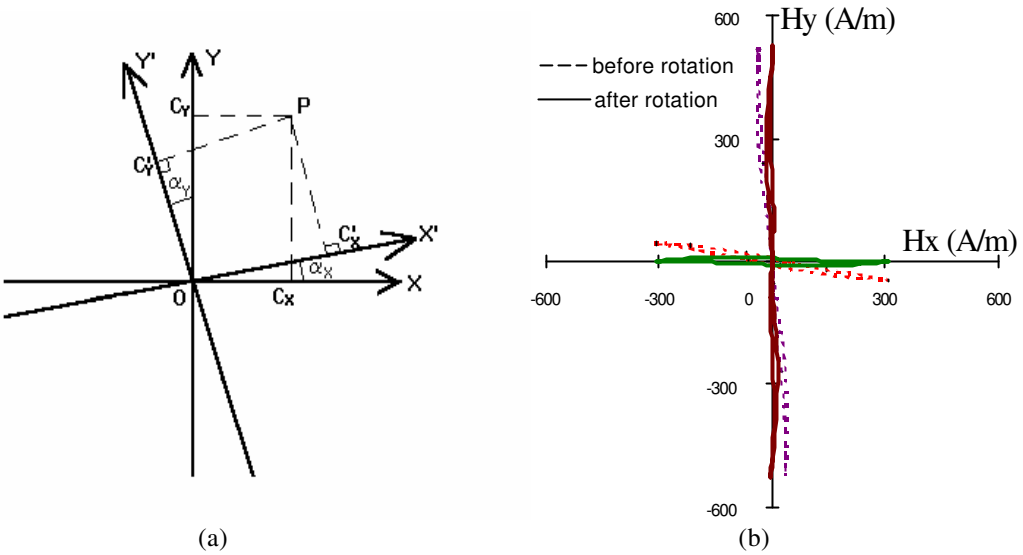

Fig.5-10 (a) Rotation of misaligned coordinate axis, and
(b) Effect of coordinate axis rotation on **H** coil results

For the same purpose, an average procedure, which averages the measurements with clockwise and anticlockwise rotating magnetic fluxes, was proposed by Sievert [152,166,174]. It was shown that the rotational loss defined in (4.15), when the angles of misalignment, α_x and α_y, were small, could be expressed approximately as

$$P_r = \frac{2\pi}{\rho_m T^2}\left[\int_0^T (H_x B_y - H_y B_x)dt \pm \alpha_x \int_0^T H_y B_y dt \pm \alpha_y \int_0^T H_x B_x dt\right] \qquad (5.9)$$

where the positive sign + stands for the measurement with anticlockwise rotating flux, and the negative sign - for the measurement with clockwise rotating flux. Obviously, only the first term, which is independent of the misalignment angles, in (5.9) remains, when the measurements with clockwise and anticlockwise rotating fluxes are averaged. Fig.5-11 illustrates the measurements with clockwise and anticlockwise rotating fluxes and the averaged results for various misalignment angles α_x of H_x coil, while H_y coil was aligned with the Y axis, i.e. α_y=0, when B=1 T at 50 Hz [154].

This method eliminates the error of rotational core loss caused by the possible small misalignment of sensing coils conveniently and effectively. Unfortunately, this method is limited to the measurement of core loss with a purely circular rotating flux density, since P_r calculated by (4.15) and hence (5.9) is incorrect for rotational loss with an elliptically rotating flux density, as pointed out by the author in [180] and will be further discussed in section 5.4, while the method of rotating the coordinate axes described above is not limited by the pattern of rotating

fluxes. Moreover, for large misalignment angles, (5.9) is no longer valid, since it is based on the assumption that $\sin\alpha \approx \alpha$, for a small α.

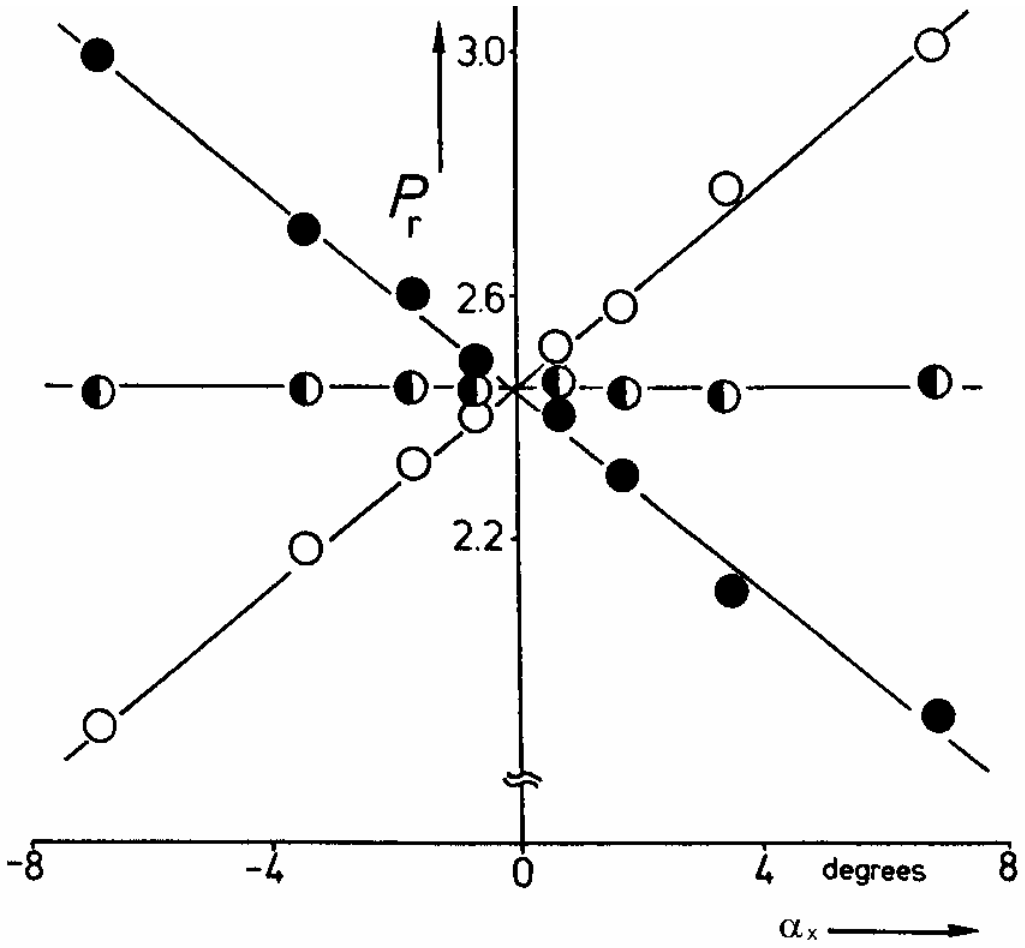

Fig.5-11 Rotational power loss Pr measured clockwise (○), anticlockwise (●), and averaged (◐), versus angular position α_x of the H_x sensing coil axis, the H_y coil being at the optimum angular position, at B=1 T, 50 Hz, with a non-oriented specimen (from [154])

5.2.4 DSP System

The DSP system (AMLAB) shown in Fig.5-2 is used for function generation and data acquisition. The hardware consists of four physical pieces: the analog module, the real time windows printed circuit board (PCB), and the master and slave PCBs [214], which fit into an IBM PC 386/486 as shown in Fig.5-12.

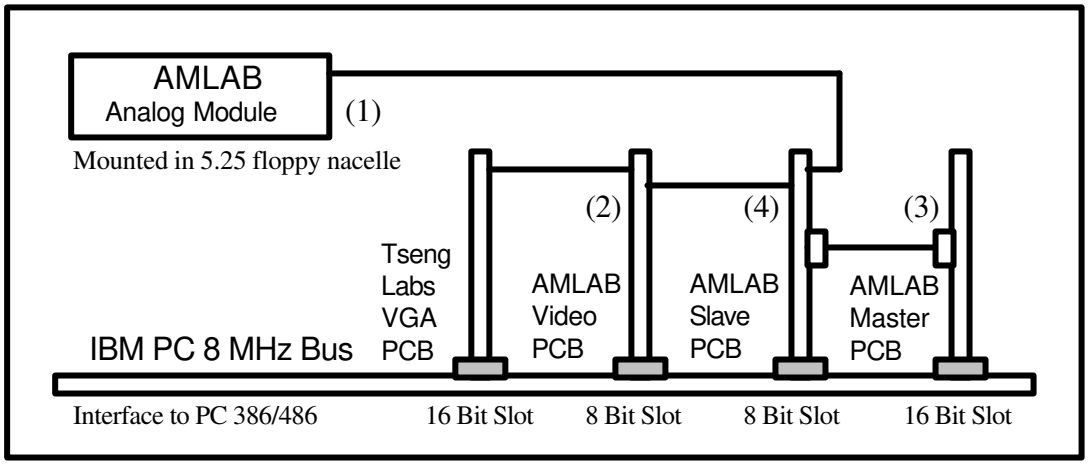

Fig.5-12 How AMLAB fits into an IBM PC 386/486

On each analog module, there are four isolated analog input channels, one general purpose input/output (GPIO) connector, and two analog output channels. Depending on the requirement, up to eight analog modules can be installed.

Each analog input channel has an input instrumentation amplifier of programmable 26-126dB gain (3 micro volts resolution at a signal to noise ratio of one), a programmable anti-alias filter, and an A/D converter of 12 bit resolution. The input signal range is ±500 mVDC or 330 mVAC. With the help of the voltage adaptor box supplied by the manufacturer, the input voltage range can be increased up to ±1000 VDC or 440 VAC. Each channel can be either AC or DC coupled with long AC coupling time constant (2 minutes) and has independent controls of AC or DC offsets which can be controlled from the user interface. The sampling rate can be 40 kHz per channel depending on the project processing load and the number of analog channels sampled. The inputs are isolated to 3.5 kV continuous to comply with IEC601-1.

Each analog output channel has a voltage output range of ±10 V and current capacity of ±100 mA, and can be used for strain gauge biasing (AC or DC driven), control outputs etc.

The digital GPIO connector consists of eight bits of ground referenced digital input (TTL signal level) provided to allow binary sense switches, such as input to rate meters, comparators or other functions to be used as part of a project, four connections for tape recorder inputs/outputs, eight bits of digital output for driving switches or relays or trigger stimuli etc., one frequency and event counter, and one 5 VDC reference with a nominal accuracy of ±5% and capable of supplying 100 mA for use as a strain gauge stimulus or for other applications that need a regulated voltage.

The AMLAB software is in three parts: the menu, the schematic, and the graphic compiler. The menus allow the user to call up AMLAB functions of two kinds - real time functions and replay functions. The real time functions are those associated with data acquisition, and the replay functions are those that provide a review of previously acquired data. The schematic is the heart of AMLAB in that it contains the information that tells AMLAB what to do, and is known as a project. The graphic compiler converts the menu choices into instructions and the schematic into a program controlled by those instructions. It checks the schematic for a wide range of possible errors and works out the order in which it has to carry out the program so as to minimise timing errors.

For function generation, the software provides icons of various voltage waveforms, such as sinusoidal, triangular, saw-tooth, and square, with adjustable frequency, magnitude and phase angle. Complex waveforms can be realised by combining several such icons with different harmonics. For very complicated waveforms, a special C program can be compiled and incorporated in the software project.

For data acquisition, it provides icons for the independent input channels of high precision pre-amplifiers with different modes of coupling and adjustable gains. AMLAB software also provides icons for digital signal processing, such as FFT, various kinds of filters, integrator, differentiator, etc.

In our rotational core loss measuring system, as illustrated in Fig.5-2, only two output channels for the X and Y axes flux density signal specifications, and four input channels for the X and Y components of the magnetic field strength and flux density were required. Therefore, only one analog module was used. Fig.5-13(a) shows the practical software project for rotational core loss measurement, and Fig.5-13(b) shows the waveforms and X-Y plots of voltage signals from **B** and **H** sensing coils.

The voltage signals of the **H** and **B** sensing coils were recorded into a comma separated data file by AMLAB, and further processed later for useful results, such as rotational core losses, loci of **B** and **H** vectors, and harmonics of the X and Y components of **H** and **B** etc., by a special program written in C. The results of measurement will be illustrated and discussed in section 5.3.

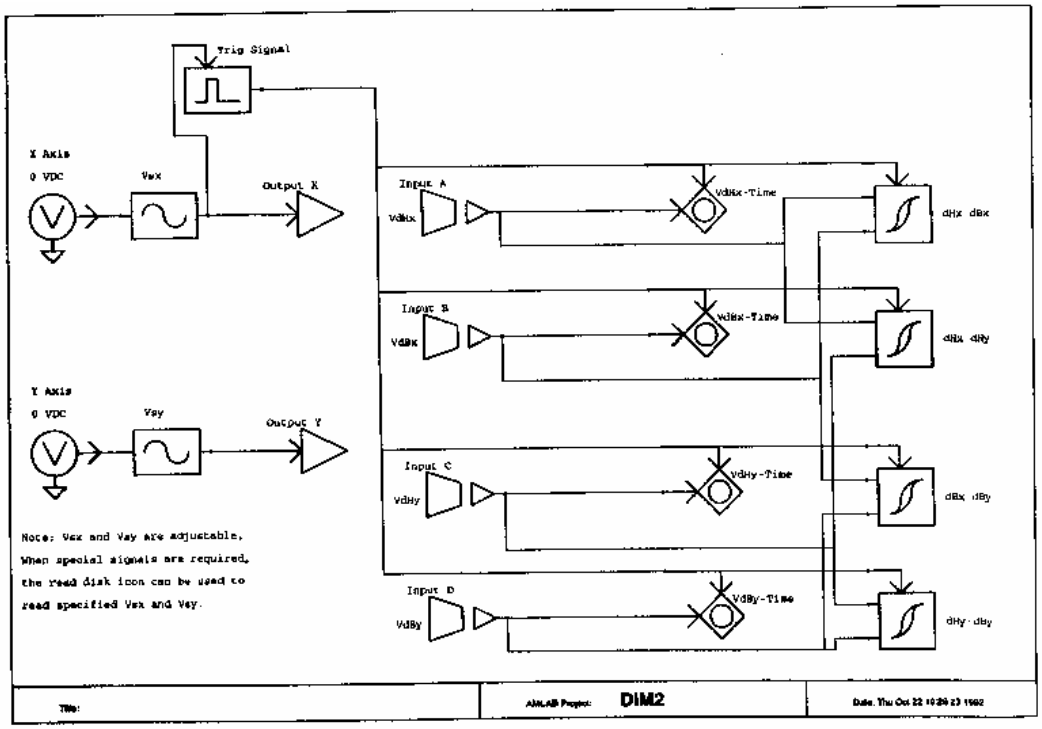

(a)

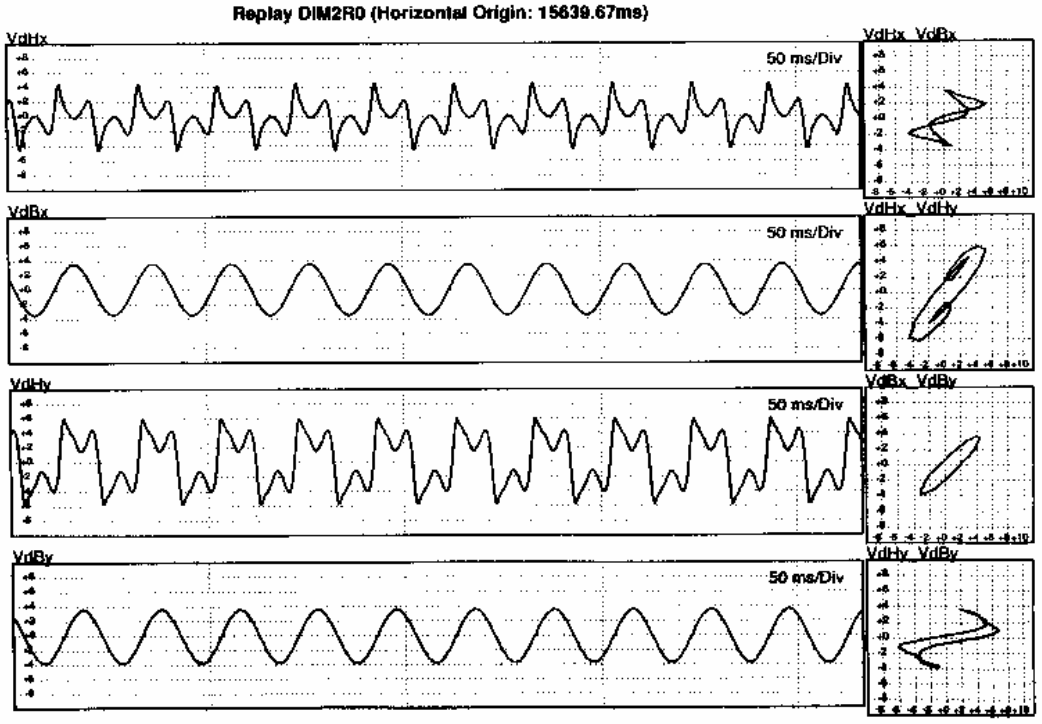

(b)

Fig.5-13 Application of an AMLAB DSP system in rotational core loss measurement,
(a) software project for rotational core loss measurement;
(b) waveforms and X-Y plots of voltage signals from **B** and **H** sensing coils, where
$V_{dHx} = A_{Hx}K_{Hx}\mu_o\frac{dH_x}{dt}$, $V_{dBx} = A_{Bx}K_{Bx}\frac{dB_x}{dt}$, $V_{dHy} = A_{Hy}K_{Hy}\mu_o\frac{dH_y}{dt}$, and $V_{dBy} = A_{By}K_{By}\frac{dB_y}{dt}$
are the voltage signals from Hx, Bx, Hy, and By sensing coils after pre-amplification, respectively, and A_{Hx}, A_{Bx}, A_{Hy}, and A_{By} are the gains of the corresponding pre-amplifiers.

5.2.5 Feedback Control of Flux Density Waveforms

5.2.5.1 System Model

Strictly speaking, the feedback control of magnetic flux density in SST under rotational magnetic field excitation is a problem of non-linear multi-variable control. But, the non-linear dependence of the magnetic flux density vector on the magnetic field strength vector in the specimen is not clear yet, when the field is rotating. Instead, the two components of magnetic flux density on the X and Y axes can be modelled and controlled independently; the effects of non-linearity and the interactions between the two components of magnetic field are considered as noise V_N to be depressed by the feedback, as shown in Fig.5-14.

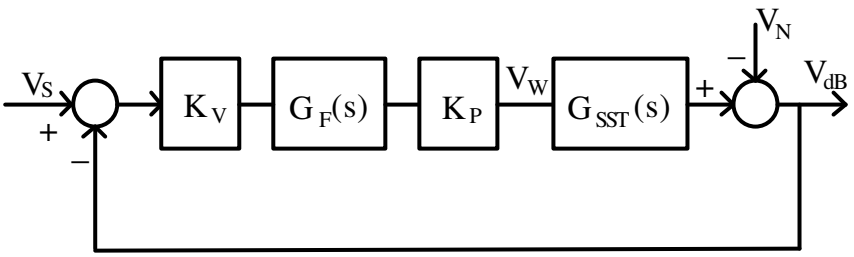

Fig.5-14 Block diagram of the system

K_V	Gain of voltage amplifier	V_S	Specified signal
K_P	Gain of power amplifier	V_W	Winding voltage of SST
$G_F(s)$	Transfer function of low pass filter	V_N	Noise due to non-linearity
$G_{SST}(s)$	Transfer function of SST	V_{dB}	Output signal of B coil

The feedback control system was designed to be able to control the flux density waveforms to a sinusoidal shape over a frequency range from 1 to 200 Hz. For measurements at higher frequency, the waveform distortion is not severe since the specimen is not saturated, and the waveform control is no longer of critical importance.

Fig.5-15 illustrates the SST on one axis, where $R=R_w+R_{ex}$, R_w is the winding resistance, R_{ex} the external resistance in series with the winding to reduce the low frequency drift of the power amplifier, N_w the number of turns of the excitation winding, and N_B the number of turns of the B sensing coil. The circuit equations are

$$v_w = Ri_w + \frac{d\lambda_w}{dt} = Ri_w + L_w\frac{di_w}{dt} \tag{5.10}$$

$$v_{dB} = N_B\frac{d\Phi_B}{dt} = N_BK_A\frac{d\Phi_S}{dt}$$

$$= \frac{N_B}{N_w}K_A\left(N_w\frac{d\Phi_w}{dt} - N_w\frac{d\Phi_a}{dt}\right) = K_NK_A(L_w - L_a)\frac{di_w}{dt} \tag{5.11}$$

where λ_w is the flux linkage of the excitation winding, $L_w = d\lambda_w/di_w$ the differential inductance of the winding, K_A is the ratio of the cross sectional area of B sensing coil to the cross sectional area of specimen, $K_N = N_B/N_w$, Φ_B is the magnetic flux linking the B sensing coil, Φ_s the magnetic flux passing through the cross section of the specimen, Φ_w the total magnetic flux generated by the excitation coils, Φ_a the magnetic flux passing through the air, and $L_a = N_w d\Phi_a/di_w$. L_w can be measured when the specimen is in the SST, while L_a can be measured approximately by taking out the specimen. By measuring the impedance at different exciting current ranging from 0.15 to 1.0 A at 50 Hz, it was determined that R_w = 1.65 Ohm, L_w = 0.12 ~ 0.11 H, and L_a = 0.086 H. From the definitions of L_w and L_a, it is understood that the magnetic flux passing through the air can account for more than half of the total magnetic flux generated by the excitation current. L_w is non-linear, but was assumed a constant, 0.12 H, in the numerical analysis. L_a is substantially a constant. The constants, K_N = 40/300 and K_A = 10/50, were determined from the dimensions of the SST and the specimen.

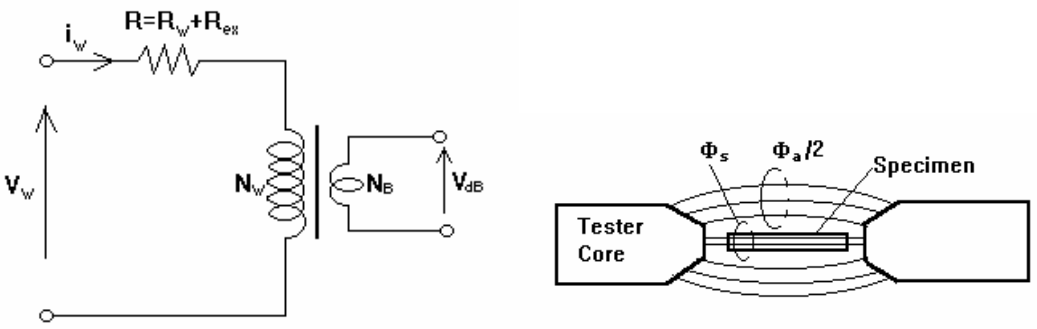

(a) (b)

Fig.5-15 SST on one axis, (a) circuit model, and (b) magnetic fluxes.

Applying the Laplace transform to (5.10) and (5.11) yields the transfer function of the SST,

$$G_{SST}(s) = K_N K_A \frac{L_w - L_a}{L_w} \frac{s}{s + R/L_w} \tag{5.12}$$

This is a first order system, and is unconditionally stable. To remove high frequency noise, a passive low pass filter with a corner frequency = 150 Hz is adopted. Hence, the open loop transfer function is

$$G_{OL}(s) = K_v K_p K_N K_A \frac{L_w - L_a}{L_w} \frac{s}{s + R/L_w} \frac{1/T_f}{s + 1/T_f} \tag{5.13}$$

where T_f is the time constant of the low pass filter. The closed loop transfer function for the specified signal V_s is

$$G_{CL}(s) = \frac{G_{OL}(s)}{1 + G_{OL}(s)} \tag{5.14}$$

The transfer function for the noise signal V_N, which represents the effects of non-linearity and interaction between two field components, is

$$G_N(s) = \frac{1}{1 + G_{OL}(s)} \tag{5.15}$$

5.2.5.2 System Responses in Frequency and Time Domains

The system responses in frequency and time domains were simulated with the linearised transfer function model, outlined by equations (5.13)-(5.15), using a MATLAB package. Fig.5-16 illustrates the open loop, and the closed loop frequency responses of the system to a specified signal V_s and to a noise signal V_N, respectively. The dotted lines in Fig.5-16 illustrate the frequency responses when $R_{ex} = 0$ and the low pass filter is absent, while the solid lines represent the frequency responses when $R_{ex} = 5$ Ohm and the filter is cascaded in the forward path. It is shown that increasing R_{ex} can effectively reduce the very low frequency drift, which is below 0.5 Hz and generated by the amplifiers in the forward path.

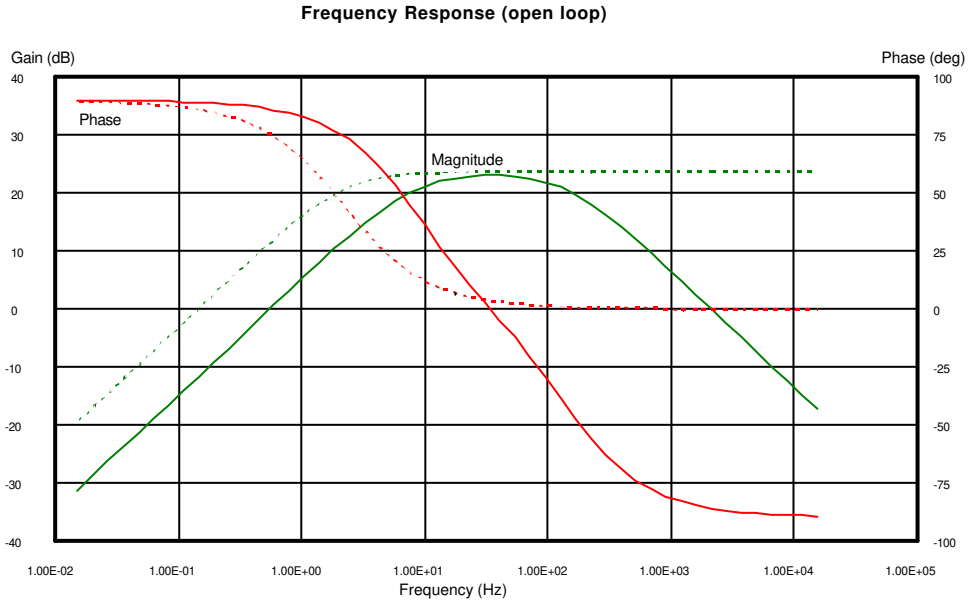

(a)

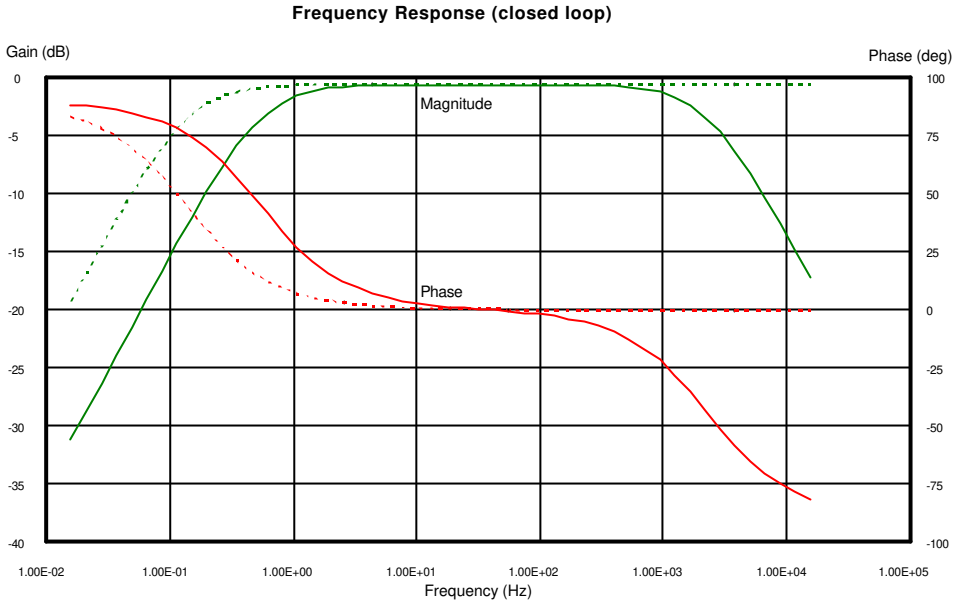

(b)

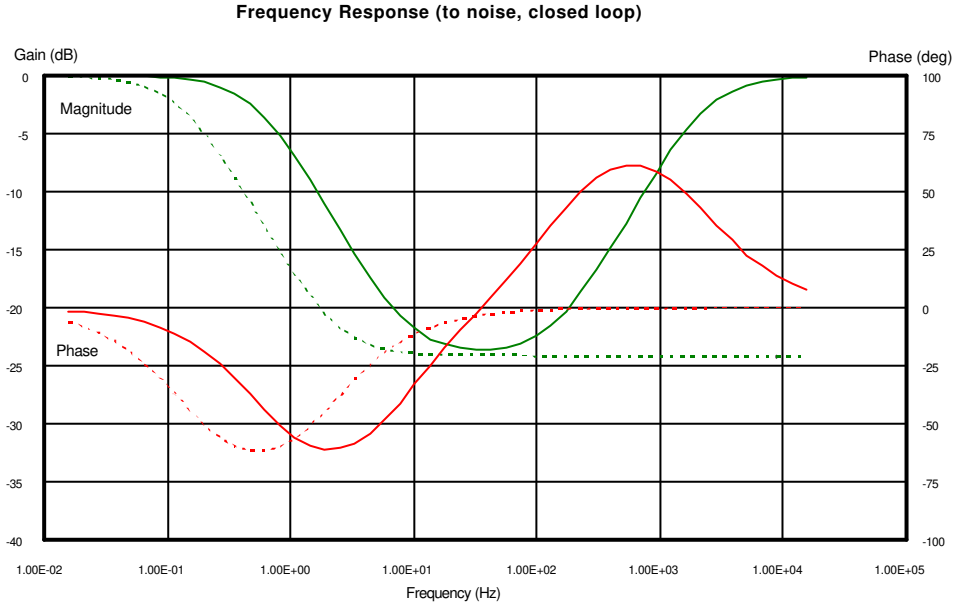

(c)

Fig.5-16 Frequency responses of the control system
(a) open loop response,
(b) closed loop response to specified signal V_S, and
(c) closed loop response to noise V_N

From the frequency responses, it can be seen that the system bandwidth is from 1 Hz to 1 kHz, which is good enough for measurements at frequencies from 1 to 200 Hz, while the noise due to the non-linear B-H relationship and the interaction between the two axis components of magnetic field can be effectively reduced.

Fig.5-17 depicts the simulated results in the time domain, when $V_s(t) = \sin\omega t$, $V_N(t) = 0.5\sin 3\omega t$, where $\omega = 2\pi f$, and f = 1 Hz. From Fig.5-17, it can be seen that by feedback control the third harmonic noise generated by the non-linearity of the magnetisation curve and the interaction between the magnetic field components on two axes can be reduced by a factor of ten. A further reduction by a factor of three can be achieved by integration since the feedback is applied on V_{dB}, a voltage proportional to dB/dt. That is, if 50% third harmonic is assumed due to the non-linearity and the field interaction, the resultant flux density B only contains about 1.7% third harmonic.

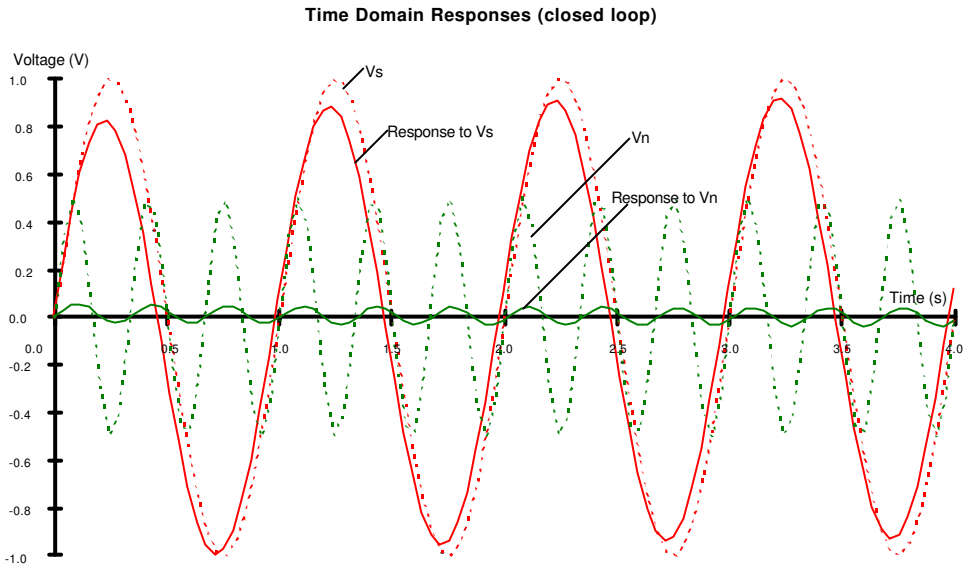

(a)

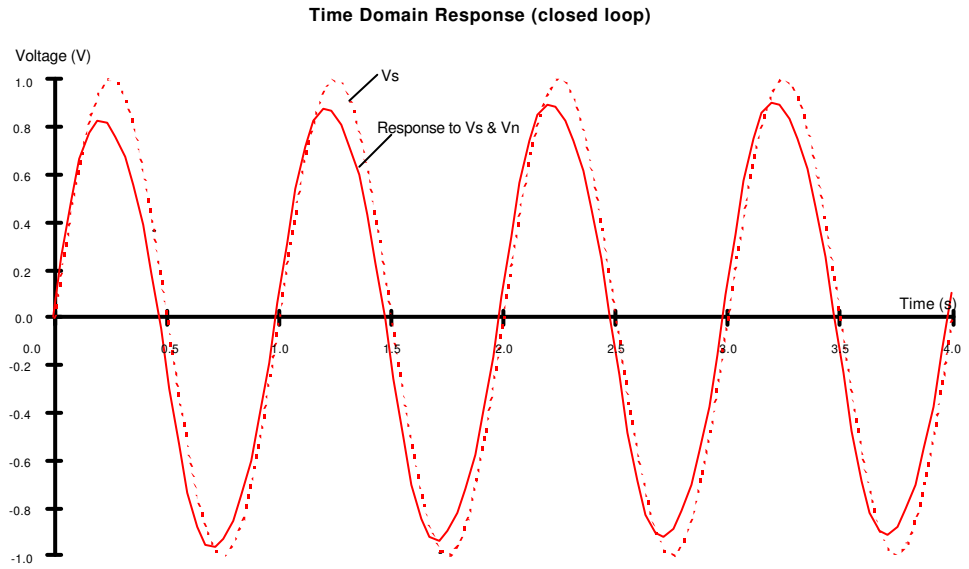

(b)

Fig.5-17 Time domain responses
(a) responses to specified signal V_s and noise signal V_N, and
(b) resultant response

5.2.5.3 Implementation of the Feedback Control

Fig.5-18 shows the circuit diagram of the differential voltage amplifier and the passive low pass filter. Between the amplifier and the low pass filter there is a high pass filter with a corner frequency about 0.3 Hz. This filter was adopted to reduce the low frequency drift generated by the voltage amplifier since it is constructed with the general purpose operational amplifier LM324. The overall performance is not affected when the frequency is higher than 1 Hz.

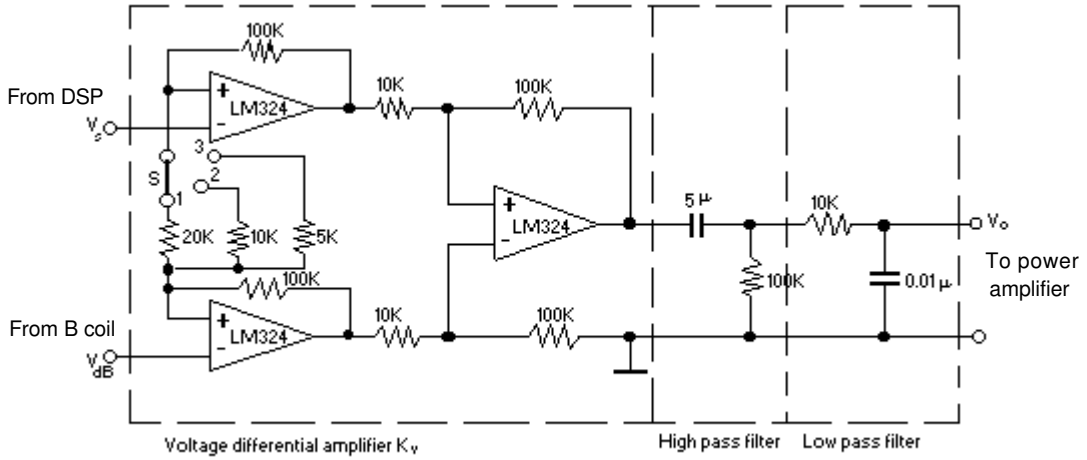

Fig.5-18 Circuit diagram of differential voltage amplifier and filters

5.2.6 Power Amplifier

The two channel power amplifier used in the system, as shown in Fig.5-2, was a modified Australian Monitor AM1600 power amplifier. The frequency response was extended in the low frequency region to meet the requirements of SST. The bandwidth of the amplifier is 1 Hz - 90 kHz. The output power is 470 W with 8 Ω resistive load, 810 W with 4 Ω resistive load, and 1050 W with 2 Ω resistive load each channel. The input impedance is 8.5 kΩ with 1 kHz sine wave. The input sensitivity is +1.5 dBm (0.92 volts rms). The intermodulation distortion is less than 0.015% with 60 Hz and 7 kHz sine waves and 0.007% with 14 kHz and 15 kHz sine waves at rated output and into a 4 Ω resistive load. The common mode rejection ratio is 97 dB at 100 Hz, 91 dB at 1 kHz, 72 dB at 10 kHz, and 67 dB at 20 kHz.

5.3 CORE LOSS MEASUREMENTS WITH ROTATING MAGNETIC FLUXES

5.3.1 Calculation of Core Losses from Measured Magnetic Field Strength and Flux Density

Fig.5-19 sketches a square specimen placed in the middle of a tester. Since the magnetic field is not uniformly distributed in all of the specimen, as mentioned in section 4.2.3.3, the X and Y components of the magnetic field strength and flux density are measured in the centre area of the specimen, where the magnetic field can be considered as uniform.

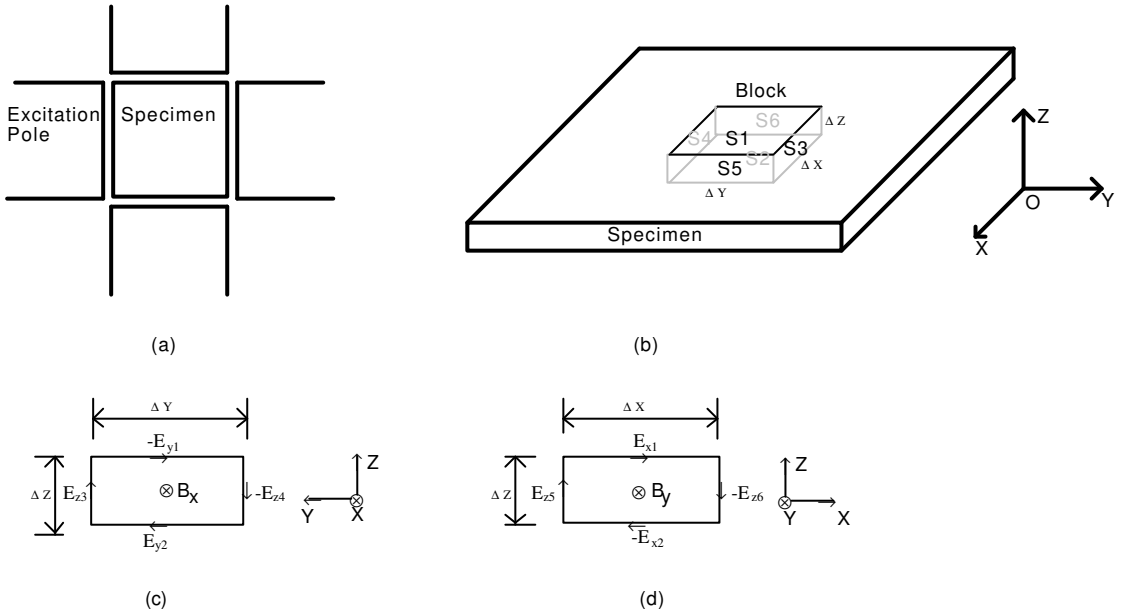

Fig.5-19 (a) A specimen placed in the middle of the tester,
(b) A small block chosen in the centre of the specimen,
(c) Relationship between **E** and B_x, and
(d) Relationship between **E** and B_y.

Consider a small block in the centre of the specimen as shown in Fig.5-19(b). The height of the block is chosen equal to the thickness of the specimen. When the thickness of the specimen is smaller than the skin depth, the magnetic field in the cross section of the specimen can be assumed uniform since the eddy current reaction can be neglected. The total power dissipated in the block at any time instant equals the net electromagnetic power entering the block through the closed surface $S = \sum_{i=1}^{6} S_i$, where S_i, (i=1,2,...,6), are the surrounding surfaces of the block. According to Poynting's theorem, this power can be calculated by

$$P = -\oint_S (\mathbf{E}\times\mathbf{H}) \bullet d\mathbf{s} \tag{5.16}$$

where **s** is the surface element with the normal direction pointing outwards, **E** and **H** are the electrical field intensity and the magnetic field strength on the block surface, and **E**×**H** is the Poynting vector standing for the power flow per unit surface area.

Let $\mathbf{E} = E_x\mathbf{i} + E_y\mathbf{j} + E_z\mathbf{k}$, and $\mathbf{H} = H_x\mathbf{i} + H_y\mathbf{j}$, where the subscripts x, y, and z, indicate the components on the X, Y, and Z axes, and **i**, **j**, and **k** are the unit vectors on the X, Y, and Z axes. The Poynting vector can then be written as

$$\mathbf{E}\times\mathbf{H} = -E_zH_y\mathbf{i} + E_zH_x\mathbf{j} + (E_xH_y - E_yH_x)\mathbf{k} \tag{5.17}$$

and the total power entering the block

$$\begin{aligned} P = &- \int_{S_1} (E_xH_y - E_yH_x)dxdy + \int_{S_2} (E_xH_y - E_yH_x)dxdy \\ &- \int_{S_3} E_zH_xdxdz + \int_{S_4} E_zH_xdxdz + \int_{S_5} E_zH_ydydz - \int_{S_6} E_zH_ydydz \\ = &\ \Delta x\,\Delta y\,(-E_{x1}H_{y1}+E_{y1}H_{x1}+E_{x2}H_{y2}-E_{y2}H_{x2}) \\ &+ \Delta x\,\Delta z\,(-E_{z3}H_{x3}+E_{z4}H_{x4}) + \Delta y\,\Delta z\,(E_{z5}H_{y5}-E_{z6}H_{y6}) \end{aligned} \tag{5.18}$$

where the numbers (1,2,...,6) in the subscripts of E and H indicate the components of E and H on the corresponding surfaces S_i, (i=1,2,..,6).

The assumption of uniform magnetic field leads to $H_x = H_{x1} = H_{x2} = H_{x3} = H_{x4}$, and $H_y = H_{y1} = H_{y2} = H_{y5} = H_{y6}$. Therefore, (5.18) can be rewritten as

$$\begin{aligned} P &= \Delta x\, H_x\,(E_{y1}\Delta y - E_{z3}\Delta z - E_{y2}\Delta y + E_{z4}\Delta z) \\ &\quad + \Delta y\, H_y\,(-E_{x1}\Delta x - E_{z6}\Delta z + E_{x2}\Delta x + E_{z5}\Delta z) \\ &= \Delta x\,\Delta y\,\Delta z\,\left(H_x\frac{dB_x}{dt} + H_y\frac{dB_y}{dt}\right) \\ &= \Delta V\left(\mathbf{H}\bullet\frac{d\mathbf{B}}{dt}\right) \end{aligned} \tag{5.19}$$

where $\Delta V = \Delta x\,\Delta y\,\Delta z$ is the volume of the block, $\frac{dB_x}{dt} = E_{y1}\Delta y - E_{z3}\Delta z - E_{y2}\Delta y + E_{z4}\Delta z$, and $\frac{dB_y}{dt} = -E_{x1}\Delta x - E_{z6}\Delta z + E_{x2}\Delta x + E_{z5}\Delta z$, by Faraday's law.

Therefore, the mean specific power (in W/kg) dissipated in the block is

$$P_t = \frac{1}{T\rho_m}\int_0^T \mathbf{H} \bullet \frac{d\mathbf{B}}{dt}\, dt \tag{5.20}$$

where T is the time period of magnetisation, ρ_m the mass density of specimen, **H** the measured surface magnetic field strength vector, and **B** the measured average magnetic flux density vector. Equation (5.20) is exactly the same as (4.13).

Rotational core loss can also be calculated by the torque on the magnetic dipoles in the specimen. The torque on a single dipole of magnetic moment **m** (Am^2) in a uniform magnetic field can be expressed as [215]

$$\mathbf{T}_m = \mu_o \mathbf{m} \times \mathbf{H} \tag{5.21}$$

Assume there are n dipoles in the block of volume ΔV shown in Fig.5-19(b). The net torque per unit volume can then be calculated, if the magnetic field in the block is uniform, by

$$\begin{aligned} \mathbf{T}_r &= \frac{\sum_{k=1}^{n} \mathbf{T}_{m(k)}}{\Delta V} \\ &= \frac{\sum_{k=1}^{n} (\mu_o \mathbf{m}_k \times \mathbf{H})}{\Delta V} \\ &= \mu_o \left(\frac{\sum_{k=1}^{n} \mathbf{m}_k}{\Delta V} \right) \times \mathbf{H} \\ &= \mu_o \mathbf{M} \times \mathbf{H} \end{aligned} \tag{5.22}$$

where $\mathbf{M} = \frac{\sum_{k=1}^{n} \mathbf{m}_k}{\Delta V}$ is defined as the magnetisation (A/m). Equation (5.22) is essentially the same as (4.14) proposed by Flanders [128,129,132-134].

Because $\mathbf{B} = \mu_o(\mathbf{H}+\mathbf{M})$ and $\mathbf{B}\times\mathbf{H} = \mu_o\mathbf{M}\times\mathbf{H}$, the expression of rotational specific core loss in the field-metric method type two can then be derived from (5.22) as

$$P_r = \frac{1}{2\pi\rho_m}\int_0^{2\pi} \mathbf{T}_r \bullet d\beta$$
$$= \frac{1}{T\rho_m}\int_0^{T} |\mathbf{B}\times\mathbf{H}|\Omega(t)dt \qquad (5.23)$$

where β is the angular displacement, and $\Omega(t) = d\beta/dt$ the angular speed of vector **B**. It should be noticed that $\Omega(t)$ is generally a function of time, and should not be taken out of the integral. It was assumed a constant and placed outside the integral to evaluate rotational core losses with both purely circular and elliptical magnetic fluxes in [149] when (4.15) was first proposed by Sievert and Enokizono, but this is thought to be incorrect, as pointed out by the author [180]. This was also agreed by Dr. Sievert in a frank discussion [186].

For a purely circular rotating magnetic flux density vector of constant velocity and magnitude, as shown in Fig.5-20, we have

$$d\mathbf{B} = |\mathbf{B}|d\beta \qquad (5.24)$$

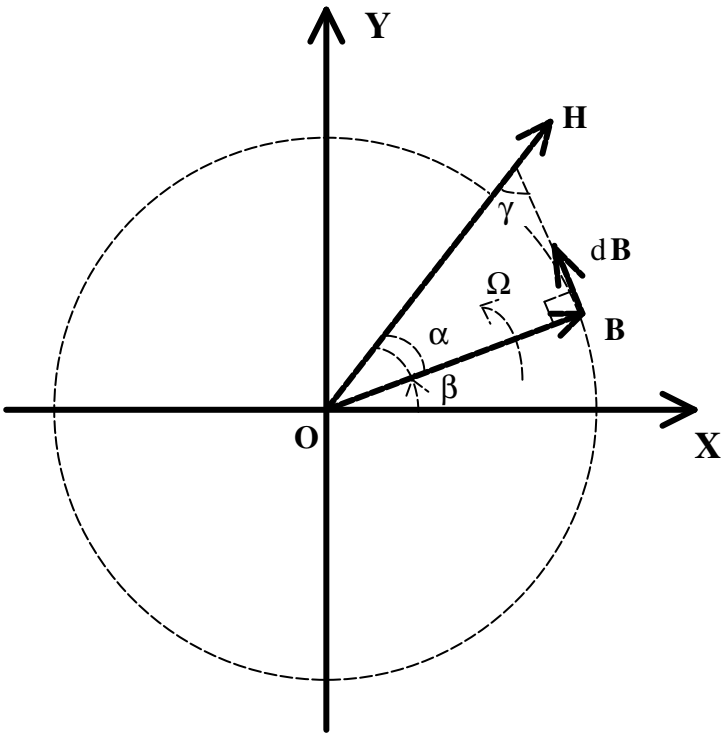

Fig.5-20 Positions of **B** and **H** vectors when **B** is a purely circular rotating vector

Thus,

$$\begin{aligned}\mathbf{H}\bullet\frac{d\mathbf{B}}{dt} &= |\mathbf{B}|\left(\mathbf{H}\bullet\frac{d\beta}{dt}\right)\\ &= |\mathbf{B}||\mathbf{H}|\left|\frac{d\beta}{dt}\right|\cos\gamma\\ &= |\mathbf{B}||\mathbf{H}|\Omega\sin\alpha\\ &= \Omega|\mathbf{H}\times\mathbf{B}|\end{aligned} \tag{5.25}$$

where $\Omega=\left|\frac{d\beta}{dt}\right|$ is a constant angular speed for a circular vector **B**, and $\gamma=\frac{\pi}{2}-\alpha$.

Therefore, (5.20) is identical to (5.23) for a circular flux density. This will also be shown experimentally in the following sections.

5.3.2 Measurement of Core Losses with Rotating Magnetic Fluxes

With the system and techniques outlined in the previous sections, the rotational core losses of Lycore-130, a non-grain oriented electrical steel sheet, has been measured at 1, 10, 50, 100 and 200 Hz, for various rotating fluxes, and the results are reported below.

5.3.2.1 P_t and P_r with a Circular Flux Density

Figs.5-21(a) and (b) illustrates the loci of circularly rotating vectors **B** and **H** at 50 Hz, and Fig.5-21(c) the core loss versus flux density, where P_t is the total core loss calculated by (5.20), and P_r the rotational core loss calculated by (5.23).

From the loci of **B** and **H** vectors, it can be seen that there exists another hard axis of magnetisation about 55° from the X axis (rolling direction) besides the difference in magnetisation properties between the rolling direction and the transversal direction. This could be attributed to the texture and the crystal anisotropy of the magnetic material, and will be explained later in section 5.5.1.

The identity $P_t=P_r$ for a purely circular rotating magnetic flux density, obtained by the mathematical analysis in the last section, is confirmed experimentally in Fig.5-21(c). The discrepancy between P_t and P_r above $|\mathbf{B}|$=1.4 T was caused by the higher harmonics of flux

density, since it was very difficult to keep a purely circular rotating flux density vector when the specimen was close to saturation.

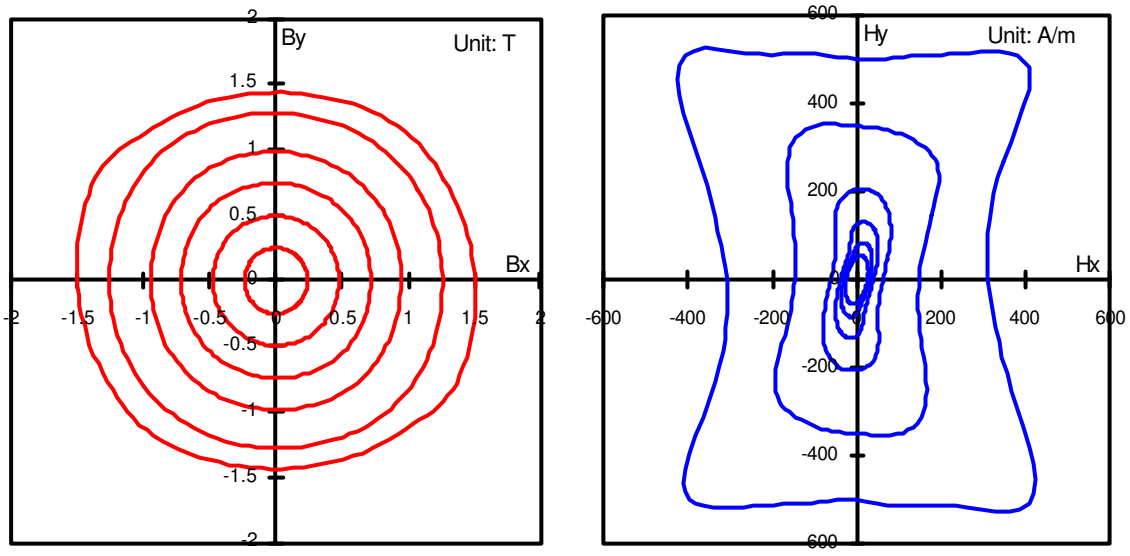

(a) (b)

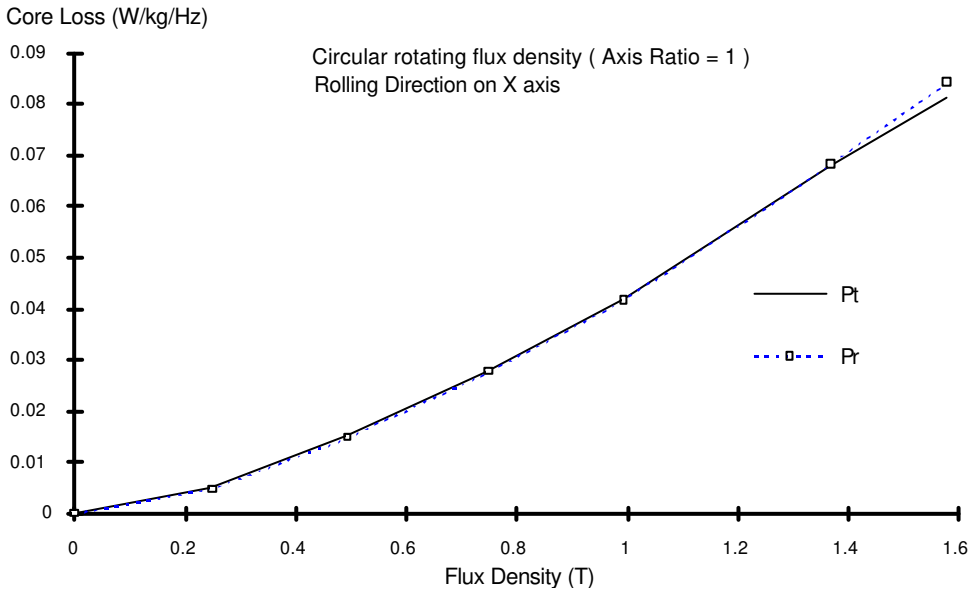

(c)

Fig.5-21 Core loss measurement of Lycore-130 with circularly rotating flux at 50 Hz
(a) loci of vector **B**, (b) loci of vector **H**, and
(c) rotational core losses.

5.3.2.2 P_t and P_r with an Elliptical Flux Density

Figs.5-22(a)-(e) are the **B** and **H** loci and the core losses of Lycore-130 versus the axis ratio, which is defined as the ratio between the minor axis and the major axis, of an elliptically rotating magnetic flux density at 50 Hz, when the major axis is on the X axis and Y axis, respectively. The major axis of the elliptical flux density is fixed at 1.25 T. In Fig.5-22(e), P_t is the total core loss calculated by (5.20), and P_r the rotational core loss calculated by (5.23).

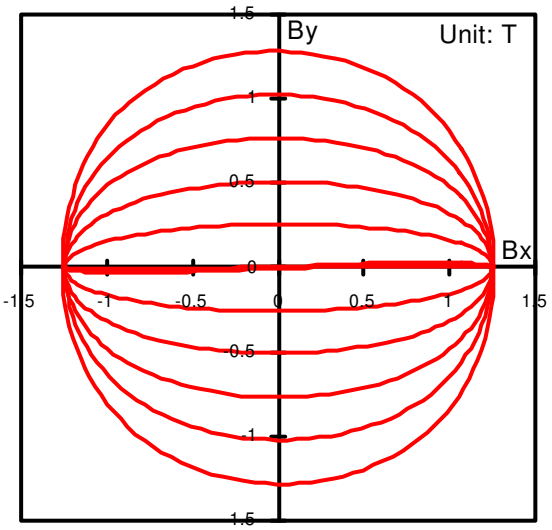

(a)

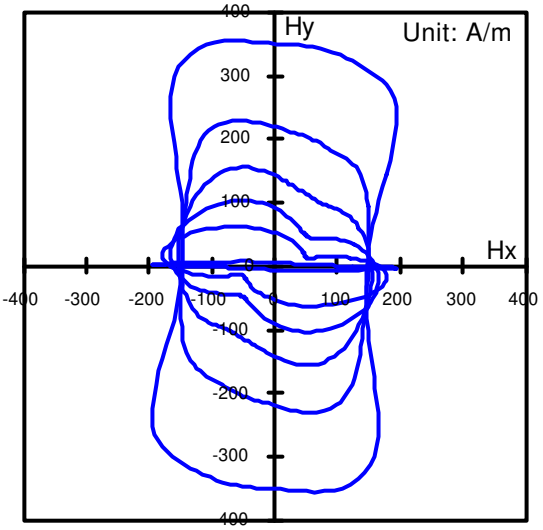

(b)

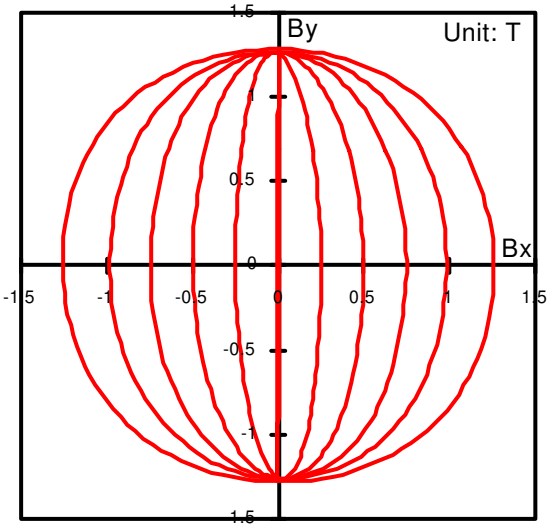

(c)

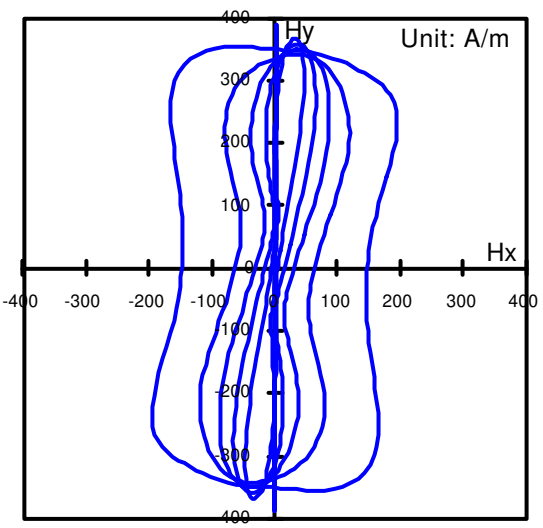

(d)

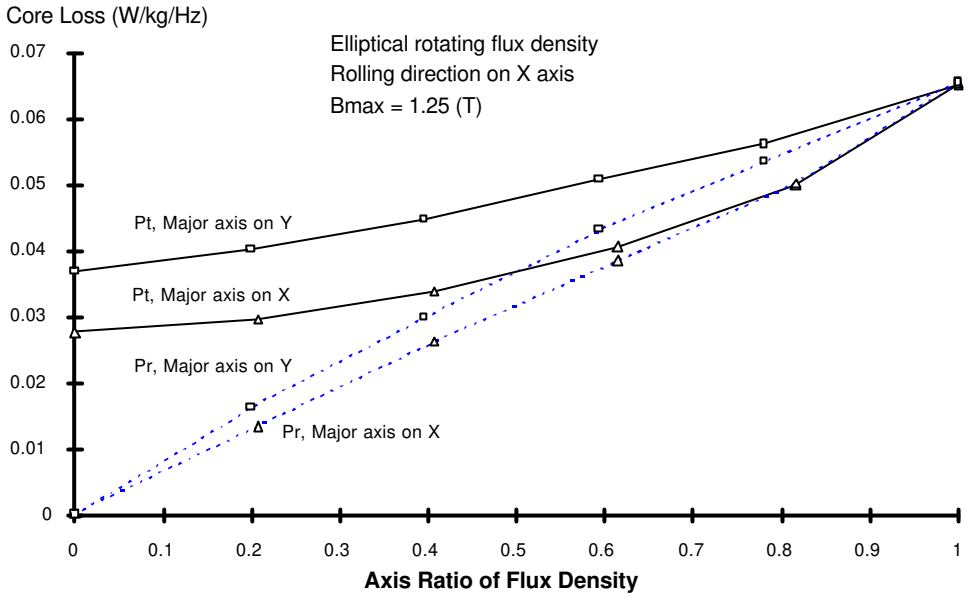

(e)

Fig.5-22 (a) Loci of elliptical vector **B** with the major axis on the X axis;
(b) Loci of vector **H** corresponding to the elliptical vector **B** in (a);
(c) Loci of elliptical vector **B** with the major axis on the Y axis;
(d) Loci of vector H corresponding to the elliptical vector **B** in (c);
(e) Core loss of Lycore-130 with elliptically rotating fluxes, when the major axis is on the X axis, and Y axis, respectively.

Our measurements, as illustrated in Fig.5-22(e), confirmed the results reported by Sievert and Enokizono [151,155,157] that $P_t \geq P_r$ for non-oriented materials in elliptically rotating magnetic flux. When the axis ratio of flux density is one (circular flux density), $P_t = P_r$. When the axis ratio is zero (alternating flux density), P_r is reduced to zero, while P_t gives the alternating core loss. That is why P_t was clarified as the total core loss, and P_r as the rotational loss due to the rotational component of magnetic flux density, by Sievert and Enokizono [121,149,151]. Further analysis, however, has shown that P_r depends not only on the rotational component of magnetic flux density but also on the rotational component of magnetic field strength [180], as will be discussed in section 5.5.2.

5.3.2.3 Ratio of Rotational Core Loss to Alternating Core Loss

Alternating core losses in the rolling direction (X axis) and the transversal direction (Y axis) were also measured at the same time when the rotational core losses were measured. Figs.5-23(a) and (b) plot the alternating core loss on the X and Y axes and the rotational core loss with purely circular flux density against the magnitude of magnetic flux density at 1 and 50 Hz, respectively. It can be seen that the alternating core losses on the X and Y axes are different due to the crystal anisotropy, but the average of the two losses can give a correct value of the

alternating core loss obtained by a ring sample or an Epstein frame, as illustrated in Fig.5-9, section 5.2.3.3.

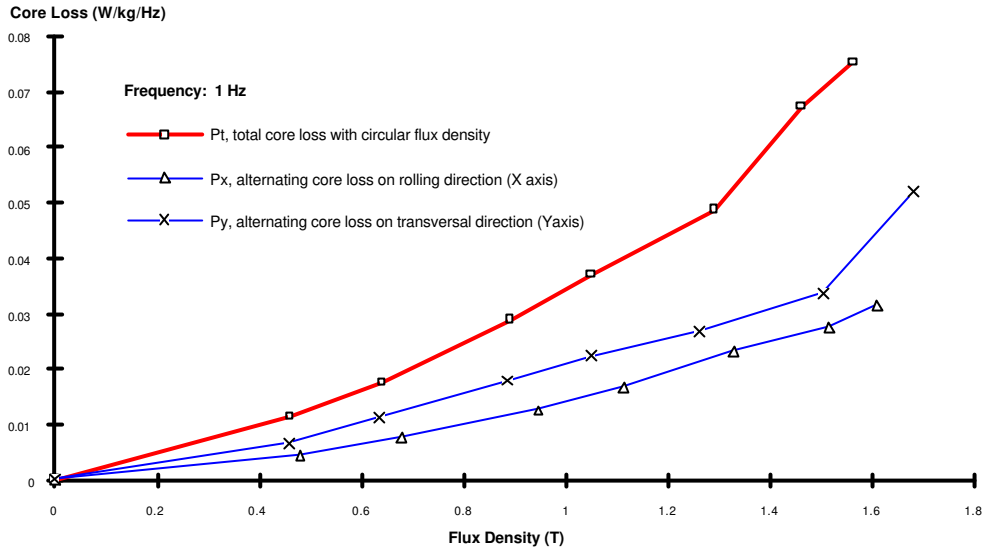

(a)

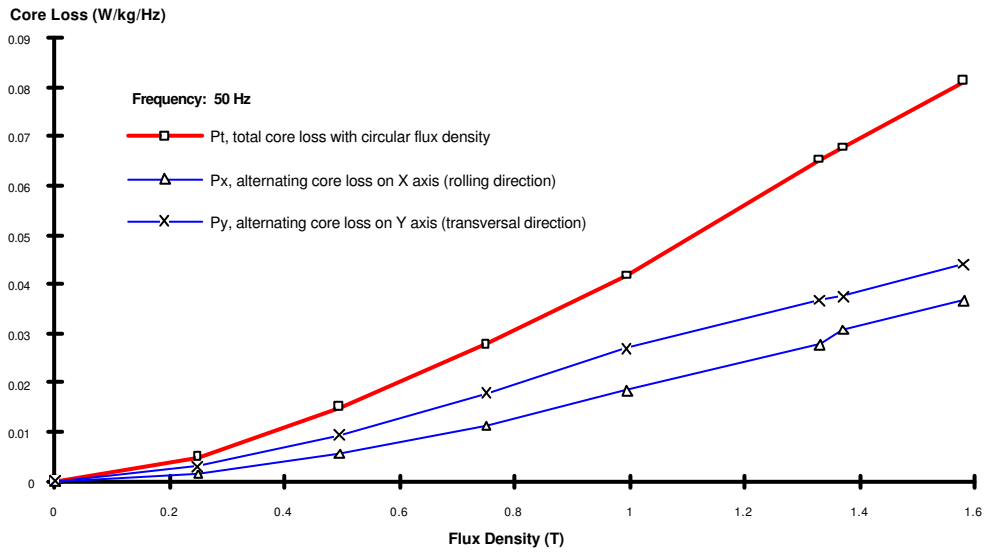

(b)

Fig.5-23 Alternating core loss on the X and Y axes and purely rotational core loss at (a) 1 Hz, and (b) 50 Hz

The ratio of rotational core loss to alternating core loss, which is defined as $2P_t/(P_x+P_y)$, was 2.07 at 1 Hz and 1.99 at 50 Hz, over a wide range of flux densities up to 1.6 T. This is close to the ratio of 2 for both the pure hysteresis losses and the losses at 50 Hz in 3% non-oriented

silicon iron observed by Boon and Thompson [127,138], and the ratio of $\pi/\sqrt{2}$ for the pure hysteresis losses in 1.2% carbon steel and mild steel observed by Grimwood, Cambell, and Evetts [132]. When the specimen is saturated, however, this ratio will no longer be held constant as rotational core loss drops very rapidly while alternating core loss increases dramatically.

5.3.2.4 Rotational Core Loss at Different Frequencies

Fig.5-24 is the specific total rotational core loss of Lycore-130 versus the magnitude of magnetic flux density at various frequencies from 1 to 200 Hz, for a purely circular flux density.

Owing to the difficulty in the control of flux density waveforms on the X and Y axes to be sinusoidal when the specimen is close to saturation, as discussed in section 4.2.3.3, the highest flux density reached in this material was 1.6 T, which is exactly the same as that reached by Sievert and Enokizono [186,187]. Therefore, the quick falling of rotational core loss in a saturated specimen was not observed.

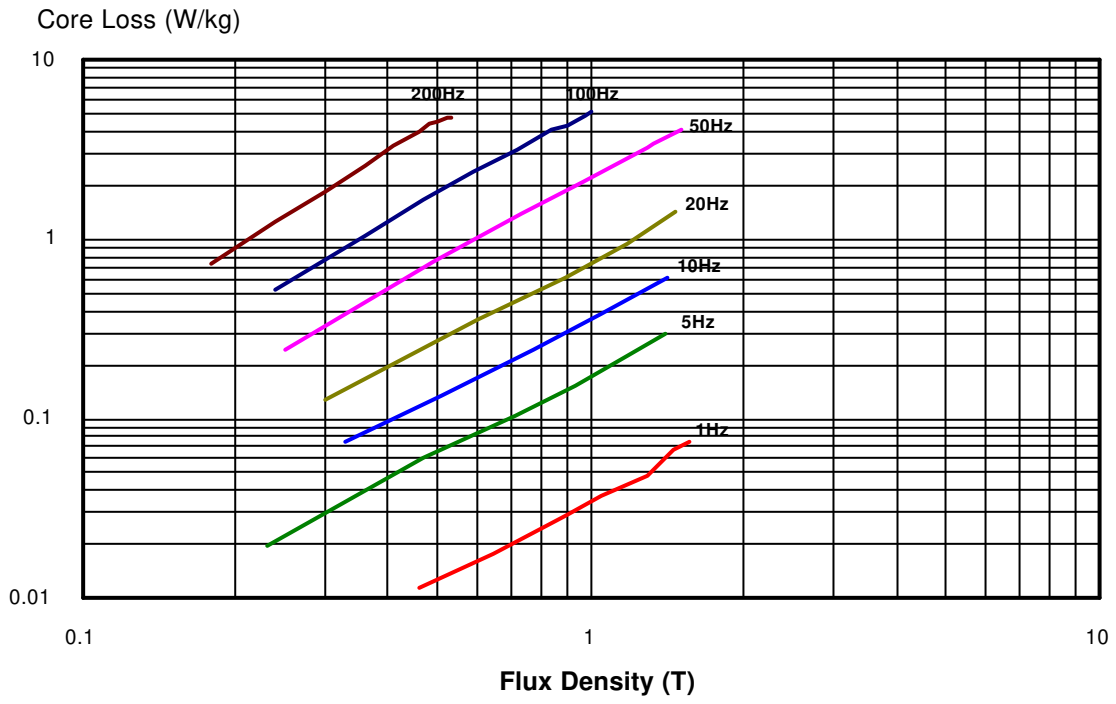

Fig.5-24 Rotational core loss of Lycore-130, for a purely circular rotating flux density

5.4 MEASUREMENT OF ROTATIONAL CORE LOSS WITH TESTER AT PTB, GERMANY

The rotational core loss testing system developed by Dr. Sievert at PTB has been described earlier in section 4.2.3.3. The field-metric method was employed for core loss measurement. **H** and **B** signals were picked up by conventional surface **H** coils and **B** tips. Generally, this system is able to control the flux density waveforms sinusoidal up to 1.2 T for grain-oriented materials and 1.6 T for non-oriented materials over a range of frequencies from about 30 to 80 Hz [187]. When the frequency is lower than 30 Hz, core loss measurement can still be performed, but the magnitudes and waveforms of the flux density components on the X and Y axes are difficult to control.

Core losses in specimens of 0.35 mm grain-oriented electrical steel sheet ORSI-100 and 0.35 mm non-oriented electrical steel sheet V270-35A were measured at 50 Hz with purely circular flux densities, elliptical flux densities with the major axis on the X axis (rolling direction) and the Y axis (transversal direction), and alternating flux densities on the X and Y axes, respectively. The results are reported and discussed below.

5.4.1 P_t and P_r with a Circular Flux Density

Fig.5-25 illustrates the results of core loss measurement for a specimen of ORSI-100 with a circular flux density, including the values of the total loss P_t and the rotational loss P_r, calculated by (5.20) and (4.15), listed against the amplitude of circular flux density B_{amp}, the loci of **B** and **H** vectors, the B/H loops on the X and Y axes, the angle between **H** and **B** vectors, and the waveforms of B and H components on the X and Y axes, where the sinusoidal waveforms are B components and the non-sinusoidal waveforms are H components. Fig.5-26 is the results of core loss measurement for a specimen of V270-35A with a circular flux density.

As proved mathematically in section 5.3.1, equations (4.15), (5.20), and (5.23) are identical for a circular flux density. This is again confirmed experimentally by the results of core loss measurement listed in Fig.5-25 and Fig.5-26. The discrepancy near saturation in Fig.5-26 is caused by the higher harmonics in B.

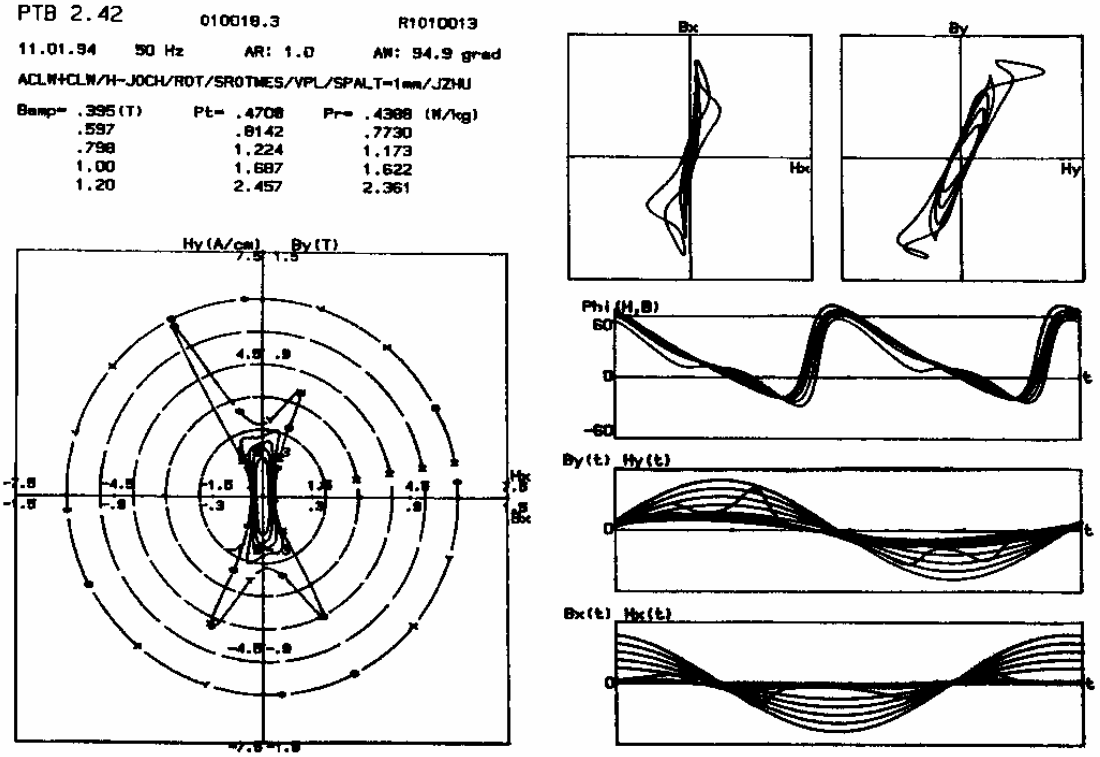

Fig.5-25 Results of core loss measurement for a specimen of ORSI-100 with circular flux density

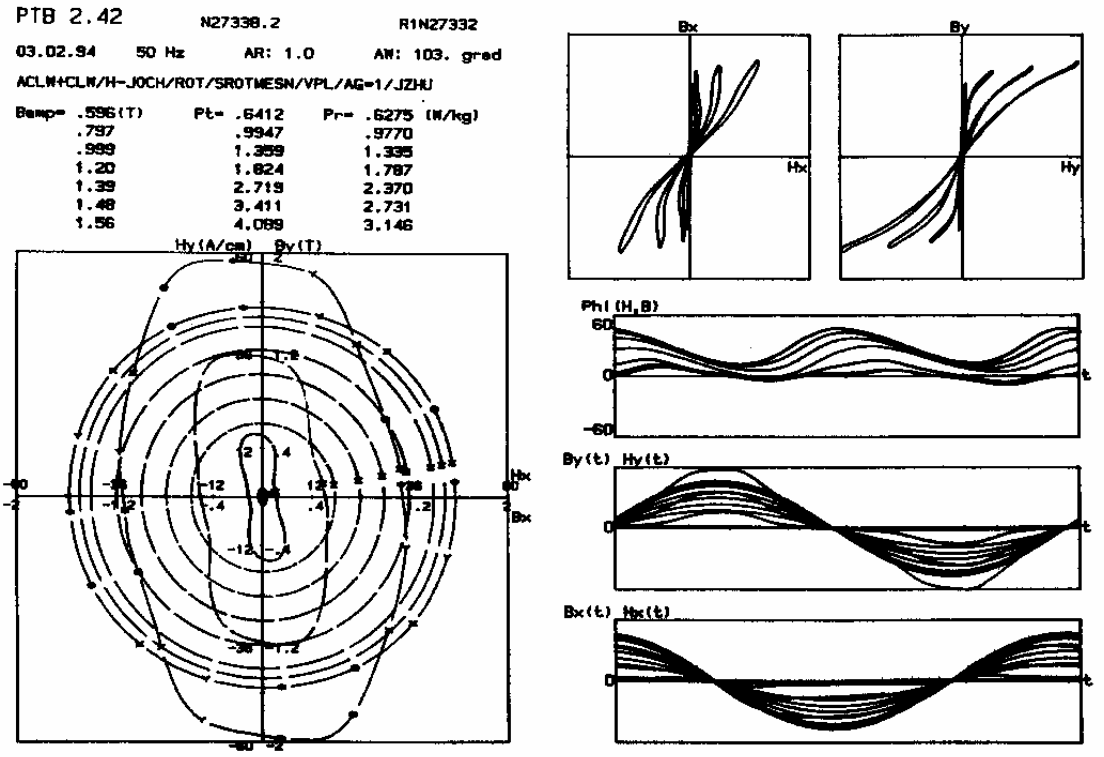

Fig.5-26 Results of core loss measurement for a specimen of V270-35A with circular flux density

Owing to the different textures of grain-oriented and non-oriented materials, as will be explained in section 5.5.1, the anisotropy on the medium axis (Y axis, transversal direction) and the hard axis, which is in the direction about 55° away from the rolling direction (X axis), of ORSI-100 is much stronger than that of V270-35A. This can be readily recognised by the large magnitude of rotating **H** in these directions. Because of the stronger anisotropy, the angle difference between **H** and **B** vectors varies dramatically from +70° to -20° in the specimen of ORSI-100, while in V270-35A, this variation is much smaller.

The angle difference between **H** and **B** vectors can generally be attributed to two factors: (1) the hindrance to the variation of **B** from the rotational hysteresis and eddy currents, and (2) the magnetic anisotropy of the material. The curves of the angle difference between **H** and **B** vectors plotted in Fig.5-25 and Fig.5-26 as Phi(H,B) are just the superpositions of these two factors. Since the magnetic hysteresis and eddy currents always resist the variation of flux density, this factor causes a positive angle difference between **H** and **B**.

The angle difference caused by the material anisotropy, however, varies with the position of **B** vector. It is difficult to pull the **B** vector off the easy axis, which is favoured by **B** since more magnetic domains are aligned in this direction, and hence, the **H** vector leads ahead of the **B** vector for a large angle when it begins to rotate from the easy axis. Once **B** is pulled off the easy axis, the angle difference between **H** and **B** vectors is reduced quickly because of the existence of the hard axis, which is not favoured by **B**. Before reaching the medium axis (transversal direction), **B** catches up with **H**, and the angle is reduced to zero. When **H** and **B** rotate further, **B** leads **H** in order to get rid of the hard axis, and the difference angle becomes negative. As **B** reaches the easy axis, it is hard to pull **B** off the easy axis again.

Because these anisotropic axes are symmetrically distributed within the plane of the specimen, the positive part of the angle difference curve is symmetric to the negative part of the curve. This means that the average angle difference caused by the material anisotropy is zero. Therefore, the average value of the angle difference between **H** and **B** for a whole cycle gives the angle difference due to the effects of rotational hysteresis and eddy currents only.

5.4.2 P_t and P_r with an Elliptical Flux Density

Fig.5-27 and Fig.5-28 are P_t and P_r in specimens of ORSI-100 and V270-35A with an elliptical flux density at 50 Hz when the major axis is on the X and Y axes. The axis ratio is

defined as the ratio of the minor axis to the major axis of an elliptical flux density. The major axis of the elliptical flux density is fixed at 1.2 T. P_t is calculated by (5.20), and $P_r(1)$ and $P_r(2)$ are calculated by (5.23) and (4.15), respectively.

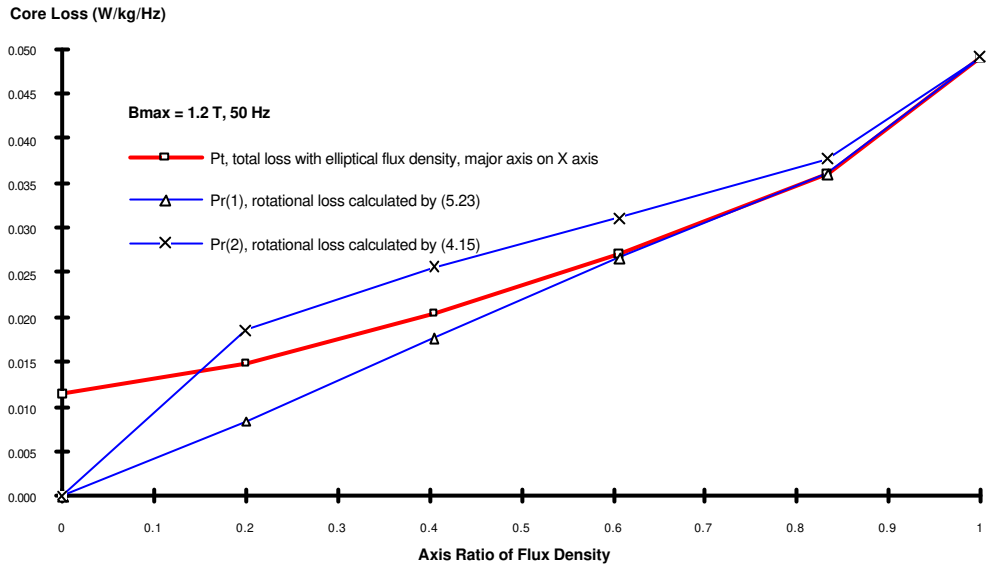

(a)

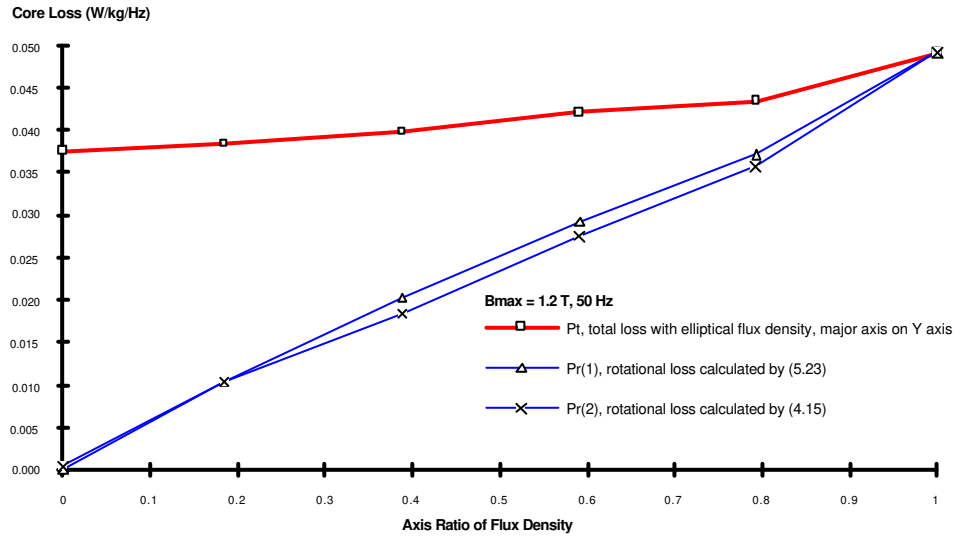

(b)

Fig.5-27 Core losses of ORSI-100 with an elliptical flux density, when the major axis is on (a) X axis, and (b) Y axis

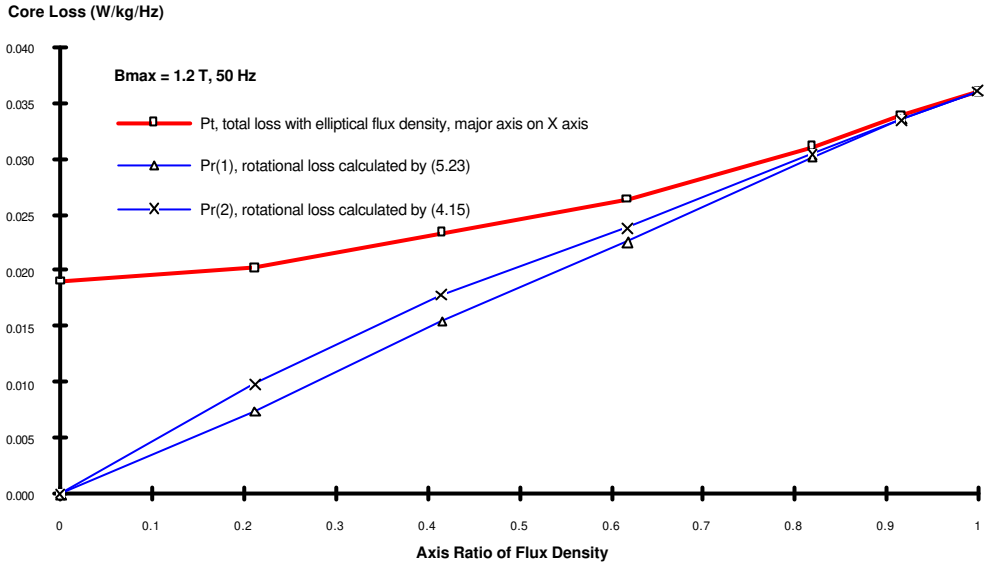

(a)

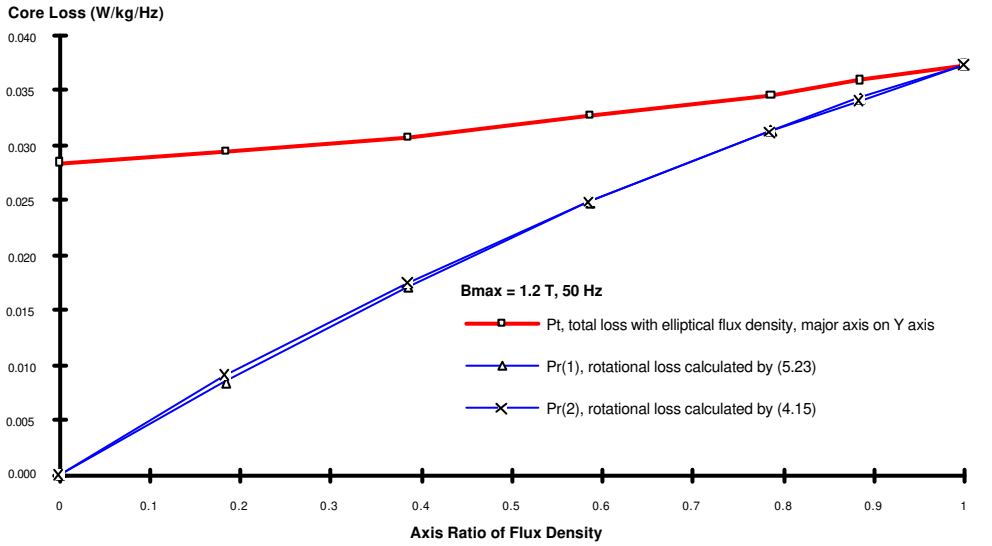

(b)

Fig.5-28 Core losses of N270-35A with an elliptical flux density, when the major axis is on (a) X axis, and (b) Y axis

Theoretically, as pointed out by the author in [180], the rotational loss P_r should not exceed the total power loss P_t in any case, since P_r is just a part of the total loss. The correctness of the results, that $P_r \geq P_t$ for grain-oriented materials with an elliptical flux density, as plotted in Fig.4-32(d) when the major axis was on the X axis, reported by Enokizono, Suzuki, Shirakawa, Sievert, and Xu in [151,155,157] was therefore questionable. The derivation of equation (5.23) for calculating P_r represented in section 5.3.1 revealed that equation (4.15) is incorrect for the case with an elliptical flux density because the angular speed of an elliptical flux density vector varies with time and should not be taken out of the time integral. This is

proved experimentally by Fig.5-27(a). When the major axis of an elliptical flux density is on the X axis (rolling direction) of the ORSI-100 specimen, the rotational loss $P_r(2)$, calculated by (4.15) assuming constant angular speed, is greater than the total loss P_t for axis ratio of flux density larger than 0.2, while the rotational loss $P_r(1)$, calculated by (5.23) assuming variable angular speed, never exceeds P_t.

In Fig.5-27(b), when the major axis of elliptical flux density is on the Y axis (transversal direction) of the ORSI-100 specimen, $P_r(1)$ and $P_r(2)$ are very close, and both are smaller than P_t. This phenomenon is very interesting, but unfortunately was not reported before.

In order to understand why $P_r(2)$ is different from $P_r(1)$ when the major axis is on the X axis, while $P_r(2)$ is close to $P_r(1)$ when the major axis is on the Y axis, the waveforms of the angular speed $\Omega(t)$, the torque $|\mathbf{B}\times\mathbf{H}|$ (in Nm/m^3), and the instantaneous power losses (in W/m^3) are plotted in Fig.5-29 and Fig.5-30, when the major axis is on the X and Y axes, respectively, with axis ratio 0.4, B_{max}=1.2 T, at 50 Hz. The instantaneous power losses were obtained by multiplying the torque $|\mathbf{B}\times\mathbf{H}|$ by the variable angular speed $\Omega(t)$ and by the constant angular speed $\omega=2\pi f$. The average values of the instantaneous power losses are proportional to $P_r(1)$ and $P_r(2)$.

In Fig.5-29, when the major axis is on the X axis, the variation of the torque $|\mathbf{B}\times\mathbf{H}|$ is large due to the fact that the effects of the material anisotropy and the elliptical flux density on the cross product of **B** and **H** are aiding each other, and hence, the error of rotational loss P_r caused by assuming a constant angular speed is large. This can be seen in Fig.5-29(b) from the difference between the average values of the instantaneous power losses.

In Fig.5-30, when the major axis is on the Y axis, however, the variation of the torque $|\mathbf{B}\times\mathbf{H}|$ is much smaller since the effects of the material anisotropy and the elliptical flux density cancel each other. Therefore, the difference between the average values of the instantaneous power losses, or the error of rotational loss P_r, caused by assuming a constant angular speed is smaller than that in Fig.5-29(b). But, the waveforms of the instantaneous power losses are still quite different. This indicates that equation (4.15) is incorrect in the case of an elliptical flux density, although sometimes the averaged value of the instantaneous power loss could be close to the correct result.

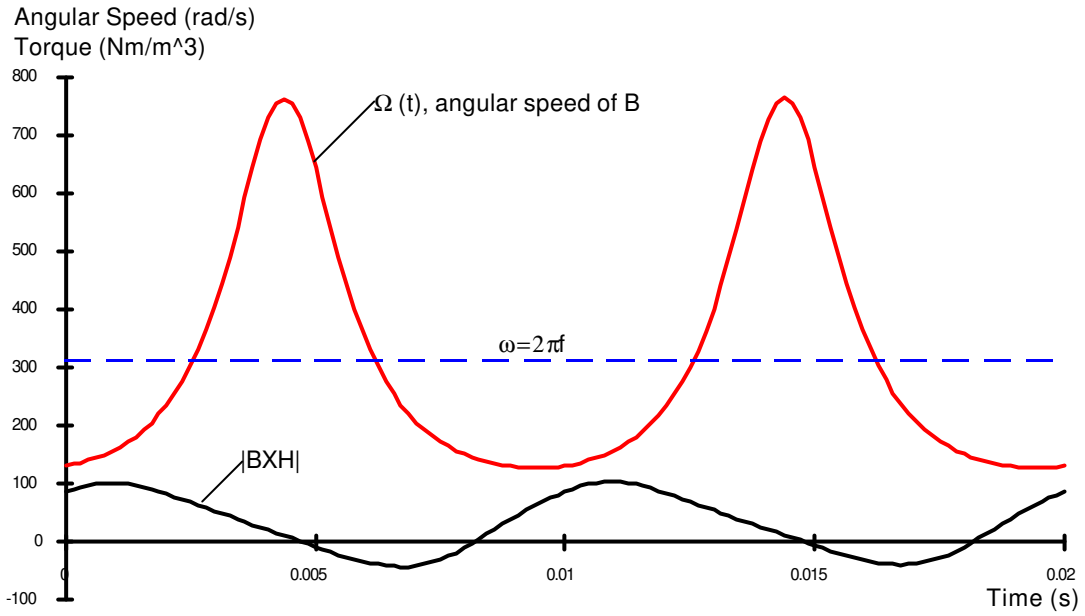

(a)

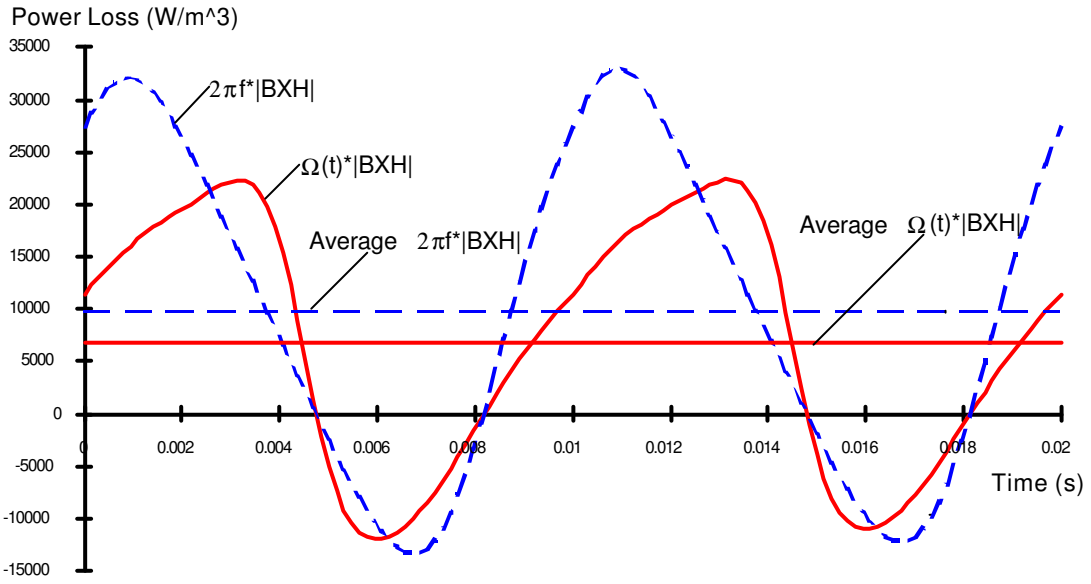

(b)

Fig.5-29 Waveforms of angular speed, torque, and power losses in a specimen of ORSI-100 with an elliptical flux density at 50 Hz, the major axis on the X axis, Bmax =1.2 T, and Axis Ratio = 0.4

(a) angular speed of vector B and torque |B×H|, and

(b) instantaneous rotational losses and the average values, calculated by using actual angular speed and constant angular speed

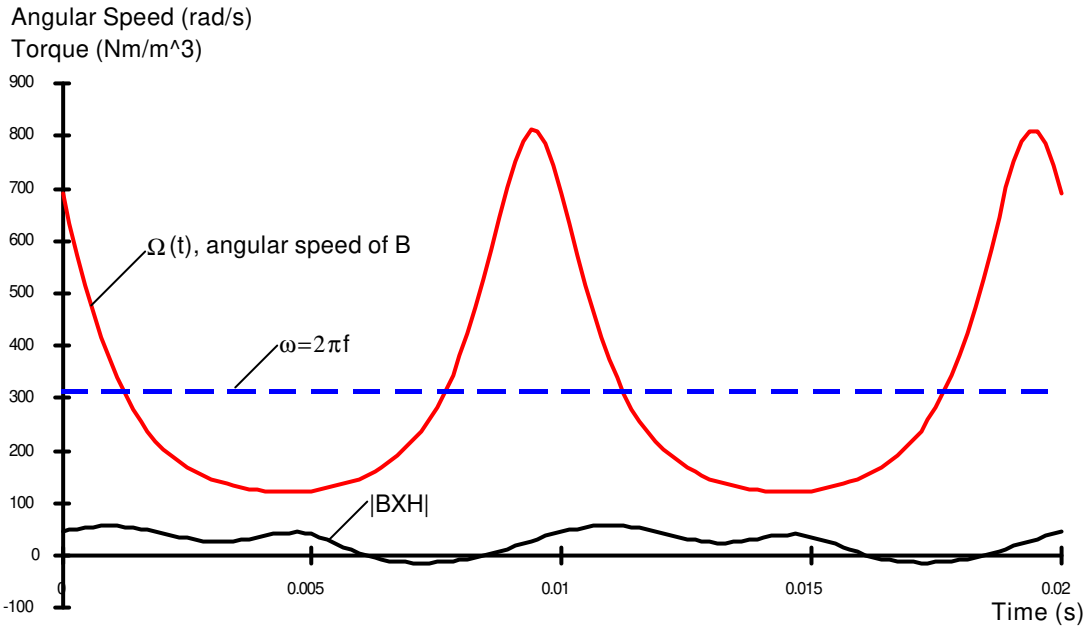

(a)

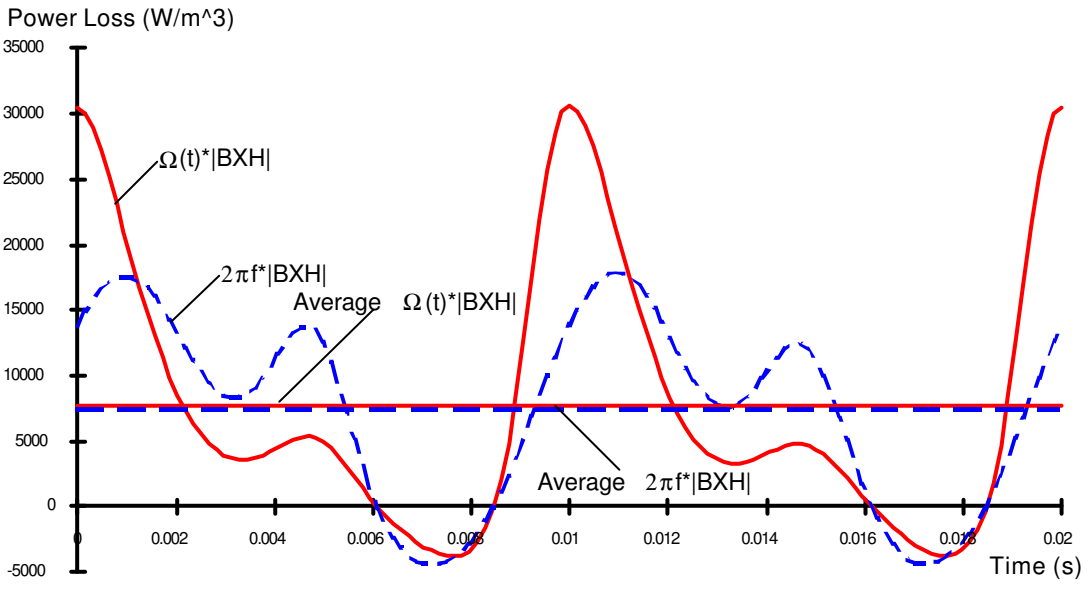

(b)

Fig.5-30 Waveforms of angular speed, torque, and power losses in a specimen of ORSI-100 with an elliptical flux density at 50 Hz, the major axis on the Y axis, Bmax =1.2 T, and Axis Ratio = 0.4

(a) angular speed of vector B and torque |B×H|, and

(b) instantaneous rotational losses and the average values, calculated by using actual angular speed and constant angular speed

In Fig.5-28, it is confirmed again that $P_t \geq P_r$ in non-oriented electrical steel sheets with an elliptical flux density. It can also be seen that the rotational loss calculated by (5.23) is different from that calculated by (4.15), although the difference is not big. This can be explained by the fact that in non-oriented materials the magnetic anisotropy due to the material texture is not as strong as that in grain-oriented materials, and hence, for non-oriented materials the error of rotational loss caused by assuming constant angular speed of flux density is smaller than that for grain-oriented materials.

5.4.3 Ratio of Rotational Core Loss to Alternating Core Loss

Fig.5-31 and Fig.5-32 show the core losses in ORSI-100 and V270-35A with circular and alternating flux densities. The ratio of total rotational core loss to alternating core loss, which is defined as $2P_t/(P_x+P_y)$, is 1.99 for a range of flux densities up to 1.2 T in ORSI-100, and 1.69 for a range of flux densities up to 1.6 T in V270-35A. Although the ratios of total rotational core loss to alternating core loss are close to 2 in both grain-oriented and non-oriented magnetic materials, the total rotational core loss is not simply the sum of the alternating core losses on the X and Y axes. It is noticed that the B/H loops on the X and Y axes for a circular flux density in Fig.5-25 and Fig.5-26 are different from those for alternating flux densities on the X and Y axes. This indicates that the mechanisms of total rotational core loss are different from that of alternating core loss.

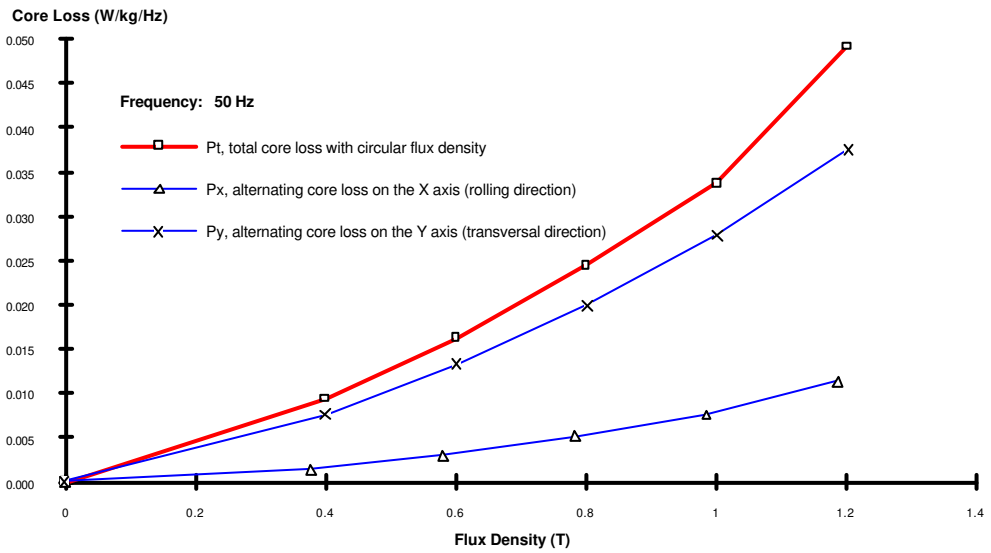

Fig.5-31 Alternating core losses on the X and Y axes and rotational core loss of ORSI-100

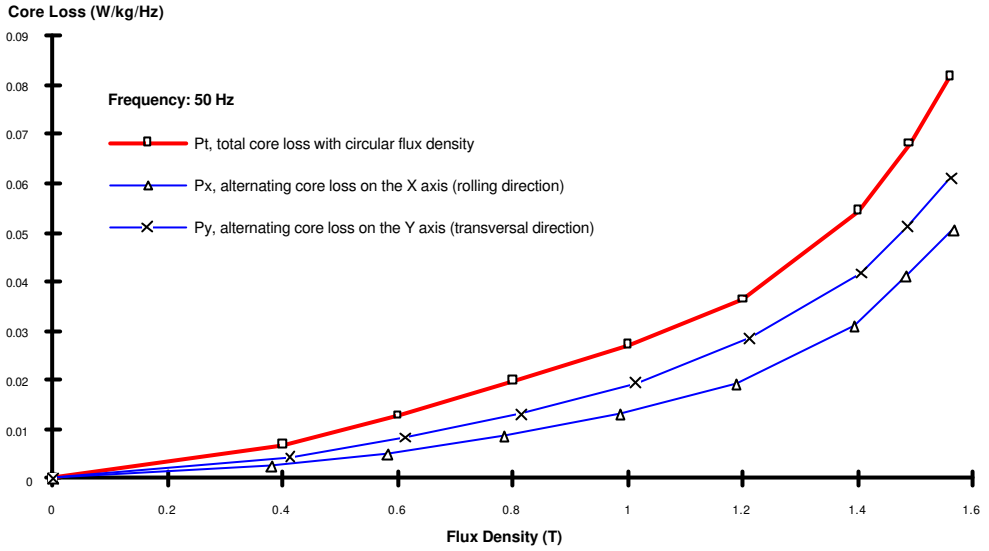

Fig.5-32 Alternating core losses on the X and Y axes and rotational core loss of V270-35A

By comparing the curves of core losses plotted in Fig.5-31 and Fig.5-32, it can be seen that in grain-oriented materials the alternating core loss in the rolling direct (X axis) is smaller than that in non-oriented materials, but the total rotational core loss in grain-oriented materials is not always smaller than that in non-oriented materials because the magnetic properties on the medium and hard axes in grain-oriented materials are inferior to those in non-oriented materials, as will be discussed in section 5.5.1.

5.5 FURTHER DISCUSSION

5.5.1 Magnetic Anisotropy due to Material Textures

From the discussions in the previous sections, it was realised that the anisotropy of magnetic materials played an important role in the measurement of rotational core loss. Most importantly, the difficulty to control the waveforms of flux density sinusoidally, when the material is close to saturation, can be related to the magnetic anisotropy of the material. As mentioned earlier, the highest value of flux density ever reached by Sievert and the author was 1.6 T in non-oriented materials and 1.2 T in grain-oriented materials.

Magnetic anisotropy simply means that the magnetic properties depend on the direction in which they are measured. There are several kinds of anisotropy, such as crystal anisotropy, shape anisotropy, stress anisotropy, and exchange isotropy, etc. Among them, only crystal

anisotropy is intrinsic to the material, and all others are induced anisotropy in specific circumstances.

Fig.5-33 depicts the normal magnetisation curves measured in the three crystal axes, <100>, <110>, and <111>, of a single iron crystal, which has a body centred cubic structure. For an iron crystal, <100> is the easy axis, <110> is the medium axis, and <111> is the hard axis. Magnetic domains in an iron crystal will therefore lie in [100] directions (the easy axes). From the magnetisation curve in <111> direction, it can be seen that the crystal begins to saturate at M=1000 emu/cm^3, or 1.26 T. When the effects of impurities and rotational hysteresis are considered in an electrical steel sheet , this value could be even lower.

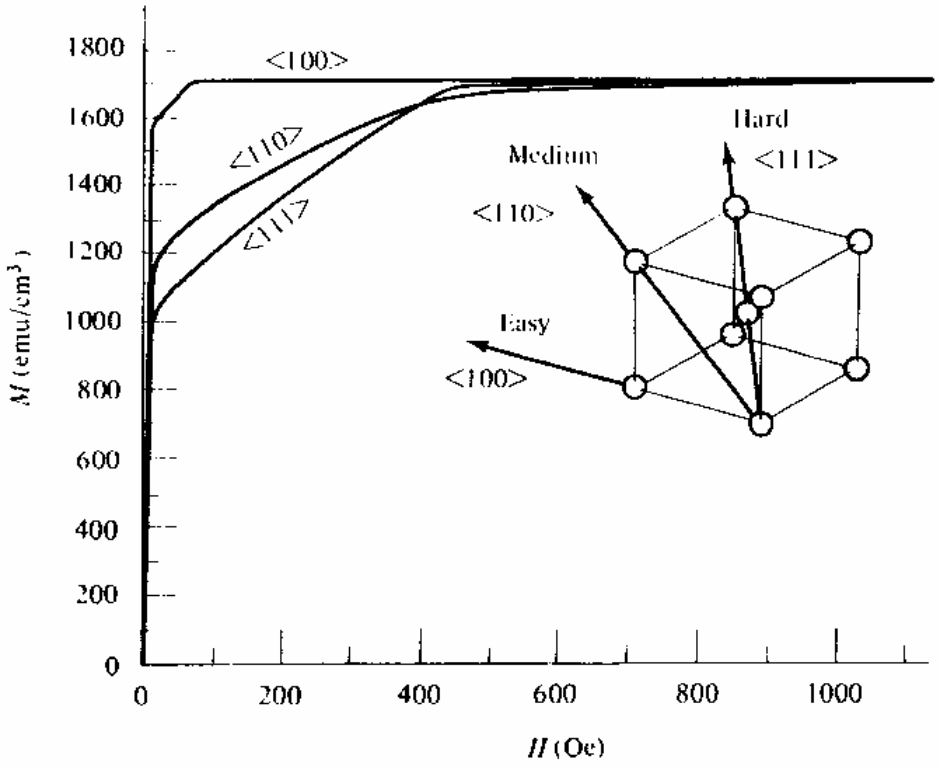

Fig.5-33 Magnetisation curves for a single crystal of iron (from [3])

In an ideally isotropic magnetic material, the iron crystals are randomly oriented. Practically, however, the crystal orientations or textures are more or less affected by fabrication and heat treatment, but the effect is complicated and imperfectly understood. In fact, it is difficult to achieve isotropy in any fabricated material, even if fabrication involves no more than solidification from the melt. When a single crystal is elongated by tension, slip occurs on a

limited number of crystal planes that, in general, are inclined to the axis of tension. As elongation proceeds, the planes on which slip is taking place tend to turn so that they are less inclined to the axis. In this way a definite crystallographic direction approaches parallelism with the length of the specimen. In a similar but more complicated way, any of the usual methods of fabrication cause the many crystals of which it is composed to assume a non-random distribution of orientations, often referred to as preferred orientations, or textures.

The relief of the internal strains in a fabricated metal by annealing proceeds only slowly at low temperatures (up to 600°C for most ferrous metals) without noticeable grain growth or change in grain orientation and is designated recovery. Near the point of complete relief, distinct changes occur in both grain size and grain orientation, and the material is said to recrystallise. At higher temperatures grain growth increases more rapidly. The specific temperatures necessary for both recovery and recrystallisation depend on the amount of previous deformation. Special orientations are also present in fabricated materials after recrystallisation.

In order to build up the required texture, rolling operation must be followed by a recrystallisation annealing at high temperature. Fig.5-34 shows schematically the preferred orientations of crystals in iron sheet after rolling and recrystallisation.

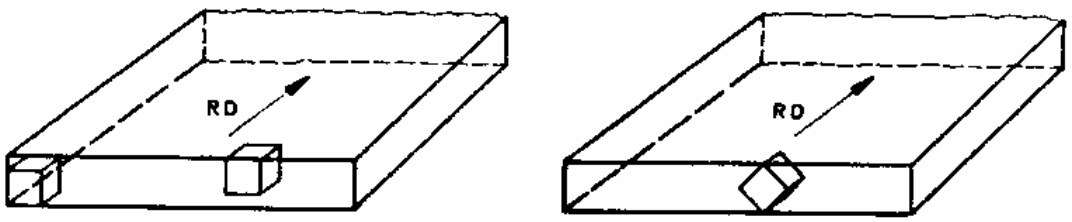

(a) (b)

Fig.5-34 The preferred orientations of crystals in iron sheet after rolling and recrystallisation (a) cubic texture, and (b) cube-on-edge or goss texture, where RD stands for rolling direction (from [217]).

Low-carbon steel sheet and pure iron can generally be considered as isotropic magnetic materials because they are fabricated by hot rolling, in which less tension is applied to the crystals to make them align with the preferred orientations, and most of the crystals are still randomly distributed.

Non-oriented silicon steel sheet is made by hot rolling almost to final thickness, pickling in acid to remove the oxide scale, slightly cold rolling to improve flatness, and batch annealing. More tension is applied to the crystals by cold rolling than by hot rolling, and hence, more crystals

take the preferred orientations, with [100] axes aligned with the rolling direction, as illustrated in Figs.5-34(a) and (b). Since better magnetic properties can be achieved in the preferred orientations, the greater the number of crystals aligned in the preferred orientations the higher the grade of the steel sheet. Stronger anisotropy, of course, is obtained in higher grade steel sheet. This was shown clearly by the loci of rotating **B** and **H** vectors in Fig.5-21 for Lycore-130 and Fig.5-25 for V270-35A non-oriented silicon steel sheets. Strictly speaking, these electrical steel sheets can be referred to as partially anisotropic magnetic materials, although technically, they are known as isotropic materials.

The fabrication of grain-oriented materials is much more complicated than non-oriented materials. Generally, grain-oriented silicon steel sheet is made by hot rolling to a thickness of about six or seven times of the final thickness, pickling in acid to remove the oxide scale, cold rolling to the final thickness, primary recrystallisation annealing in moist hydrogen, and secondary recrystallisation annealing in dry hydrogen to form the cube-on-edge texture.

In modern grain-oriented silicon steel sheet, such as ORIENTCORE.HI-B (commonly abbreviated to HI-B) by Nippon Steel Corporation, Japan, a high degree of grain orientation is obtained. The average deviations of <100> axis from the rolling direction are about 3^{o} in HI-B and about 7^{o} in conventional grain-oriented steel sheets. A surface coating which consists of a glass-film and a phosphate coating as shown in Fig.5-35, is used to improve the magnetic properties. The surface coating not only functions as interlaminar insulation, but also places the material under tensile stress in the rolling direction. This helps keep the preferred grain orientation.

The cube-on-edge texture makes the easy <100> directions in all grains almost parallel to one another and to the rolling direction of the sheet. The magnetic properties in this direction are therefore excellent, and almost all properties quoted by the manufacturers for grain-oriented sheet refer to this direction. The magnetic properties in the other directions in grain-oriented sheet are drastically inferior to those in the rolling direction, since the hard <111> direction and the medium <110> direction lie at 55^{o} and 90^{o} to the rolling direction in the plane of the sheet. This is also be confirmed by the loci of rotating **B** and **H** vectors of a grain-oriented steel sheet ORSI-100, reported in Fig.5-26.

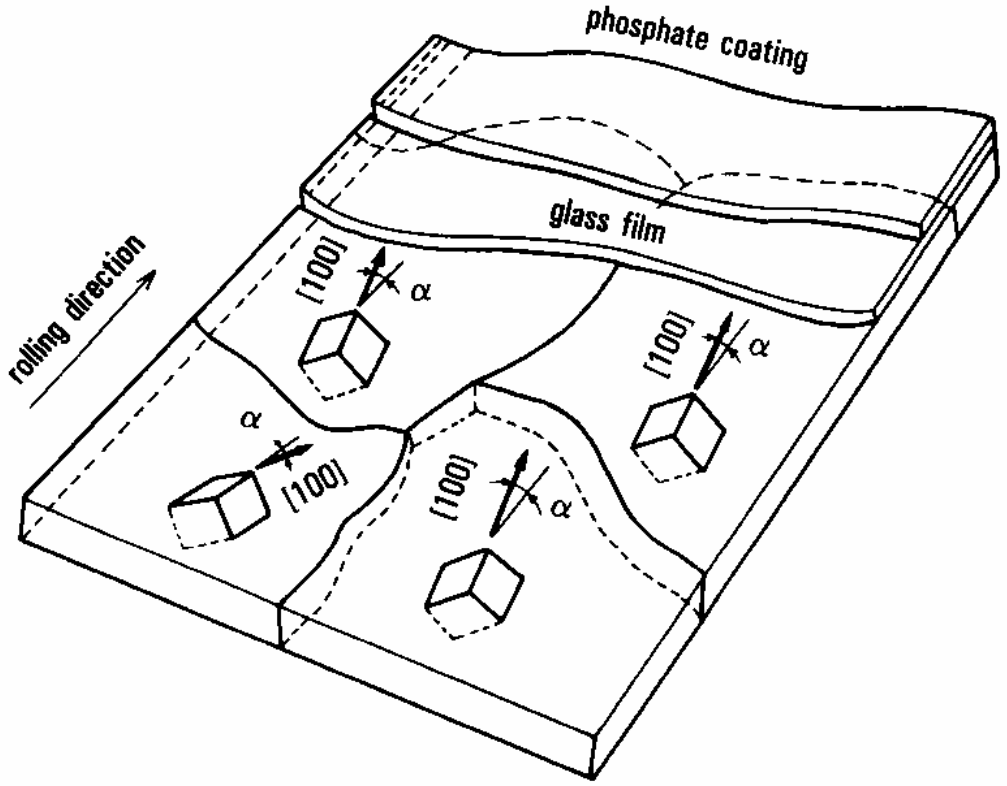

Fig.5-35 Schematic diagram of the surface coating of HI-B (from [216])

To have a quantitative comparison, the normal magnetisation curves, obtained by joining the tip points of alternating B/H loops, in the easy, medium, and hard directions were measured in a specimen of grain-oriented sheet steel ORSI-100 with alternating flux densities at 50 Hz using the single sheet rotational core loss tester at PTB, and plotted in Fig.5-36. Since the measurement was performed at 50 Hz, extra magnetic field strength was required to overcome the resistance of the eddy currents, but the level of flux density to saturate the specimen was not affected. At about 1.2 T, the specimen is saturated in the hard axis. Any further increase of flux density in this direction requires a great increase of magnetic field strength, and in turn the excitation current. If only alternating magnetic field is involved, this is not a problem, since the hard axis is almost never used as mentioned earlier. In rotational core loss measurement, however, the inferior magnetic property in the hard axis will certainly cause difficulty in saturating the specimen. This is believed to be the major reason why the highest flux density that can be reached is 1.2 T in grain-oriented materials, and 1.6 T in non-oriented materials. This is also believed to be a problem for other kinds of rotational core loss testers whenever the flux density vector is to be controlled.

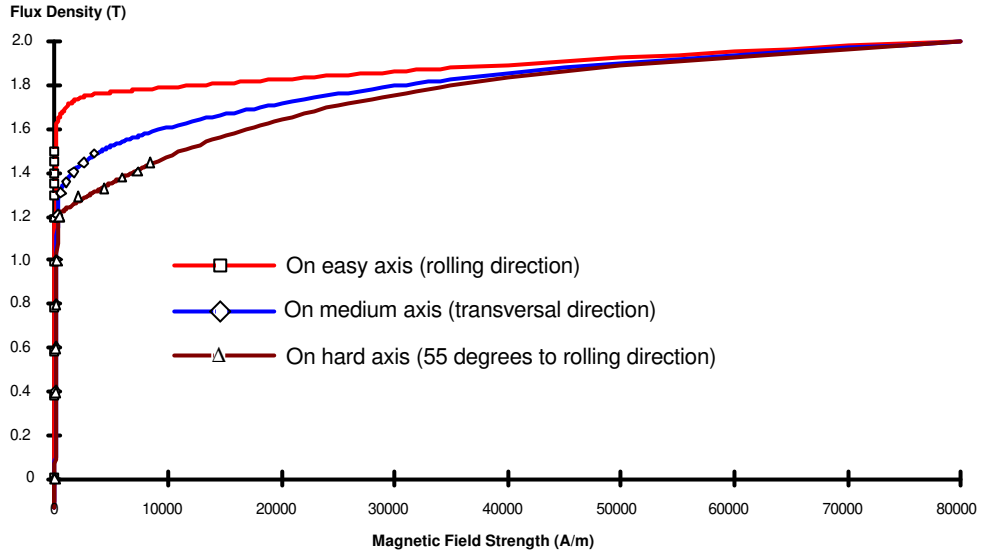

Fig.5-36 Normal magnetisation curves of ORSI-100 on the easy, medium, and hard axis at 50 Hz

To solve the problem, the time constant of the control system must be very small so that it responds quickly to meet the requirement of sudden increase of excitation current when the rotating magnetic flux density vector is on the hard axis. A two channel power amplifier of large capacity and bandwidth is also necessary.

5.5.2 More Discussion about Total Loss P_t and Rotational Loss P_r

Fig.5-37 compares the losses in a specimen of non-oriented silicon steel sheet Lycore-130 with elliptically and purely circular rotating magnetic flux densities and throws further light on the meaning of P_r. Curves 1 and 2 are P_t and P_r, calculated by (5.20) and (5.23), with an elliptical flux density at 50 Hz versus the axis ratio, which is defined as the ratio of the major axis to the minor axis of the elliptical flux density. The major axis is on the X axis and fixed at 1.25 T. Curve 3 plots the total loss with a purely circular rotating magnetic flux density against B/B_{max}, where B_{max}=1.25 T, the same B_{max} value used for the results with elliptically rotating magnetic flux density. The figure shows that P_r (Curve 2) with an elliptically rotating magnetic flux density is higher than that with a purely circular rotating magnetic flux density, when the circular flux density equals the resolved rotational component of the elliptical flux density. This implies that P_r with an elliptical flux density depends not only on the resolved rotational component of the flux density, but also on some other components as well.

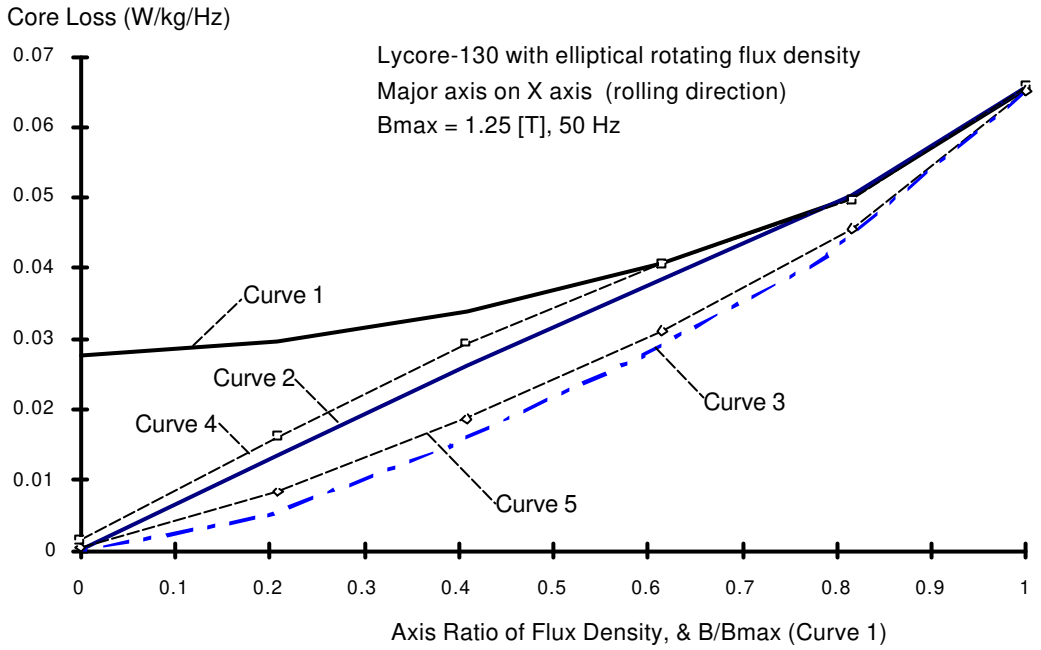

Fig.5-37 Comparison of core losses with elliptical flux and with circular flux at 50 Hz

Further conclusions can be drawn by resolving the elliptical magnetic field strength and flux density into alternating and rotational components. Using Fourier series expansions, (5.20) becomes

$$P_t = \frac{1}{T\rho_m}\int_0^T (\Sigma \mathbf{H}_k)\cdot(\Sigma \frac{d\mathbf{B}_k}{dt})dt = \frac{1}{T\rho_m}\Sigma\int_0^T \mathbf{H}_k\cdot\frac{d\mathbf{B}_k}{dt}dt \tag{5.26}$$

where $\mathbf{H}_k$ and $\mathbf{B}_k$ (k=1,3,5,...) are the *k*-th harmonics of $\mathbf{H}$ and $\mathbf{B}$, and $\mathbf{H}_k$ and $\mathbf{B}_k$ are both elliptically rotating vectors. These vectors can be further resolved into rotational components and alternating components, as $\mathbf{H}_k = \mathbf{H}_{rk}+\mathbf{H}_{ak}$, where $\mathbf{H}_{rk}$ is a purely circular rotating magnetic field strength of constant velocity and magnitude, and $\mathbf{H}_{ak}$ an alternating magnetic field strength, and similarly for $\mathbf{B}_k$. Thus, the total loss P_t in (5.26) can be divided into four portions as follows

$$\begin{aligned} P_t &= \frac{1}{T\rho_m}\Sigma\int_0^T \mathbf{H}_{rk}\cdot\frac{d\mathbf{B}_{rk}}{dt}dt + \frac{1}{T\rho_m}\Sigma\int_0^T \mathbf{H}_{ak}\cdot\frac{d\mathbf{B}_{rk}}{dt}dt \\ &+ \frac{1}{T\rho_m}\Sigma\int_0^T \mathbf{H}_{rk}\cdot\frac{d\mathbf{B}_{ak}}{dt}dt + \frac{1}{T\rho_m}\Sigma\int_0^T \mathbf{H}_{ak}\cdot\frac{d\mathbf{B}_{ak}}{dt}dt \\ &= P_1 + P_2 + P_3 + P_4 \end{aligned} \tag{5.27}$$

where $\mathbf{H}_{rk}$, $\mathbf{H}_{ak}$, $\mathbf{B}_{rk}$, and $\mathbf{B}_{ak}$, are the rotational and the alternating components of $\mathbf{H}_k$ and $\mathbf{B}_k$, and P_i, i = 1,2,...,4 are the four loss components corresponding to the integral terms.

In Fig.5-37, the total loss P_t (Curve 1) with an elliptically rotating magnetic flux density is resolved into four portions by the method outlined above, and the losses P_1+P_2 and $P_1+P_2+P_3$ are plotted as the curves 4 and 5. It can be seen that P_1+P_2 (Curve 5) is close to the loss measured with a circular flux density (Curve 3), and this is consistent with the fact that both P_1 and P_2 contain $d\mathbf{B}_r/dt$, and P_3 and P_4 contain $\mathbf{B}_a$ which is zero for a purely circular rotating magnetic flux density. It can also be seen that $P_1+P_2+P_3$ (Curve 4) is close to P_r (Curve 2) calculated by (5.23), and this is consistent with the fact that P_3 depends on $\mathbf{H}_r$. P_4 is the only term containing both $\mathbf{H}_a$ and $\mathbf{B}_a$, and should not contribute to a rotational component of core loss.

Therefore, the rotational loss P_r with an elliptical flux density depends on the rotational components of both the magnetic field strength and flux density, and is only a fraction of the total loss P_t.

5.6 CONCLUSION

The developed square specimen tester can be successfully used for both alternating and rotational core loss measurements with arbitrary magnetic flux patterns. The precision of magnetic field measurement in a two dimensional single sheet tester is improved by the sandwich arrangement of magnetic field sensing coils.

The rotational core loss of a non-grain-oriented electrical steel, Lycore-130, has been measured with purely circular and elliptically rotating magnetic flux densities for up to 1.6 T over a range of frequencies from 1 to 200 Hz.

Because of insufficient time, it has not been possible to complete and include the results of an inter-comparison between the rotational core loss testers at PTB and UTS. Much useful information was obtained, however, from the measurements on grain-oriented silicon steel sheet ORSI-100 and non-oriented silicon steel sheet V270-35A with both alternating and rotating magnetic flux densities using the tester at PTB.

The ratio of rotational core loss to alternating core loss is about 2 for both grain-oriented and non-oriented materials for a wide range of flux density (up to 1.2 T in grain-oriented steel sheet and up to 1.6 T in non-oriented steel sheet). This is consistent with the results reported by other researchers [127,132,138]. This, however, does not mean that the total rotational core loss with a circular flux density is the sum of the alternating core losses on the X and Y axes, since the mechanisms are different.

Mathematical derivation and experimental measurements of rotational core losses in both grain-oriented and non-oriented magnetic materials have shown that equations (4.15), (5.20), and (5.23) are identical with a circular flux density, but with an elliptical flux density, equation (4.15) is incorrect for calculating P_r, since the angular speed varies with time. It was also found that the error caused by using a constant angular speed in (4.15) depended on the magnetic anisotropy of the material. The stronger the anisotropy of the material, the larger the error of equation (4.15).

Further analysis in section 5.5.2 has shown that with an elliptical flux density, rotational loss P_r is only a fraction of total loss P_t, and should never exceed P_t. By resolving the magnetic field strength and flux density into rotational and alternating components, the total loss P_t can be divided into four portions, and P_r is possibly explained by the first three portions in (5.27).

The experimental results have shown that the magnetic anisotropy of materials played an important role in rotational core loss measurement with a circular flux density. Because of the higher degree of grain orientation, or stronger anisotropy, the alternating core loss on the easy axis (rolling direction) in grain-oriented materials is generally smaller than that in non-oriented materials, but the rotational core loss in grain-oriented materials is not always smaller than that in non-oriented materials because the magnetic properties on the medium and hard axes in grain-oriented materials are much inferior to those in non-oriented materials.

The analysis of the magnetic anisotropy due to the textures of magnetic materials and the measurements of the normal magnetisation curves on the easy, medium, and hard axes in a specimen of grain-oriented silicon steel sheet ORSI-100 revealed that the difficulty in flux density waveform control, when the specimen was to be saturated by a purely circular rotating flux density, could be attributed to the inferior magnetic properties on the hard axis of the specimen. This problem is common for any rotational core loss testers whenever the flux

density waveforms are to be controlled. In order to saturate the specimen with a rotating flux density, the control system must be improved to have a much quicker current response to meet the requirement of a sudden increase of excitation current.

CHAPTER 6. MODELLING OF ROTATIONAL CORE LOSSES

6.1 INTRODUCTION

In this chapter, rotational core losses with various kinds of rotating magnetic fluxes are modelled. Because of the very complicated mechanisms, as discussed in chapter 4, it has not been possible to develop models with a physical background. Instead, phenomenological models have been developed, and applied to core loss analysis in rotating electrical machines.

In section 6.2, the purely circular rotational core loss of a non-oriented silicon steel sheet, Lycore-130, is first separated into rotational hysteresis, eddy current, and anomalous losses using a conventional core loss separation procedure, and then modelled by a three term model generalised from the corresponding alternating core loss model.

Section 6.3 presents a novel analogical approach to rotational hysteresis loss based on the strong analogy between the profile of rotational hysteresis loss per cycle versus flux density and the torque/slip curve of a single phase induction machine. The rotational hysteresis losses of different magnetic materials reported by various researchers and the author show excellent agreement with the model.

In section 6.4, a new formulation for predicting the total core loss with an elliptically rotating flux density from the core losses with a purely circular rotating flux density and with a purely alternating flux density is reported. Experimental verification is also given.

Section 6.5 outlines the method used for core loss analysis in rotating electrical machines. The finite element method was used to determine the magnetic field distribution in a permanent magnet motor. The locus of the rotating magnetic flux density vector in each finite element was assembled from a sequence of finite element solutions. The total core loss dissipated in each element was then calculated according to the locus of flux density in that element. A model of the core losses with an arbitrary two dimensional rotating magnetic flux density based on the models reported in the previous sections is presented in this section. The predicted results are compared with the experimental data.

6.2 ROTATIONAL CORE LOSS SEPARATION WITH A CIRCULAR FIELD

As for alternating core loss, rotational core loss (in W/kg) can also be separated into three portions as [184]

$$P_r = P_{hr} + P_{er} + P_{ar} \tag{6.1}$$

where P_{hr} is rotational hysteresis loss, P_{er} rotational eddy current loss, and P_{ar} rotational anomalous loss.

With a purely circular rotating magnetic flux density, the rotational eddy current loss in thin laminations can be calculated by

$$P_{er} = 2C_e(fB)^2 \tag{6.2}$$

where $C_e = \dfrac{\pi^2 b^2 \sigma}{6\rho_m}$ is the coefficient of eddy current loss, the same for both rotational and alternating eddy current losses, b the thickness of the lamination, σ the conductivity, ρ_m the material mass density, f the frequency, and B the magnitude of the rotating flux density.

Similarly, the rotational anomalous loss is given by

$$P_{ar} = C_{ar}(fB)^{3/2} \tag{6.3}$$

where C_{ar} is the coefficient of rotational anomalous loss, a function of flux density. C_{ar} eventually reduces to zero when the material is saturated and all magnetic domain walls disappear [219].

This model has been employed to separate the rotational core loss of Lycore-130, reported in section 5.3.2, Fig.5-24. First, the curves of the total rotational loss per cycle P_r/f versus frequency were extrapolated to f=0 Hz to obtain the rotational hysteresis loss per cycle P_{hr}/f. In the calculation of P_{er}/f, the theoretical C_e was assumed. Subtracting $P_{hr}/f+P_{er}/f$ from P_r/f, the rotational anomalous loss per cycle P_{ar}/f was obtained. Finally, C_{ar} was obtained by fitting over a range of B and f values, and found to be a constant over a range of B up to 1.4 T. Fig.6-1 illustrates this separation procedure when B=0.5, 0.7, 0.9, 1.0, 1.2, and 1.4 T. The deduced parameters are $C_e=6.54\times10^{-5}$ W/kg/T^2/Hz^2, and $C_{ar}=1.07\times10^{-3}$ W/kg/T$^{1.5}$/Hz$^{1.5}$.

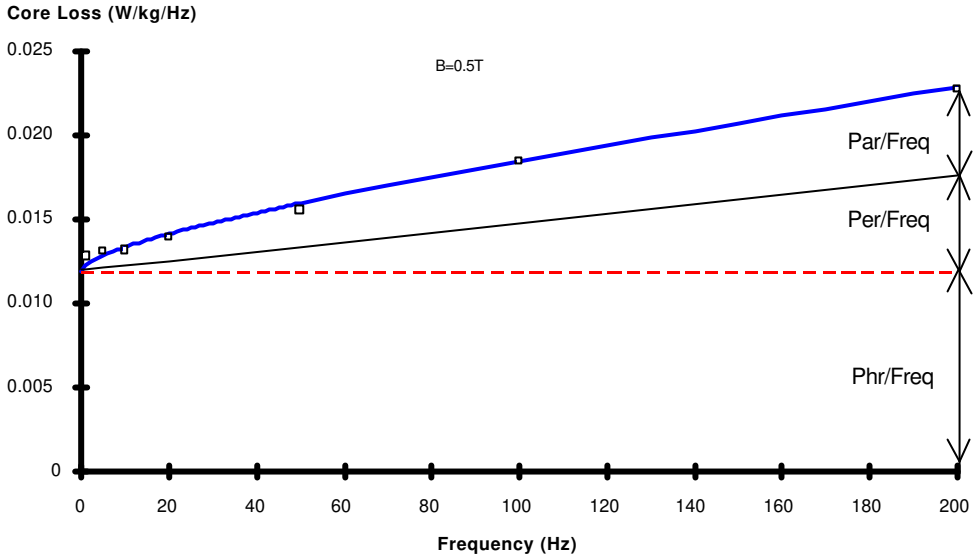
Core Loss (W/kg/Hz)
B=0.5T
Par/Freq
Per/Freq
Phr/Freq
0.025
0.020
0.015
0.010
0.005
0
0
20
40
60
80
100
120
140
160
180
200
Frequency (Hz)

(a)

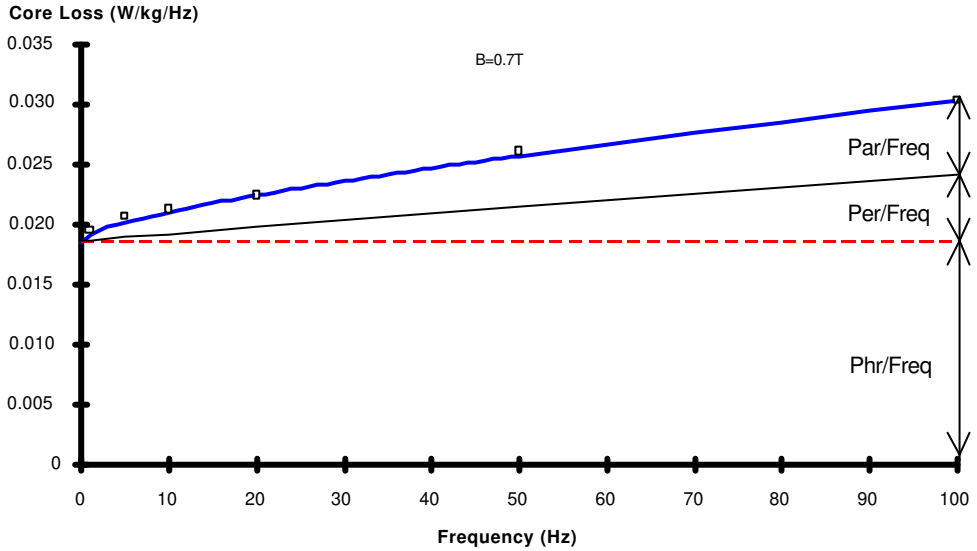
Core Loss (W/kg/Hz)
B=0.7T
Par/Freq
Per/Freq
Phr/Freq
0.035
0.030
0.025
0.020
0.015
0.010
0.005
0
0
10
20
30
40
50
60
70
80
90
100
Frequency (Hz)

(b)

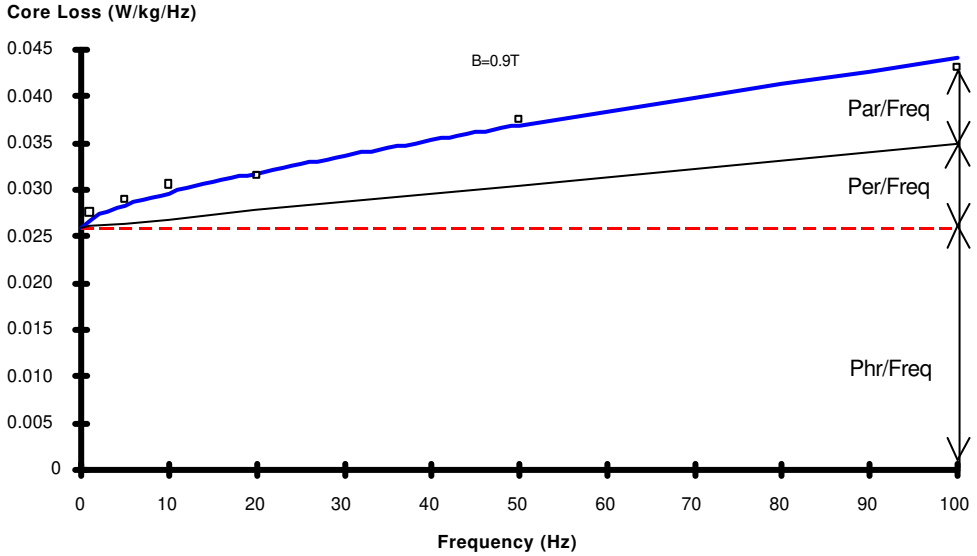
Core Loss (W/kg/Hz)
B=0.9T
Par/Freq
Per/Freq
Phr/Freq
0.045
0.040
0.035
0.030
0.025
0.020
0.015
0.010
0.005
0
0
10
20
30
40
50
60
70
80
90
100
Frequency (Hz)

(c)

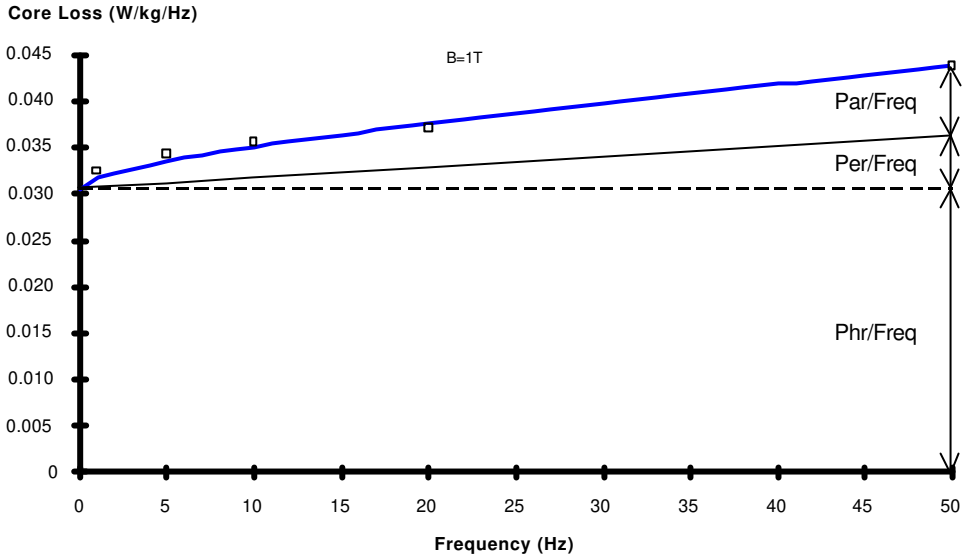

(d)

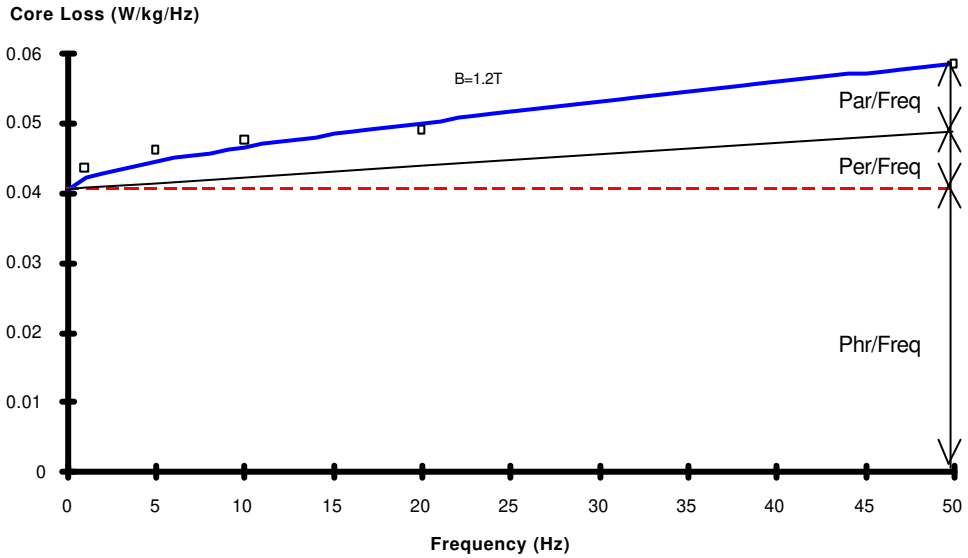

(e)

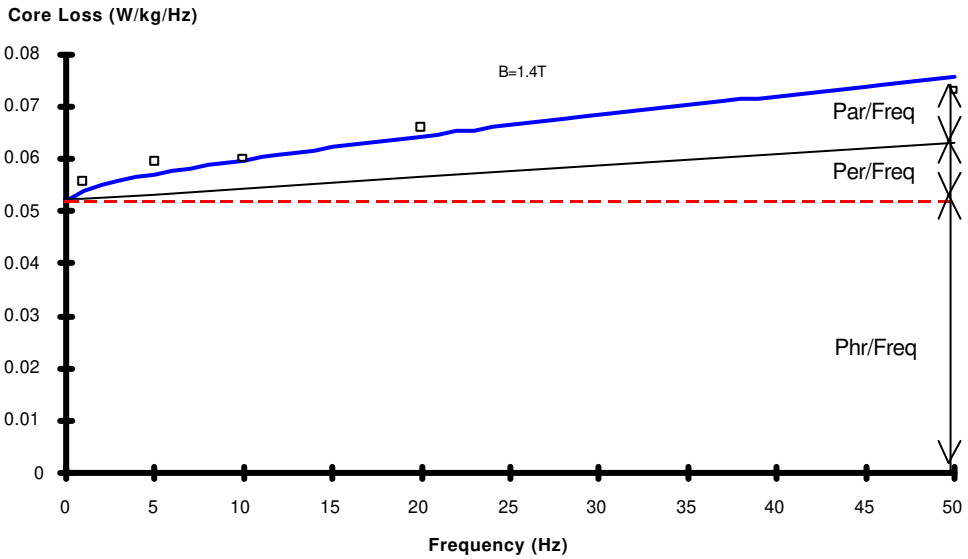

(f)

Fig.6-1 Rotational core loss separation of Lycore-130 at (a) 0.5, (b) 0.7, (c) 0.9, (d) 1.0, (e) 1.2, (f) 1.4 T

6.3 A MODEL FOR ROTATIONAL HYSTERESIS LOSS WITH A CIRCULAR FIELD

As discussed in section 4.4, rotational hysteresis loss was first modelled by Archenhold, Sandham, and Thompson [126] using the basic Stoner-Wohlfarth model (4.17) of a small particle in 1960, but the discrepancy between the experimental and the predicted results was enormous, as illustrated in Fig.4-27. In 1962, Strattant and Young [137] simulated rotational hysteresis loss with elliptically rotating magnetic fields, using an empirical model (4.19) without any physical background. The error between the calculated and measured losses was also large as shown in Fig.4-29.

This section presents an analogical model for rotational hysteresis loss with a circular field, based on the strong analogy between the curve of rotational hysteresis loss versus flux density or magnetisation and the torque/slip curve of a single phase induction machine.

6.3.1 Rotational Hysteresis Loss

With a purely circular rotating flux density at low speed, the instantaneous torque due to rotational hysteresis is proportional to the cross product of the rotating flux density or magnetisation vector and the rotating magnetic field strength vector, as described by (5.22). For the convenience of analysis, it is restated here as

$$T_r = \mu_0|\mathbf{M}\times\mathbf{H}| = \mu_0 MH\sin\delta \tag{6.4}$$

where T_r is the torque due to rotational hysteresis of the magnetic material, M the magnitude of the magnetisation vector **M**, H the magnitude of the magnetic field vector **H**, and δ the angle difference between vectors **H** and **M**. Because $\mathbf{B}=\mu_0(\mathbf{H}+\mathbf{M})$, and $\mathbf{B}\times\mathbf{H}=\mu_0\mathbf{M}\times\mathbf{H}$, M in (6.4) can be replaced by B, and δ is then the angle difference between **H** and **B**. Since the angular speed of the flux density vector is constant, the average hysteresis loss equals the average torque multiplied by the constant angular speed, as shown in equation (5.23).

Fig.6-2 illustrates the rotational hysteresis loss in 3% non-oriented silicon steel at 1 Hz reported by Cecchitti, *et al*, [131] in 1978. At first, the rotational hysteresis loss increases with the magnitude of rotating magnetisation slowly, segment *a-b* in Fig.6-2. Above a certain magnetisation level, about 0.6-0.7 of the saturation magnetisation, the increment of rotational hysteresis loss becomes larger and larger with increasing magnitude of magnetisation, segment *b-c* in Fig.6-2. After reaching the maximum value at about 0.8 of the saturation magnetisation,

point *c* in Fig.6-2, the rotational hysteresis loss drops quickly to zero when the specimen is saturated, segment *c-d* in Fig.6-2.

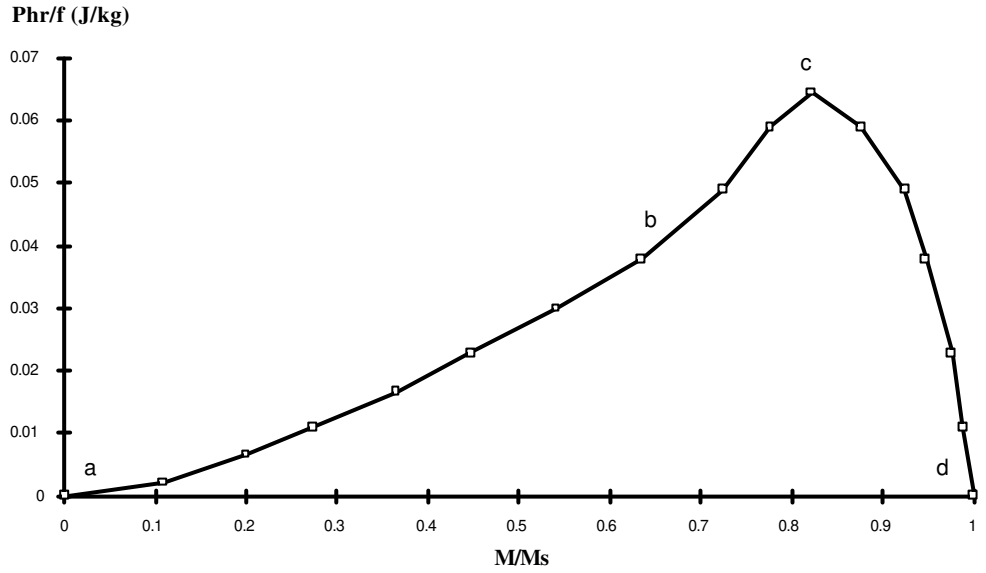

Fig.6-2 Rotational hysteresis loss in non-oriented 3% silicon steel measured at 1 Hz (after [131])

The shape of the hysteresis loss curve in Fig.6-2 can be explained qualitatively by using the domain theory of magnetisation. Consider an isotropic specimen of a simple domain structure as shown in Fig.6-3. The magnetic domains, large or small each saturated to saturation magnetisation M_s, are equally distributed along two easy axes of magnetisation at right angles to one another. In the unmagnetised state, the magnetic domains are balanced, and the resultant magnetisation is zero. The average torque and hence the rotational hysteresis loss is zero when the magnetisation or flux density is zero, point *a* in Fig.6-2.

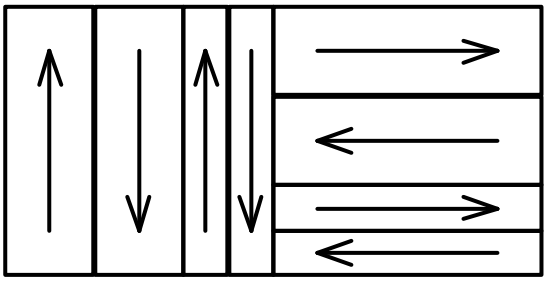

Fig.6-3 Magnetic domain structure of an isotropic specimen in the unmagnetised state

As the applied magnetic field strength increases, the volumes of the magnetic domains whose orientations are close to the direction of the magnetic field increase and the volumes of the oppositely oriented magnetic domains decrease, as illustrated in Fig.6-4(a). The amount of domain wall movement depends on the magnitude of the applied magnetic field strength. Thus, a nonzero resultant magnetisation is induced. When the applied magnetic field rotates, the resultant magnetisation vector follows the field vector. Because of the pinning of domain walls by defect sites inside the specimen, which causes an opposing force to resist any changes in magnetisation, as discussed in section 2.1, there exists an angle difference between the field and the magnetisation vectors. When the magnitude of the applied magnetic field strength is small, there is no domain wall annihilation and creation involved in the domain wall movement, as illustrated in Figs.6-4(a)-(c) when the induced magnetisation vector rotates for 90°. The rotational hysteresis loss is small, and increases slowly with the magnetisation, as illustrated by segment *a-b* in Fig.6-2.

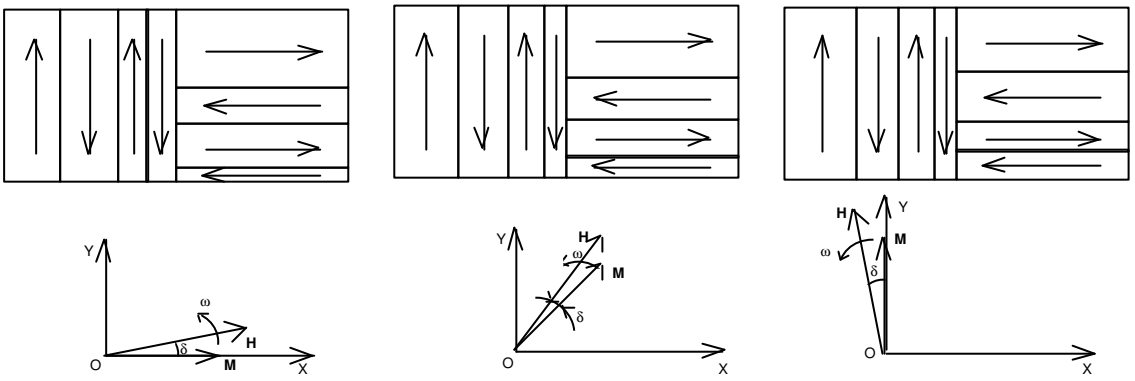

(a) (b) (c)

Fig.6-4 Domain wall movement when a small magnetisation vector rotates to 90° from position (a) 0°, to (b) 45°, and further to (c) 90°

As the applied magnetic field strength increases, smaller magnetic domains with opposing magnetisation direction will disappear, and as the applied field rotates, reappear again when they are no longer in the opposing direction, as shown in Fig.6-5. Since extra energy is required for the annihilation and recreation of magnetic domain walls, the rotational hysteresis loss increases quickly with the increasing magnetisation, as illustrated by segment *b-c* in Fig.6-2.

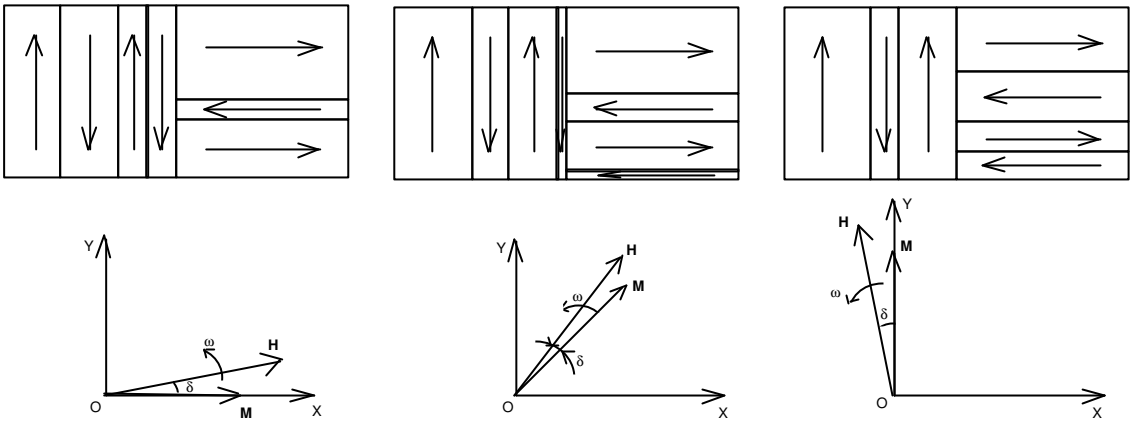

Fig.6-5 Domain wall movement when a large magnetisation vector rotates to 90° from position (a) 0°, to (b) 45°, and further to (c) 90°

When the specimen is close to saturation, there remain only a few large domains, and these domains begin to rotate with the applied magnetic field, that is, the magnetic domain walls will jump onto the other easy axis in order to be less inclined to the applied magnetic field, as shown in Fig.6-6. This is feasible since there are fewer domain walls by then and hence less hysteresis to the movement of domain walls. The rotational hysteresis loss falls quickly with the increasing magnetisation, corresponding to segment *c-d* in Fig.6-2.

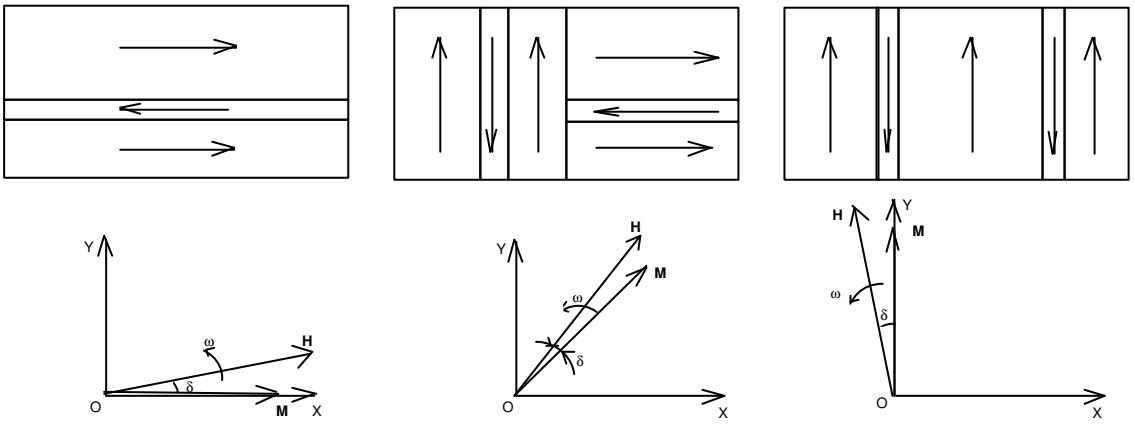

Fig.6-6 Domain wall movement when the specimen is close to saturation, and the magnetisation vector rotates to 90° from position (a) 0°, to (b) 45°, and further to (c) 90°

When the specimen is deeply saturated, all magnetic domain walls disappear, and there remains only one large magnetic domain, as illustrated in Fig.6-7. Therefore, the resistance to

the rotation of this domain due to rotational hysteresis reduces to zero, and so does the rotational hysteresis loss, corresponding to point *d* in Fig.6-2.

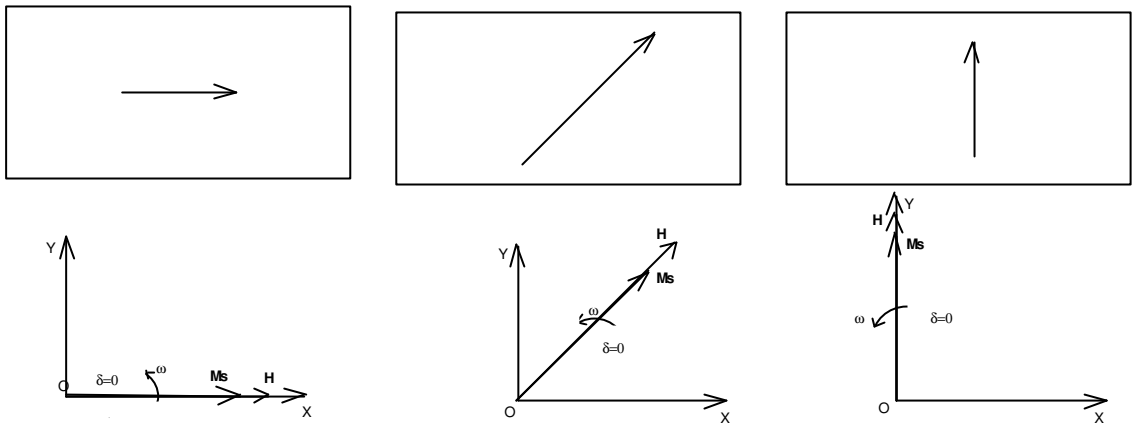

(a) (b) (c)

Fig.6-7 Domain rotation when the specimen is deeply saturated, and the magnetisation vector rotates to 90° from position (a) 0°, to (b) 45°, and further to (c) 90°

Of course, the mechanism of rotational hysteresis is still far from being fully understood yet. The actual magnetic domain configurations at different magnetisation levels are much more complicated than those illustrated above, so the above explanation only provides an approximate qualitative understanding of rotational hysteresis.

6.3.2 Electromagnetic Torque in a Single Phase Induction Machine

In a single phase induction machine, the instantaneous electromagnetic torque acting on the rotor can be calculated by

$$T_r = K\Phi_s\Phi_r\sin\delta \tag{6.5}$$

where K is a constant coefficient, Φ_s the resultant rotating component of the stator magnetic flux, Φ_r the resultant rotating component of the rotor magnetic flux, which is induced by the stator magnetic flux, and δ the angle between the vectors Φ_s and Φ_r.

In terms of the machine circuit parameters, the resultant electromagnetic torque can be calculated by

$$T_r = T_f + T_b \tag{6.6}$$

where

$$T_f = \frac{V^2}{2\omega_{syn}} \frac{R_2 / s}{(R_1 + R_2 / s)^2 + (X_1 + X_2)^2}$$

and

$$T_b = -\frac{V^2}{2\omega_{syn}} \frac{R_2 / (2 - s)}{(R_1 + R_2 / (2 - s))^2 + (X_1 + X_2)^2}$$

are the electromagnetic torques generated by the forward and the backward rotating stator and rotor magnetic fluxes, V is the terminal voltage of the stator winding, R_1 and X_1 are the resistance and the leakage reactance of the stator winding, R_2 and X_2 are the resistance and the leakage reactance of the rotor winding referred to the stator side, respectively, $s = \frac{\omega_{syn} - \omega_r}{\omega_{syn}}$ is the slip, ω_r the rotor speed, and ω_{syn} the synchronous speed, or the speed of the rotating stator magnetic flux.

Fig.6-8 illustrates the torque/slip curve of a single phase induction motor. When the rotor is at standstill, both the stator and rotor fluxes are alternating. The resultant rotating stator and rotor fluxes equal zero. An alternating magnetic flux can be resolved into two rotating flux components of identical magnitudes but opposite rotating directions. The electromagnetic torques generated by the forward and the backward rotating magnetic fluxes cancel each other, and hence the resultant torque equals zero, point *a* in Fig.6-8.

If the rotor rotates in the forward direction, the backward rotating components of both the stator and the rotor magnetic fluxes are weakened, while the forward rotating components are enhanced. The resultant rotating components of the stator and rotor magnetic fluxes are no longer zero, and the magnitudes of these resultant rotating fluxes increase when the rotor speed increases. Therefore, the resultant electromagnetic torque also increases with increasing rotor speed.

At a low speed (high slip), a large emf at a high frequency is induced in the rotor winding, but the resultant rotating rotor flux is small. Because of the high rotor frequency, the angle difference between Φ_s and Φ_r is dominated by the rotor winding inductance, and thus δ is small. Therefore, the resultant torque increases slowly with the rotor speed, segment *a-b* in Fig.6-8. When the rotor speed increases (slip decreases), the effect of the rotor winding resistance becomes significant, and a larger δ is obtained. The resultant electromagnetic torque also increases more quickly, segment *b-c* in Fig.6-8. When the effect of the rotor winding resistance balances with the effect of the rotor winding inductance, the maximum resultant

torque is obtained, point *c* in Fig.6-8. When the speed is close to the synchronous speed (very small slip), δ is dominated by the rotor winding resistance, and is close to 90°. The backwardly rotating stator and rotor fluxes are negligible. Because the relative speed between the rotor winding and the rotating fluxes is very small, the induced emf is very small at a very low rotor frequency. Therefore the resultant torque drops quickly, segment *c*-*d* in Fig.6-8, and reaches zero slightly before the rotor speed reaches the synchronous speed, point *d* in Fig.6-8, because of the existence of a very small backward torque.

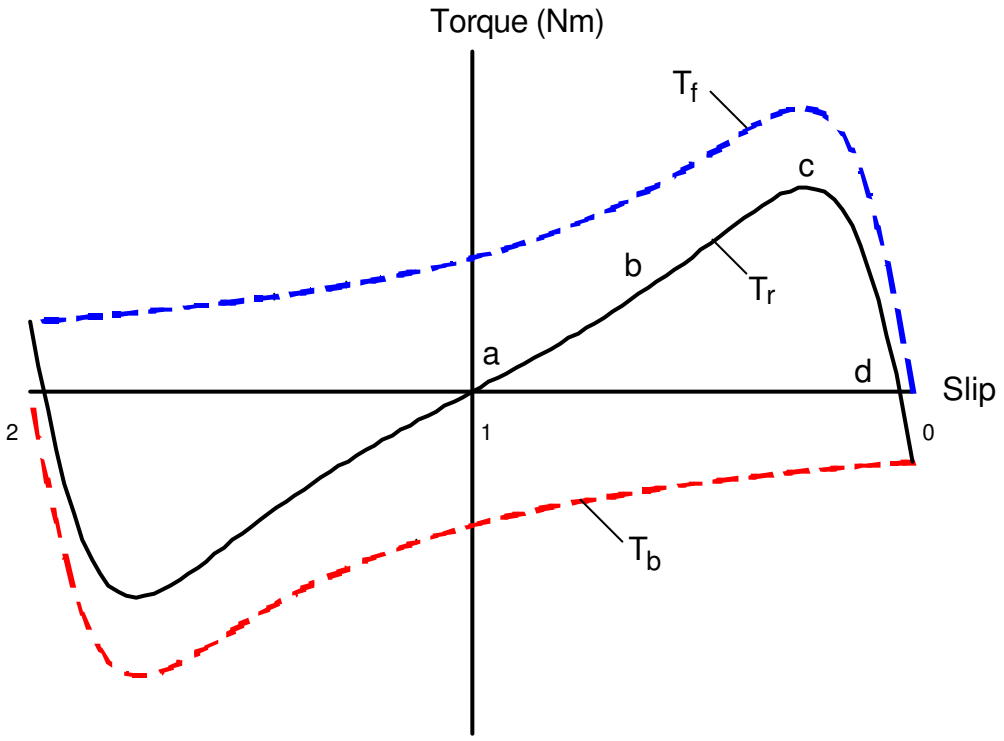

Fig.6-8 Torque/slip curve of a single phase induction machine, where T_f and T_b are electromagnetic torques generated by the forward and the backward rotating fluxes, respectively, and $T_r = T_f + T_b$ is the resultant electromagnetic torque.

6.3.3 An Analogical Approach to Rotational Hysteresis Loss

From the analysis in sections 6.3.1 and 6.3.2, it can be seen that there exists a strong analogy between the rotational hysteresis loss in an electrical steel sheet and the resultant electromagnetic torque in a single phase induction machine, although the mechanisms are rather different.

Fig.6-9 illustrates the analogy between the rotational hysteresis loss per cycle in an electrical steel sheet and the torque in a single phase induction machine. It can be seen that the

torque/slip curve of a single phase induction machine can be readily adapted to model the rotational hysteresis loss per cycle in an electrical steel sheet.

Let $a_1 = \dfrac{V^2}{2\omega_{syn} R_2}$ (in J/kg or Erg/cm^3), $a_2 = \dfrac{R_1}{R_2}$ (non-dimensional), and $a_3 = \left(\dfrac{X_1 + X_2}{R_2}\right)^2$ (non-dimensional). Equation (6.6) can be adapted to model rotational hysteresis loss as

$$P_{hr}/f = a_1 \left[\frac{1/s}{(a_2 + 1/s)^2 + a_3} - \frac{1/(2-s)}{(a_2 + 1/(2-s))^2 + a_3} \right] \tag{6.7}$$

with fewer parameters, where P_{hr}/f is the rotational hysteresis loss per cycle, and f is the frequency. When (6.7) is used to model the loss per cycle due to the rotational hysteresis in an electrical steel sheet, the slip can be defined as

$$s = 1 - \frac{M}{M_s'} = 1 - \frac{M}{M_s}\frac{M_s}{M_s'} \tag{6.8}$$

where M_s' is the intercept of the fictitious induction motor forwards field torque/slip curve with the zero torque axis, as shown in Fig.6-9.

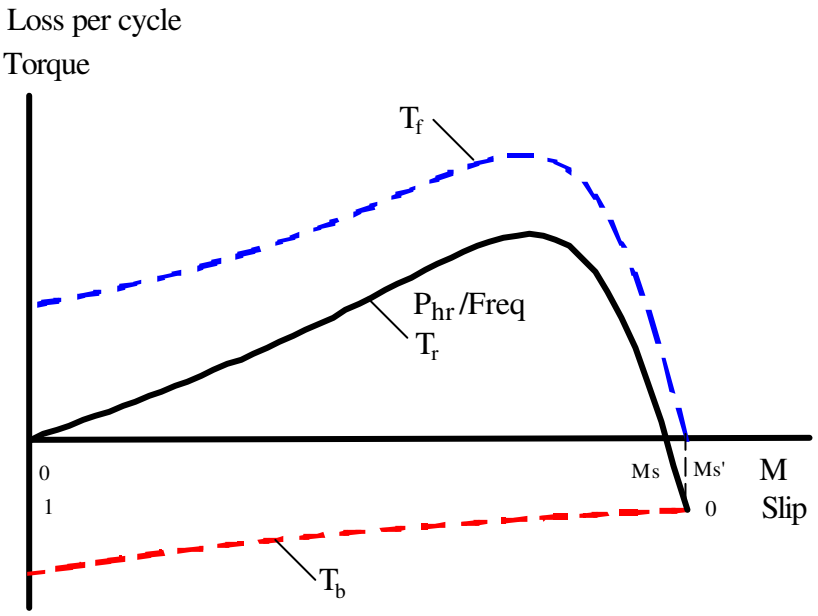

Fig.6-9 Analogy between torques due to rotational hysteresis and due to induced rotor current

Let $P_{hr}/f=0$, and one obtains

$$s_1 = 1, \qquad \text{for } M=0 \tag{6.9}$$

and

$$s_{2,3} = 1 \mp \sqrt{1 - \frac{1}{a_2^2 + a_3}} \qquad \text{for } M=\pm M_s \tag{6.10}$$

From the definition of s, we have

$$s_2 = 1 - \frac{M_s}{M_s'} \tag{6.11}$$

Hence,

$$\frac{M_s}{M_s'} = \sqrt{1 - \frac{1}{a_2^2 + a_3}} \tag{6.12}$$

and (6.8) can be rewritten as

$$s = 1 - \frac{M}{M_s}\sqrt{1 - \frac{1}{a_2^2 + a_3}} \tag{6.13}$$

It is postulated that the rotational hysteresis loss per cycle in an electrical steel sheet can be expressed by (6.7) and (6.13) in terms of three parameters, a_1, a_2, and a_3.

6.3.4 Verification of the Model

The model is verified by fitting the curves of hysteresis loss per cycle versus magnetisation or flux density for different electrical steel sheets reported by various researchers and measurements reported earlier in this chapter. To assess the accuracy of the model, an error estimator is employed. The error is defined as

$$\begin{aligned} \text{Err} &= \frac{\sigma}{\text{Max}\left\{P_{i(\text{Test})}\right\}} \\ &= \frac{\sqrt{\dfrac{1}{N-1}\sum_{i=1}^{N}\left(P_{i(\text{Test})} - P_{i(\text{cal})}\right)^2}}{\max\left\{P_{i(\text{Test})}\right\}} \end{aligned} \tag{6.14}$$

where σ is the standard deviation, N is the number of measured data, $P_{i(Test)}$ and $P_{i(Cal)}$ (i=1,2,...,N) are the measured and calculated losses, respectively, and max{} is a function to find the maximum element in an array. The curve fitting was performed using an optimisation routine to minimise the error. The results are reported below.

Fig.6-10 to Fig.6-16 plot the measured and predicted curves of rotational hysteresis losses per cycle in different materials with a circular field, and Table 6-1 lists the corresponding model parameters and the errors. In the curve fitting of the rotational hysteresis loss per cycle of Lycore-130 deduced from the loss separation in section 6.2, the saturation flux density B_s was also taken as a model parameter, since the specimen was not saturated in the measurement. It was determined that B_s = 1.80 T for Lycore-130.

From the curve fittings shown in Fig.6-10 to Fig.6-16 and Table 6-1, it can be seen that the agreement between the measured hysteresis losses for a circular field and the predicted results in different magnetic materials is excellent.

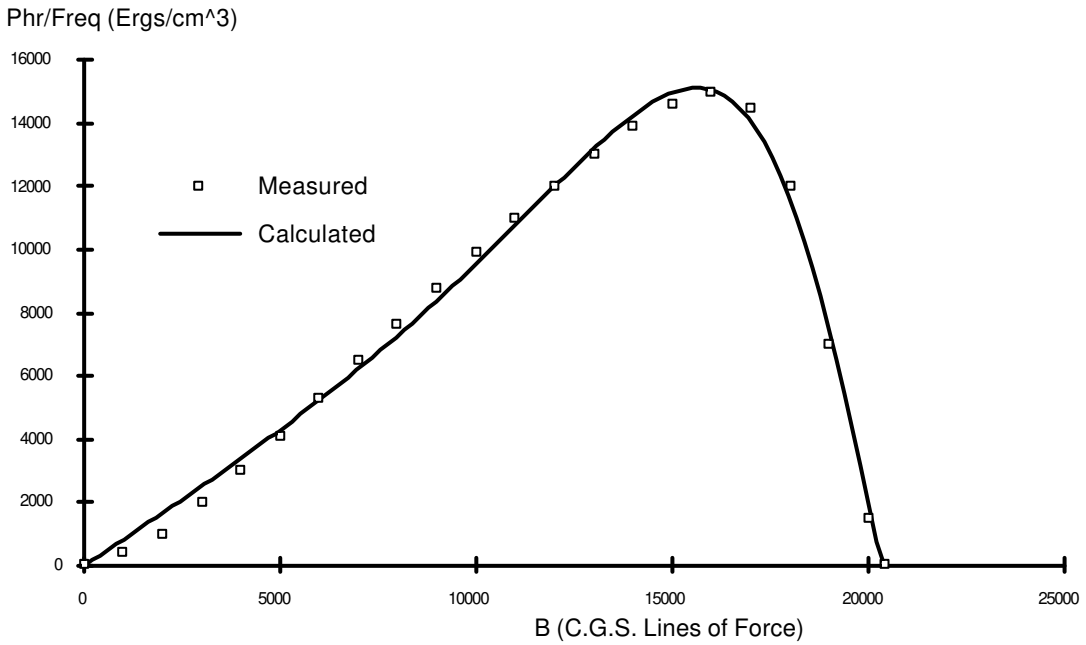

Fig.6-10 Modelling of rotational hysteresis loss in soft iron measured by Baily [120]

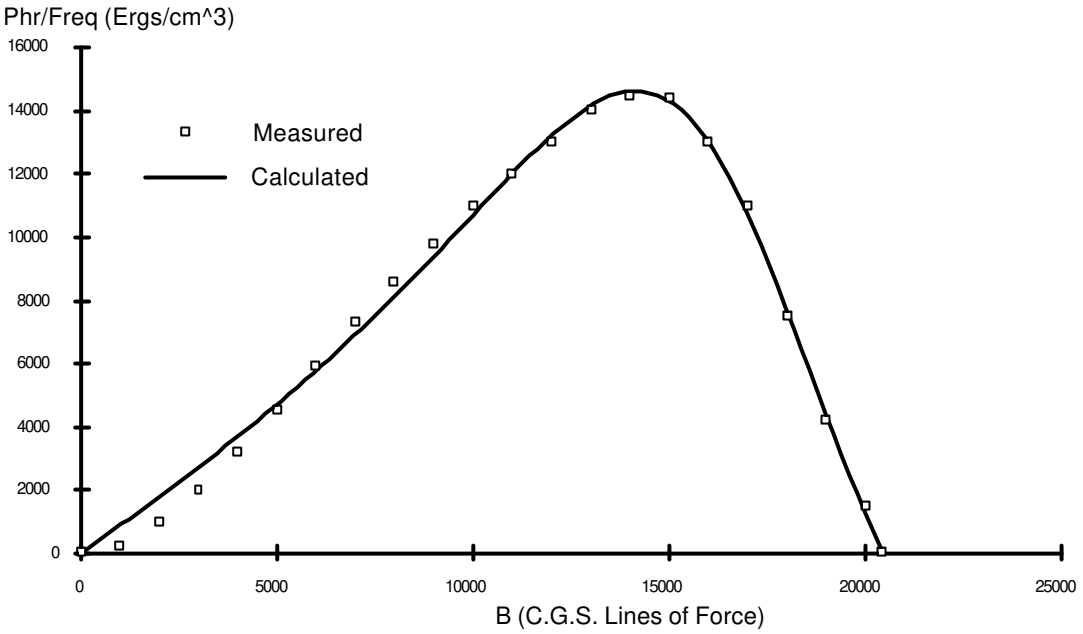

Fig.6-11 Modelling of rotational hysteresis loss in hard steel measured by Baily [120]

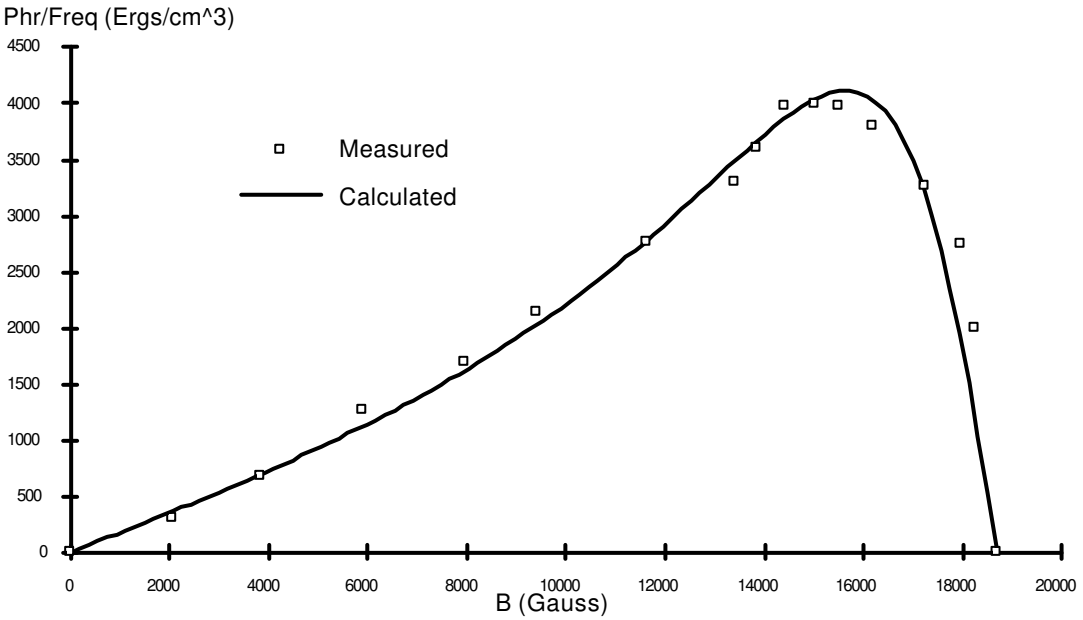

Fig.6-12 Modelling of rotational hysteresis loss in cold rolled silicon steel measured by Brailsford [125]

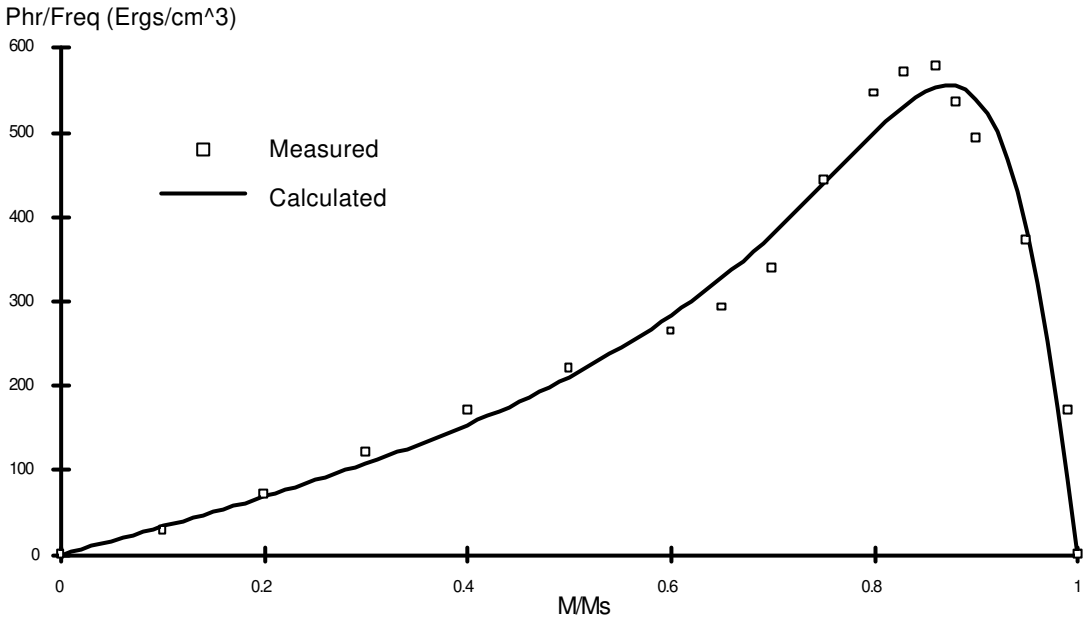

Fig.6-13 Modelling of rotational hysteresis loss in single crystal discs of 4% silicon iron with (001) surfaces measured by Narita and Yamaguchi [130]

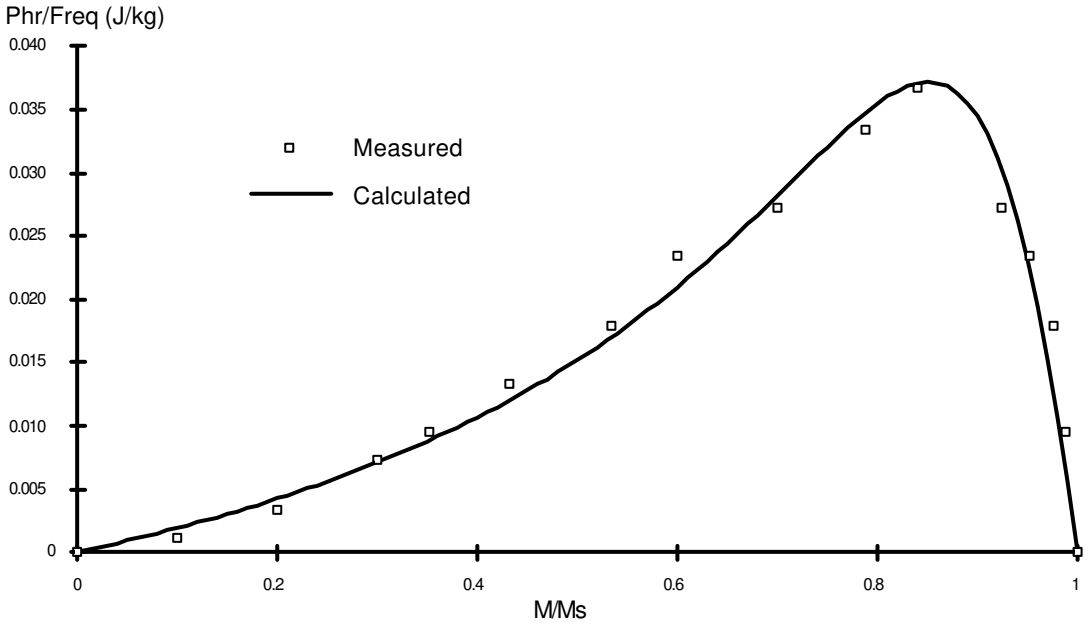

Fig.6-14 Modelling of rotational hysteresis loss in grain-oriented 3% silicon steel measured by Cecchitti, *et al* [131]

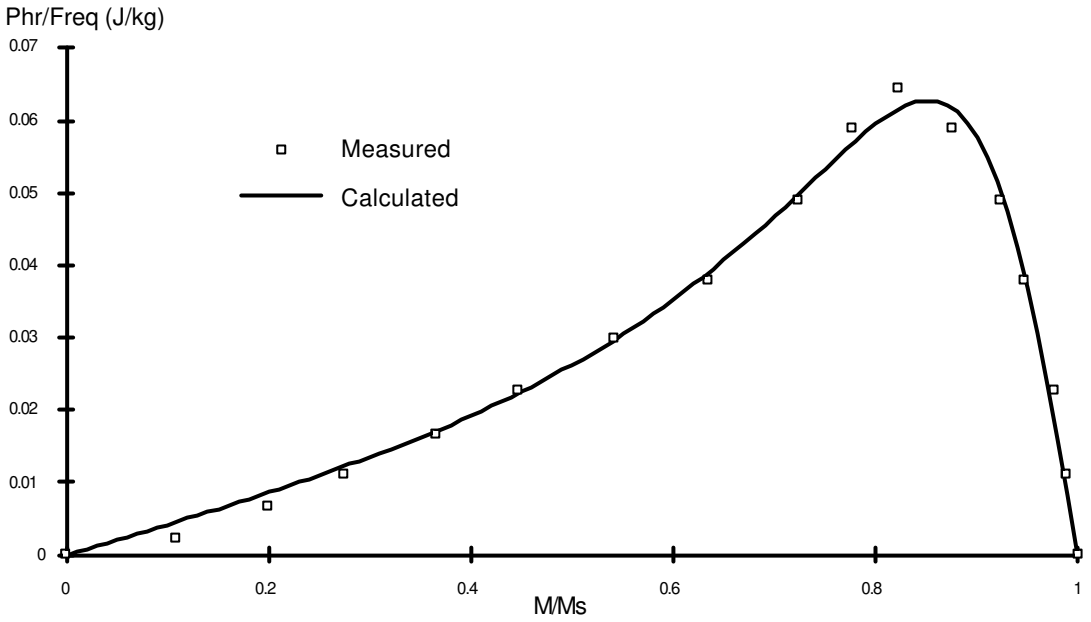

Fig.6-15 Modelling of rotational hysteresis loss in non-oriented 3% silicon steel measured by Cecchitti, *et al* [131]

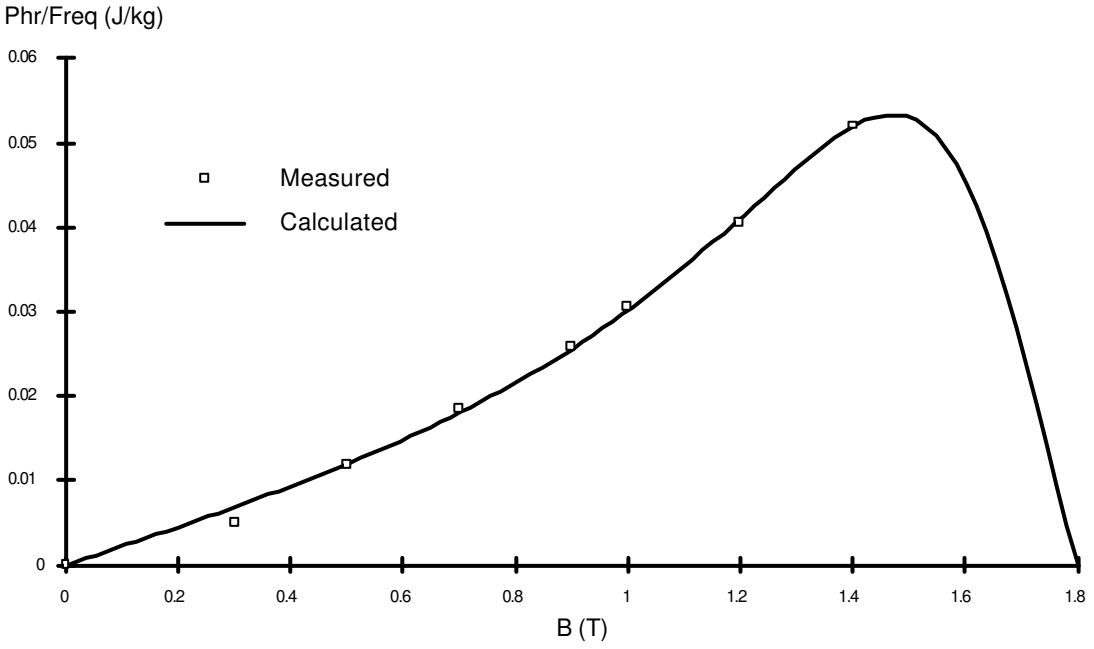

Fig.6-16 Modelling of rotational hysteresis loss in Lycore-130

Table 6-1 Modelling of rotational hysteresis losses in different materials

Fig.	Author	Year	Ref.	Material	a1	a2	a3	Error (%)
6-10	Baily	1896	[120]	Soft iron	1.21×10^5 Ergs/cm^3	–0.74	13.28	2.35
6-11	Baily	1896	[120]	Hard steel	4.07×10^4 Ergs/cm^3	–1.66	4.75	2.49
6-12	Brailsford	1938	[125]	Cold rolled silicon steel	1.44×10^5 Ergs/cm^3	6.48	–3.54	3.64
6-13	Narita and Yamaguchi	1974	[130]	A single crystal specimen of 4% non-oriented silicon steel with (001) surface	9.38×10^3 Ergs/cm^3	–0.072	52.95	5.55
6-14	Cecchitti *et al*	1978	[131]	Grain oriented 3% silicon steel	0.85 J/kg	2.80	36.36	4.73
6-15	Cecchitti *et al*	1978	[131]	Non-oriented 3% silicon steel	0.81 J/kg	–0.76	37.92	2.73
6-16	Author of the thesis	1993	–	Non-oriented silicon steel Lycore-130	0.43 J/kg	–1.53	21.89	1.45

6.4 PREDICTING TOTAL ROTATIONAL CORE LOSS WITH AN ELLIPTICAL FLUX DENSITY

In computer aided design of electromagnetic devices with rotating magnetic fluxes, it is often required to predict the total core loss with an elliptical flux density, as will be discussed in section 6.5. For the power frequency losses in silicon iron alloys due to an elliptically rotating magnetic field, Strattant and Young [137] proposed an empirical model as illustrated by equations (4.18)-(4.20), but there is a large discrepancy between the experimental data and the model. A linear interpolation between the core losses with a circular flux density and with an alternating flux density was used by Bertotti *et al* [192] in predicting the core loss in an induction machine, and Zhu and Ramsden [196] in the core loss modelling of a permanent magnet motor. From the core loss measurements in grain-oriented and non-oriented electrical steel sheets with an elliptical flux density, reported in section 5.3 and 5.4, however, it can be seen that the linear interpolation was only a very rough estimation.

In this section, a better model for predicting the total rotational core loss with an elliptical flux density from the purely rotational and alternating losses is to be developed. The model is verified with the experimental data in both grain-oriented and non-oriented electrical silicon steel sheets.

6.4.1 Elliptically Rotational Core Loss in Terms of Flux Density Axis Ratio

Consider a body subject to an elliptically rotating magnetic flux density **B**. The applied rotating magnetic field strength **H** may not be an elliptically rotating vector because of the possible nonlinear **B**–**H** relationship and magnetic anisotropy. When it is expanded into a Fourier series, however, it can be shown by (5.24) in section 5.5.2 that the higher harmonics of **H** do not contribute to the total core loss as long as **B** contains only the fundamental component.

Fig.6-17 illustrates schematically the loci of **B** and the fundamental component $\mathbf{H}_1$ of field strength. The loci of **B** and $\mathbf{H}_1$ vectors can be expressed as

$$\begin{cases} B_x = B_{maj} \cos\omega t \\ B_y = B_{min} \sin\omega t \end{cases} \tag{6.15}$$

and

$$\begin{cases} H_{1x'} = H_{1maj} \cos(\omega t + \phi) \\ H_{1y'} = H_{1min} \sin(\omega t + \phi) \end{cases} \tag{6.16}$$

where B_x and B_y are the X and Y components of **B** in the XOY coordinate system, B_{maj} and B_{min} are the major and minor axes of elliptical **B**, $\omega=2\pi f$ is the angular frequency of magnetisation, f the frequency, $H_{1x'}$ and $H_{1y'}$ are the X' and Y' components of $\mathbf{H}_1$ in the X'OY' coordinate system, H_{1maj} and H_{1min} are the major and minor axes of elliptical $\mathbf{H}_1$, respectively, and ϕ is the phase angle by which $\mathbf{H}_1$ leads **B** in time.

The standard equation (6.16) of elliptical $\mathbf{H}_1$ in the X'OY' coordinate system can be transferred into the XOY system by a coordinate rotation as following

$$\begin{pmatrix} H_{1x} \\ H_{1y} \end{pmatrix} = \begin{pmatrix} \cos\alpha & -\sin\alpha \\ \sin\alpha & \cos\alpha \end{pmatrix} \begin{pmatrix} H_{1x'} \\ H_{1y'} \end{pmatrix} \tag{6.17}$$

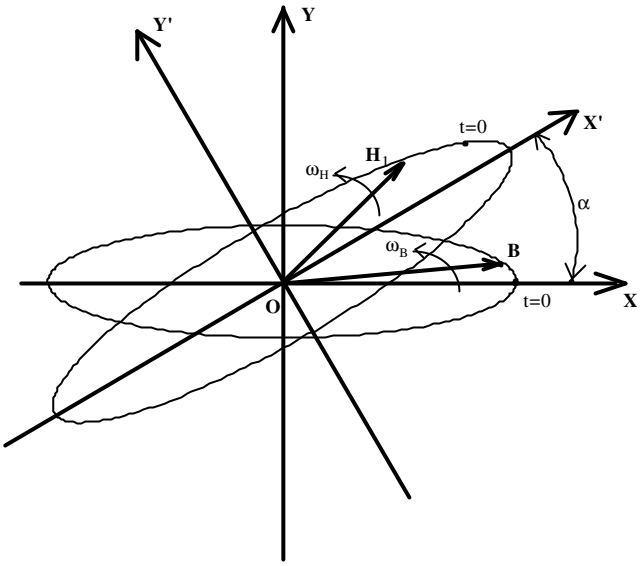

Fig.6-17 Positions of elliptical **B** and $\mathbf{H}_1$ vectors in a body

Substituting (6.15)-(6.17) into (5.20) gives the total rotational core loss in the body with an elliptical flux density

$$P_t = \frac{1}{T\rho_m}\int_0^T (H_x \frac{dB_x}{dt} + H_y \frac{dB_y}{dt})dt$$

$$= \frac{1}{T\rho_m}\int_0^{2\pi} \{(-B_{maj}\sin\omega t)\left[H_{1maj}\cos(\omega t+\phi)\cos\alpha - H_{1min}\sin(\omega t+\phi)\sin\alpha\right] + (B_{min}\cos\omega t)\left[H_{1maj}\cos(\omega t+\phi)\sin\alpha + H_{1min}\sin(\omega t+\phi)\cos\alpha\right]\}d\omega t$$

$$= \frac{\pi}{T\rho_m}\left[(B_{maj}H_{1min} + B_{min}H_{1maj})\sin(\alpha+\phi) + (B_{maj}-B_{min})(H_{1maj}-H_{1min})\cos\alpha\sin\phi\right]$$

$$= \frac{\pi}{T\rho_m} B_{maj}H_{1maj}\left[(R_H+R_B)\sin(\alpha+\phi) + (1-R_B)(1-R_H)\cos\alpha\sin\phi\right] \quad (6.18)$$

where T=1/f is the time period of magnetisation, ρ_m the mass density of the body, $R_B=B_{min}/B_{maj}$ and $R_H=H_{1min}/H_{1maj}$ are the axis ratio of elliptical **B** and $\mathbf{H}_1$, respectively.

In an isotropic body, $R_H=R_B$, and hence (6.18) can be rewritten as

$$P_t = \frac{\pi}{T\rho_m} B_{maj} H_{1maj} \left[2R_B \sin(\alpha+\phi) + (1-R_B)^2 \cos\alpha \sin\phi \right] \tag{6.19}$$

When R_B=1, the total rotational core loss in an isotropic body with a purely circular flux density

$$P_{cr} = P_t = \frac{2\pi}{T\rho_m} B_{maj} H_{1maj} \sin(\alpha+\phi) \tag{6.20}$$

When R_B=0, the total core loss in an isotropic body with a purely alternating flux density

$$P_{alt} = P_t = \frac{\pi}{T\rho_m} B_{maj} H_{1maj} \cos\alpha \sin\phi \tag{6.21}$$

Therefore, (6.19) can be rewritten as

$$P_t = R_B P_{cr} + (1-R_B)^2 P_{alt} \tag{6.22}$$

Equation (6.22) is independent of the magnetisation frequency, since it is derived directly from the formula of the total rotational core loss, which is valid for any magnetisation frequency, and should therefore be applicable to both hysteresis and total losses.

6.4.2 Experimental Verification

In the above analysis, equation (6.22) is obtained under the assumption of an isotropic body. Practically, there is hardly any magnetic material that is strictly isotropic. This, however, does not mean that equation (6.22) is useless for calculation of rotational core loss in electromagnetic devices made of anisotropic magnetic materials.

In the core loss analysis of three phase rotating electrical machines, isotropic magnetic materials are generally assumed because all points of the core are exposed to the rotating field. In the T joints of three phase transformers, where rotational core losses occur, grain-oriented silicon steel sheets are over-lapped with the grain-orientations perpendicular to each other, as illustrated in Fig.6-18, and hence the silicon steel sheets in the over-lapped regions can also be approximately considered isotropic.

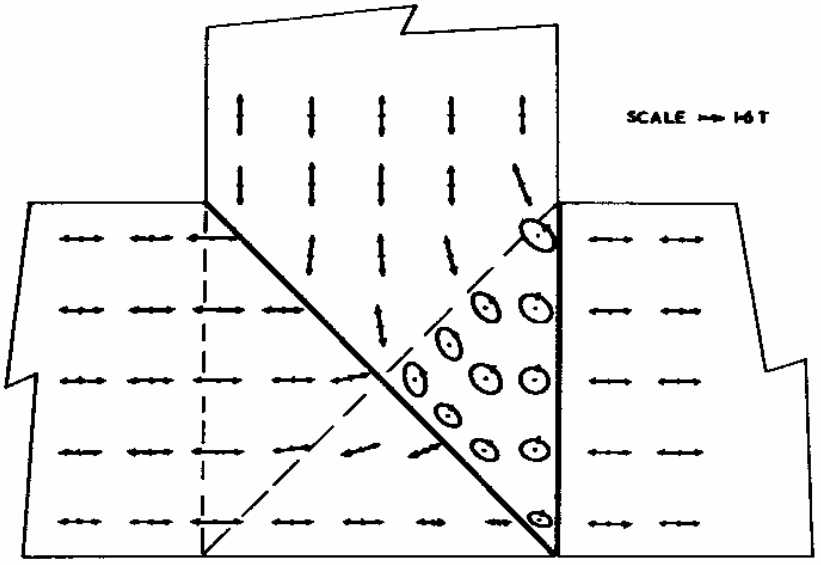

(a)

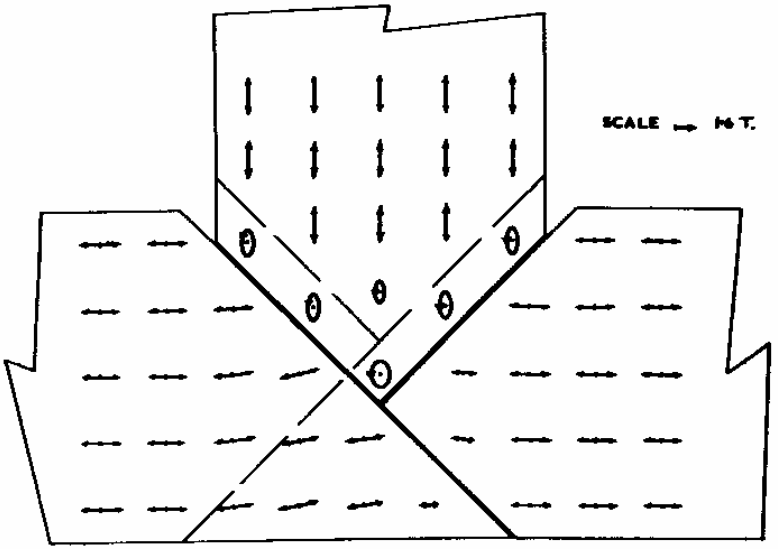

(b)

Fig.6-18 Loci of the fundamental component of the localised flux density within (a) a 45^{o}-90^{o} T joint, and (b) a 45^{o} offset T joint (from [181])

Fig.6-19 illustrates the modelling of the average total core loss in a non-oriented electrical steel sheet Lycore-130 with an elliptical flux density at 1 Hz. The average is the average value of the core losses measured when the major axis is on the X (rolling direction) and Y (transversal direction) axes respectively. Encouraging agreement was shown between the model (6.22) and the average total core loss. The error is 2.82%, which is defined as the standard deviation normalised to the maximum value of the measured data, as defined in (6.14).

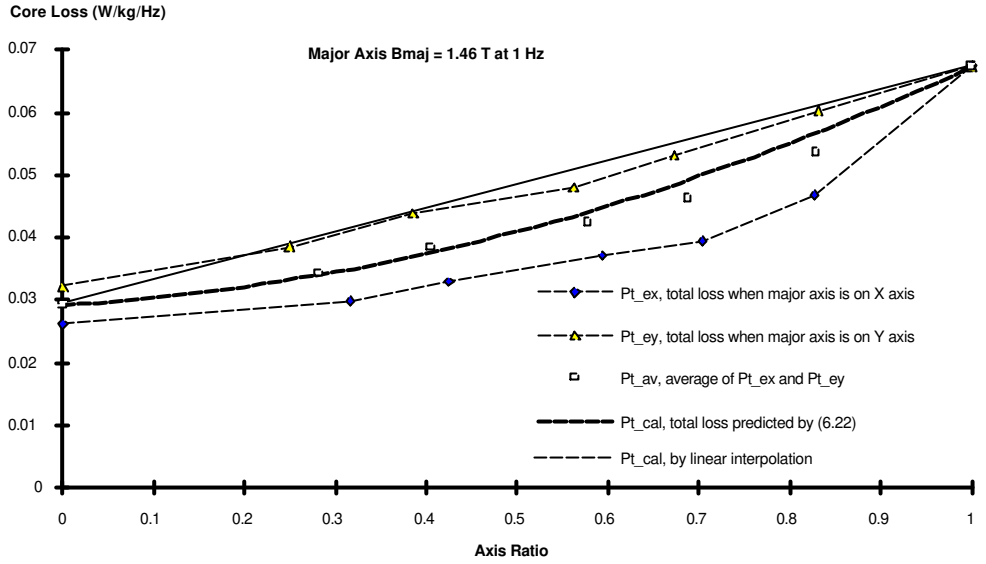

Fig.6-19 Modelling of total rotational core loss in Lycore-130 with an elliptical flux density at 1 Hz (this is almost pure hysteresis loss).

Fig.6-20 is the modelling of the average total core loss in Lycore-130 with an elliptical flux density at 50 Hz. The error is 1.66%.

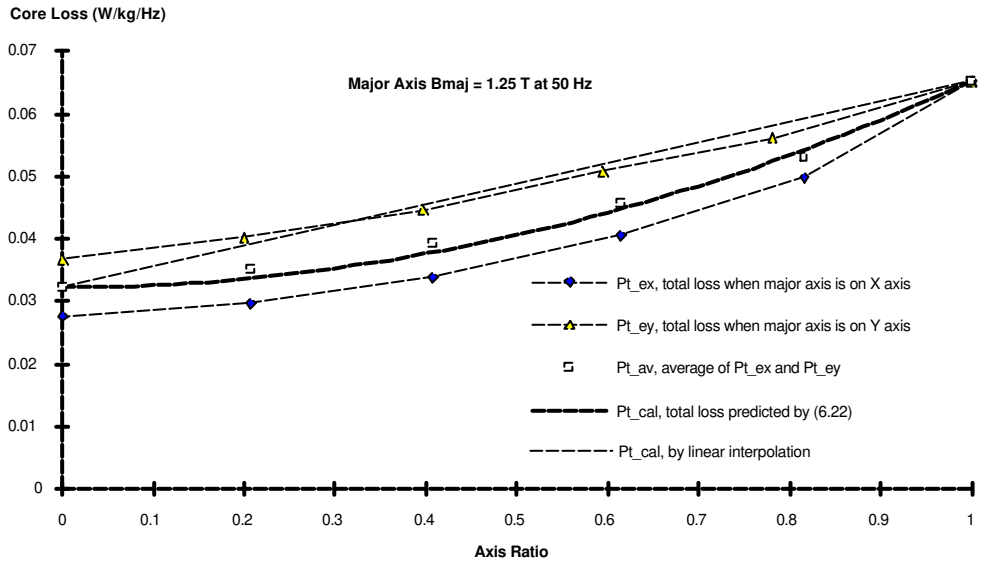

Fig.6-20 Modelling of total rotational core loss in Lycore-130 with an elliptical flux density at 50 Hz

Fig.6-21 is the modelling of the average total core loss in a grain-oriented electrical steel sheet ORSI-100 at 50 Hz. The error is 2.43%.

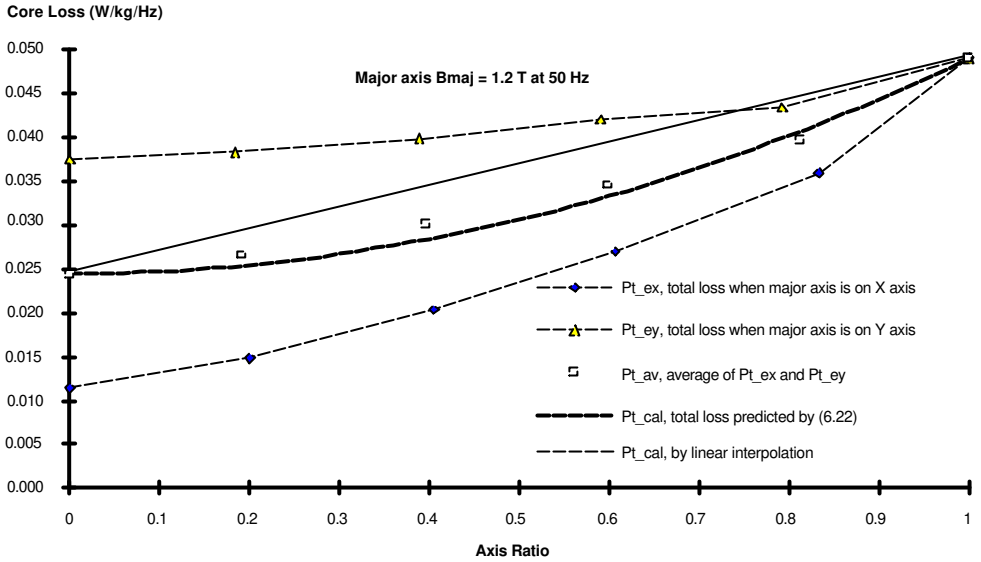

Fig.6-21 Modelling of total rotational core loss in ORSI-100 with an elliptical flux density at 50 Hz

As a comparison, the results linearly interpolated from the purely rotational and alternating core losses are also plotted in Fig.6-19 to Fig.6-21. Apparently, the linear interpolation approach is a rough estimation.

The above analysis and the modelling results illustrated in Fig.6-19 to Fig.6-21 show that model (6.22) can correctly predict the average (over two directions) rotational core losses in both grain-oriented and non-oriented electrical steel sheets with an elliptically rotating flux density. Therefore, the model can be used for rotational core loss analysis in both rotating electrical machines and three phase transformers, as a better estimate then linear interpolation method. The model is valid for rotational hysteresis loss as well as total loss (independent of magnetisation frequency).

6.5 CORE LOSS MODELLING IN ROTATING ELECTRICAL MACHINES

6.5.1 Rotating Flux Density in the Stator Core of a Permanent Magnet Motor

To illustrate the method for core loss analysis in a rotating electrical machine, a permanent magnet motor has been chosen as an example. The outline and the dimensions of the motor are depicted in Fig.6-22. This is a three phase six pole surface mounted NdFeB permanent magnet motor. The stator lamination is Lycore-130, 0.35 mm silicon steel sheet, and the rotor material is solid mild steel. There are 36 slots in the stator, and each contains 117 conductors of the stator winding. For various considerations, two motors of the same cross sectional

dimensions but different axial lengths (76 mm and 38 mm respectively) were designed and constructed as part of another project [223].

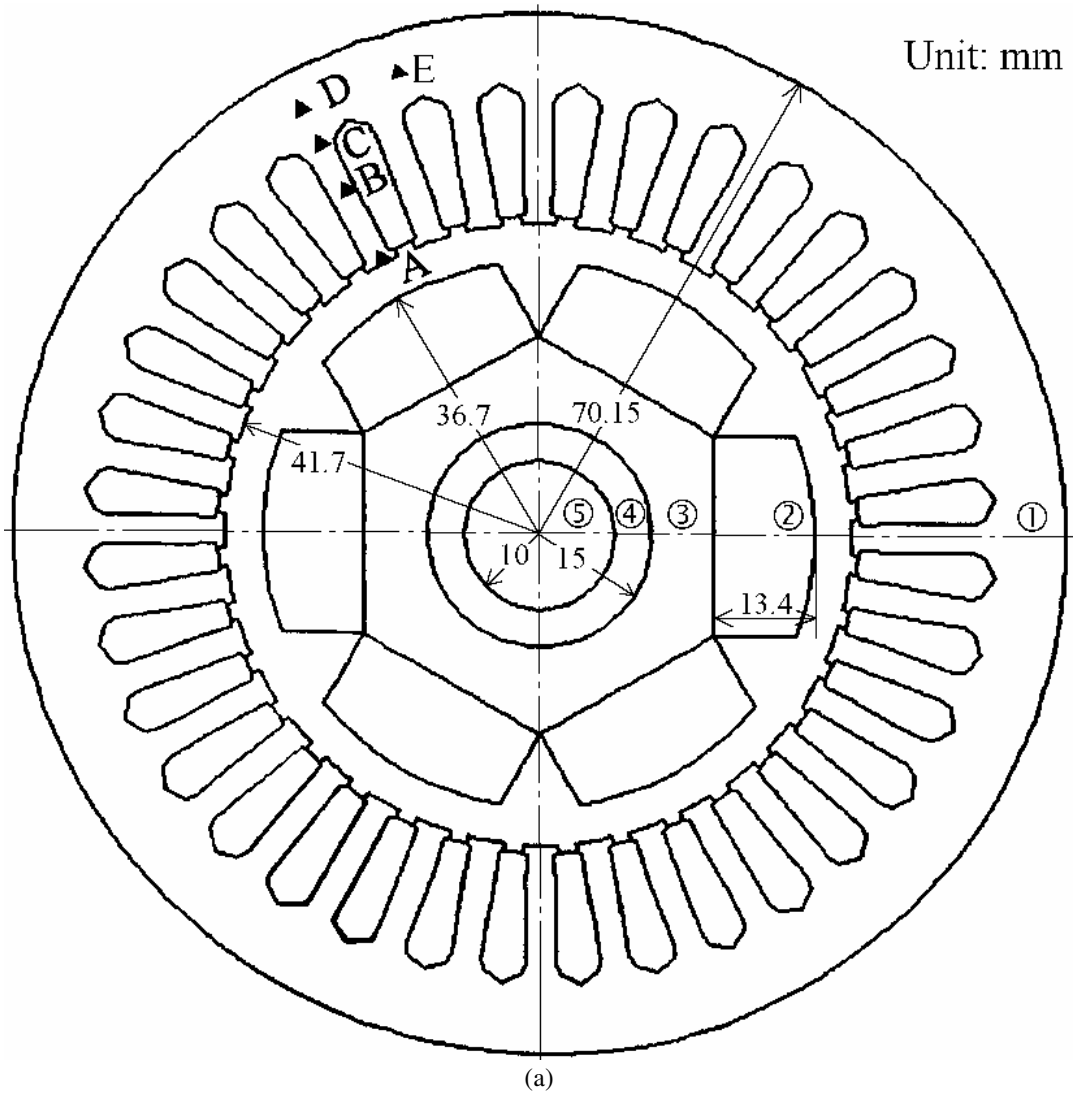

(a)

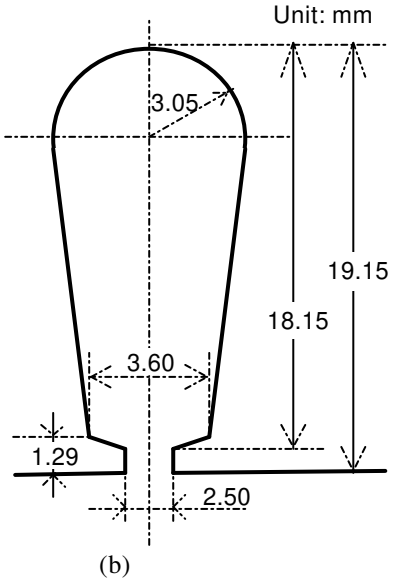

(b)

Fig.6-22 Outline and dimensions of the permanent magnet motor used as an example
(a) cross sectional view, where
① -- stator core (Lycore-130 silicon steel sheet)
② -- NdFeB permanent magnets
③ -- rotor core (solid mild steel)
④ -- plastic cylinder
⑤ -- rotor shaft, and
(b) dimension of a stator slot

Because the rotor rotates at the synchronous speed, the core loss in the rotor was assumed zero, and only the stator core loss was calculated. The total core loss was obtained by summing up the core losses dissipated in each element according to the locus of the rotating magnetic flux density vector in that element.

6.5.1.1 Finite Element Analysis of the No-Load Magnetic Field

The magnetic flux density distribution in the cross section of the motor was determined by the two dimensional finite element method using a FORTRAN code, MOTOR-CAD, which was initially written in 1989 by Hameed and Binns [218], Liverpool University, U.K., and corrected and further improved later by Dr. Watterson, senior research fellow, School of Electrical Engineering, University of Technology, Sydney, and the author incorporating Powell's method, the iterative Incomplete Cholesky Conjugate Gradient (ICCG) solution method, and other utilities for optimum design of permanent magnet motors [220,221].

Because of the symmetric motor structure, it is sufficient to pick only one pole pitch as the solution region with anti-periodic magnetic vector potential boundary conditions. First order triangular finite elements were used to discretise the solution region into 1320 elements and 702 nodes, as illustrated in Fig.6-23.

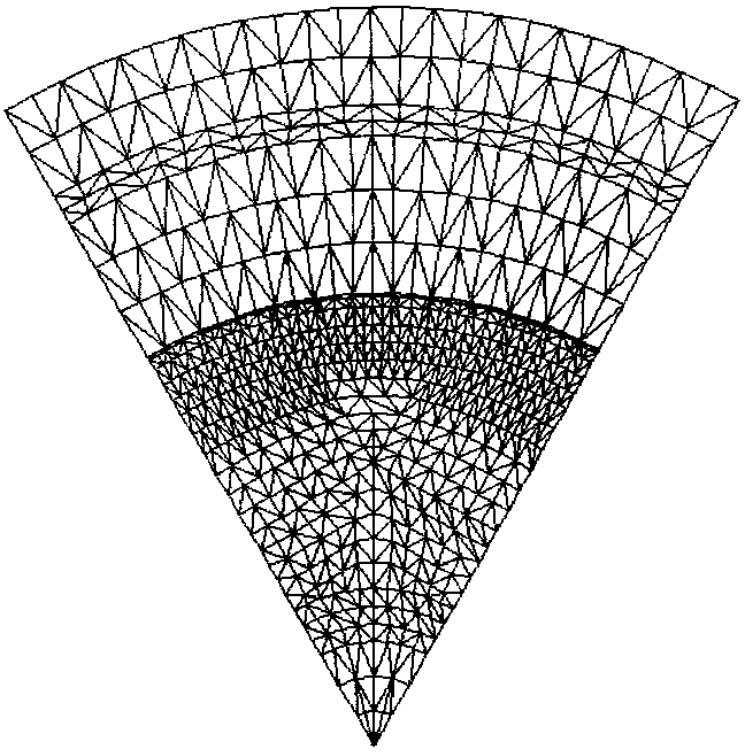

Fig.6-23 Mesh of two dimensional triangular finite elements for the permanent magnet motor

Fig.6-24 is the magnetic flux density contour plot of the permanent magnet motor at no load, when the stator winding currents in the conductors were set to be zero. Fig.6-25 depicts the radial component profile of the magnetic flux density in the mid-airgap. The magnitude of flux density is about 0.8 T.

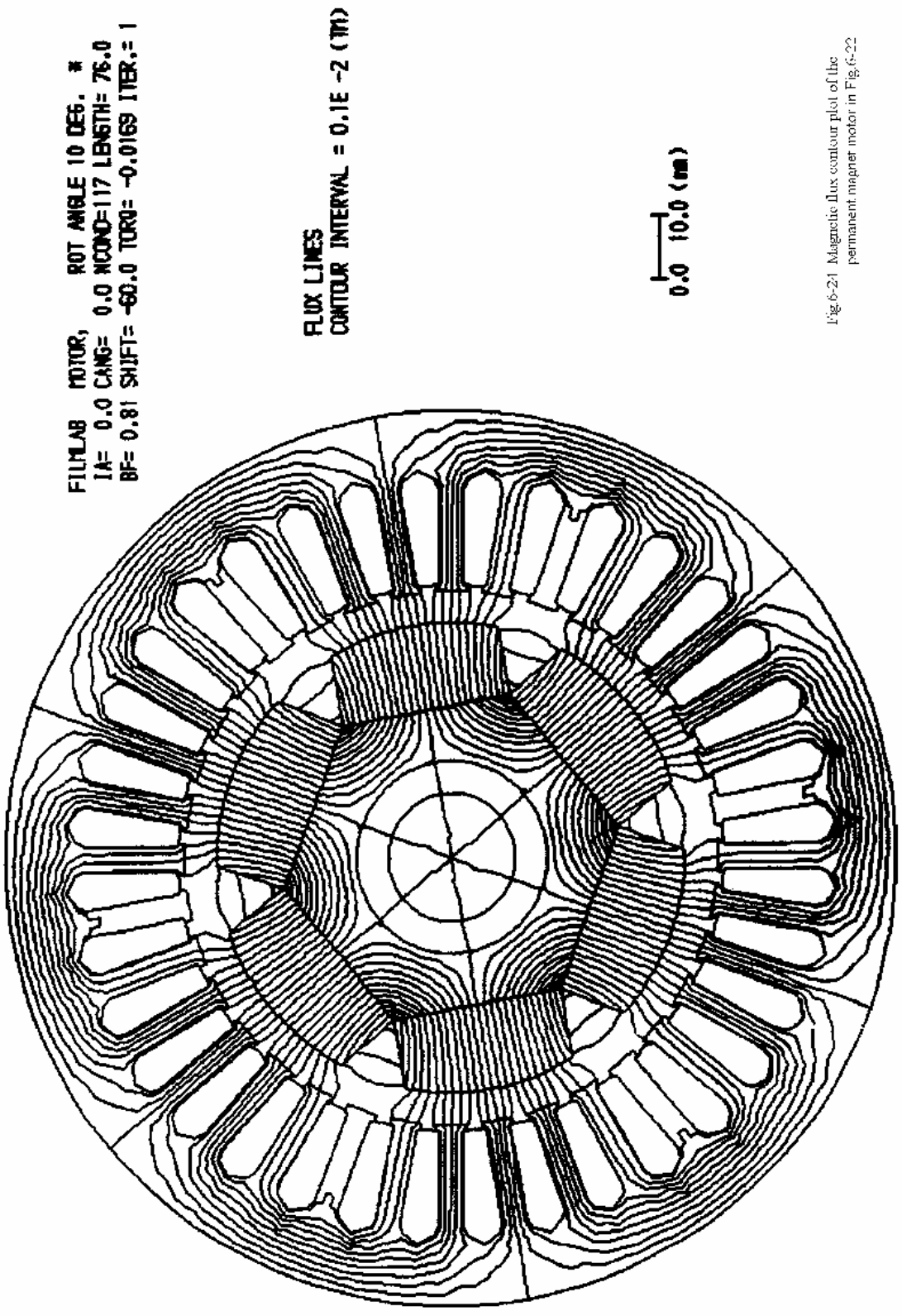

Fig.6-24 Magnetic flux contour plot of the permanent magnet motor in Fig.6-22

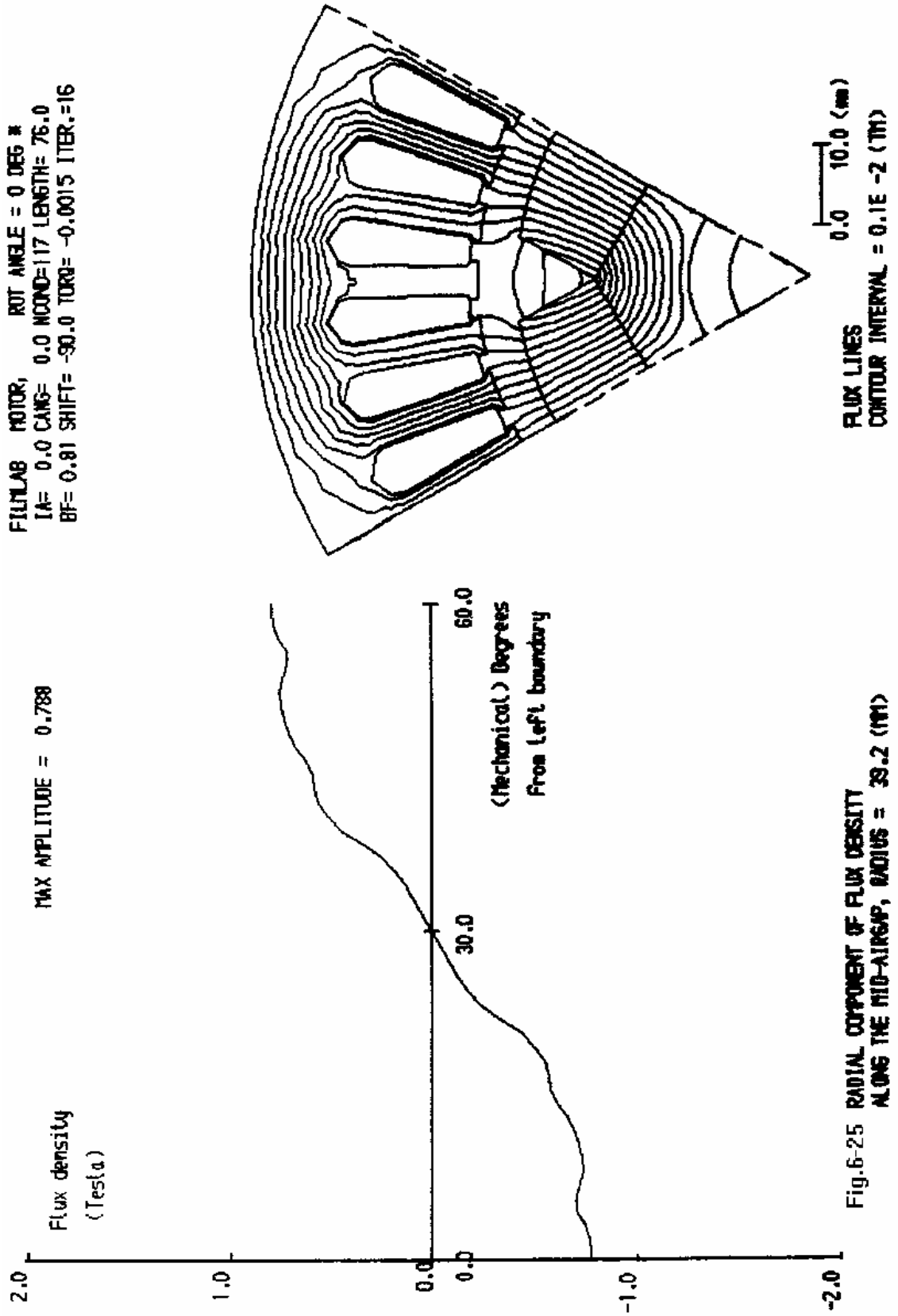

Fig.6-25 RADIAL COMPONENT OF FLUX DENSITY ALONG THE MID-AIRGAP, RADIUS = 39.2 (MM)

6.5.1.2 Determination of Rotating Magnetic Flux Density

The radial and circumferential component waveforms of the magnetic flux density were obtained from a sequence of finite element solutions, and the full waveforms for any element could be assembled from the corresponding elements in different slot pitches as the rotor rotated through only half a slot pitch in five steps.

Fig.6-26 depicts the trajectories of the flux density vectors at positions A, B, C, D, and E of Fig.6-22, and the typical time variations are shown in Fig.6-27. Only in the middle of the teeth (position B) is the field nearly purely alternating (Fig.6-26(b) and Fig.6-27(b)). At the other positions, the flux density vectors are all elliptically rotational (Fig.6-26(a), (c)-(e), and Fig.6-27(a), (c)-(e)). Higher harmonics are also contained in the radial and circumferential components of the flux density.

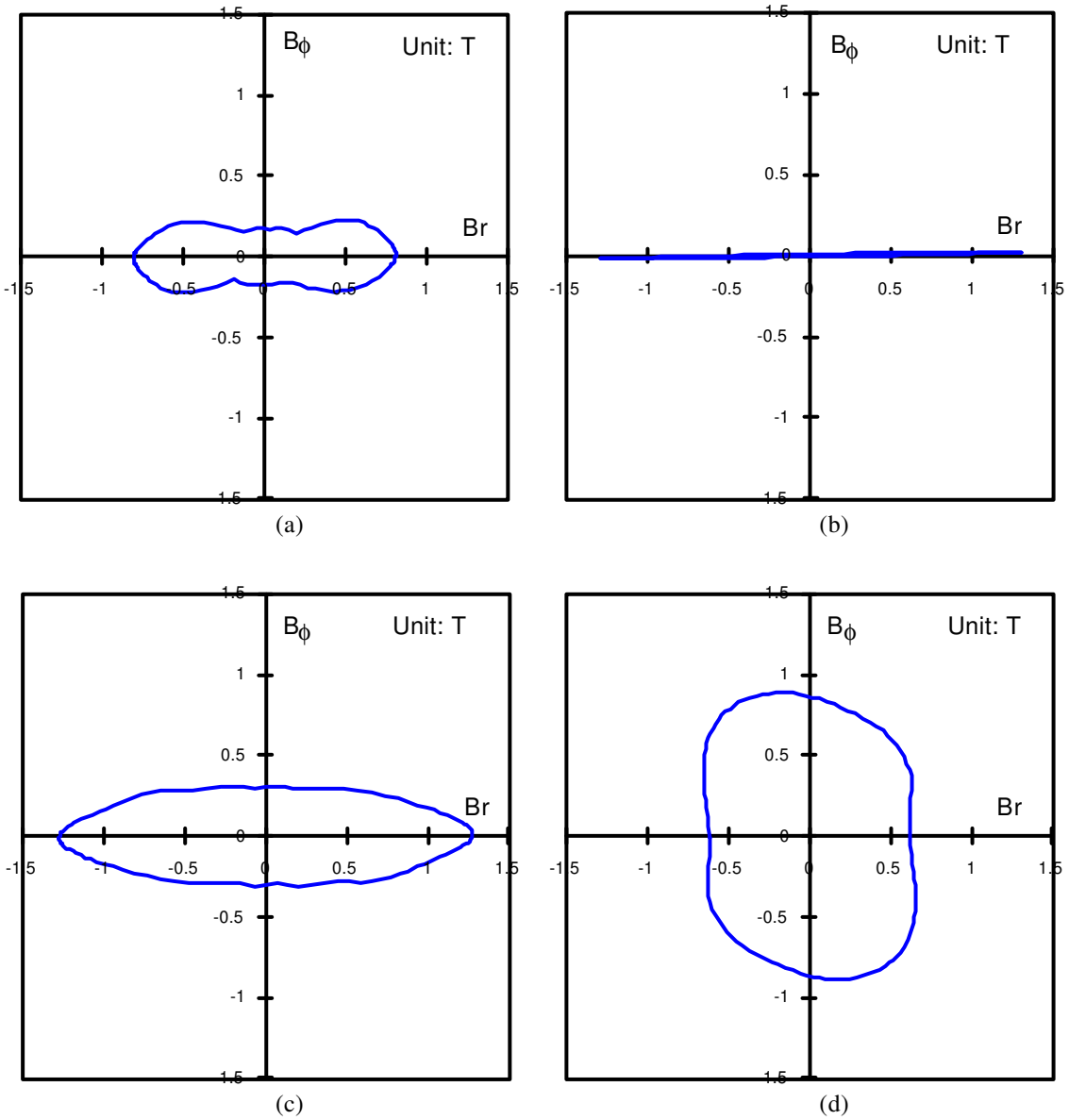

(a) (b)

(c) (d)

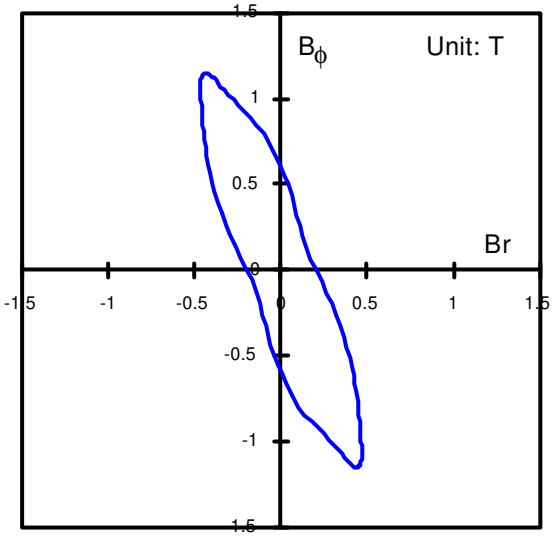

(e)

Fig.6-26 Trajectories of flux density vectors at different positions in the stator core, (a), (b), (c), (d), and (e) corresponding to positions A, B, C, D, and E in Fig.6-22

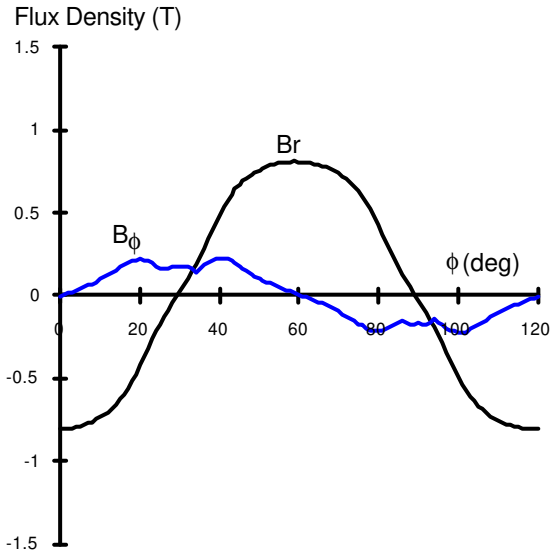

(a)

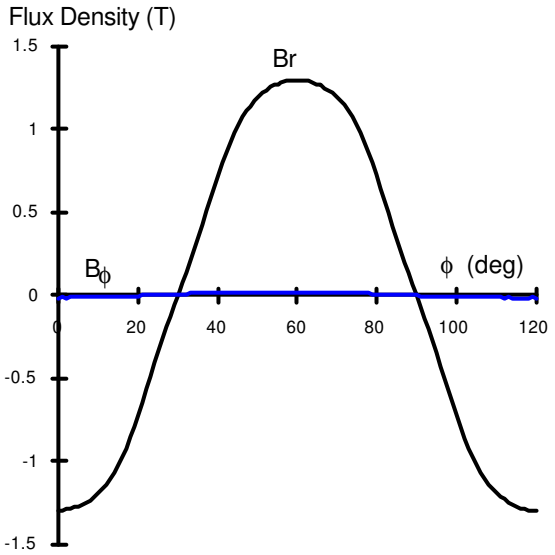

(b)

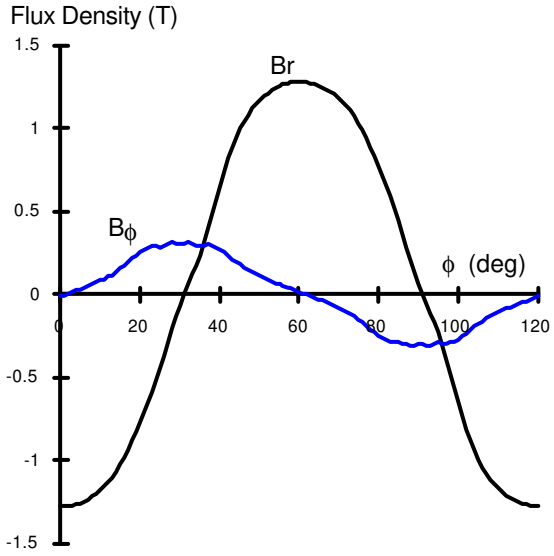

(c)

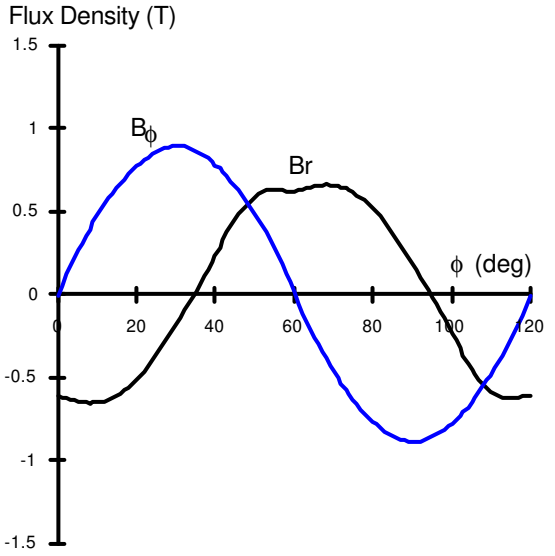

(d)

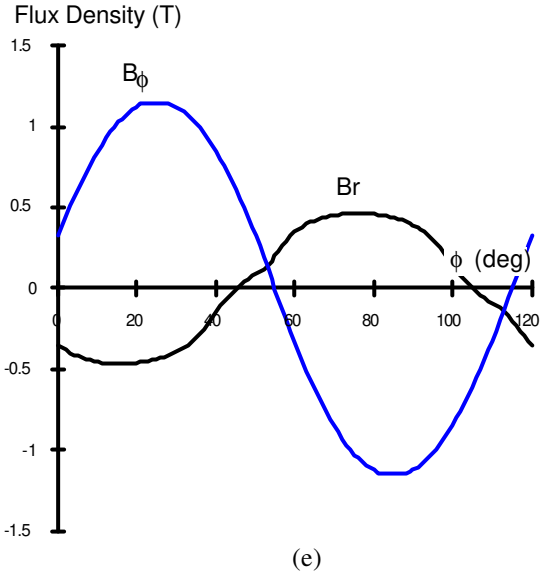

Fig.6-27 Typical time variation of flux density at different positions in the stator core, (a), (b), (c), (d), and (e) corresponding to positions A, B, C, D, and E in Fig.6-22

6.5.2 Core Loss Model for Rotating Electrical Machines

In each element, the total core loss due to an arbitrary rotating flux density vector **B** can be calculated in terms of rotational hysteresis, eddy current, and anomalous losses as following

$$P_t = P_{th} + P_{te} + P_{ta} \tag{6.23}$$

where P_{th}, P_{te}, and P_{ta} are the total hysteresis, eddy current, and anomalous losses in that element.

A series of elliptically rotating harmonic flux density vectors can be obtained, when an arbitrary rotating flux density is expanded into a Fourier series

$$B_r(t) = \sum_{k=0}^{\infty} B_{mk} \sin(2\pi kft + \theta_{rk}) \tag{6.24a}$$

$$B_\phi(t) = \sum_{k=0}^{\infty} B_{\phi mk} \sin(2\pi kft + \theta_{\phi k}) \tag{6.24b}$$

where B_r and B_ϕ are the radial and circumferential components of the rotating flux density, B_{rmk} and $B_{\phi mk}$ are the k-th harmonic magnitudes of B_r and B_ϕ, and θ_{rk} and $\theta_{\phi k}$ are the phase angles of these harmonics. The major axis B_{kmaj} and the minor axis B_{kmin} of the elliptical trajectory of each flux density harmonic vector can be determined by a coordinate rotation for the standard equation.

The total hysteresis loss in an element can be obtained by summing up the contributions from these flux density harmonics. For each elliptically rotating flux density harmonic, as illustrated in section 6.4, the hysteresis loss can be predicted from the corresponding alternating and rotational hysteresis losses according to the axis ratio of the elliptical flux density by (6.22). Therefore, the total hysteresis loss

$$P_{th} = \sum_{k=0}^{\infty} \left[P_{rhk} R_{Bk} + (1 - R_{Bk})^2 P_{ahk} \right] \tag{6.25}$$

where $R_{Bk}=B_{kmin}/B_{kmaj}$ is the axis ratio of the k-th harmonic flux density, P_{rhk} is the purely rotational hysteresis loss with flux density B_{kmaj} determined by equations (6.7) and (6.13), and $P_{ahk}=C_h k f B_{kmaj}^n$, (for Lycore-130, $C_h=0.0192$, and n=1.79), is the alternating hysteresis loss approximately determined by the Steinmetz law.

The total eddy current loss in an element can be calculated analytically by

$$P_{te} = \frac{\sigma b^2}{12\rho_m} \frac{1}{T} \int_0^T \left[\left(\frac{dB_r(t)}{dt} \right)^2 + \left(\frac{dB_\phi(t)}{dt} \right)^2 \right] dt$$

$$= C_e \sum_{k=0}^{\infty} (kf)^2 \left(B_{kmaj}{}^2 + B_{kmin}{}^2 \right) \tag{6.26}$$

where $C_e = \frac{\sigma \pi^2 b^2}{6\rho_m}$ is the eddy current loss coefficient same as in (6.2) (for Lycore-130, $C_e=6.54\times10^{-5}$, as deduced in section 6.2).

The total anomalous loss in an element is calculated for a vector **B**

$$P_{ta} = \frac{C_{ar}}{(2\pi)^{3/2}} \frac{1}{T} \int_0^T \left[\left(\frac{dB_r(t)}{dt} \right)^2 + \left(\frac{dB_\phi(t)}{dt} \right)^2 \right]^{\frac{3}{4}} dt \tag{6.27}$$

where C_{ar} is the anomalous loss coefficient (for Lycore-130, $C_{ar}=1.07\times10^{-3}$, as deduced in section 6.2), and constant $(2\pi)^{3/2}$ is a factor applied to C_{ar} so that (6.27) is consistent with (6.3) for a circular flux density. The integration can be calculated numerically.

6.5.3 Comparison of Calculation with Experiment

6.5.3.1 Measurement

To measure the core loss of the permanent magnet motor, a calibrated DC motor was used to drive it. The power fed into the DC motor would be the sum of core loss and mechanical loss (friction and windage) of both the DC motor and the permanent magnet motor. Subtracting the losses of the DC motor yields the core loss and mechanical loss of the permanent magnet motor alone.

The mechanical loss of the permanent magnet motor was measured by replacing the stator of the permanent magnet motor with a plastic tube (to imitate the windage), and then repeating the previous procedure. The core loss of the permanent magnet motor was obtained by subtraction of the mechanical loss from the sum of the core loss and mechanical loss.

To remove the effect of the motor ends where the field is not two dimensional, the core loss was measured in the above way for two motors of active length 38 mm and 76 mm. Fig.6-28 shows measured results of the no-load power loss, which is the sum of the mechanical loss and the core loss, and the mechanical loss of the permanent magnet motors of two different active lengths. Fig.6-29 is the measured core losses before the removal of end effects obtained by subtracting the mechanical losses from the no-load losses.

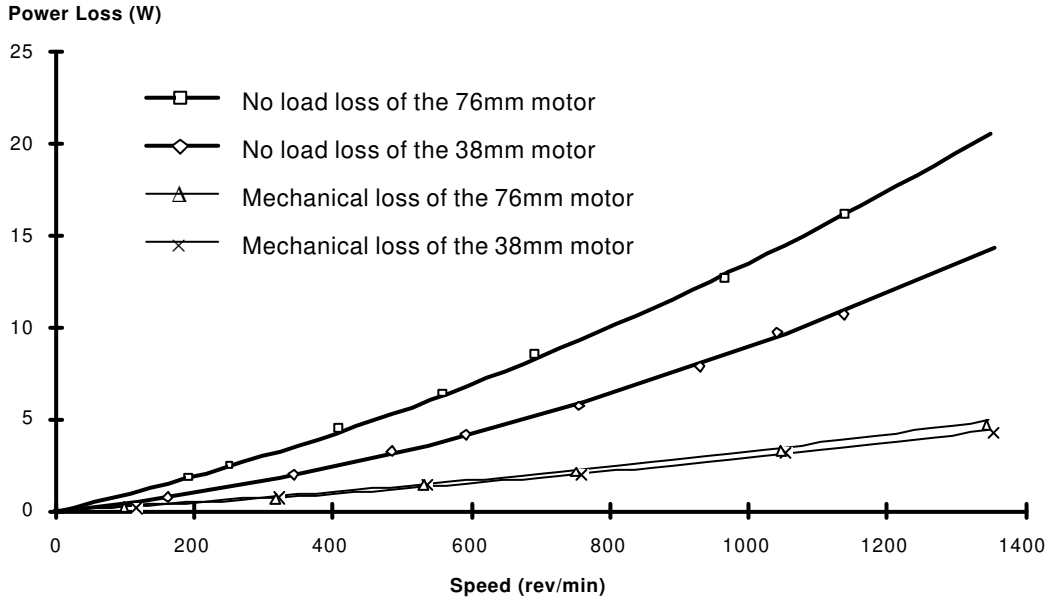

Fig.6-28 Measured no-load power loss and mechanical loss of the permanent magnet motors of active length 38 mm and 76 mm

Assume two motors of different active lengths have the same end effects because of the same end structures. The net core loss after the removal of the end effects in the 76 mm motor should be twice as much as that in the 38 mm one. Thus, the core loss due to the end effects can be deduced by

$$P_{end} = 2P_{38}-P_{76} \tag{6.28}$$

where P_{38} and P_{76} are the core losses in the 38 mm and 76 mm motors, respectively, before the removal of the end effects. The core loss due to the end effects is plotted in Fig.6-29 by the dotted line.

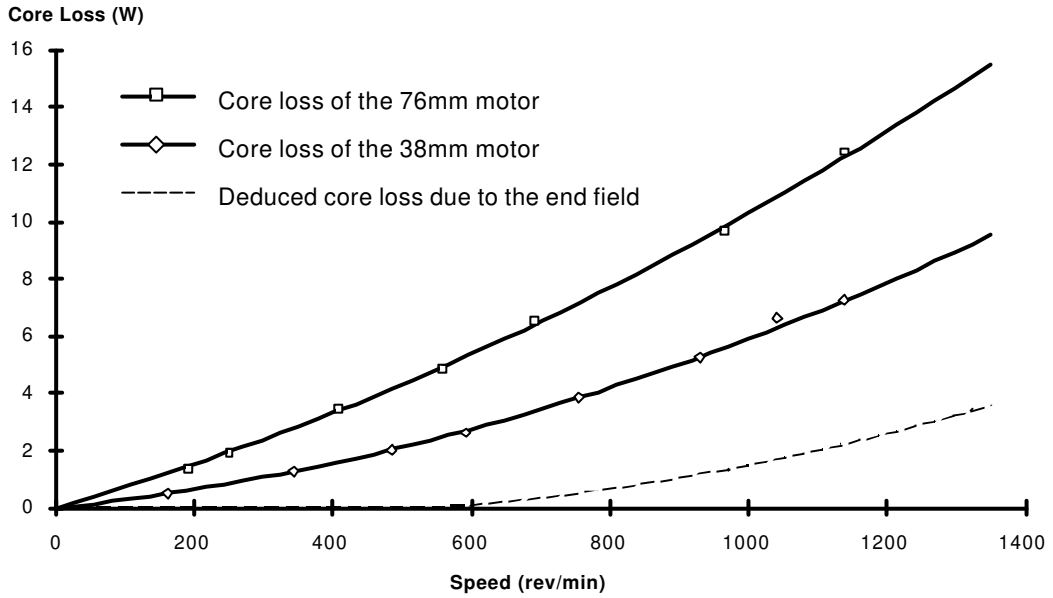

Fig.6-29 Measured core losses of the permanent magnet motors of active length 38 mm and 76 mm before removal of end effects

The inferred end effect has been subtracted from the core loss of the 76 mm motor, and reported below.

6.5.3.2 Comparison

Figs.6-30(a) and (b) show the total core loss and the core loss torque (core loss over angular speed) by measurement and calculation for a motor of active length 76 mm versus speed, after the removal of end effects.

Initially, the core loss was calculated by summing up alternating hysteresis loss, rotational eddy current loss, and rotational anomalous loss in all finite elements, because the data for rotational hysteresis loss were not available. In the calculation, the Steinmetz law was used for alternating hysteresis loss, and (6.26) and (6.27) were used for rotational eddy current and anomalous losses. The calculated core loss and core loss torque of the 76 mm motor are plotted in Figs.6-30(a) and (b) by the dotted lines (Alt.Hyst.+Rot.Eddy+Rot.Anom.). These dotted lines are about 20% lower than the measured results at 1200 rev/min.

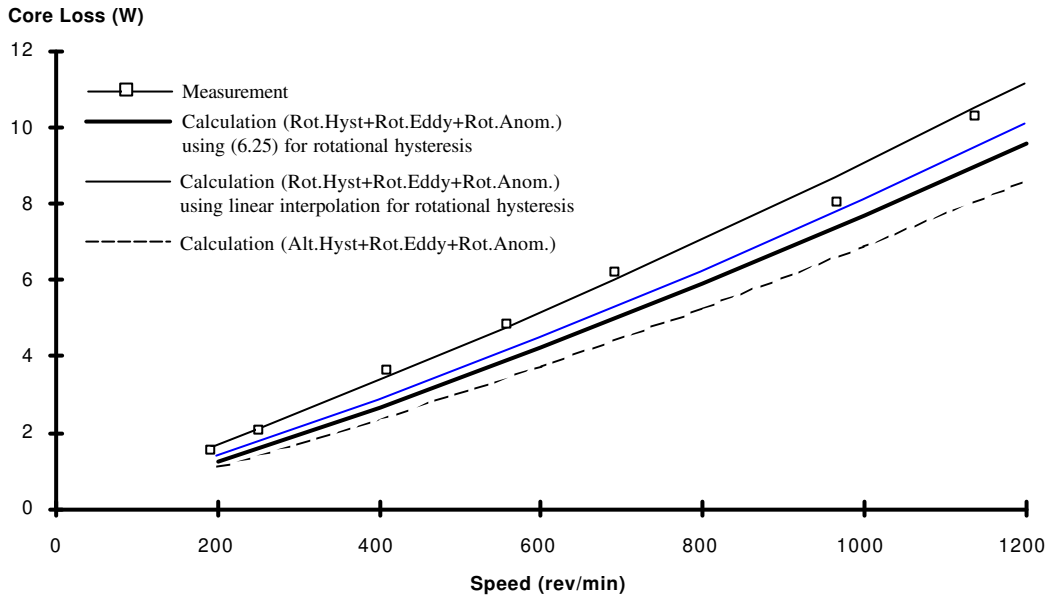

(a)

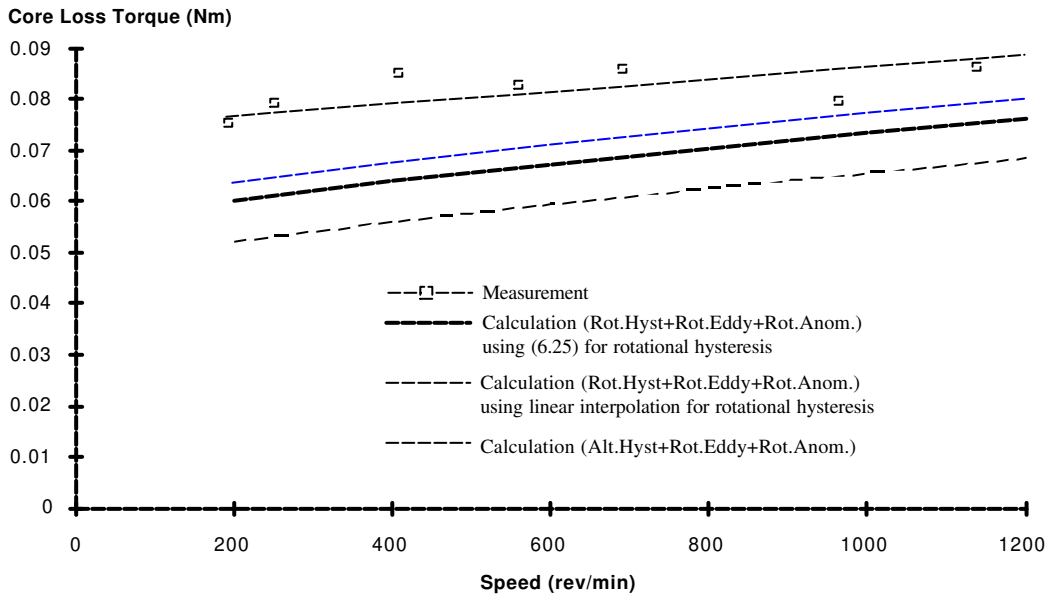

(b)

Fig.6-30 Comparison of measured and calculated (a) core loss and (b) core loss torque of the 76 mm permanent magnet motor after the removal of end effects

As soon as the rotational core loss was measured, the rotational hysteresis loss was included in the core loss calculation. The rotational hysteresis loss in each element with an elliptically rotating flux density harmonic was predicted by a simple model of linear interpolation between the purely rotational hysteresis loss and the alternating hysteresis loss corresponding to B_{kmaj} as explained earlier, and the total hysteresis loss in an element was calculated by

$$P_{th} = \sum_{k=0}^{\infty} \left[P_{rhk} R_{Bk} + (1 - R_{Bk}) P_{ahk} \right] \tag{6.29}$$

The calculated total core loss and the core loss torque are plotted in Figs.6-30(a) and (b) by the thin solid lines labelled as "Calculation (Rot.Hyst.+Rot.Eddy+Rot.Anom.) using linear interpolation for rotational hysteresis". The discrepancy between the measurement and the calculation is reduced to about 9% at 1200 rev/min.

As discussed in section 6.4, the linear interpolation approach for elliptical hysteresis loss is a very rough estimation. The core loss was recalculated later with a better model (6.25) for elliptical rotational hysteresis loss. The results are shown in Fig.6-30 by the thick solid lines labelled as "Calculation (Rot.Hyst.+Rot.Eddy+Rot.Anom.) using (6.25) for rotational hysteresis". Although the discrepancy 13% at 1200 rev/min between this calculation and the measurement is higher than that obtained by using the linear interpolation approach, this calculation is believed to be of higher accuracy since this model agrees with the measurements in electrical steel sheets with an elliptical flux density much better than the linear interpolation approach, as illustrated in section 6.4.

From Fig.6-30, it can also be seen that the rotational hysteresis loss has contributed a significant component of the total, as estimated in [195]. The discrepancy between the measured and calculated results has been reduced from 20% to 13% at 1200 rev/min. The remaining discrepancy may be due to one or more of the following: rotor core loss caused by tooth ripple, eddy current loss in the stator case, inadequate representation of non-sinusoidal fields, or unknown changes in material properties during manufacture due to punching and heat treatment.

6.6 CONCLUSION

The rotational core loss in an electrical steel sheet with a purely circular flux density can be separated into components of rotational hysteresis, eddy current, and anomalous losses, and modelled by the three term core loss model, in a similar way to alternating core loss separation and modelling. The rotational eddy current loss is twice as much as the alternating eddy current

loss with the same magnitude of flux density. As for alternating anomalous loss, the rotational anomalous loss can also be given in terms of $(fB)^{3/2}$. The rotational anomalous loss coefficient was found a constant over a range of flux density up to 1.4 T for non-oriented silicon steel Lycore-130.

Owing to the strong analogy between the electromagnetic torque in a single phase induction machine and the rotational hysteresis loss per cycle with a circular field, an analogical model was developed. Excellent agreement was achieved between the model and experimental data for different magnetic materials reported in earlier publications and measured here. Further work is required on physical understanding of rotational hysteresis loss.

Measurements of rotational core losses with elliptical flux densities in both grain-oriented and non-oriented electrical steel sheets have shown that the linear interpolation between purely rotational and alternating core losses for elliptically rotational core loss is a very rough estimation. Derived from the formula (5.20) for total core loss, equation (6.22) can give much better prediction, and is independent of magnetisation frequency, and therefore applicable to hysteresis as well as total losses.

The rotating flux density vector at any position in the stator core of a rotating electrical machine can be obtained by the finite element method. Smooth curves of flux density can be obtained from a sequence of finite element solutions as the rotor rotates for half a slot pitch in a number of steps. In optimum design, approximate curves can be assembled from only one solution by considering adjacent teeth in order to save time.

The core loss in a rotating electrical machine was calculated by summing up the core losses in all finite elements. In each element, the core loss with an arbitrary rotating flux density vector was evaluated in terms of rotational hysteresis, eddy current and anomalous losses by (6.25) to (6.27).

The comparison between the measured core loss and the core losses calculated by three different hysteresis models has shown that the rotational hysteresis does contribute a considerable component to the total core loss. Although the total core loss calculated by using (6.25) for rotational hysteresis loss in a finite element is lower than that calculated by the linear interpolation approach, it is still believed to be of higher accuracy, since this model agrees better with the measurements in both grain-oriented and non-oriented electrical steel sheets.

The remaining discrepancy between the measurement and calculation in the core loss of the permanent magnet motor may be due to other loss components which are not included in the

model, and on which further work is required: eddy current loss in the motor case, loss in the rotor due to the tooth ripple flux density, and extra loss caused by the unknown changes in material properties during manufacture. A better representation of loss caused by non-sinusoidal fields is also required.

CHAPTER 7. CONCLUSIONS AND FUTURE WORK

For computer aided design of electromagnetic devices, various novel models of magnetic materials were developed. These models are:

(1) a normal Preisach model of magnetic hysteresis,

(2) a generalised Preisach model of magnetic hysteresis,

(3) a dynamic discrete circuit model of laminated magnetic cores,

(4) a generalised dynamic discrete circuit model of solid magnetic cores for both low and high frequency applications,

(5) an analogical model of pure rotational hysteresis loss,

(6) an analytical model for predicting the core loss with an elliptical flux density from alternating and pure rotational core losses, and

(7) a model of core losses in rotating electrical machines using finite element analysis.

The normal Preisach model features simple formulation and easy parameter identification. It provides correct results, but fails when the hysteresis loop to be predicted is close to the origin of the B-H plane due to intrinsic defects of the model, such as zero initial susceptibility and congruent minor loops.

These defects are eliminated in the generalised Preisach model. The extra data required by the generalised model is the normal magnetisation curve. Verifications using minor loops of same H_b and H_Δ, major loops, and normal and incremental permeabilities showed that the generalised Preisach model gives better accuracy than the normal Preisach model.

The dynamic circuit model of laminated magnetic cores takes all kinds of alternating core losses into consideration and has shown satisfactory accuracy. It can simulate the performance of a magnetic core under arbitrary excitation since the Preisach model is used to trace the magnetisation process. This model is limited to simulations of magnetic cores which are effectively thin at the excitation frequency.

The generalised dynamic circuit model includes skin effect by using a ladder network. This model reduces to the model of laminated cores when only one stage of the ladder network is used. The validity of the theory was verified by comparisons with experimental results at both low and high frequencies.

All information required for identifying the circuit parameters of these dynamic core models, such as the limiting hysteresis loop and specific core losses with sinusoidal flux densities at different frequencies, can be identified from manufacturers' data sheets or through simple measurements.

To provide data for rotational core loss modelling, a single sheet square specimen tester was developed. This tester can be successfully used for both alternating and rotational core loss measurements with arbitrary magnetic flux patterns at different excitation frequencies. The precision of magnetic field measurement in a two dimensional single sheet tester is improved by a new sandwich arrangement of magnetic field sensing coils.

Because of insufficient time, it has not been possible to complete and include the results of an intercomparison between the rotational core loss testers at PTB and UTS. Much useful information was obtained, however, from the measurements on grain oriented silicon steel sheet ORSI-100 and non-oriented silicon steel sheet V270-35A with both alternating and rotating magnetic flux densities using the tester at PTB.

Mathematical derivation and experimental measurements of rotational core losses in both grain oriented and non-oriented silicon steel sheets showed that the formula proposed by Enokizono *et al* [151,155,157] for calculation of core loss due to the rotational component of an elliptically rotating magnetic flux density is incorrect. This formula was corrected and clarified in chapter 5.

The total core loss in an electrical steel sheet with a purely circular flux density can be separated into components of rotational hysteresis, eddy current, and anomalous losses. With a circular flux density, the rotational eddy current loss is twice as much as alternating eddy current loss. The rotational anomalous loss can be modelled using the same formula as for alternating anomalous loss, but the coefficient of rotational anomalous loss is generally a function of flux density, and eventually reduces to zero when the material is saturated and all domain walls disappear.

The analogical model of rotational hysteresis loss was developed based on the strong analogy between the electromagnetic torque in a single phase induction machine and the torque due to rotational hysteresis with a circular field. Excellent agreement was achieved between the model and experimental data for different magnetic materials reported in earlier publications and measured here.

Derived from the formula for total core loss used in measurement, equation (6.22) predicts core loss with an elliptical flux density from alternating and pure rotational core losses. This model is independent of excitation frequency and therefore applicable to hysteresis as well as total core losses.

Using finite element analysis, the core loss in a permanent magnet motor was calculated by summing up the core losses in all finite elements. In each element, the core loss with an arbitrary rotating flux density vector was evaluated in terms of rotational hysteresis, eddy current, and anomalous losses by (6.25) to (6.27). The discrepancy between the calculation and measurement is about 13%.

Further work is required on the following aspects:

(1) Further checks of the generalised Preisach model of magnetic hysteresis, e.g. using experimental minor hysteresis loops and losses.

(2) Development of a model of rotational hysteresis, i.e. the B-H relationship when the field is rotating, suitable for engineering applications. Although the Preisach model has been extended to cover rotational hysteresis [60-67], the method for parameter identification is impractical for engineering applications, and experimental verification was not reported.

(3) Improvement of rotational core loss measuring techniques. A new control strategy is required in order to control the locus of the rotating flux density vector when the specimen is saturated. There is also a requirement for new probes of two dimensional magnetic field strength and flux density, which can provide accurate results and are convenient for batch measurements.

(4) Intercomparison between the testers at PTB and UTS. Four specimens of grain oriented (ORSI-100) and non-oriented (V270-35A) silicon steel sheets (part of the specimen set used for the European intercomparison) have been measured with

various flux patterns using the tester at PTB, and the measurements will be repeated using the tester at UTS.

(5) Further understanding of the mechanisms of rotational hysteresis loss. Although good agreement was achieved between the experimental results and the analogical model of rotational hysteresis loss, the underlying physical principle is still not very clear.

(6) Investigation of other loss components that are not included in the core loss model of rotating electrical machines, such as core loss in the end region of the stator core, eddy current loss in the case, and loss in the rotor due to the tooth ripple flux density, and evaluation of spread due to manufacture tolerances and variation of material properties caused by manufacturing and assembly process.

APPENDIX A. A LIST OF PUBLICATIONS

1. A Methodology for Generating 1-D Profiles from 2-D Finite Element Solutions
   P.A. Watterson, V.S. Ramsden, and J.G. Zhu
   Proceedings of the Sixth International Conference in Australia on Finite Element Methods, Sydney, Australia, July 8th-10th, 1991, pp121-124

2. Optimization of Permanent Magnet Motors using Field Calculations of Increasing Precision
   P.A. Watterson, J.G. Zhu, and V.S. Ramsden
   IEEE Trans. MAG-28, No.2, March 1992, pp1589-1592

3. Finite Element Calculation of Core Losses in Motors with Non-Sinusoidal Fields
   J.G. Zhu, V.S. Ramsden, and P.A. Watterson
   Proceedings of the International Conference on Electrical Machines (ICEM'92), Manchester, U.K., 15th-17th September 1992, pp1182-1186

4. Dynamic Simulation of Laminated Iron Cores under Non-Sinusoidal Flux
   J.G. Zhu, S.Y.R. Hui, and V.S. Ramsden
   Proceedings of the Australasia Universities Power and Control Engineering Conference (AUPCEC'92), 1-2 October 1992, Brisbane, Queensland, Australia, pp501-506

5. A Dynamic Circuit Model for Solid Magnetic Cores
   J.G. Zhu, S.Y.R. Hui, and V.S. Ramsden
   Record of the 24th Annual IEEE Power Electronics Specialists Conference (PESC'93), Seattle, Washington, USA, June 20-24, 1993, pp1111-1115

6. Discrete Modelling of Magnetic Cores Including Hysteresis Eddy Current and Anomalous Losses
   J.G. Zhu, S.Y.R. Hui, and V.S. Ramsden
   IEE Proceedings Part-A, Vol.140, No.4, July 1993, pp317-322

7. Core Loss Modelling in Rotational Electrical Machines
   J.G. Zhu and V.S. Ramsden
   Proceedings of the International Conference on Electrical Machines in Australia (ICEMA'93), Adelaide, Australia, 14-16 September 1993, pp52-57

8. Numerical Implementation of a Dynamic Circuit Model of Magnetic Cores
J.G. Zhu, S.Y.R. Hui, and V.S. Ramsden
Proceedings of the Australasia Universities Power Engineering Conference (AUPEC'93), Wollongong, New South Wales, Australia, 29th September to 1st October 1993, pp576-581

9. Two Dimensional Measurement of Magnetic Field and Core Loss Using a Square Specimen Tester
J.G. Zhu and V.S. Ramsden
The digest printed in Proceedings of the International Magnetics Conference (INTERMAG'93), Stockholm, Sweden, 13-16 April 1993, ppCB-11, and the full paper in IEEE Trans. MAG-29, No.6, November 1993, pp2995-2997

10. Magnetic Hysteresis Modelling and Simulation using Preisach Theory and TLM Technique
S.Y.R. Hui and J.G. Zhu
Record of the 25th Annual IEEE Power Electronics Specialists Conference (PESC'94), Taipei, Taiwan, Republic of China, June 20-24, 1994, pp837-842

11. A Dynamic Equivalent Circuit Model for Solid Magnetic Cores for High Frequency Operation
J.G. Zhu, S.Y.R. Hui, and V.S. Ramsden
To be published in IEEE Transactions on Power Electronics in 1994

12. Prediction of Core Loss with Elliptical Flux from Measurements with Alternating and Circular Fluxes in Electrical Steel Sheets
J.G. Zhu, V.S. Ramsden, and J.D. Sievert
Accepted by the International Symposium on Advanced Computational and Design Techniques in Applied Electromagnetic Systems (ISEM'94), June 22-24, 1994, Seoul, Korea
To be published in International Journal of Applied Electromagnetics in Materials in 1994

13. Numerical Modelling and Simulation of Hysteresis Effects in Magnetic Cores Using Transmission Line Modelling and Preisach Theory
S.Y.R Hui and J.G. Zhu
Accepted by IEE Proceedings Part-B

14. A Generalised Dynamic Circuit Model of Magnetic Cores for Low- and High-Frequency Applications, Part I: Theoretical Calculation of the Equivalent Core Loss Resistance
J.G. Zhu, S.Y.R. Hui, and V.S. Ramsden
Submitted to IEEE Transactions on Power Electronics

15. A Generalised Dynamic Circuit Model of Magnetic Cores for Low- and High-Frequency Applications, Part II: Circuit Model Formulation and Implementation
S.Y.R. Hui, J.G. Zhu, and V.S. Ramsden
Submitted to IEEE Transactions on Power Electronics

APPENDIX B. MAGNETIC CIRCUIT DESIGN OF A SQUARE SPECIMEN TESTER

B.1 INTRODUCTION

As discussed in chapter 4, the rotational core loss tester using a single sheet square specimen is very flexible and suitable for measurements under various complex magnetic flux conditions. Hence, a similar apparatus was designed. The designing method and results are reported in this appendix.

For the magnetic circuit design of a square specimen tester, the method of magnetic reluctance network was used. This method yields acceptable results, when high quality grain-oriented silicon steel sheet is to be used for the tester yoke, and most of the magnetic flux is restrained within the tester core. Section B.2 gives the reluctance network and the parameters.

Section B.3 deals with the design of the excitation windings which are mounted on the four poles of the tester core. Every two excitation windings on the same axis can be connected either in series or in parallel so that they produce aiding magnetic flux on that axis.

In order to saturate the specimen, a very large excitation current may be required due to the non-linear magnetisation characteristics and the effects of rotational hysteresis. Therefore, a thermal analysis appears to be essential. An equivalent heat transfer network was employed for thermal modelling. The thermal analysis of the excitation winding and the magnetic core is illustrated in section B.4.

In the design, specimens of different magnetic materials from lower grade to high grade silicon steels and amorphous materials are considered. The results of the magnetic circuit analysis and thermal modelling are reported in section B.5.

B.2 RELUCTANCE NETWORK

Fig.B-1 labels the dimensions of the tester yoke and the specimen illustrated in Fig.5-3. For high precision measurement, the power loss dissipated in the magnetic core of the tester should be kept as low as possible. Thus, low core loss ORIENTCORE.HI-B, grade M-0H grain-oriented silicon steel [213] manufactured by Nippon Steel Corporation, Japan, was chosen as the lamination material. To reduce the reluctance of the core, the lamination was designed to be continuous between the magnetisation poles and the yoke. The yoke laminations were arranged vertically so as to reduce leakage flux between the poles of two axes. The magnetisation poles

had a wedged shape to concentrate magnetic flux into the specimen. This type of structure, according to the analysis by Enokizono and Sievert [154], gives better results for **H** measurement, as discussed in section 4.2.3.3.

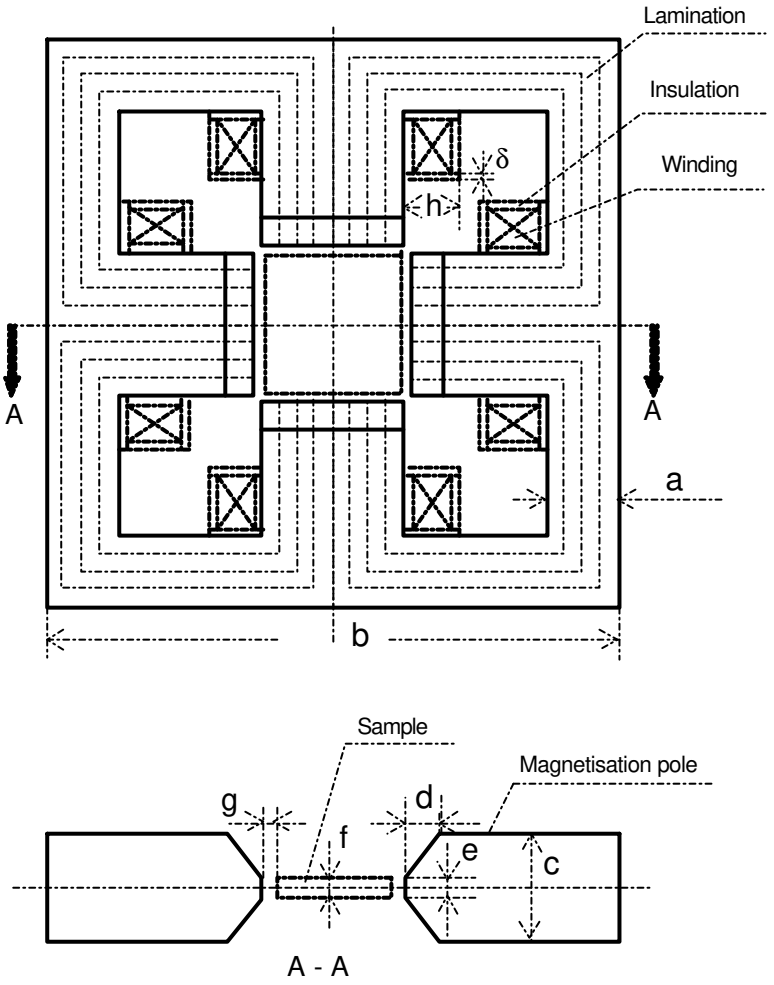

Fig.B-1 Dimension labels of rotational core loss tester

The width of the excitation poles was determined by the possible minimum width of the electrical steel sheet to be measured. This was found to be 50 mm for MetGlas 2605S-2, a thin amorphous material. The length of the poles was determined by the size of the excitation windings, which in turn was determined by the required mmf and the temperature rise limit.

Fig.B-2 shows the magnetic reluctance network corresponding to the magnetic circuit shown in Fig.B-1.

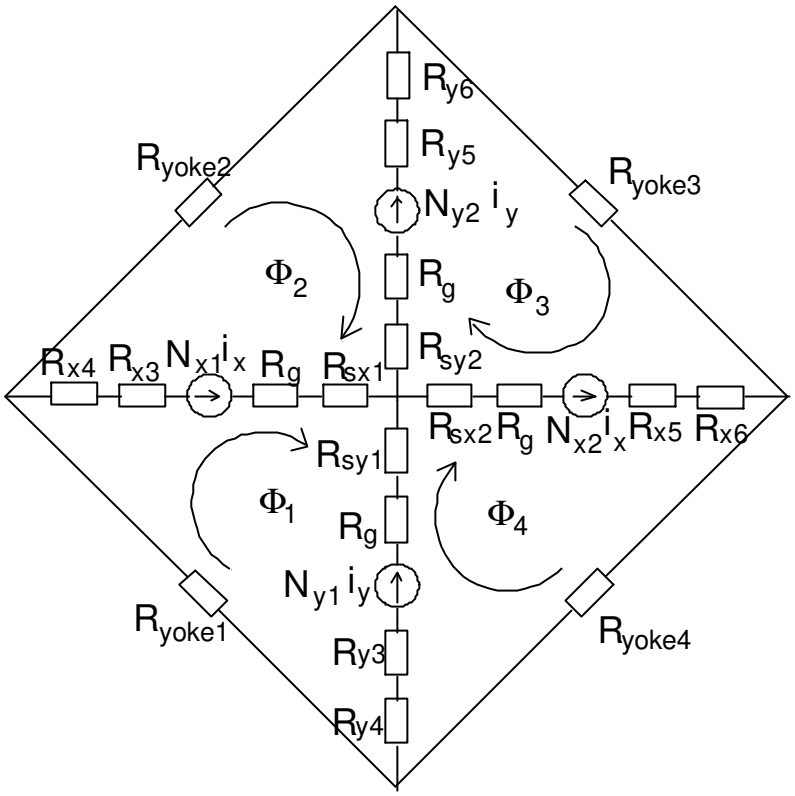

Fig.B-2 Magnetic reluctance network of rotational core loss tester

The reluctances in the network can be calculated as

$$R_{sij} = \frac{1}{2f\mu_{ij}} \qquad \text{(i=x,y; and j=1,2)} \qquad \text{(B.1)}$$

$$R_g = \frac{g}{2a(e-f)\mu_0} \ln\frac{e}{f} \qquad \text{(B.2)}$$

$$R_{ij} = \frac{d}{2a(c-e)\mu_{ij}} \ln\frac{c}{e} \qquad \text{(i=x,y; and j=3,5)} \qquad \text{(B.3)}$$

$$R_{ij} = \frac{b-3a-2(g+d)}{4ac\mu_{ij}} \qquad \text{(i=x,y; and j=4,6)} \qquad \text{(B.4)}$$

$$R_{yokei} = \frac{b-a}{ac\mu_{yokei}} \qquad \text{(i=1,2,3,4)} \qquad \text{(B.5)}$$

where R_{sij} (i=x,y; and j=1,2) are the four reluctances of the specimen on the X and Y axes, R_g the reluctance of the air-gap, R_{ij} (i=x,y; and j=3,5) are the reluctances of the wedged part of the magnetisation poles, R_{ij} (i=x,y; and j=4,6) the reluctances of the un-wedged part of the magnetisation poles, R_{yokei} (i=1,2,3,4) the reluctances of the yoke, $\mu=B/H$ is the permeability of each part, and $\mu_0=4\pi\times10^{-7}$ the permeability of a vacuum.

The required mmf to saturate the specimen was determined by solving the network for a specified flux density. First, the magnetic reluctance network was solved for the loop flux Φ_i (i=1,2,3,4) by non-linear iterations. Then, the flux and the flux density in each part of the magnetic circuit were evaluated in turn. After a few trials, the mmf required to saturate the specimen was finally determined.

B.3 DESIGN OF EXCITATION WINDINGS

The number of turns and the wire diameter of the excitation windings are subject to various constraints: the space available in the tester, temperature rise limit, the rating of the power amplifiers, and skin effect. Among them, the most important factor is that the required magnetisation current and the terminal voltage of the windings should match the rating of available power amplifiers.

When the number of turns and the wire diameter are determined, the winding resistance can then be calculated by

$$R_w = \rho \frac{4l_w}{\pi d_w{}^2} \tag{B.6}$$

where ρ is the resistivity of copper, l_w the total length of the wire, and d_w the diameter of the wire.

The winding inductance was calculated by

$$L_w = \frac{d\lambda}{di} \tag{B.7}$$

using numerical difference, where λ is the flux linkage of the winding, and i the current flowing through the winding.

In the design, skin effect was checked at high frequency. In a concentrated winding, the skin effect in a conductor is caused by the leakage flux it links as shown in Fig.B-3. As an approximate check on the effect, the skin depth in an isolated conductor was used.

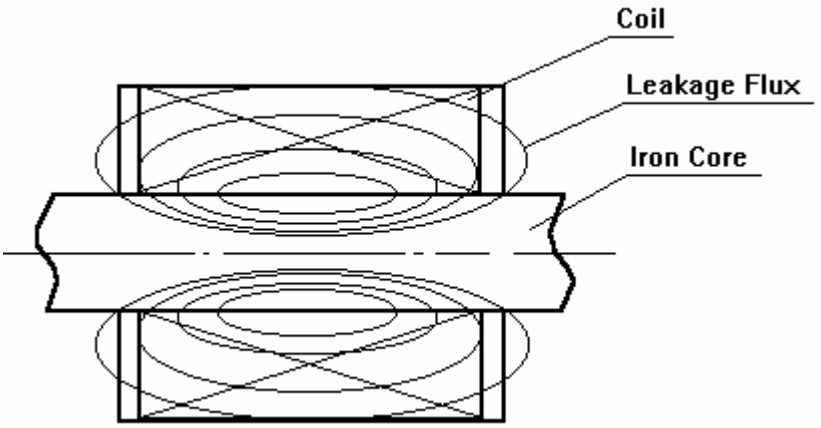

Fig.B-3 Concentrated winding and leakage flux

Table B-1 lists the skin depth of copper at different frequencies. It can be seen that the skin effect would not be severe when the frequency is below or equal to 1 kHz if the wire radius is smaller than the skin depth of 2.11 mm.

Table B-1. Skin depth in copper versus frequency

Frequency f (Hz)	1	10	100	1,000	10,000	100,000
Skin Depth (m)	6.66E-02	2.11E-02	6.66E-03	2.11E-03	6.66E-04	2.11E-04

B.4 THERMAL MODELLING

Because the maximum value of the excitation current is limited by the temperature rise, thermal modelling is essential for determining the sizes of the tester magnetic core and the excitation windings. Heat transfer is a very complicated problem. In order to determine the temperature distribution in the tester magnetic core and the excitation windings accurately, sophisticated numerical methods and software packages would be required. In this case, an approximate equivalent heat transfer network [222] was employed.

B.4.1 Equivalent Heat Transfer Network

This method divides the whole system to be modelled into many small solid elements according to the structure and the materials, and assumes that the heat is transferred by conduction within a solid element and between solid elements, and by convection and radiation between the surfaces of a solid element and the air.

In a solid element, one dimensional heat transfer by conduction can be modelled by an equivalent heat transfer resistance R, as illustrated in Fig.B-4. The resistance is defined as

$$R = \frac{T_2 - T_1}{Q} \tag{B.8}$$

where Q is the heat flow through the solid element, and T_1 and T_2 are the temperature of the end surfaces.

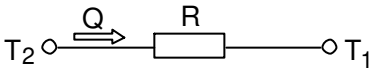

Fig.B-4 Equivalent heat transfer resistance in a solid element

Fig.B-5 shows the three dimensional heat conduction model of a solid element, where Q_S is the heat generated in the solid element, R_x, R_y, and R_z are the equivalent heat transfer resistances on the X, Y, and Z axes, respectively.

The heat transfer resistance on the X, Y, and Z axes can be calculated as following

$$R_x = \frac{\Delta x}{2\lambda_x \Delta y \Delta z} \tag{B.9}$$

$$R_y = \frac{\Delta y}{2\lambda_y \Delta z \Delta x} \tag{B.10}$$

$$R_z = \frac{\Delta z}{2\lambda_z \Delta x \Delta y} \tag{B.11}$$

where λ_x, λ_y, and λ_z are the heat conductivities on the X, Y, and Z axes, Δx, Δy, and Δz the side lengths of the solid element.

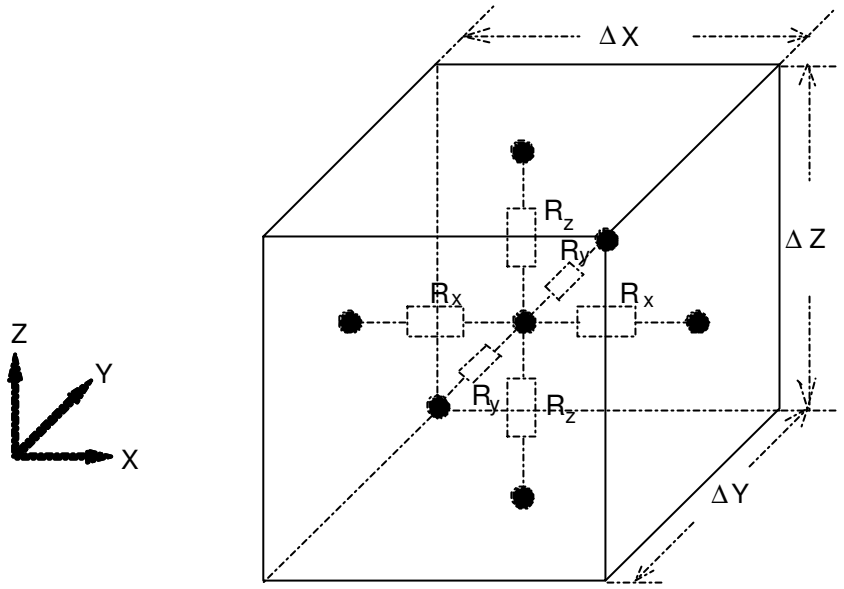

Fig.B-5 Three dimensional heat conduction model of a solid element

The convection and radiation of a solid element surface can be evaluated by Newton's law of cooling, namely

$$Q = (h_r + h_c) A \Delta T \tag{B.12}$$

where Q is the heat transferred, h_r and h_c are the coefficients of radiation and convection, respectively, A is the surface area, and ΔT the temperature difference between the surface and the air. The equivalent resistance to the heat radiation and convection of the surface can be calculated as

$$R_s = \frac{1}{(h_r + h_c) A} \tag{B.13}$$

Therefore, the whole system can be modelled by a network of equivalent heat transfer resistances. The potential of a node is the temperature of that point, and the reference potential is the air (ambient) temperature. The temperature rise of a node is defined as the difference between the node temperature and the ambient temperature.

B.4.2 Thermal Analysis of the Tester

Because of the geometrical symmetry, only one fourth of the tester is to be modelled, as depicted in Fig.B-6.

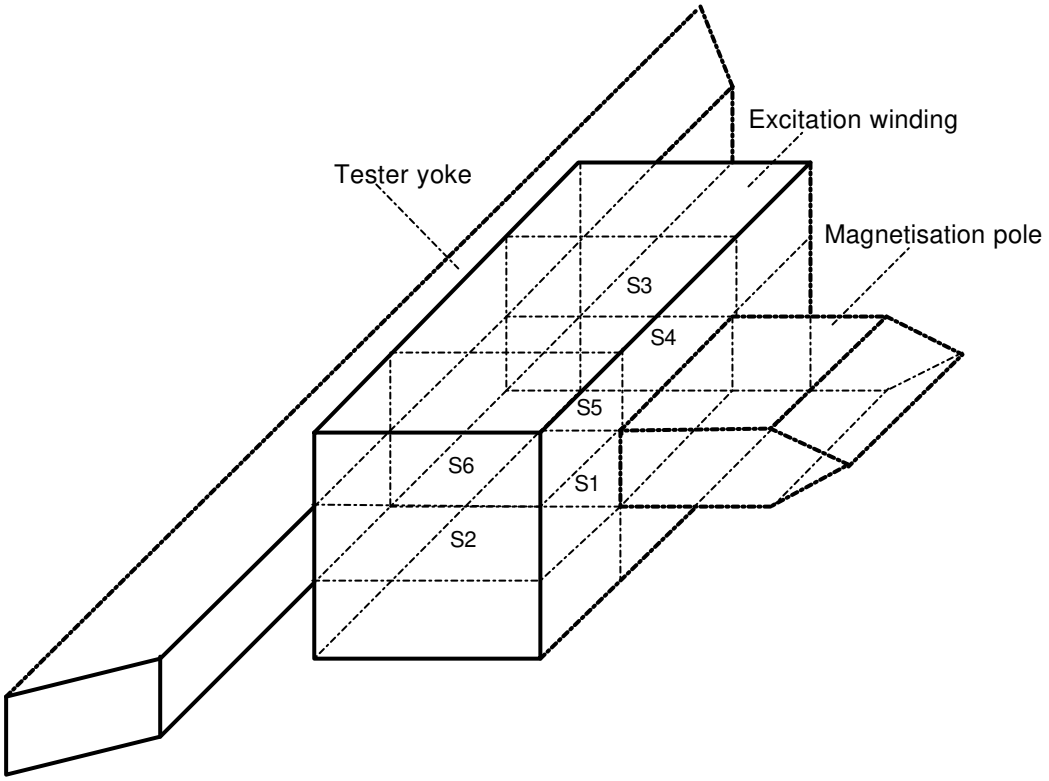

Fig.B-6 Part of the tester for thermal modelling

Generally, a three dimensional equivalent heat transfer network is required. To simplify the calculation, the conductivities of electrical steel and copper were assumed to be infinite, and the heat conduction in the insulation layer between two steel sheets and in the winding insulation between conductors was assumed one dimensional, that is, only the heat penetration in the direction of the thickness was considered.

Applying the thermal network model described in section B.4.1 yields a network as illustrated in Fig.B-7. This network consists of three heat transfer paths:

(1) Winding - Tester Core - Air (Path 1),
(2) Winding - Coil Former - Air (Path 2), and
(3) Winding - Wrap Insulation - Air (Path 3);

and two heat sources:

(1) P_{Cu} -- the copper loss due to the winding resistance, and

(2) P_{Fe} -- the iron loss of the tester core.

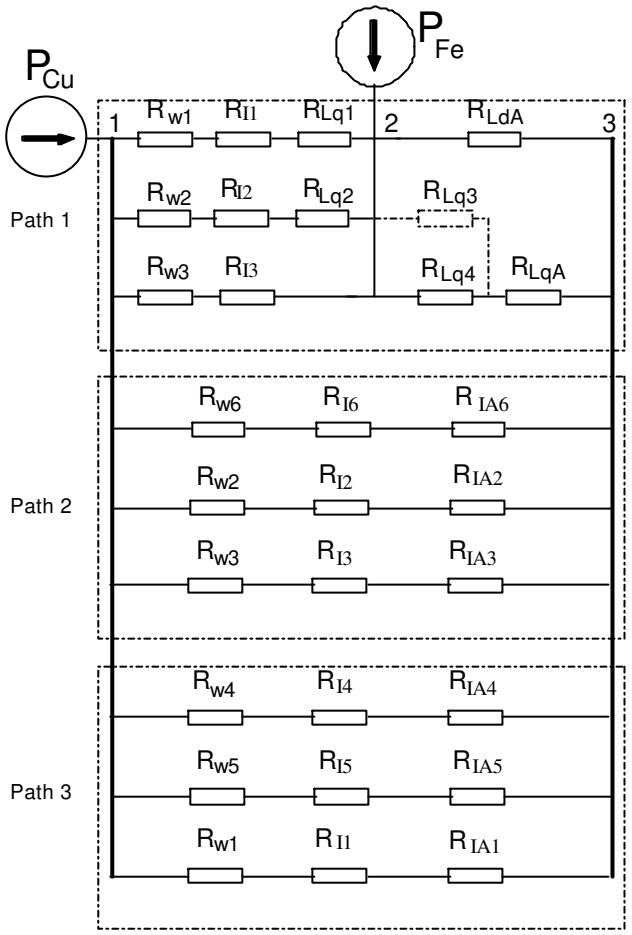

Fig.B-7 Equivalent heat transfer network of the rotational core loss tester
1 -- winding centre, 2 -- lamination centre, and 3 -- the air

The equivalent heat transfer resistances were calculated as follows

$$R_{Wi} = \frac{\frac{b-4a}{4} - 2\delta}{2\lambda_W A_i} \qquad (i = 1,4,5) \tag{B.14}$$

$$R_{Wi} = \frac{h}{2\lambda_W A_i} \qquad (i = 2,3,6) \tag{B.15}$$

$$R_{Ii} = \frac{\delta}{\lambda_I A_i} \qquad (i = 1,2,\ldots,6) \tag{B.16}$$

$$R_{IAi} = \frac{1}{(h_c + h_r)_{IA}\ A_i} \qquad (i = 1,2,\ldots,6) \tag{B.17}$$

$$R_{Lq1} = \frac{a}{2\lambda_{Lq} A_1} \tag{B.18}$$

$$R_{Lq2} = \frac{a}{\lambda_{Lq} A_2} \tag{B.19}$$

$$R_{Lq3} = \frac{a}{2\lambda_{Lq}(2b - 4a - 2h)c} \tag{B.20}$$

$$R_{Lq4} = \frac{a}{2\lambda_{Lq}(\frac{b - 4a}{4} - \frac{d}{2} - g)c} \tag{B.21}$$

$$R_{LdA} = \frac{1}{(h_c + h_r)_{LdA}\ A_{LdA}} \tag{B.22}$$

$$R_{LqA} = \frac{1}{(h_c + h_r)_{LqA}\ A_{LqA}} \tag{B.23}$$

where R_{wi} (i=1,2,...,6) are the equivalent heat transfer resistance from the centre to the surfaces of the winding in the direction of S_i, R_{Ii} (i=1,2,...,6) the equivalent heat transfer resistance of the insulation including the plastic former in the direction of S_i, R_{IAi} (i=1,2,...,6) the equivalent heat transfer resistance from the insulation surface S_i to the air, R_{Lqi} (i=1,2,...,4) the equivalent heat transfer resistance from the centre to the surfaces of the laminations in the direction of S_i, R_{LdA} is the equivalent heat transfer resistance from the horizontal surfaces, which are perpendicular to the plane of the laminations, of the magnetic core to the air, R_{LqA} is the equivalent heat transfer resistance from the vertical surfaces, which are parallel to the plane of the laminations, of the magnetic core to the air, the dimensions a, b, c, d, g, h, and δ are shown in Fig.B-1, λ_W is the average heat conductivity in the cross section of the excitation winding, λ_I is the heat conductivity of the plastic former and the winding insulation, λ_{Lq} is the average heat conductivity of the tester core in the direction perpendicular to the laminations, $(h_C+h_r)_{IA}$ is the convection and radiation coefficient of the winding insulation surface in touch with the air, $(h_C+h_r)_{LqA}$ is the convection and radiation coefficient of the tester core surface in parallel with the laminations, $(h_C+h_r)_{LdA}$ is the convection and radiation coefficient of the tester core surface perpendicular to the laminations, A_i (i=1,2,...,6) is the area of surface S_i, A_{LdA} is the area of the tester core surface perpendicular to the laminations, and A_{LqA} is the area of the tester core surface parallel to the laminations. These areas were calculated as:

$$A_1 = 2hc \tag{B.24}$$

$$A_2 = 2c(\frac{b-4a}{4} - 2\delta) \tag{B.25}$$

$$A_3 = 4a(\frac{b-4a}{4} - 2\delta) \tag{B.26}$$

$$A_4 = 8ah \tag{B.27}$$

$$A_5 = 8h^2 \tag{B.28}$$

$$A_6 = 8h(\frac{b-4a}{4} - 2\delta) \tag{B.29}$$

$$A_{LdA} = 2a[b - a + 2(\frac{b-4a}{4} - g - d + \sqrt{d^2 + \frac{c^2}{4}})] \tag{B.30}$$

$$A_{LqA} = 2c(b - 2a - h + \frac{b-4a}{4} - g - \frac{d}{2}) \tag{B.31}$$

The copper loss P_{Cu} was calculated by

$$P_{Cu} = I^2 R_W \tag{B.32}$$

where I is the rms value of the current flowing in the winding. The core loss P_{Fe} was obtained by interpolation of the loss curves provided by the manufacturer.

The heat conductivities of materials were chosen as λ_W=1.3, λ_I=0.2, λ_{Lq}=0.65 [222]. The convection and radiation coefficients of the surfaces in touch with the air were all assumed to be 14 W/m^{2}K [222].

The temperature rise of each part of the tester was obtained by solving the network. An approximate calculation, which assumes that all the heat generated by the losses is transferred to the tester core and that the temperature rise of the core is determined by Newton's law of cooling, gives a mean value of temperature rise between the temperature rises of the winding and the magnetic core obtained by the network method.

B.5 Design of the Tester

By using the methods of magnetic reluctance network and heat transfer network outlined in the previous sections, the tester dimensions and winding parameters were determined after a few trial iterations. Magnetic flux, flux density, and field strength in different parts of the tester, required excitation currents and terminal voltages of the excitation windings were calculated for specimens of three different materials, Lycore-800, Lycore-140, and MetGlas 2605S-2. The copper loss in the excitation windings, the core loss in the tester core, and the temperature rises in the centre of the winding and in the centre of the laminated core were also checked. The results are printed in Table B-2. The structure and dimensions of the tester yoke are illustrated in Fig.5-3, and the design of the excitation winding is depicted in Fig.B-8.

Table B-2 Design of the single sheet rotational core loss tester

==========

DESIGN OF SINGLE SHEET ROTATIONAL CORE LOSS TESTER

1. Dimensions of the tester core (as shown in Fig.B-1, unit: mm)

a	b	c	d	e	f	g	δ
25	240	20	10	1	0.3	0.5	1

Material of the tester core: M-0H Grain-oriented silicon steel, 0.3 mm sheet
Weight of the tester core: 5.416 kg

2. Winding parameters

Number of turns of each coil: 300 turns
Wire length: 76.64 m
Wire diameter: 1.6 mm
Thickness of enamel insulation: 0.1 mm
Height of winding: 27.2 mm
Width of winding: 33 mm
Winding resistance (two coils in series) 1.663 Ohm

3. Performances

Excitation currents: Ix = sqrt(2)*Ix_rms*sin(2πf*time+phi_Ix) (A)
Iy = sqrt(2)*Iy_rms*sin(2πf*time+phi_Iy) (A)

With a specimen of Lycore-800 (0.3 mm sheet)

Ix_rms=	5 A	Phi_Ix=	90 deg
Iy_rms=	5 A	Phi_Iy=	0 deg
Freq.=	100 Hz	Time=	0 s

Solution (168 iterations, Err.=0.00000E+000):

Flux (Wb), flux density (T), and field strength (A/m) in the yoke:

Yoke1:	0.000014	0.028722	1.4287
Yoke2:	-1.4E-05	-0.02871	-1.42809
Yoke3:	-1.4E-05	-0.02871	-1.42809

Yoke4:	0.000014	0.028722	1.428701

Flux (Wb), flux density (T), and field strength (A/m) in the magnetisation poles:

Pole X1:	0.000029	0.054697	2.520057	0.028716	1.428397
Pole X2:	0.000029	0.054697	2.520057	0.028716	1.428397
Pole Y1:	0	0	0	0	0
Pole Y2:	0	0	0	0	0

Flux density (T) and field strength (A/m) in air gaps:

X axis:	0.883564	703117.7	0.883564	703117.7
Y axis:	0	0.044539	0	0.044539

Flux density (T) and field strength (A/m) in the specimen:

X axis:	1.914389	69113.41	1.914389	69113.41
Y axis:	0	0.000154	0	0.000154

The position of B is 0.000004(Deg) from X-axis

Winding inductances at the specified time instant (two coils in series):

X-axis:	0.138 mH	Y-axis:	11.713 mH

Terminal voltages at the specified time instant:

Vx=	11.856 V	Vy=	51.186 V

Max total copper loss:	83.155 W
Max core loss in yoke:	0.028 W
Winding temperature rise:	48.822 deg C
Lamination temperature rise:	23.864 deg C
Approximate temperature rise:	31.495 deg C

With a specimen of Lycore-140 (0.3 mm sheet)

Ix_rms=	2.5 A	Phi_Ix=	90 deg
Iy_rms=	2.5 A	Phi_Iy=	0 deg
Freq.=	100 Hz	Time=	0 s

Solution (44 iterations, Err.=0.00000E+000)

Flux (Wb), flux density (T) and field strength (A/m) in the yoke:

Yoke1:	0.000015	0.030896	1.527318
Yoke2:	-1.5E-05	-0.0309	-1.52747
Yoke3:	-1.5E-05	-0.0309	-1.52747
Yoke4:	0.000015	0.030896	1.527317

Flux (Wb), flux density (T) and field strength (A/m) in the poles:

Pole X1:	0.000031	0.058852	2.676971	0.030897	1.527395
Pole X2:	0.000031	0.058852	2.676971	0.030897	1.527395
Pole Y1:	0	0	0	0	0
Pole Y2:	0	0	0	0	0

Flux density (T) and field strength (A/m) in air gaps:

X axis:	0.950689	756534.6	0.950689	756534.6
Y axis:	0	-0.04454	0	-0.04454

Flux density (T) and field strength (A/m) in the specimen:

X axis:	2.059827	25491.36	2.059827	25491.36
Y axis:	0	-1.3E-05	0	-1.3E-05

The position of B is 0.000003(deg) from X-axis

Winding inductances at the specified time instant (two coils in series):

X-axis:	1.854 mH	Y-axis:	12.958 mH

Terminal voltages at the specified time instant:

Vx=	6.522 V	Vy=	28.314 V

Max total copper loss:	20.789	W
Max core loss in yoke:	0.032	W
Winding temperature rise:	12.213	deg C
Lamination temperature rise:	5.980	deg C
Approximate temperature rise:	7.883	deg C

With a specimen of MetGlas2605S-2 (0.03mm sheet)

Ix_rms=	1.5 A	Phi_Ix=	90 deg
Iy_rms=	1.5 A	Phi_Iy=	0 deg
Freq.=	100 Hz	Time=	0 s

Solution (39 iterations, Err.=0.00000E+000):

Flux (Wb), flux density (T) and field strength (A/m) in the yoke:

Yoke1:	0.000015	0.030554	1.511879
Yoke2:	-1.5E-05	-0.03056	-1.51194
Yoke3:	-1.5E-05	-0.03056	-1.51194
Yoke4:	0.000015	0.030554	1.511879

Flux (Wb), flux density (T) and field strength (A/m) in the poles:

Pole X1:	0.000031	0.058198	2.652606	0.030554	1.511908
Pole X2:	0.000031	0.058198	2.652606	0.030554	1.511908
Pole Y1:	0	0	0	0	0
Pole Y2:	0	0	0	0	0

Flux density (T) and field strength (A/m) in air gaps:

X axis:	0.940128	748130.3	0.940128	748130.3
Y axis:	0	0	0	0

Flux density (T) and field strength (A/m) in the specimen:

X axis:	2.036945	8708.918	2.036945	8708.918
Y axis:	0	0	0	0

The position of B is 0.000000(deg) from X-axis

Winding inductances at the specified time instant (two coils in series):

X-axis:	4.214 mH	Y-axis:	13.124 mH

Terminal voltages at the specified time instant:

Vx=	4.403 V	Vy=	17.206 V

Max total copper loss:	7.484	W
Max core loss in yoke:	0.032	W
Winding temperature rise:	4.402	deg C
Lamination temperature rise:	2.164	deg C
Approximate temperature rise:	2.846	deg C

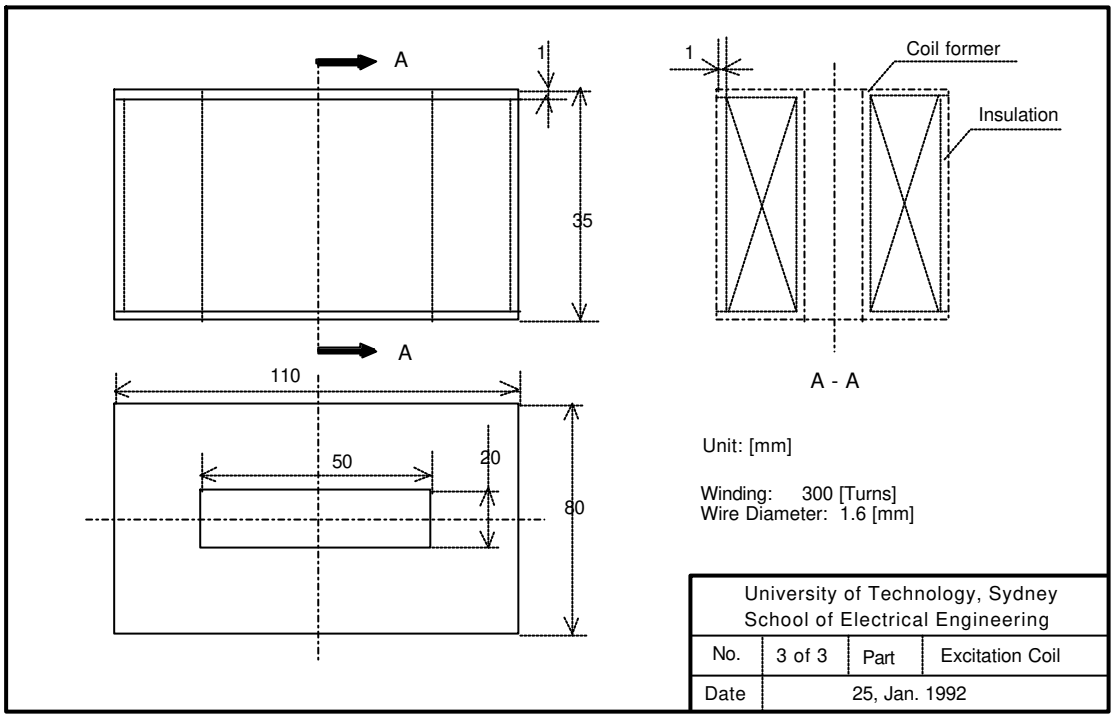

Fig.B-8 Design of excitation winding

From the results listed in Table B-2, it can be seen that the tester in this design is able to magnetise a specimen of Lycore-800 at up to 1.9 T with an excitation current of 5 A in the windings on both X and Y axes. Because high quality grain-oriented electrical steel sheet is used for the lamination material, the core loss occurring in the magnetic core is very low. The temperature rise, in this case, is 49°C in the centre of the excitation windings, and 24°C in the centre of the yoke laminations. For materials of higher grade, such as Lycore-140 and MetGlas 2605S-2, even smaller excitation current is required to magnetise the specimen, and the temperature rises are also much smaller. Therefore, the design is satisfactory.

REFERENCES

[1] J.C. Maxwell, "Electricity and magnetism", Oxford University Press, 1873

[2] R.M. Bozorth, "Ferromagnetism", D. Van Nostrand Company, Inc., 1951

[3] B.D. Cullity, "Introduction to magnetic materials", Addison-Wesley, 1972

[4] E.C. Snelling, "Soft ferrites, properties and applications", Butterworths & Co. (Publishers) Ltd., Second edition 1988

[5] D.C. Jiles, "Introduction to magnetism and magnetic materials", Chapman and Hall, 1991

[6] J.R. Brauer, "Simple equations for the magnetization and reluctivity curves of steel", IEEE Trans. MAG-11, 1975, pp81

[7] G.F. Dionne, J.A. Weiss, and G.A. Allen, "Hysteresis loops modelled from coercivity, anisotropy, and microstructure parameters", J. Appl. Phys., Vol.61, No.8, April 1987, pp3862-3864

[8] J.R. Lucas and P.G. McLaren, "B-H loop representation for transient studies", Int. J. Elect. Enging. Educ., Vol.28, 1991, pp261-270

[9] J. Fischer and H. Moser, "Die Nachbildung von Magnetisie-rungskuurven durch einfache algebraische oder transzendente Funktionen", Archiv. fur Elektrotecnik, XLII. Band, Heft 5, 1956, pp286-299

[10] F.C. Trutt, E.A. Erdelyi, and R.E. Hopkins, "Representation of the magnetization characteristic of dc machines for computer use", IEEE Trans. PAS-87, 1968, pp665-669

[11] G.F.T. Widger, "Representation of magnetization curves over extensive range by rational-fraction approximations", Proc. IEE, Vol.116, 1969, pp156-160

[12] C.E. Lin, J.B. Wei, C.L. Huang, and C.J. Huang, "A new model for transformer saturation characteristics by including hysteresis loops", IEEE Trans. MAG-25, No.3, May 1989, pp2706-2712

[13] G.J. Frame, N. Mohan, T.H. Liu, "Hysteresis modelling in an electro-magnetic transients program", IEEE Trans. PAS-101, No.9, Sept. 1982, pp3403-3411

[14] S.H. Charap, "Magnetic hysteresis model", IEEE Trans. MAG-10, No.4, Dec. 1974, pp1091-1096

[15] R.I. Potter and R.J. Schmulian, "Self-consistently computed magnetization patterns in thin magnetic recording media", IEEE Trans. MAG-7, No.4, Dec. 1971, pp873-879

[16] J. Rivas, J.M. Zamarro, E. Martin, and C. Pereira, "Simple approximation for magnetization curves and hysteresis loops", IEEE Trans. MAG-17, No.4, July 1981, pp1498-1502

[17] E.C. Stoner, F.R.S. and E.P. Wohlfarth, "A mechanism of magnetic hysteresis in heterogeneous alloys", Phil. Trans. Roy. Soc., Vol.240A, May 4, 1948, pp599-642

[18] D.L. Atherton, and J.R. Beattie, "A mean field Stoner-Wohlfarth hysteresis model", IEEE Trans. MAG-26, No.6, Nov. 1990, pp3059-3063

[19] D.C. Jiles and D.L. Atherton, "Theory of ferromagnetic hysteresis", Journal of Magnetism and Magnetic Materials, Vol.61, 1986, pp48-60

[20] D.C. Jiles and J.B. Thoelke, "Theory of ferromagnetic hysteresis: determination of the model parameters from experimental hysteresis loops", IEEE Trans. MAG-25, No.5, Sept. 1989, pp3928-3930

[21] D.C. Jiles, J.B. Thoelke, and M.K. Devine, "Numerical determination of hysteresis parameters for the modelling of magnetic properties using the theory of ferromagnetic hysteresis", IEEE Trans. MAG-28, No.1, Jan. 1992, pp27-35

[22] Von F. Preisach, "Uber die magnetische Nachwirkung", Z. fur Physik, Bd. 94, 1935, pp277-302

[23] M.A. Coulson, R.D. Slater, and R.R.S. Simpson, "Representation of magnetic characteristic, including hysteresis, using Preisach's theory", Proc. IEE, Vol.124, No.10, Oct.1977, pp895-898

[24] R.M. Del Vecchio, "An efficient procedure for modelling complex hysteresis processes in ferromagnetic materials", IEEE Trans. MAG-16, No.5, Sept. 1980, pp809-811

[25] I.D. Mayergoyz, "Hysteresis models from the mathematical and control theory points of view", J. Appl. Phys., Vol.57, No.1, 15 April 1985, pp3803-3805

[26] T. Doong and I.D. Mayergoyz, "On numerical implementation of hysteresis models", IEEE Trans. MAG-21, No.5, Sept. 1985, pp1853-1855

[27] I.D. Mayergoyz, "Mathematical models of hysteresis", Physical Review Letters, Vol.56, No.15, April 1986, pp1518-1521

[28] I.D. Mayergoyz, "Mathematical models of hysteresis", IEEE Trans. MAG-22, No.5, Sept. 1986, pp603-608

[29] G. Kadar, "On the Preisach function of ferromagnetic hysteresis", J. Appl. Phys., Vol.61, No.8, April 1987, pp4013-4015

[30] D.L. Atherton, B. Szpunar, and J.A. Szpunar, "A new approach to Preisach diagram", IEEE Trans. MAG-23, No.3, May 1987, pp1856-1865

[31] I.D. Mayergoyz and G. Friedman, "Generalized Preisach model of hysteresis", IEEE Trans. MAG-24, No.1, Jan. 1988, pp212-217

[32] G. Kadar, and E.D. Torre, "Determination of the bilinear product Preisach function", J. Appl. Phys., Vol.63, No.8, April 1988, pp3001-3003

[33] G. Friedman and I.D. Mayergoyz, "Computation of magnetic field in media with hysteresis", IEEE Trans. MAG-25, No.5, Sept. 1989, pp3934-3936

[34] S.R. Naidu, "Simulation of the hysteresis phenomenon using Preisach's theory", IEE Proc.-A, Vol.137, No.2, March 1990, pp73-79

[35] E.D. Torre, J. Oti, and G. Kadar, "Preisach modelling and reversible magnetization", IEEE Trans. MAG-26, No.6, Nov. 1990, pp3052-3058

[36] I.D. Mayergoyz, "The classical Preisach model of hysteresis and reversibility", J. Appl. Phys., Vol.69, No.8, April 1991, pp4602-4604

[37] D. Pescetti, "Some remarks on Preisach modelling", J. Appl. Phys., Vol.69, No.8, April 1991, pp4605-4607

[38] G. Friedman and I.D. Mayergoyz, "Input-dependent Preisach model and hysteretic energy losses", J. Appl. Phys., Vol.69, No.8, April 1991, pp4611-4613

[39] O. Benda, "Possibilities and limits of the Preisach model", Journal of Magnetism and Magnetic Materials, Vol.112, 1992, pp443-446

[40] G.S. Park, S.Y. Hahn, K.S. Lee, and H.K. Jung, "Implementation of hysteresis characteristics using the Preisach model with M-B variables", IEEE Trans. MAG-29, No.2, March 1993, pp1542-1545

[41] I.D. Mayergoyz, "Mathematical models of hysteresis", Springer-Verlag, 1991

[42] S. Sawamura and S. Iwasaki, "Application of internal reaction field on the analysis of anhysteretic magnetization process", IEEE Trans. MAG-6, No.3, Sept. 1970, pp646-649

[43] I.D. Mayergoyz, G. Friedman, C. Salling, "Comparison of the classical and general Preisach hysteresis models with experiments", IEEE Trans. MAG-25, No.6, Sept. 1989, pp3925-3927

[44] F. Ossart, G. Meunier, "Comparison between various hysteresis models and experimental data", IEEE Trans. MAG-26, No.5, Sept. 1990, pp2837-2839

[45] S.Y.R. Hui, and J.G. Zhu, "Magnetic hysteresis modelling and simulation using Preisach theory and TLM technique", Record of the 25th Annual IEEE Power Electronics Specialists Conference (PESC'94), Taipei, Taiwan, Republic of China, June 20-24, 1994, pp837-842

[46] S.Y.R. Hui and J.G. Zhu, "Numerical modelling and simulation of hysteresis effects in magnetic cores using the transmission line modelling and Preisach theory", Submitted to IEE Proceedings Part-B

[47] I.D. Mayergoyz, "Dynamic Preisach models of hysteresis", IEEE Trans. MAG-24, No.6, Nov. 1988, pp2925-2927

[48] J. Oti, F. Vajda, and E.D. Torre, "Identification of parameters in a moving model", J. Appl. Phys., Vol.69, No.8, April 1991, pp4826-4828

[49] E.D. Torre, "Existence of magnetization-dependent Preisach models", IEEE Trans. MAG-27, No.4, July 1991, pp3697-3699

[50] F. Vajda and E.D. Torre, "Efficient numerical implementation of complete-moving-hysteresis models", IEEE Trans. MAG-29, No.2, March 1993, pp1532-1537

[51] E.D. Torre, "Energy considerations in hysteresis models", IEEE Trans. MAG-28, No.5, Sept. 1992, pp2608-2610

[52] F. Vajda and E.D. Torre, "Characteristics of magnetic media models", IEEE Trans. MAG-28, No.5, Sept. 1992, pp2611-2613

[53] G. Kadar and E.D. Torre, "Hysteresis modelling: I. Noncongruency", IEEE Trans. MAG-23, No.5, Sept. 1987, pp2820-2822

[54] E.D. Torre and G. Kadar, "Hysteresis modelling: II. Accommodation", IEEE Trans. MAG-23, No.5, Sept. 1987, pp2823-2825

[55] F. Vajda and E.D. Torre, "Measurements of output-dependent Preisach functions", IEEE Trans. MAG-27, No.6, Nov. 1991, pp4757-4762

[56] F. Vajda and E.D. Torre, "Relationship between the moving and the product Preisach models", IEEE Trans. MAG-27, No.5, Sept. 1991, pp3823-3826

[57] M. Brokate and E.D. Torre, "The wiping-out property of the moving model", IEEE Trans. MAG-27, No.5, Sept. 1991, pp3811-3814

[58] G. Kadar, E. Kisdi-Koszo, L. Kiss, L. Potocky, M. Zatroch, and E.D. Torre, "Bilinear product Preisach modelling of magnetic hysteresis curves", IEEE Trans. MAG-25, No.5, Sept. 1989, pp3931-3933

[59] F. Vajda and E.D. Torre, "Minor loops in magnetization-dependent Preisach models", IEEE Trans. MAG-28, No.2, March 1992, pp1245-1248

[60] R.M. Del Vecchio and S.H. Charap, "Two dimensional hysteresis model", IEEE Trans. MAG-20, No.5, Sept. 1984, pp1437-1439

[61] E.D. Torre, "A vector phenomenological model for digital recording", J. Appl. Phys., Vol.61, No.8, April 1987, pp4016-4018

[62] K. Wiesen and S.H. Charap, "Vector Preisach modelling", J. Appl. Phys., Vol.61, No.8, April 1987, pp4019-4021

[63] I.D. Mayergoyz and G. Friedman, "Isotropic vector Preisach model of hysteresis", J. Appl. Phys., Vol.61, No.8, April 1987, pp4022-4024

[64] I.D. Mayergoyz, "Vector Preisach hysteresis models", J. Appl. Phys., Vol.63, No.8, April 1988, pp2995-3000

[65] E.D. Torre and G. Kadar, "Vector Preisach and the moving model", J. Appl. Phys., Vol.63, No.8, April 1988, pp3004-3006

[66] I.D. Mayergoyz and G. Friedman, "Identification problem for 3D Anisotropic Preisach model of vector hysteresis", IEEE Trans. MAG-24, No.6, Nov. 1988, pp2928-2930

[67] I.D. Mayergoyz, "Dynamic vector Preisach models of hysteresis", J. Appl. Phys., Vol.69, No.8, April 1991, pp4829-4831

[68] B.D. Coleman and M.L. Hodgdon, "A constitutive relation for rate-independent hysteresis in ferromagnetical soft materials", Int. J. Engng. Sci., Vol.24, No.6, 1986, pp897-919

[69] B.D. Coleman and M.L. Hodgdon, "On a class of constitutive relations for ferromagnetic hysteresis", Arch. Rational Mech. Anal., Vol.99, No. 4, 1987, pp375-396

[70] M.L. Hodgdon, "Applications of a theory of ferromagnetic hysteresis", IEEE Trans. MAG-24, No.1, Jan. 1988, pp218-221

[71] M.L. Hodgdon, "Mathematical theory and calculations of magnetic hysteresis curves", IEEE Trans. MAG-24, No.6, Nov. 1988, pp3120-3122

[72] C.D. Boley and M.L. Hodgdon, "Model and simulation of hysteresis in magnetic cores", IEEE Trans. MAG-25, No.5, Sept. 1989, pp3922-3924

[73] L.O. Chua and K.A. Stromsmoe, "Lumped-circuit models for non-linear inductors exhibiting hysteresis loops", IEEE Trans. CT-17, No.4, Nov. 1970, pp564-574

[74] Y. Saito, S. Hayano, T. Yamamura, and N. Tsuya, "A representation of magnetic hysteresis", IEEE Trans. MAG-20, No.5, Sept. 1984, pp1434-1436

[75] S. Hayano, M. Namiki, and Y. Saito, "A magnetization model for computational magnetodynamics", J. Appl. Phys., Vol.69, No.8, April 1991, pp4614-4616

[76] J.G. Zhu and H.N. Bertram, "Micromagnetic studies of thin metallic films", J. Appl. Phys., Vol.63, April 15, 1988, pp3248-3253

[77] D.R. Fredkin and T.R. Koehler, "Numerical micromagnetics of small particles", IEEE Trans. MAG-24, 1988, pp2362-2367

[78] R. Klein and J.J. Niez, " A new method for finite element calculation of micromagnetic problems", IEEE Trans. MAG-24, 1988, pp2371-2373

[79] W. Williams and D.J. Dunlop, "Three dimensional micromagnetic modelling of ferromagnetic domain structure", Nature, Vol.337, Feb. 1989, pp634-637

[80] D. Favier, P. Guelin, and R Cammarano, "Application of a phenomenological elastohysteresis theory to the modelling of magnetisation", 7th Int. Symposium on Magnetic Anisotropy & Coercivity in RE-TM Alloys, Canberra, Australia, 1992, Session 2, pp137-150

[81] R.H. Pry and C.P. Bean, "Calculation of the energy loss in magnetic sheet materials using a domain model", J. Appl. Phys., Vol.29, No.3, March 1958, pp532-533

[82] F. Brailsford and R. Fogg, "Anomalous iron losses in cold reduced grain-oriented transformer steel at very low frequencies", Proc. IEE, Vol.113, No.9, Sep. 1966, pp1562-1564

[83] C.R. Boon and J.A. Robey, "Eddy current loss and domain wall motion in grain oriented silicon iron sheets", Proceedings of the Conference on Magnetic Materials and Their Applications, 26th-28th Sept. 1967, London, U.K., pp105-109

[84] C.R. Boon, "Ferromagnetic domains in grain-oriented silicon-iron under alternating field conditions", Proceedings of the Conference on Magnetic Materials and Their Applications, 26th-28th Sept. 1967, London, U.K., pp110-112

[85] J.A. Robey, "Domain-wall motion and eddy-current loss in grain-oriented silicon-iron sheet", Journal of Science & Technology, Vol.36, No.1, 1969, pp3-10

[86] M.R.G. Sharp, R. Phillips, and K.J. Overshott, "Dependence of loss on domain-wall spacing in polycrystalline material", Proc. IEE Vol.120, No.7, July 1973, pp822-824

[87] M.R.G. Sharp, and K.J. Overshott, "Losses in silicon iron", IEEE Trans. MAG-10, No.2, June 1974, pp113-115

[88] F.J. Young, S.K. Bhate, and W.M. Swift, "Theory of eddy current losses in finite width sheet exhibiting simple bar-like domain structures", IEEE Trans. MAG-10, No.2, June 1974, pp814-816

[89] W.M. Swift, J.W. Shilling, S.K. Bhate, and F.J. Young, "Eddy current losses in a (110)[001] single crystal of 3% Si-Fe", IEEE Trans. MAG-10, June, 1974, pp810-813

[90] C.D. Graham, Jr., "Physical origin of losses in conducting ferromagnetic materials", J. Appl. Phys., Vol.53, No.11, Nov. 1982, pp8276-8280

[91] G. Bertotti, Fiorillo, P. Mazzetti, and G.P. Soardo, "Dynamics of microscopic magnetization processes and magnetic losses", J. Appl. Phys., Vol.53, No.11, Nov. 1982, pp8287-8292

[92] K. Foster, F.E. Werner, and R.M.D. Vecchio, "Loss separation measurements for several electrical steels", J. Appl. Phys., Vol.53, No.11, Nov. 1982, pp8308-8310

[93] J.E.L. Bishop, "Eddy current dominated magnetization processes in grain oriented silicon iron", IEEE Trans. MAG-20, No.5, Sept. 1984, pp1527-1532

[94] G. Bertotti and F. Fiorillo, "Power losses and domain structure dynamics in 3% SiFe single crystals", IEEE Trans. MAG-20, No.5, Sept. 1984, pp1475-1477

[95] G. Bertotti, "Physical interpretation of eddy current losses in ferromagnetic material considerations", J. Appl. Phys., Vol.57, No.6, 15 March 1985, pp2110-2126

[96] J.E.L. Bishop, "Domain models of eddy current loss due to normal magnetization in slightly misoriented (100)[001] SiFe", IEEE Trans. MAG-22, No.4, July 1986, pp272-281

[97] G. Bertotti, "General properties of power losses in soft ferromagnetic materials", IEEE Trans. MAG-24, No.1, 1988, pp621-630

[98] T. Sato and Y. Sakaki, "Physical meaning of equivalent loss resistance of magnetic cores", IEEE Trans. MAG-26, No.5, Sep. 1990, pp2894-2897

[99] F. Fiorillo and A. Novikov, "An improved approach to power losses in magnetic laminations under nonsinusoidal induction waveform", IEEE Trans. MAG-26, No.5, Sep. 1990, pp2904-2910

[100] F. Fiorillo and A. Novikov, "Power losses under sinusoidal, trapezoidal and distorted induction waveform", IEEE Trans. MAG-26, No.5, Sept. 1990, pp2559-2561

[101] H. Pfutzner, P. Schonhuber, B. Erbil, G. Harasko, and T. Klinger, "Problems of loss separation for crystalline and consolidated amorphous soft magnetic materials", IEEE Trans. MAG-27, No.3, May 1991, pp3426-3432

[102] T. Barradi and A. Mailfert, "Incidence of the dynamic behaviour of the domain walls on the iron losses in grain oriented Si-Fe sheets using sinusoidal and non-sinusoidal waveform induction", Journal of Magnetism and Magnetic Materials, Vol.112, 1992, pp6-8

[103] V. Wiglasz, "Power losses in grain-oriented electrical steels", Journal of Magnetism and Magnetic Materials, Vol.112, 1992, pp33-35

[104] T. Nakata, Y. Ishihara, and M. Nakano, "Iron losses of silicon steel core produced by distorted flux", Electron. Eng., Japan, Vol.90, 1970, pp10-20

[105] J.D. Lavers, P.P. Biringer, and H. Hollitscher, "Estimation of core loss when the flux waveform contains the fundamental plus a single odd harmonic component", IEEE Trans. MAG-13, 1977, pp1128-1130

[106] J.D. Lavers, P.P. Biringer, and H. Hollitscher, "A simple method for estimating the minor loop hysteresis loss in thin laminations", IEEE Trans. MAG-14, No.5, 1978, pp386-388

[107] P. Brissonneau and D. Lebouc, "Core losses with trapezoidal waveform of induction", IEEE Trans. MAG-20, No.5, 1984, pp1484-1486

[108] T. Nakata, N. Takahashi, K. Fujiwara, and M. Nakano, "Iron loss under square wave voltage excitation", Physica Scripta, Vol.39, 1989, pp645-647

[109] G.W. Ludwig and S.A. El-Hasmamsy, "Coupled inductance and reluctance models of magnetic components", IEEE Trans. PE-6, No.2, April 1991, pp240-250

[110] J.M. Lopera, A.M. Pernia, J. Diaz, J.M. Alonso, and F. Nuno, "A complete transformer electrical model, including frequency and geometry effects", Record of the IEEE Power Electronics Specialists Conference (PESC'92), June 29 - July 3, 1992, pp1247-1252

[111] V.A. Niemela, H.A. Owen Jr., and T.G. Wilson, "Frequency independent element cross coupled secondaries model for multiwinding transformers", Record of the IEEE Power Electronics Specialists Conference (PESC'92), June 29- July 3, 1992, pp1261-1268

[112] H.A. Owen Jr., V.A. Niemela, and T.G. Wilson, "Enhanced cross coupled secondaries model for multiwinding transformers", Record of the IEEE Power Electronics Specialists Conference (PESC'92), June 29- July 3, 1992, pp1269-1276

[113] R.M. Nelms, and L.L. Grigsby, "Simulation of power electronic circuits containing nonlinear inductances using a sampled data model", Record of the IEEE Power Electronics Specialists Conference (PESC'90), 1990, pp746-749

[114] P.W. Tuinenga, "SPICE a guide to circuit simulation and analysis using PSpice", Prentice-Hall, Englewood Cliffs, NJ, 1987

[115] J.G. Zhu, S.Y.R. Hui, and V.S. Ramsden, "Discrete modelling of magnetic cores including hysteresis, eddy current and anomalous losses", IEE Proc.-A, Vol.140, No.4, July 1993, pp317-322

[116] J.G. Zhu, S.Y.R. Hui, and V.S. Ramsden, "A dynamic circuit model for solid magnetic cores", Record of Power Electronics Specialists Conference (PESC'93), Seattle, Washington, USA, June 20-24, 1993, Vol. , pp1111-1115

[117] J.G. Zhu, S.Y.R. Hui, and V.S. Ramsden, "A generalised dynamic circuit model of magnetic cores for low- and high frequency applications, Part I: Theoretical calculation of the equivalent core loss resistance", Submitted to IEEE Transactions on Power Electronics

[118] S.Y.R. Hui, J.G. Zhu, and V.S. Ramsden, "A generalised dynamic circuit model of magnetic cores for low- and high frequency applications, Part II: Circuit model formulation and implementation", Submitted to IEEE Transactions on Power Electronics

[119] A.J. Moses, "Electrical steels: past, present and future developments", IEE Proc., Vol.137, Pt.A, No.5, Sept. 1990, pp233-245

[120] F.G. Baily, "The hysteresis of iron and steel in a rotating magnetic field", Phil. Trans. Royal Soc. A, 1896, pp715-746

[121] J. Sievert, "Recent advances in the one- and two-dimensional magnetic measurement technique for electrical sheet steel", IEEE Trans. MAG-26, No.5, Sept. 1990, pp2553-2558

[122] K.A. Hempel, "Ferromagnetic materials in a rotating magnetic field: a centennial", First International Workshop on Magnetic Properties of Electrical Sheet Steel under Two-Dimensional Excitation, Proceedings of the 93. PTB-Seminar, Physikalisch-

Technische Bundesanstalt (PTB), Braunschweig (Germany), 16 and 17, Sept., 1991, pp1-10

[123] J. Sievert, "On measuring the magnetic properties of electrical sheet steel under rotational magnetization", Journal of Magnetism and Magnetic Materials 112 (1992), pp50-57

[124] J. Sievert, "Magnetic anisotropy and two-dimensional magnetic phenomena in electrical steel", ISEM Nagoya Conference 1992, paper No.B0-5-2

[125] F. Brailsford, "Rotational hysteresis loss in electrical sheet steels", JIEE, 1938, 83, pp566-575

[126] W.F. Archenhold, H.F. Sandham, and J.E. Thompson, "Rotational hysteresis loss in grain-oriented silicon-iron", British J. Appl. Phys., Vol.11, Jan. 1960, pp46-49

[127] C.R. Boon and J.E. Thompson, "Rotational hysteresis loss in single-crystal silicon iron", Proc. IEE, Vol.111, No.3, Mar. 1964, pp605-609

[128] P.J. Flanders, "The rotating-sample magnetometer", J. Appl. Phys., Vol.38, No.3, March 1967, pp1293-1294

[129] P.J. Flanders, "Utilization of a rotating sample magnetometer", The Review of Scientific Instruments, Vol.41, No.5, May 1970, pp697-710

[130] K. Narita and T. Yamaguchi, "Rotational loss in silicon-iron single crystal with (001) surfaces", IEEE Trans. MAG-10, No.2, June 1974, pp165-167

[131] A. Cecchitti, G. Ferrari, F. Masoli, and G.P. Soardo, "Rotational power losses in 3% SiFe as a function of frequency", IEEE Trans. MAG-14, No.5, Sept. 1978, pp356-358

[132] G.C. Grimwood, A.M. Cambell, and J.E. Evetts, "Rotational hysteresis in polycrystalline alloys", IEEE Trans. MAG-14, No.5, Sept. 1978, pp359-361

[133] P.J. Flanders, "A Hall sensing magnetometer for measuring magnetization, anisotropy, rotational loss and time effects", IEEE Trans. MAG-21, No.5, Sept. 1985, pp1584-1589

[134] K.S. Tan, A. Datta, P.J. Flanders, and C.D. Graham, Jr., "Rotational loss in thin gauge soft magnetic materials", IEEE Trans. MAG-21, No.5, Sept. 1985, pp1921-1923

[135] F.J. Young and H.L. Schenk, "Method for measuring iron losses in elliptically polarized magnetic fields", J. Appl. Phys., Vol.31, No.5, May 1960, pp194s-195s

[136] A. Kaplan, "Magnetic core losses resulting from a rotating flux", J. Appl. Phys., Vol.32, No.3, March 1961, pp370s-371s

[137] R.D. Strattant and F.J. Young, "Iron losses in elliptical rotating fields", J. Appl. Phys., Vol.33, No.3, March 1962, pp1285-1286

[138] C.R. Boon and J.E. Thompson, "Alternating and rotational power loss at 50c/s in 3% silicon-iron sheets", Proc. IEE, Vol.112, No.11, Nov. 1965, pp2147-2151

[139] K. Narita, M. Yanagisawa, M. Tanaka, "Method for measuring rotational core losses in silicon iron sheets", Bull. Electrotech. Lab. (Japan), 1966, 30, pp827-833 (in Japanese)

[140] A.J. Moses and B. Thomas, "Measurement of rotating flux in silicon iron laminations", IEEE Trans. MAG-9, No.4, Dec. 1973, pp651-654

[141] A. Basak and A.J. Moses, "Influence of stress on rotational loss in silicon iron", Proc. IEE, Vol.125, No.2, Feb. 1978, pp165-168

[142] W. Brix, K.A. Hempel, and W. Schroeder, "Method for the measurement of rotational power loss and related properties in electrical steel sheets", IEEE Trans. MAG-18, No.6, Nov. 1982, pp1469-1471

[143] W. Brix, "Verlust und Anisotropie von nichtorientiertem Elektroblech in magnetschen Drehfeldern", Von der Fakultät für Elektrotechnik der Rheinisch-Westfälischen Technischen Grades eines Doktor-Ingenieurs genehmigte Dissertation, 1983

[144] W. Brix, K.A. Hempel, and F.J. Schulte, "Improved method for the investigation of the rotational magnetization process in electrical steel sheets", IEEE Trans. MAG-20, No.5, Sept. 1984, pp1708-1710

[145] T. Sasaki, M. Imamura, S. Takada, and Y. Suzuki, "Measurement of rotational power losses in silicon-iron sheets using wattmeter method", IEEE Trans. MAG-21, No.5, Sept. 1985, pp1918-1920

[146] E. Reisinger, "Measurement of iron losses due to alternating and rotating magnetization", Electric Energy Conference 1987, Adelaide, 6-9 Oct. 1987, pp388-392

[147] F. Fiorillo and A.M. Reitto, "Extended induction range analysis of rotational losses in soft magnetic materials", IEEE Trans. MAG-24, 1988, pp1960-1962

[148] F. J. Schulte, "Eine Meßeinrichtung zur zweidimensionalen Erfassung der magnetischen Eignschaften von Elektroblech", Dissertation RWTH Aachen 1989, Fakultät für Elektrotechnik

[149] M. Enokizono and J.D. Sievert, "Magnetic field and loss analysis in an apparatus for the determination of rotational loss", Physica Scripta, Vol.39, 1989, pp356-359

[150] M. Enokizono, T. Suzuki, and J.D. Sievert, "Measurement of dynamic magnetostriction under rotating magnetic field", IEEE Trans. MAG-26, No.5, Sept. 1990, pp2067-2069

[151] M. Enokizono, T. Suzuki, J. Sievert, and J. Xu, "Rotational power loss of silicon steel sheet", IEEE Trans. MAG-26, No.5, Sept. 1990, pp2562-2564

[152] J. Sievert, J. Xu, L. Rahf, M. Enokizono, and H. Ahlers, "Studies on the rotational power loss measurement problem", Anales de Fisica Serie B, Vol.86 (1990), pp35-37

[153] M. Enokizono and J. Sievert, "Numerical analysis of accuracy of rotational magnetic loss measurement apparatus", IEEE Translation Journal on Magnetics in Japan, Vol.5, No.9, Sept. 1990, pp742-748

[154] M. Enokizono, J. Sievert, and H. Ahlers, "Optimum yoke construction for rotational power loss measurements apparatus", Anales de Fisica, Vol.86, 1990, pp320-322

[155] M. Enokizono, T. Suzuki, and J. Sievert, "Measurement of iron loss using rotational magnetic loss measurement apparatus", J. Applied Mag. in Japan, Vol.14, No.2, 1990, pp455-458, (in Japanese)

[156] M. Enokizono, T. Suzuki, and J. Sievert, "Rotational dynamic magnetostriction of Si-Fe sheet", J. Applied Mag. in Japan, Vol.15, No.2, 1991, pp261-264, (in Japanese)

[157] M. Enokizono, G. Shirakawa, T. Suzuki, and J. Sievert, "Two-dimensional magnetic properties of silicon steel sheet", J. Applied Mag. in Japan, Vol.15, No.2, 1991, pp265-270, (in Japanese)

[158] M. Enokizono and S. Nagata, "Non-destructive testing with magnetic sensor using rotational magnetic flux", J. Applied Mag. in Japan, Vol.15, No.2, 1991, pp455-460, (in Japanese)

[159] M. Enokizono, T. Todaka, T. Sashikata, J.D. Sievert, and H. Ahlers, "Magnetic field analysis of rotational loss tester with vertical yoke", SMM10, 1991 in Dresden

[160] M. Enokizono, G. Shirakawa, and J. Sievert, "Anomalous anisotropy and rotational magnetic properties of amorphous sheet", SMM10, 1991 in Dresden

[161] W. Salz and K.A. Hempel, "Anisotropy of grain-oriented steel sheet under various elliptical field conditions", J. Appl. Phys. 70(10), 15 Nov. 1991, pp6268-6270

[162] G.S. Radley, "Domain observation and wall velocity measurement under rotating field in grain-oriented silicon iron", First International Workshop on Magnetic Properties of Electrical Sheet Steel under Two-Dimensional Excitation, Proceedings of the 93. PTB-Seminar, Physikalisch-Technische Bundesanstalt (PTB), Braunschweig (Germany), 16 and 17, Sept., 1991, pp25-35

[163] A. Kedous-Lebouc, S. Zouzou, and P. Brissonneau, "On the magnetization processes in electrical steel in unidirectional and rotational field", First International Workshop on Magnetic Properties of Electrical Sheet Steel under Two-Dimensional Excitation, Proceedings of the 93. PTB-Seminar, Physikalisch-Technische Bundesanstalt (PTB), Braunschweig (Germany), 16 and 17, Sept., 1991, pp36-47

[164] T. Tanaka, S. Takada, and T. Sasaki, "Measurement of rotational power loss and magnetization curves in a strip sample", First International Workshop on Magnetic

Properties of Electrical Sheet Steel under Two-Dimensional Excitation, Proceedings of the 93. PTB-Seminar, Physikalisch-Technische Bundesanstalt (PTB), Braunschweig (Germany), 16 and 17, Sept., 1991, pp71-81

[165] M. Enokizono, "Studies on two-dimensional magnetic measurement and properties of electrical steel sheets at Oita University", First International Workshop on Magnetic Properties of Electrical Sheet Steel under Two-Dimensional Excitation, Proceedings of the 93. PTB-Seminar, Physikalisch-Technische Bundesanstalt (PTB), Braunschweig (Germany), 16 and 17, Sept., 1991, pp82-101

[166] J. Sievert, "Studies on the measurement of two dimensional magnetic phenomena in electrical sheet steel at PTB", First International Workshop on Magnetic Properties of Electrical Sheet Steel under Two-Dimensional Excitation, Proceedings of the 93. PTB-Seminar, Physikalisch-Technische Bundesanstalt (PTB), Braunschweig (Germany), 16 and 17, Sept., 1991, pp102-116

[167] M. Enokizono and G. Shirakawa, "Rotational dynamic magnetostriction of silicon steel sheets", First International Workshop on Magnetic Properties of Electrical Sheet Steel under Two-Dimensional Excitation, Proceedings of the 93. PTB-Seminar, Physikalisch-Technische Bundesanstalt (PTB), Braunschweig (Germany), 16 and 17, Sept., 1991, pp151-161

[168] F. Fiorillo and A.M. Rietto, "The measurement of rotational losses at I.E.N.: Use of the thermometric method", First International Workshop on Magnetic Properties of Electrical Sheet Steel under Two-Dimensional Excitation, Proceedings of the 93. PTB-Seminar, Physikalisch-Technische Bundesanstalt (PTB), Braunschweig (Germany), 16 and 17, Sept., 1991, pp162-172

[169] A.M. Gumaidh, W.L. Mahadi, Y. Alinejad-Beromi, A.J. Moses, and T. Meydan, "Measurement and analysis of rotational power loss in soft magnetic materials", First International Workshop on Magnetic Properties of Electrical Sheet Steel under Two-Dimensional Excitation, Proceedings of the 93. PTB-Seminar, Physikalisch-Technische Bundesanstalt (PTB), Braunschweig (Germany), 16 and 17, Sept., 1991, pp173-190

[170] T. Nakata, "Improvements of measuring equipment for rotational power loss", First International Workshop on Magnetic Properties of Electrical Sheet Steel under Two-Dimensional Excitation, Proceedings of the 93. PTB-Seminar, Physikalisch-

Technische Bundesanstalt (PTB), Braunschweig (Germany), 16 and 17, Sept., 1991, pp191-203

[171] Y. Ishihara, "Measuring method of magnetic characteristics in any direction for silicon steel", First International Workshop on Magnetic Properties of Electrical Sheet Steel under Two-Dimensional Excitation, Proceedings of the 93. PTB-Seminar, Physikalisch-Technische Bundesanstalt (PTB), Braunschweig (Germany), 16 and 17, Sept., 1991, pp204-206

[172] W. Salz and K.A. Hempel, "Magnetic properties of staboperm", Journal of Magnetism and Magnetic Materials 112 (1992), pp242-244

[173] M. Enokizono, G. Shirakawa, and J. Sievert, "Anomalous anisotropy and rotational magnetic properties of amorphous sheet", Journal of Magnetism and Magnetic Materials 112 (1992), pp195-199

[174] J. Sievert, H. Ahlers, M. Enokizono, S. Kauke, L. Rahf, and J. Xu, "The measurement of rotational power loss in electrical sheet steel using a vertical yoke system", Journal of Magnetism and Magnetic Materials 112 (1992), pp91-94

[175] M. Enokizono, T. Todaka, T. Sashikata, J.D. Sievert, and H. Ahlers, "Magnetic field analysis of rotational loss tester with vertical yoke", Journal of Magnetism and Magnetic Materials 112 (1992), pp81-84

[176] Y. Alinejad-Beromi, A.J. Moses, and T. Meydan, "New aspects of rotational field and flux measurement in electrical steel", Journal of Magnetism and Magnetic Materials 112 (1992), pp135-138

[177] H. Morino, Y. Ishihara, and T. Todaka, "Measuring method of magnetic characteristics in any direction for silicon steel", Journal of Magnetism and Magnetic Materials 112 (1992), pp115-119

[178] S. Zouzou, A. Kedous-Lebous, and P. Brissonneau, "Magnetic properties under unidirectional and rotational field", Journal of Magnetism and Magnetic Materials 112 (1992), pp106-108

[179] F. Fiorillo and A.M. Rietto, "Rotational and alternating energy loss vs. magnetizing frequency in SiFe laminations", Journal of Magnetism and Magnetic Materials 83 (1993), pp402-404

[180] J.G. Zhu and V.S. Ramsden, "Two dimensional measurement of magnetic field and core loss using a square specimen tester", IEEE Trans. MAG-29, No.6, Nov. 1993, pp2995-2997

[181] A.J. Moses and B. Thomas, "The spatial variation of localized power loss in two practical transformer T-joints", IEEE Trans. MAG-9, No.4, Dec. 1973, pp655-659

[182] J. Sievert, "On the situation regarding the standardization of the determination of magnetic properties of electrical steel under 2-dimensional excitation", Second International Workshop on Magnetic Properties of Electrical Sheet Steel under Two-Dimensional Excitation, Oita (Japan), Jan. 1992

[183] R. Phillips and K.J. Overshott, "Domain configuration under rotational flux and applied stress conditions in silicon-iron", IEEE Trans. MAG-10, No.2, June 1974, pp168-169

[184] F. Fiorillo, "A phenomenological approach to rotational power losses in soft magnetic laminations", First International Workshop on Magnetic Properties of Electrical Sheet Steel under Two-Dimensional Excitation, Proceedings of the 93. PTB-Seminar, Physikalisch-Technische Bundesanstalt (PTB), Braunschweig (Germany), 16 and 17, Sept., 1991, pp11-24

[185] T. Nakata, M. Nakano, and H. Fujii, "Magnetic characteristics in arbitrary direction of grain oriented silicon steel", Papers of National Convention, Magnetics Society of Japan, No.10aG-1 (1990)

[186] Private discussions with Dr. Sievert, head of the Magnetic Measurement Techniques Laboratory, Physikalisch-Technische Bundesanstalt (PTB), Braunschweig, Germany, in April 1993, when the author visited PTB after attending the International Magnetics Conference (INTERMAG'93), Stockholm, Sweden.

[187] Private discussions with Dr. Sievert, head of the Magnetic Measurement Techniques Laboratory, Physikalisch-Technische Bundesanstalt (PTB), Braunschweig, Germany, and practical measurements using the rotational core loss testers at PTB, during

December 8, 1993 to February 24, 1994, when the author visited PTB as a guest scientist for a cooperative research project of rotational core loss measurement.

[188] F.A. Fouad, "Finite element analysis for design of classical and electronically operated machines", Ph.D dissertation, Virginia Polytechnic Institute and State University, 1981

[189] T. Nakata, "Numerical analysis of flux and loss distributions in electrical machinery", IEEE Trans. MAG-20, No.5, Sept. 1984, pp1750-1755

[190] G.R. Slemon and X. Liu, "Core losses in permanent magnet motors", IEEE Trans. MAG-26, No.5, Sep. 1990, pp1653-1655

[191] R. Rabinovici, "Eddy current losses of permanent magnet motors", IEE Proc.-electr. Power Appl., Vol.141, No.1, Jan. 1994, pp7-11

[192] G. Bertotti, A. Boglietti, M. Chiampi, D. Chiarabaglio, F. Fiorillo, and M. Lazzari, "An improved estimation of iron losses in rotating electrical machines", IEEE Trans. MAG-27, No.6, Nov. 1991, pp5007-5009

[193] K. Atallah, Z.Q. Zhu, and D. Howe, "The prediction of iron losses in brushless permanent magnet dc motors", Proceedings of International Conference on Electrical Machines (ICEM), Manchester, U.K., 15th-17th Sept. 1992, pp814-818

[194] K. Atallah, Z.Q. Zhu, and D. Howe, "An improved method for predicting iron losses in brushless permanent magnet dc drives", IEEE Trans. MAG-28, No.5, Sept. 1992, pp2997-2999

[195] J.G. Zhu, V.S. Ramsden, and P.A. Watterson, "Finite element calculation of core losses in motors with non-sinusoidal fields", Proceedings of International Conference on Electrical Machines (ICEM), Manchester, U.K., 15th-17th Sept. 1992, pp1182-1186

[196] J.G. Zhu and V.S. Ramsden, "Core loss modelling in rotational electrical machines", Proceedings of the International Conference on Electrical Machines in Australia (ICEMA), Adelaide, Australia, 14-16 September 1993, pp52-57

[197] N.F. Astbury, "Industrial magnetic testing", The Institude of Physics, London, 1952

[198] V.S. Ramsden, "The loss in solid poles of synchronous machines on load", Ph.D dissertation, The University of Aston in Birmingham, U.K., 1972

[199] D. O'Kelly, "Flux penetration and losses in steel plate with nonsinusoidal magnetisation", IEE Proc. A, Vol.135, No.4, April 1988, pp193-198

[200] D. O'Kelly, "Losses and flux penetration in non-grain-oriented low loss steel with nonsinusoidal excitation", IEE Proc. A, Vol.135, No.4, April 1988, pp199-207

[201] N. Burais and G. Grellet, "Numerical modelling of iron losses in ferromagnetic steel plate", IEEE Trans. MAG-18, No.2, Mar. 1982, pp558-562.

[202] S.R. Naidu, "Time domain model for the ferromagnetic core, including the effects of hysteresis and eddy currents", IEE Proc. A, Vol.138, No.1, Jan. 1991, pp44-50.

[203] S.Y.R. Hui and C. Christopolous, "Discrete transform technique for solving coupled integro-differential equations in digital computers", IEE Proc. A, Vol.138, No.5, Sept. 1991, pp273-280

[204] S.Y.R. Hui and C. Christopolous, "Discrete transform technique for solving non-linear circuits and equations", IEE Proc. A, Vol.139, No.6, Nov. 1992, pp321-328

[205] S.Y.R. Hui, K.K. Fung, M.Q. Zhang and C. Christopolous, "Variable time step technique for transmission line modelling", IEE Proc. A, Vol. 140, No.4, 1993, pp299-302

[206] R.L. Stoll, "The analysis of eddy currents", Clarendon Press. Oxford, 1974

[207] SIEMENS, "Ferrites and Accessories, data book 1990/1991"

[208] International Electrotechnical Commission, "Magnetic Materials, Part 3: Methods of measurements of the magnetic properties of magnetic sheet and strip by means of a single sheet tester", 404-3 © IEC

[209] E. Werner, Austria Patent No.19115 (1949)

[210] R.E. Tompkins, L.H. Stauffer, and A. Kaplan, "New Magnetic Core Loss Comparator", J. Appl. Phys., Vol.29, No.3, Mar. 1958, pp502-503

[211] W. Salz and K.A. Hempel, "Which field sensors are suitable for a rotating flux apparatus", First International Workshop on Magnetic Properties of Electrical Sheet Steel under Two-Dimensional Excitation, Proceedings of the 93. PTB-Seminar, Physikalisch-Technische Bundesanstalt (PTB), Braunschweig (Germany), 16 and 17, Sept., 1991, pp117-126

[212] T. Nakata, Y. Kawase, and M. Nakano, "Improvement of measuring accuracy of magnetic field strength in single sheet testers by using two H coils", IEEE Trans. MAG-23, No.5, Sept. 1987, pp2596-2598

[213] Nippon Steel Corporation, "ORIENT.HiB, Grain oriented electrical steel sheets", Data book

[214] Associative Measurement Pty Ltd, Sydney, Australia, "AMLAB reference manual, Version 1.84", 1993

[215] P. Silvester, "Modern electromagnetic fields", Prentice-Hall, 1968

[216] Nippon Steel Corporation, "Technical data on ORIENTCORE.HI-B", Fourth edition, 1984

[217] Dr-Ing. Carl Heck, "Magnetic materials and their applications", Butterworths & Co. (Publishers) Ltd, 1974

[218] A. Hameed and K.J. Binns, "MOTOR-CAD, A finite element package for designing electrical machines with or without magnets", Liverpool University, U.K., 1989

[219] Private discussions with Dr. Fiorillo in April 1993, at the International Magnetics Conference (INTERMAG'93), Stockholm, Sweden.

[220] P.A. Watterson, J.G. Zhu, and V.S. Ramsden, "Optimization of permanent magnet motors using field calculations of increasing precision", IEEE Trans. MAG-28, No.2, March 1992, pp1589-1592

[221] P.A. Watterson, V.S. Ramsden, and J.G. Zhu, "A methodology for generating 1-D profiles from 2-D finite element solutions", Proceedings of the sixth international

conference in Australia on finite element methods, University of Sydney, July 8-10, 1991, pp121-124

[222] Shi Kung Chen, "Design of electrical machines", (in Chinese), Mechanical Industry Press, Beijing, China, 1982

[223] V.S. Ramsden, P.A. Watterson, and J.B. Dunlop, "Optimisation of REPM motors for specific applications", Proceedings of the 12th International Workshop on Rare-Earth Magnets and Their Applications, Canberra, Australia, July 1992, pp296-307